

**A study on the near-surface flow and acoustic emissions of trailing edge serrations
For the purpose of noise reduction of wind turbine blades**

Arce León, Carlos

DOI

[10.4233/uuid:ee9b5495-fde2-4bb1-807d-e7547f2a393d](https://doi.org/10.4233/uuid:ee9b5495-fde2-4bb1-807d-e7547f2a393d)

Publication date

2017

Document Version

Final published version

Citation (APA)

Arce León, C. (2017). *A study on the near-surface flow and acoustic emissions of trailing edge serrations: For the purpose of noise reduction of wind turbine blades*. [Dissertation (TU Delft), Delft University of Technology]. <https://doi.org/10.4233/uuid:ee9b5495-fde2-4bb1-807d-e7547f2a393d>

Important note

To cite this publication, please use the final published version (if applicable).
Please check the document version above.

Copyright

Other than for strictly personal use, it is not permitted to download, forward or distribute the text or part of it, without the consent of the author(s) and/or copyright holder(s), unless the work is under an open content license such as Creative Commons.

Takedown policy

Please contact us and provide details if you believe this document breaches copyrights.
We will remove access to the work immediately and investigate your claim.

A STUDY ON THE NEAR-SURFACE FLOW AND ACOUSTIC EMISSIONS OF TRAILING EDGE SERRATIONS

FOR THE PURPOSE OF NOISE REDUCTION OF WIND TURBINE
BLADES

A STUDY ON THE NEAR-SURFACE FLOW AND ACOUSTIC EMISSIONS OF TRAILING EDGE SERRATIONS

FOR THE PURPOSE OF NOISE REDUCTION OF WIND TURBINE
BLADES

Proefschrift

ter verkrijging van de graad van doctor
aan de Technische Universiteit Delft,
op gezag van de Rector Magnificus prof. ir. K.C.A.M. Luyben,
voorzitter van het College voor Promoties,
in het openbaar te verdedigen op donderdag 14 september 2017 om 15:00 uur.

door

Carlos Andrés ARCE LEÓN

Masters of Science in Scientific Computing,
Uppsala Universitet, Uppsala, Sweden,
geboren te San José, Costa Rica.

Dit proefschrift is goedgekeurd door de

promotor: prof. dr. F. Scarano

copromotor: dr. D. Ragni

Samenstelling promotiecommissie:

Rector Magnificus,	voorzitter
Prof. dr. F. Scarano,	Technische Universiteit Delft
Dr. D. Ragni,	Technische Universiteit Delft

Onafhankelijke leden:

Prof. dr. P. Joseph	University of Southampton
Prof. dr. T.P. Chong	Brunel University
Prof. dr. D. Cassalino	Technische Universiteit Delft
Dr. A. Fischer	Danish Technical University
Dr. S. Oerlemans	Siemens Gamesa



Keywords: Aeroacoustics, Trailing Edge Serrations, Wind Turbine Blades, Particle Image Velocimetry, Acoustic Array Beamforming

Printed by: Gildeprint

Front & Back: Design inspired by the [painted ox carts of Costa Rica](#), a national symbol that embodies the cultural and historical significance of coffee production in that country, and the labor of its farmers. By [Pieter Buijs](#), Inga and Carlos.

Copyright © 2017 by C.A. Arce León

The work here presented was supported by Innovation Fund Denmark, Industrial PhD Programme project 11-109522, and LM Wind Power.

ISBN 978-94-92516-68-8

An electronic version of this dissertation is available at
<http://repository.tudelft.nl/>.

To my parents and Inga,
for your unrelenting support.

CONTENTS

Summary	xi
Samenvatting	xiii
Preface	xvii
1 Introduction	1
1.1 A brief recount of wind as a means to produce electricity	2
1.2 The issue of wind turbine noise	3
1.3 Sources of wind turbine noise	5
1.4 Mitigating TBL-TE noise	11
1.5 Economic impact of noise reduction by serrations	14
1.6 Objectives and motivation	15
Bibliography	17
2 Overview of aeroacoustics and airfoil trailing edge noise	23
2.1 Airfoil trailing edge noise	24
2.1.1 The Amiet model	25
2.1.2 The Howe model	26
2.1.3 The TNO-Blake model	27
2.2 Variable-shape trailing edge noise models	29
2.2.1 The Howe model	29
2.2.2 The Lyu model	31
2.3 Overview of research on trailing edge serrations	32
Bibliography	41
3 Measurement methodology	47
3.1 Wind tunnel facility	48
3.2 Particle image velocimetry	50
3.2.1 Working principle of PIV	50
3.2.2 Imaging and optical considerations	52
3.2.3 The Scheimpflug principle	53
3.2.4 Optimal PIV seeding and timing guidelines	55
3.2.5 Stereoscopic particle image velocimetry	55
3.2.6 Error quantification	57
3.3 Acoustic beamforming	58
3.3.1 Working principle of conventional beamforming	60
Bibliography	61

4	Mean-flow and acoustics of serrations, and their departure from the analytical approach	65
4.1	Experimental setup	67
4.1.1	Stereoscopic PIV	68
4.1.2	Acoustic measurements	70
4.1.3	Angle of attack correction	70
4.2	Results and discussion	71
4.2.1	Mean flow topology	71
4.2.2	Boundary layer across serrations.	76
4.2.3	Turbulence statistics	76
4.2.4	Noise emissions	85
4.3	Conclusions.	88
	Bibliography	88
5	Boundary layer and acoustic emission characterization of flow-aligned serrations	93
5.1	Experimental setup	96
5.1.1	Stereoscopic PIV	96
5.1.2	Microphone array	100
5.2	Results	101
5.2.1	Mean flow characterization of the turbulent boundary layer	102
5.2.2	Turbulence statistics and qualitative analysis of surface pressure	106
5.2.3	Beamforming results.	117
5.3	Conclusions.	119
	Bibliography	121
6	Effect of trailing edge serration-flow misalignment on airfoil noise emissions	125
6.1	Experimental setup	127
6.1.1	Flow facility, model, and flow conditions.	127
6.1.2	Acoustic measurements	128
6.1.3	Velocity measurements	129
6.2	Results	132
6.2.1	Acoustic emissions.	132
6.2.2	Crossover frequency scaling	135
6.2.3	Near-edge flow characterization	137
6.2.4	Characterization of the near-edge time-resolved flow	140
6.3	Conclusions.	142
	Bibliography	143
7	Acoustic emissions of semi-permeable trailing edge serrations	147
7.1	Experimental setup	148
7.2	Measurement methodology.	149
7.3	Results	150
7.4	Discussion	152
7.5	Conclusions.	153
	Bibliography	154

8 Conclusion	157
Bibliography	164
Epilogue	167
Acknowledgements	169
Acronyms	175
Index	177
External art and work attributions	179
Curriculum Vitæ	181
List of Publications	183

SUMMARY

The flow near the surface, and the acoustic emissions of trailing edge serrations are investigated in this work.

The use of this family of aerodynamic devices on airfoils is intended for the reduction of turbulent boundary layer-trailing edge noise (TBL-TE noise). This purpose has been well demonstrated in wind tunnel and numerical experiments. Particularly, their use in the wind turbine industry has been of great interest in recent years. A growing number of field measurements have shown that a noticeable noise reduction of TBL-TE noise in state-of-the-art blades is also obtained.

A full explanation on the mechanism of how noise is reduced is nevertheless lacking. Existing experimental research on serrations offers only a limited characterization of the relevant flow parameters. Fundamental concerns pertaining to the conditions at which that data has been previously gathered are furthermore recurrent. The persistent use of flow-misaligned serrations creates a situation in which flow structures may be observed and misinterpreted as necessary for the attainment of noise reduction. This circumstance complicates the discussion and isolation of the relevant noise reduction mechanism.

The current work highlights this situation. It uses a symmetric airfoil as a baseline on which serrations are installed parallel to its chord-line. This geometry allows the attainment of serration-flow alignment by attempting equal flow conditions over the upper and lower serration surfaces. High-speed particle image velocimetry (PIV) is utilized to characterize the flow in the turbulent boundary layer. Particular attention is paid to the description of the flow near the trailing edges of both the unserrated and the serrated airfoil. A detailed description of the hydrodynamic field is thereby obtained. It is used to discuss streamwise variations along the serration edges. Elements of the TNO-Blake equation are further employed, along with a Reynolds stress quadrant analysis, to approximate a qualitative description of the surface pressure streamwise evolution.

The condition of serration-flow misalignment is further investigated, and its effect on the mean flow and turbulence statistics in the boundary layer is assessed. It is prescribed through a combination of angles of attach and serration flap angles. The measurements are used to assess the sensitivity of the flow to either these parameters. The alterations in the flow field are found to result in significant flow deflection near the serration surface. The formation of strong streamwise vortices in the wake is also evidenced, and seen to originate from the serration tooth sides.

Throughout this work, acoustic beamforming is used to evaluate the changes made to the acoustic emissions of the airfoil by the introduction of the trailing edge serrations. This method allows to obtain a credible evaluation of the isolated trailing edge noise source. This is achieved by the direct assessment of the acoustic sources in the acoustic field of view, allowing an immediate evaluation of the experimental setup. The results are further integrated solely in the region of interest, allowing a selective exclusion of

unrelated sources. As these extraneous sources are typically known to originate from the tunnel nozzle, the side plate trailing edges, and the side plate boundary layer interaction with the airfoil, their inclusion in the results would be almost inevitable when using single-microphone methods, risking inaccurate observations.

The availability of these acoustic measurements provide confirmation of the noise reduction by the introduction of trailing edge serrations. They are further used to assess the analytical models, which have been known to significantly overestimate the levels of noise reduction, or incorrectly predict the resulting spectral shape of the emitted noise. These findings are replicated here. The analytic models are further discussed within the premise of the flow behavior assumed by the models. When flow-aligned, no such large flow modification is observed that could substantiate the observed noise reduction discrepancies.

The acoustic measurements have further been evaluated along with the hydrodynamic characterization of near-surface PIV measurements, for the flow-misaligned serrations. An increase in noise above a certain frequency has previously been reported for serrations, and assumed to be caused by their misalignment with the flow. A constant Strouhal number used to describe this frequency has further been proposed. The high-frequency noise increase is confirmed in this study, as is its relation to the flow-misalignment. The detailed flow measurements allow a more critical evaluation of its relationship to a Strouhal number. What is found is that the latter, while not constant, *does* correlate well with the freestream velocity and the airfoil incidence angle. High-speed PIV is additionally used to localize the source of the high-frequency noise increase. While it had earlier been speculated to be due to increased turbulence *between* the serration teeth due to their misalignment, it is here shown that it originates from the increase in energy of the smaller turbulent eddies convecting past the pressure side serration edge.

Finally, an investigation of several serration geometries is conducted. Surface permeability is prescribed to two of them by the use of a slitted design. Promising results had been previously reported for one of these designs, especially for avoiding the aforementioned high-frequency noise increase. While those results could not be replicated here, the semi-permeable designs were shown to provide a good reference case for the investigation of the edge scattering efficiency. Available flow measurements of the flow-aligned slitted and solid serrations have shown only modest flow modification. The large differences in the acoustic emissions between them must therefore be driven by means other than a beneficial flow alteration. This evidence therefore supports the argument that the fundamental noise reduction mechanism offered by the serrations remains the beneficial modification of the scattering efficiency at the trailing edges.

SAMENVATTING

De stroming nabij het oppervlak, en de akoestische emissie van de achterrand vertanding zijn onderzocht in dit werk.

Het gebruik van deze familie van aerodynamische hulpmiddelen op profielen is bedoeld om de turbulente grenslaag-achterraand (*Turbulent Boundary Layer-Trailing Edge*, TBL-TE, in het Engels) geluidsemissie te reduceren. Dit doel is al goed gedemonstreerd in wind tunnel en numerieke experimenten. Vooral hun gebruik in de wind industrie is van groot interesse geweest de afgelopen jaren. Een groeiend aantal veldtesten hebben ook een waarneembare reducering in TBL-TE geluidsemissie in moderne wind turbine bladen laten zien.

Een volledige verklaring van het mechanisme hoe de reducering van geluidsemissie tot stand komt is nog niet gevonden. Bestaand experimenteel onderzoek op vertanding stellen gelimiteerde karakteristieke van de relevante stromingsparameters beschikbaar. Fundamentele problemen in verband met de omstandigheden waarbij de gegevens eerder verzameld zijn ook terugkerend. Het aanhoudende gebruik van niet op de stroming uitgelijnde vertandingen, genereren een situatie waarin stromingsstructuren kunnen worden waargenomen en verkeerd worden geïnterpreteerd als noodzakelijk voor het bereiken van geluidsreducering. Deze omstandigheden vermoeilijken de discussies en isolering van relevant geluid reducerende mechanismen

Het huidige werk benadrukt deze situatie. Het maakt gebruik van een symmetrisch vleugelprofiel als basis waarop vertandingen evenwijdig aan diens koorde zijn geïnstalleerd. Deze geometrie maakt het bereiken van uitgelijnde stroming over de vertanding mogelijk door te proberen gelijke stromingsomstandigheden over de bovenste en onderste oppervlakken van de vertanding te genereren. Hoge snelheid Particle Image Velocimetry (PIV) wordt gebruikt om de stroming in de turbulente grenslaag te karakteriseren. In het bijzonder wordt aandacht besteed aan de beschrijving van de stroming nabij de achterrand van zowel het profiel met vertanding als het profiel zonder vertanding. Een gedetailleerde beschrijving van het hydrodynamische veld wordt hierbij verkregen. Het wordt gebruikt om variaties in de stromingsrichting langs de vertanding randen te bespreken. Elementen van de TNO-Blake vergelijking worden verder toegepast, samen met een Reynolds spanningskwadrant analyse, voor het verkrijgen van een benadering van een kwalitatieve beschrijving van de oppervlaktedruk evolutie in stromingsrichting.

De conditie van niet uitgelijnde stroming over de vertanding is verder onderzocht, en het effect op de gemiddelde stroming en statistieke van de turbulentie in de grenslaag wordt bepaald. Het wordt beschreven door een combinatie van bevestigingshoeken en vertanding flap hoeken. De metingen worden gebruikt om de gevoeligheid van de stroming te beoordelen voor elke van deze variabelen. De veranderingen in het stromingsveld blijken te resulteren in aanzienlijke stroomafbuiging nabij het oppervlak van de vertanding. De vorming van sterke wervels in de stromingsrichting in het zog zijn ook bewezen en zijn afkomstig van de vertanding tandzijden.

In dit rapport wordt akoestische bundelvorming gebruikt om de veranderingen van de geluidsemissie van het profiel door de introductie van de achterrاند vertanding te evalueren. Deze werkwijze maakt het mogelijk een betrouwbare evaluatie van de geïsoleerde achterrاند geluidsemissie te verkrijgen. Dit wordt bereikt door directe bepaling van de geluidsbronnen in het akoestische gezichtsveld, waardoor een onmiddellijke evaluatie van de experimentele opstelling wordt verkregen. De resultaten worden verder geïntegreerd, afgezonderd in het interessegebied, waardoor een selectieve uitsluiting van ongerelateerde bronnen plaatsvindt. Aangezien deze externe bronnen typisch afkomstig zijn uit de tunnel straalbuis, de zijplaat achterranden en de zijplaat grenslaag interactie met het profiel, zouden hun opname in de resultaten bijna onvermijdelijk zijn bij gebruik van één-microfoon methodiek, waardoor onnauwkeurige waarnemingen worden gerisikeerd.

De beschikbaarheid van deze akoestische metingen bevestiging de geluidsreducering door de introductie van achterrاند vertandingen. Ze worden verder gebruikt om de analytische modellen te evalueren, die bekend zijn om de niveaus van geluidsreducering aanzienlijk te overschatten of de resulterende spectrale vorm van het voortgebrachte geluid onjuist te voorspellen. Deze bevindingen worden hier herhaald. De analytische modellen worden verder besproken onder de premisse van het stromingsgedrag aangenomen door elk model. Bij uitgelijnde stroming, is een dergelijke grote verandering in stroming dat de waargenomen geluidsreducering kan onderbouwen niet waargenomen.

Voor de niet uitgelijnde stroming over de vertandingen, zijn de akoestische metingen verder geëvalueerd met de hydrodynamische karakterisering met PIV metingen nabij het oppervlak. Een geluidsverhoging boven een bepaalde frequentie is eerder vermeld voor vertandingen, en verondersteld te worden veroorzaakt door incorrecte uitlijning met de stroming. Een constante Strouhal-getal gebruikt om deze frequentie te beschrijven is verder voorgesteld. De geluidsverhoging bij hoge frequenties wordt bevestigd in dit onderzoek, net als de relatie met de onjuiste uitlijning met de stroming. De gedetailleerde stromingsmetingen laten een kritische evaluatie van de relatie met het Strouhal-getal toe. Wat hierbij is gevonden, hoewel niet constant, is een goede correlatie met de stromingssnelheid in het verre veld en de invalshoek van het profiel. Hoge snelheid PIV is ook gebruikt om de bron van hoogfrequente geluidsverhoging te lokaliseren. Hoewel eerder was gespeculeerd dat het komt door de toegenomen turbulentie tussen de tanden als gevolg van de foutieve uitlijning, wordt hier aangetoond dat het afkomstig is van de toename van de energie in de convectie van de kleinere turbulente wervels langs de drukzijde van de vertanding rand.

Tot slot wordt een onderzoek naar de verschillende geometrieën voor de vertanding uitgevoerd. Oppervlak permeabiliteit wordt voorgeschreven aan twee van hen, door het gebruik van spleten in het ontwerp. Veelbelovende resultaten zijn eerder gemeld voor een van deze ontwerpen, in het bijzonder voor het vermijden van de hiervoor genoemde hoogfrequente geluidsverhoging. Hoewel deze resultaten hier niet konden worden herhaald, bleken de semipermeabele ontwerpen een goede referentie te zijn voor het onderzoek van het randverstrooiingsrendement. Beschikbare stromingsmetingen van de stroming uitgelijnde gespleten en vaste vertandingen, vertoonde slechts geringe veranderingen in de stroming. De grote verschillen in de akoestische emissie moet dus worden gedreven door andere mechanisme dan een gunstige stromingsverandering. Dit bewijs

ondersteunt daardoor ook de stelling dat het fundamentele mechanisme voor geluidsreducering door de vertanding, de gunstige modificatie van het achterrand verstrooiingsrendement blijft.

PREFACE

This thesis presents experimental work conducted to investigate the effect that trailing edge serrations have on the flow and on the acoustic emissions.

While it is known that serrations are an effective device to reduce TBL-TE noise, fundamental questions remain as to how this is accomplished. PIV has been extensively used in this work to characterize the flow in the boundary layer at different locations over the serrations, and compare it to that over the straight trailing edge. Thanks to the extraordinary benefits of the PIV methods employed, the level of description that has been achieved is unprecedented.

To capture and compare the acoustic emissions of the different configurations, acoustic beamforming was used. This method greatly alleviates the drawbacks of single microphone measurements by reducing the risk of capturing spurious noise sources. This could otherwise naturally lead to the formulation of erroneous conclusions. It further provides an *in situ* evaluation of the setup acoustic sources. This is of course important because unwanted noise is abundant in an experimental setting. It is emitted from sources such as the wind tunnel nozzle, and the interaction of the airfoil with the side-plate boundary layers. The availability of such an approach was therefore crucial to the success of this research.

The implementation of both techniques was exceptionally carried out thanks to the great team that has been part of this research. Unmeasurable gratitude is therefore extended to all, and especially to Daniele Ragni, Stefan Pröbsting, and Roberto Merino-Martínez, for their remarkable talent, patience and technical skill.

A further abundance of appreciation goes to my friends and colleagues at LM Wind Power, without whom this project would not exist. A conveniently skewed timeline permitted me to get much closer to you and to the world of blade aerodynamics and design. Your trust and patience allowed me to carry this assignment through to successful completion. Especial mention goes to Jesper Madsen. Thanks for the insightful conversations, many around improvised and unscheduled times, for your time, and your mentorship. I look forward to doing much more together.

The work here presented was conducted under the brilliant concept of the Industrial PhD Programme, funded by Innovation Fund Denmark, project 11-109522.

Carlos Andrés Arce León
Delft, September 2017

1

INTRODUCTION

Mire vuestra merced –respondió Sancho– que aquellos que allí se parecen no son gigantes, sino molinos de viento, y lo que en ellos parecen brazos son las aspas, que, volteadas del viento, hacen andar la piedra del molino.

(Look, your worship –said Sancho– what we see there are not giants but windmills, and what seem to be their arms are the blades that turned by the wind make the millstone go.)

Miguel de Cervantes, *El Ingenioso Hidalgo Don Quijote de la Mancha*

This introduction serves to lay a background to the research topic presented in this thesis. It justifies the experimental campaign by giving an overview of the problematic of wind turbine noise, along with a summary of noise reduction techniques in industrial wind turbine applications. The discussion is then focused on the development of trailing edge serrations as one such technique, outlining the theory of how they reduce noise.

THE ADOPTION OF WIND TO PRODUCE ELECTRICAL ENERGY has seen a tremendous increase over the past years, from about 17,4 GW of installed capacity in 2000 to almost 433 GW in 2015 ([1.1]). As this number is expected to double by the year 2020, our tasks as researchers must focus, not only on the monumental challenges that we need to surpass to build these massive structures, but also on easing their acceptance and bringing them into a healthy coexistence with ourselves. In the end, their purpose should be to help shine a brighter and more sustainable light on our future, and not to aggravate it even further.

1.1. A BRIEF RECOUNT OF WIND AS A MEANS TO PRODUCE ELECTRICITY



Figure 1.1: la Cour's experimental turbines at Askov, Denmark, as they stood in 1897. Source: Vejen Lokalhitoriske Arkiv.

Wind powered devices have been around for thousands of years, and have been conceived in many forms. From ships fitted with sails, to the Flettner ship, which provides forward movement using the Magnus effect. From wind driven mills to crushers, sawmills, pumps and presses. The essence is the same; to convert wind into mechanical power for the completion of a task often too daunting for human strength alone. Wind turbines go further, using this power to drive an electric generator, making them a solution to countless other purposes. Today, winds over distant rough seas move our trains

and heat water for our morning brew.

While several types of devices exist that are capable of completing the latter example of power transformation, the so-called Danish design horizontal axis wind turbines, often shortened to HAWTs, has become its predominant form for large-scale energy production. In 1887 James Blyth, a Scottish electrical engineer, build the first wind turbine used for the production of electricity ([1.2]), a vertical axis cloth-sailed device standing 10 m tall. This achievement is shared with American Charles F. Bush, who built the first horizontal axis wind turbine around the same time ([1.3]). With a 17 m diameter rotor, it produced 12 kW of energy, and powered Mr. Bush's home, reportedly, for the better part of 20 years.

Early accomplishments in wind turbine development were indeed inspiring by themselves, and may well have been ahead of their times. In 1891, entrusted with funding from the Danish government, Poul la Cour ([1.4]) began to solve some of the technical problems that were limiting widespread use of wind energy. As a visionary, he also led other, less technical but equally critical events, including the formation of the Danish Wind Electricity Society and the training of electricians. His turbines, pictured in figure 1.1, continued to spin and produce energy well into the 1960s, and without a doubt



Figure 1.2: The 58.7 m GloBlade® 3 blade being transported with cradles in the factory yard at Lunderskov, Denmark. Source: LM Wind Power.

served as a critical platform on which the technology could start to gain ground as a cost-effective energy solution.

To compare those marvelous but rudimentary constructions to the scales of today would be misguided. It has taken the minds of many, working in an array of vastly different fields, to bring us to the current state-of-the-art. Equally misguided would be for this author to give today's records on dimensions and production, as they are being shattered every year or two. But at least, at the time this work was written, LM Wind Power has unveiled a blade that, by itself, towers 88.4 m into the sky. Turbines producing 8 MW are flying, and surely the 10 MW milestone is just around the corner. But it is not these numbers that should enthuse a researcher (make one proud, without a doubt, yes), but rather the challenges that come with them. Avoiding to dwell on about their astounding wide range, attention is given further to a single one: noise.

1.2. THE ISSUE OF WIND TURBINE NOISE

Imagine for a moment an empty field, its horizon accented only by a wind turbine standing in the distance. It rotates, prompted by what we sense from our vantage point, is a gentle breeze. This is, more often than not, the closest experience people will have with them, and plenty of the details in their seemingly tranquil lives will go undiscovered.

But look a little closer and you will find a machine build to fight a battle against the ravages of nature. Blades that span outwards, reaching today beyond 80 meters each, and nearing 20 tons in mass, spin, driving their tips to speeds nearing 360 km/h. They are powered by around 150 tons of air as it passes around them every second, pushed with the roughly equivalent weight of 8 elephants. Their design is a trade-off between aerodynamic efficiency and structural integrity; between lowering the cost of energy and avoiding their own destruction.

If such imagery helps to grasp how such a massive rotating structure can generate at least a bit of noise as it cuts through the air, it is already a good start. For people that are often around them, it is an old story.

Barring any unwanted behavior in the blades, the typical sound power level emitted by a megawatt-scale wind turbine is of around 106 dB.

One must be careful when trying to compare such a number to a more common source. Yet online sources will tell you that 106 dB would be somewhat similar to the

loudness of a chainsaw. Nevertheless, intensity is but *one* part of what forms the character of sound. Different sources, even at the same intensity will sound and disturb a person differently. And higher annoyance does not necessarily follow higher intensity. Take the faint buzz of a mosquito, which can easily keep one up at night, while the heavy rumble of ocean waves crashing on the beach could well be a lullaby. And that again, depends on who you ask.

But the 106 dB of sound power from a wind turbine is unquestionably loud. It is not a steady sound either, heard with increasing and decreasing intensity as the blades pass, if one stands nearby. Its frequency will also appear to change as they do—blame the Doppler effect. Further away, it cannot even be well defined.

Such a tall, moving source will refract in the atmosphere, bending in complicated ways that are hard to calculate and, as the state of the atmosphere is transient anyway, pretending to predict the sound at one given place becomes impossible to achieve. The complicated propagation of wind turbine noise through the atmosphere and the conditions imposed by the terrain have important consequences, such as the appearance of fleeting foci and shadows. One or two kilometers away, one could be standing at a sound focus, perceiving the sound of a wind turbine as if it was right there, while a neighbor, just a few meters away, could find himself in a shadow, becoming oblivious to its presence. The curious reader is referred to [1.5] for more information on the subject of wind turbine noise propagation.

So, as any other industrial installation with significant noise emissions, wind turbines are heavily regulated in many places. Let the preceding paragraph be a glimpse at the difficult task laid on those involved in writing said regulations. Let it also suggest that they are a work in progress, and amendments will become necessary as we improve our understanding of wind turbine noise. From the point of view of the wind turbine manufacturer, it is a game of balancing the adherence of current governance, foreseeing what could become regulated in the future by keeping a close eye on current research, and keeping the cost of production low as to maintain the attractiveness of wind generated electricity.

But, as manufacturers focus all their effort on lowering the cost of energy to benefit the end users, it is the concerns those end users that must be heard when designing a set of regulations that is fair to both them and wind farm developers.

The effect of wind turbine noise on the general population has fortunately become a widely researched subject—with of course many improvements warranted. A review of the relevant work is omitted for brevity, and the reader is referred to [1.6–10] for an overview of recent findings.

But the research is often complicated by the anecdotal nature of the health impact of wind turbine noise by the respondents, with ways of scientifically measuring its effects often found impractical and imprecise. As explained above, wind turbine noise is transient, changing in relatively small periods of time, so measurement campaigns, which often average results over time, may result in lost information about short periods when noise may be most disturbing to nearby dwellers. And again, while intensity is an easily quantifiable factor, it is but one component of the character of sound. Other elements, such as periodicity and presence, which can easily increase the level of annoyance, are harder to measure, and their description by the subjects of wind turbine noise studies

are not easily quantified.

It is this why a microphone can only do so much to characterize our relationship with sound. When we consider its perception and its effects on our psychology, the realm we enter is that of psychoacoustics. Factors unrelated to sound itself are also known to exacerbate the effects of noise in people. Visual presence, for example, will sometimes increase the sensitivity to wind turbine noise compared to similar settings where turbines are not in a direct line of sight ([1.11]).

A predisposition to annoyance also plays a mayor role in the acceptance of wind turbines. Unfortunately, a myriad of pseudo-science reports have increased the public's fear of wind turbines, often relating misconceptions to real and menacing side effects. Infrasound, defined as acoustic energy with frequencies below those audible to humans, has been blamed, for example, to cause a “seemingly incongruous constellation of symptoms” when emitted by wind turbines, from insomnia and nausea to cancer ([1.12]). It has been called Wind Turbine Syndrome by the author. While this research has widely been debunked and proven as flawed (read for example Harrison [1.13]), stoked fear is difficult to qualm. Such unfounded discussion greatly harms the advancement of real research, led by ethically unbiased and concerned institutes and scientists. It also hurts the credibility of the population that has legitimate complaints and calls for improved regulations.

This discussion of wind turbine noise has so far illustrated a research field that is multidimensional and multidisciplinary, with stakeholders in the industrial and public sectors. To advance it, and to construct ways to find the right balance between the people and the technology, a wide range of aspects must be investigated. In the current work, focus is paid to the very source of the noise.

1.3. SOURCES OF WIND TURBINE NOISE

Sound, in the current setting, will be narrowed to mechanical waves in the air that can be perceived by our auditory system.

In general, it can be classified in two branches, depending on the nature of its driving source. The first is vibroacoustics, in which the acoustic waves in the air have been created by its excitation from a vibrating surface. Examples of this kind are easy to find: drums, horns, and the sound of our voice, which is created by the vibration of our vocal chords, are a few of them.

Mechanical devices are also often sources of vibroacoustic sound. Inside a wind turbine, the largest are housed inside the nacelle (see figure 1.3 for a schematic of the major elements of a wind turbine). These include the gearbox, the generator and the cooling system, all of which can be sources of vibroacoustic noise. Fortunately, smart design has succeeded at avoiding strong sound sources from these components. Additionally, nacelles are often equipped with acoustic liners that help absorb some of the acoustic energy and prevent it from transmitting efficiently to the outside. Such ad-

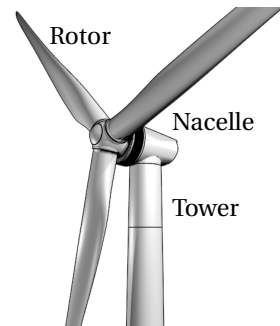


Figure 1.3: Schematic showing the three major external elements of a state-of-the-art horizontal axis wind turbine.

vances have made vibroacoustic sources not heavily contributing to the overall noise of the turbine ([1.14]).

The second classification is aeroacoustics, in which sound is created entirely by bodies of air, often (but not necessarily) in contact with surfaces. It must be stressed that it is not produced by the aerodynamic *excitation* of structures, causing them to vibrate and emit sound, as this would again fall into the classification of vibroacoustics by flow-structure interaction. In the case of aeroacoustics, the structure is considered infinitely stiff, which is often a good approximation to real life applications.

Jet engine noise is a well-known example of aeroacoustic noise. It is a complex case, with several sources at different stages in the turbine, the fan and the exhaust. In turbojet engines, for example (often used in fighter jets or older commercial airliners), the exhaust nozzle focuses a high-speed jet core onto surrounding air with relatively much lower speed. This causes strong instabilities in the shear layer as the two mix. These instabilities are strong enough to produce oscillations that efficiently propagate outward as acoustic waves. It was this problem that inspired James Lighthill, often considered the father of aeroacoustics, to develop the acoustic analogy theory ([1.15, 16]).

A second well-known example can sometimes be heard as wind passes thin and long cylindrical bodies, such as power lines, guy wires or the rigging of a sail-powered ship. The interaction with these bodies causes the air to shed vortices behind them in a periodic way. This results in the efficient radiation of an acoustic wave with energy centered near a single frequency, producing sounds of single tones. A similar result occurs when people whistle or when flow passes by a cavity—such as a thin and sharp hole made in an otherwise smooth surface. While the latter is sometimes the cause of tonal noise in wind turbine blades, it is often the result of an abnormal condition or a design flaw.

The aeroacoustic noise from wind turbine blades can be separated into six different mechanisms, as outlined in [1.17, 18]. A brief description of each shall be given next.

Tip noise

As the blade produces lift, a strong streamwise-coherent vortex is generated at the tip, with flow rotating rapidly inside its core (figure 1.4a). It has negative effects for the blade aerodynamics in general, producing energy losses, and it can also be the source of noise. It is known from flap noise theory that this type of vortex, at low Mach number freestream velocities, becomes a source of noise when it interacts with solid surfaces ([1.19]). This can happen for square tips, where a vortex is developed at the leading vertex of the tip and impinges on its surface further downstream. For state-of-the-art wind turbine blade tips, this is not a concern due to the sharp geometry commonly used, as it helps the surface avoid the vortex before impingement occurs. Its low or non-existing contribution to the overall noise of wind turbines is confirmed in the measurements of Oerlemans and Méndez López [1.14]

Stalled flow noise

Once an airfoil exceeds a certain angle of attack and passes the maximum lift it can provide, flow separation occurs (figure 1.4b). This forms a large recirculation bubble of highly unsteady flow. This creates noise of a broadband quality that has been reported to increase airfoil noise by levels considerably (for example, by

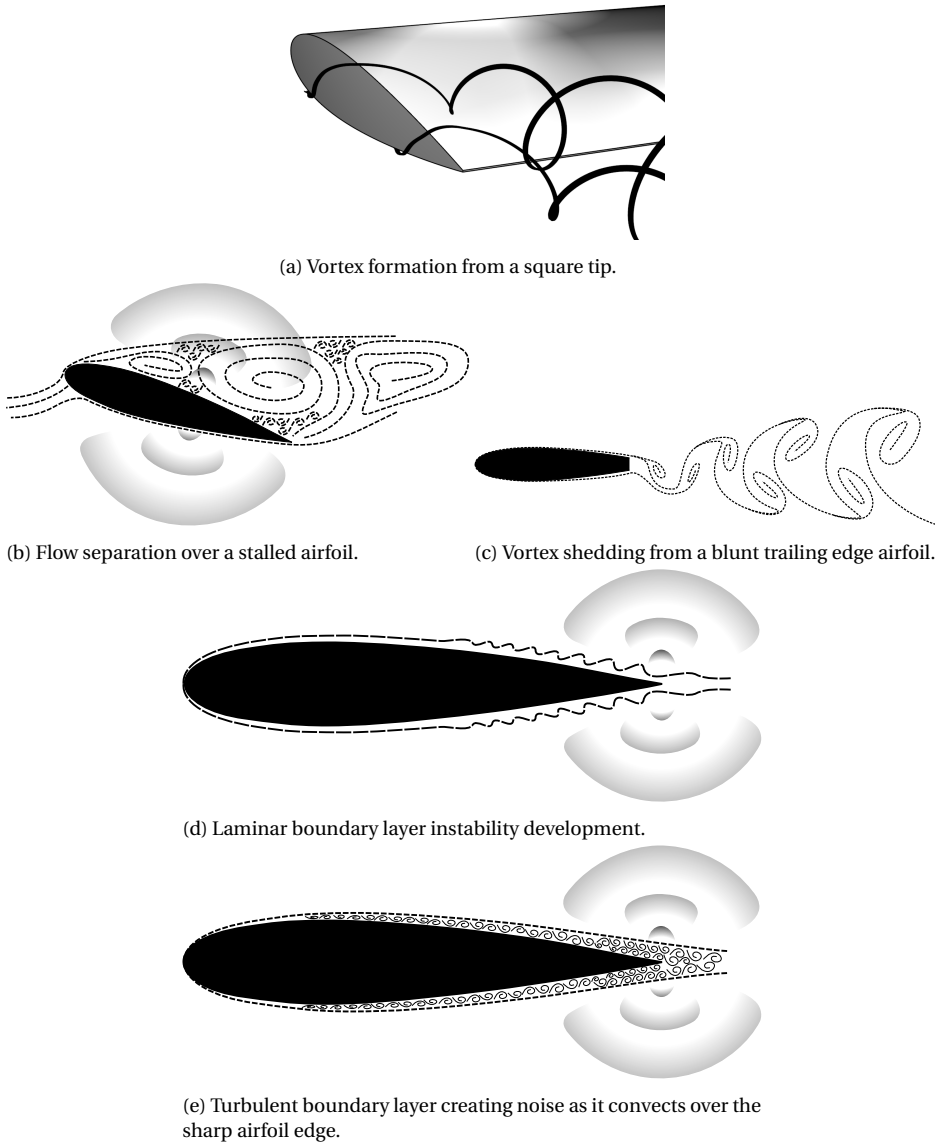


Figure 1.4: Schematics of five flow conditions that drive different blade noise mechanisms.

10 dB as reported in [1.20], but which is very case-dependent), despite inhibiting other noise mechanisms. While this is true for two-dimensional airfoil profiles in wind tunnels, separation in blades or wings in sections that are below the known stall angle of attack can be promoted by nearby sections that have stalled. This is especially important in wind turbine blades, where the very thick airfoils between

the circular root section and the max-chord region tend to stall. Aerodynamic devices can be installed to prevent the propagation of stall, such as stall fences, or to help avoid it, such as vortex generators. This effect happens at the inboard sections of the blade, where the flow speed is not very high, and as a consequence, the contribution of the stalled flow noise is not large. Its occurrence at the higher speed sections of the outboard was more prevalent with stall-regulated wind turbine blades ([1.21]). Modern blades are pitch-regulated ([1.22]), and as such, the aerodynamic sections of the blade are kept at angles of attack below stall. While this is the intention, gusts and wind shear can rapidly increase the angle of attack of some blade sections, stalling them. It has been suggested that this is the source of amplitude modulated noise in wind turbines ([1.23, 24]). While still a debated subject, it is quite certainly a mechanism that is effective at transmitting over very long distances ([1.25]).

Blunt trailing edge noise

Airfoils can be designed to have sharp or blunt trailing edges, the latter (called flatback airfoils) offer certain benefits, such as having a larger structural strength, increased lift curve slope and maximum lift, and better performance when leading edge roughness is present ([1.26]). Nevertheless, it can promote the formation of von Kármán style vortex streets in the wake (figure 1.4c), causing a periodic fluctuation of the pressure near the trailing edge, efficiently resulting in the emission of noise with a tonal character. As large flatbacks are more commonly found near the low-speed root sections of blades, they do not commonly present acoustic issues. Nevertheless, solutions to avoid them exist, typically in the form of splitter plates that obstruct the development of the vortex streets ([1.27, 28]). The typical trailing edge of airfoils in the fast outboard sections of the blade has a thickness of about 2 mm. The formation of vortex streets is thus inhibited by the incident turbulent boundary layer, which is several times thicker ([1.17]).

Laminar boundary layer-instability noise

The flow over the surface of an airfoil can remain in the laminar regime, given the right conditions and airfoil design. This can happen over one or both sides of the airfoil and can promote the formation of Tollmien-Schlichting waves. As these flow instabilities convect over the surface, they induce periodic surface pressure fluctuations underneath them. The latter scatter as they reach the edge, resulting in the generation of outward-radial propagating acoustic pressure waves. As these waves expand, they form a feedback mechanism with the Tollmien-Schlichting waves approaching the trailing edge in the upstream direction, effectively amplifying them, and which in turn generate amplified acoustic waves. The outcome is a very efficient mechanism that generates highly undesirable loud and narrowband sound.

The transition of the flow from laminar to turbulent, and the prevalence of the latter as the flow convects over the trailing edge, is often enough to suppress this mechanism. In wind turbine blades, airfoils are generally designed to avoid laminar flow convection over aft sections of the airfoil, having the point of maximum thickness relatively upstream, thus resulting in larger downstream areas under ad-

verse pressure gradients. If at certain conditions airfoils on production blades remain problematic, an easy solution is to force transition from the laminar to turbulent regimes by employing a tripping device (zigzag tapes being an example), but which which may also be achieved unaided if blade soiling is sufficient. While efforts to avoid this kind of noise should ideally be made at the design stage, that may not always be possible, but with a retrofit solution that is relatively easy to implement, laminar boundary layer-instability noise is not a common issue in modern wind turbine blades.

Inflow noise

This mechanism refers to the noise produced when an airfoil encounters turbulence in the flow. As described by Amiet [1.29], the unsteadiness of the flow, referred to as gusts, causes unsteady loading on the airfoil as a function of time, and resulting in the production of noise, being scattered from the leading and trailing edges. It can be low-frequency, if the turbulent eddy is larger than the local chord, or high-frequency if it is smaller ([1.17]). Its contribution to the overall blade noise emissions is still debated, but it has been suggested that it may play a part in causing amplitude modulation ([1.23]), and otherwise can contribute to the low-frequency part of the emitted noise ([1.30]).

TBL-TE noise

As mentioned above, airfoils commonly used in modern wind turbines will exhibit natural transition from laminar to turbulent flow, or roughness near their leading edges due to erosion or dirt will promote it. After this transition period, a turbulent boundary layer will be formed between the airfoil and the surrounding freestream (figure 1.4e). Within this boundary layer, eddies of a range of sizes and energies convect downstream, creating a broadband spectrum of surface pressure frequencies on the surface underneath them. As these unsteady and relatively incoherent surface pressure waves encounter the trailing edge, they will scatter as a product of the sharp jump in impedance. Their scattering results in the creation and propagation of outward-traveling acoustic waves with a broadband quality. This mechanism will be contracted as “TBL-TE noise.”

It is considered the predominant source of wind turbine noise under the most prevalent operating conditions for which blades are designed ([1.14, 31, 32]). It is wise therefore to prioritize it in the formulation of a noise mitigation strategy. In the following section, 1.4, a synopsis is given on different ways that this can be achieved.

As it is evident from their description, the occurrence of these mechanisms cannot happen simultaneously, as flow conditions are fundamentally different between them. Nevertheless, a blade in operation could potentially present all five mechanisms at different locations throughout its span.

Because blades have such a high aspect ratio, locally airfoils can be considered to be two-dimensional, with little spanwise variation over a length much larger than the characteristic scales of the flow conditions here presented. The tip would be the most

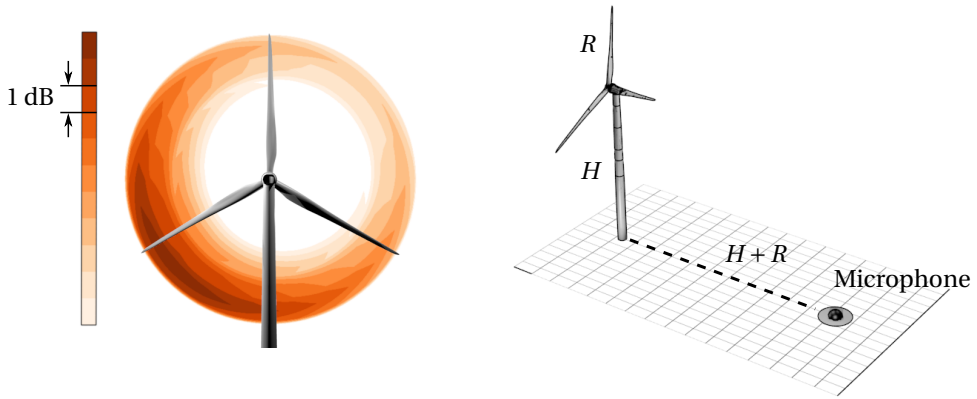


Figure 1.5: Predicted rotor noise emission map (A-weighted) for a 61.2 m blade at a wind speed of 11 m/s, measured downwind at a distance equaling the tower height (H) plus rotor radius (R), as per the IEC 61400-11 standard.

obvious exception to this assumption, as its noise mechanism description is three-dimensional. A similar situation is encountered in the more inboard sections of the blade, where the use of very thick airfoils promotes separation and flow often suffers a strong radial component.

It is with the aforementioned assumption that blade noise can be modeled as the contribution of a set of independent airfoils with the right geometric and operational characteristics. Precision in the model can thus partly be controlled by the amount of sections that are considered, whether a constant or variable distribution is chosen, in which the latter can be based on the local geometric complexity. It is with this general principle that several wind turbine noise prediction algorithms have been developed, such as in [1.33, 34], and in the LM Wind Power rotor noise prediction code.

While TBL-TE noise is considered the predominant source of noise in a nominally operating wind turbine, rotor noise prediction helps to further the identification of specific sections of the blade that are most contributing to the overall noise. Figure 1.5 shows an example of a rotor noise prediction result using a realistic blade geometry, following the IEC 61400-11 wind turbine noise measurement standard. The blade is an LM 61.2 P operating at 11 m/s wind speed.

Such a simulation helps to locate the region of largest noise emission from a blade. Like here, it is typically located at around 30% of the outboard sections of the blades, and drops before reaching the tip (a consequence of lesser loading achieved by the twist design of the blade). The asymmetry of the disk is due to convective amplification caused by the higher relative velocity of the blade with respect to the observer. In this case the measurement is carried out from the ground, thus the blade has a higher apparent velocity as it comes down in its rotation (which is anticlockwise, as seen from a downwind perspective). If the measurement was to be taken instead at tower height, the contour curves would look concentric. This result agrees with the observations performed in field measurements using acoustic cameras, such as in [1.31, 32].

The information in this section is sufficient to consider an efficient blade noise reduction strategy which addresses the most contributing mechanism of noise generation at its predominant location on the blade. With this in mind, the following section will list a few different ways by which it can be achieved, including a brief discussion on their potential benefits and disadvantages.

1.4. MITIGATING TBL-TE NOISE

As seen in the previous section, TBL-TE noise is accepted to contribute to the largest portion of the noise emitted by well-designed and non-faulty modern wind turbines, operating within their design envelope ([1.14, 31, 32]).

Three components are present in triggering its onset, as its definition infers: a turbulent boundary layer, a set of unsteady pressure waves on the airfoil surface (driven by the boundary layer flow and pressure variations), and an edge on which these scatter due to the impedance jump between the solid edge and the wake. Addressing any of these factors can result in changes to the emitted acoustic signal. A detailed examination of this mechanism will be provided later in chapter 2, and a non-exhaustive list of different proposed ways of mitigating this source is here outlined.

Modified operational settings

TBL-TE noise is a dipole sound source (see chapter 2), of which its intensity is well known to scale with the fifth power of the mean flow velocity of the freestream ([1.18, 35]). It makes thus sense that slowing down the wind turbine blades would result in an effective way to reduce their noise. And it is. An empiric relation to the rotor noise, known as the Hagg model, is given in [1.36] as

$$L_{WA} = 50 \log_{10} V_{\text{Tip}} + 10 \log_{10} D - C_H, \quad (1.1)$$

where L_{WA} refers to the A-weighted sound power level, V_{Tip} is the blade tip speed and D is the rotor diameter. C_H , taken as 4 by Hagg, is a constant that is dependent on the turbine operation and blade geometry. The significant contribution of the tip speed to L_{WA} is evident.

Wind turbines, depending on their manufacturer, may come equipped with low-noise operational modes, which basically is an application of this method. The trade-off is a loss in energy production by a less efficient capturing of the wind's energy. Depending on the economic viability of using these settings, which might be better than, for example, shutting down a wind farm during the night because of stricter noise regulations (common in countries like Germany ([1.37])), they may prove useful without becoming a loss to the operator.

Alternatively, a slower rotating rotor could be manufactured that would capture the same amount of energy from the wind, but this must be done at the design stage of the blades and turbine. With slower rotating blades, to capture the same amount of energy, the torque that they produce must be increased. The trade-off is therefore found in having to increase the safety limits of the entire system, including blades, tower and, very critically, the drivetrain. This results in a very steep hike in the cost of the turbine, often making it prohibitively expensive for the expected return and benefit of having lower noise emissions.

Airfoil design

Airfoils can be made quieter by designing them in such a way that the boundary layer flow results in less noise compared to airfoils that perform aerodynamically similar. Nevertheless, the similarity of airfoils (for the purpose of stating that one is low-noise compared to another) is a broad and open question that is purpose driven.

Efforts to achieve this have been undertaken in [1.38–42]. The SIROCCO project ([1.31]) designed and tested a full-scale blade designed with low-noise airfoils with moderate success. Undeniably though, the design of modern custom airfoils for wind turbine applications should always account for noise emissions. To what point such a parameter is weighed in the holistic approach to airfoil design is left up to the expected requirements of the application.

Flow injection

A way to modify the properties of the boundary layer such that a beneficial change in acoustic emissions is obtained is through flow injection, either upstream of the trailing edge or from it. Numerical experiments addressing this solution can be found in [1.43, 44]. Experimental studies on fan noise, involving rotor-stator interaction, have been conducted in [1.45–47].

While successfully demonstrated as a proof-of-concept at small scales, its implementation in scaled-down and industrial-scale wind turbine applications is still challenging. Issues involving the instrumentation and maintenance of blades to carry blowing systems are troublesome. Passive methods would be preferred.

Porous materials

The use of porous materials for the purpose of noise reduction has been proposed in [1.48–51]. Conclusions generally find that such an approach is successful at various frequency ranges, with some potential penalty in the aerodynamic performance of the airfoils. The porous media itself is complex to design, with a range of parameters to settle. While some research has been done, finding the corresponding mechanism for the noise reduction and its correlation with the material's properties is needed. Furthermore, it is yet unclear if the underlying mechanism lies in a modification of either of the three aforementioned factors in edge noise production. Industrialization concerns point towards the durability of the materials, and how well they hold up in weather without the need for recurring maintenance.

Brushed trailing edges

The concept of brushed trailing edges refers to using materials at the edge that adapt with the flow, typically in the form of thin and flexible fibers. Studies showing the potential of this solution have been undertaken in [1.52–54] with satisfactory results. The mechanism of their action is not entirely resolved, but it has been proposed that they function as a dampening device for turbulent eddies near the edge, making them less efficient at creating the scattering unsteady surface pressure. Their use in a full-scale blade test has also been performed under the SIROCCO project ([1.31]), although unsuccessfully. Private communication with

some of the project participants suggested that at least part of the underperformance may have been attributed to a non-optimal attachment method to the blade.

Part of the attractiveness of this approach remains in that they would only insignificantly modify the aerodynamic loading forces on the blade, and they would passively adapt to different flow conditions, thus relaxing some of the design requirements of stiff and passive trailing edge devices.

Non-straight trailing edges

The concept of using a non-straight trailing edge to reduce noise from airfoils is not a recent one. The effects of such a geometry on noise production were addressed analytically by Howe [1.55]. A wide array of studies, both experimental and numerical, have been carried out on such geometries. The results, addressed in chapter 2, show that the effectiveness of this method to reduce TBL-TE noise is unquestionably established.

While it has become a reliable method for noise reduction, the mechanism by which it achieves this is still disputed. Establishing it has become critical and is a necessary step to optimizing its efficiency. Efforts to achieve this are strongly driven by a large interest on behalf of the wind energy industry, as large players have started to develop it as a product. Among these are Enercon ([1.56]), General Electric ([1.57]), Siemens ([1.58]) and LM Wind Power.

Challenges encountered with this technology are mainly led by low maintenance requirements and long expected lifetime of the blades—usually 20 years. Aeroacoustic and aerodynamic optimization calls for using a thin device, while structural safeties will demand a thicker one, resulting in a trade-off between the two objectives. The method by which the serration panels need to be attached to the blades is also non-trivial, as it needs to sustain heavy loads, survive static and dynamic fatigue, and avoid damage to the blade.

These obstacles have in fact been successfully addressed, and the aeroacoustic testing of them has been thoroughly complimented by aerodynamic and structural validation (LM Wind Power internal projects). The development of a reliable and relatively simple device that can either be installed before the blades roll out of the factory, or retrofitted on blades that are already installed on turbines, remains highly attractive as a go-to solution to inhibit TBL-TE noise.

The appeal of the last of the listed TBL-TE noise reduction methods has motivated the present work. Specifically, the research has concentrated on sawtooth shaped trailing edges ([1.59]) because of their previous success in noise reduction compared to other similar geometries, and the amount of questions that remain unresolved. A review of the theory and previous findings shall be given in chapter 2, while the research objectives and motivation are addressed in section 1.6.

The following section will expose a brief analysis of the economic impact that the application of trailing edge serrations can have on the expected return obtained with wind energy.

1.5. ECONOMIC IMPACT OF NOISE REDUCTION BY SERRATIONS

In field measurements, serrations have been reported to reduce the noise from blades from around 1.5 to 3 dB. Public record of this can be found in [1.31, 33, 58, 60]. These results have been further supported by several field measurement campaigns conducted by LM Wind Power.

While tempting, decibels should not be the sole measure for success in the application of a noise reduction technology. Instead, they should be weighed in terms of their global benefit to the entire system. This includes their effect on energy production costs, and the economic attractiveness of wind energy developments to investors.

With a wider range of factors to consider, the valorization of such a technology becomes complicated, as do its design parameters. Longevity of the different elements in the device becomes paramount when weighing long term cost-benefit. In the long run, the maintenance costs of a badly designed product can become crippling, adding up quickly for each service cycle. They include loss of production due to the down-time of the turbine, man-hours and the use of expensive equipment such as cranes to access the blades. Initial research, invested towards finding a reliable application method and a robust construction, is therefore critical and must balance the aerodynamic and aeroacoustic requirements with the structural safety limits.

Noise reduction can also have a wider implication to the design of the entire wind turbine. It can become, for example, a means by which the design constraints of individual turbine elements, or entire wind farms, can be relaxed. In such a way, a noise reduction technology could help broaden the distance between the emitted noise and the noise design targets, using that gain for later capitalization by other means. A good design can then be used to significantly improve production while maintaining an equivalent noise emission level.

Under this premise, serrations can be used to achieve higher rotational speeds while maintaining the same level of emissions than a slower blade without them. Such a solution would help to reduce the cost of the drivetrain, along with other benefits to the overall system. A potential increase of 6% in the annual energy production (AEP) of a single turbine can be achieved this way.

The construction of longer blades is another example, where, without the use of serrations, the overall noise would be increased by the added span and the faster tip speed. Instead, by using serrations, noise could be kept equivalent to a shorter blade. The turbine would benefit from an increase in swept area, to which the extracted power is proportional.

The benefits of using a noise reduction technology are also evident when considering wind farms. A simplified model will show that the reduction of just 1.5 dB on three wind turbines in a wind farm allows the installation of a fourth and keep the same overall sound levels, obtaining a 33% increase in AEP. One could double the amount to six turbines in the farm if 3 dB are reduced on all of them.

Noise curtailed wind turbine operation, such as the use of low-noise turbine settings, could be avoided, resulting in a potential increase of 6% on AEP. This number could be higher if the situation was such that stricter nighttime noise limits are forcing parts, or the entirety of a wind farm, to shut down.

To provide a more tangible sense to an AEP gain, a 4% of increase over the turbine's

lifetime would be expected to pay off a blade set ([1.61]), evidencing the attractiveness of such a solution to wind farm developers.

Needless to say, nothing comes without a price, but in this case that can be shown to be quite low. The addition of elements to a blade will impact its cost structure. Depending whether the serrations will be installed during the blade production, or if they will be retrofitted on already installed blades, the results of the impact will be different. To perform such a cost analysis, the levelized cost of electricity (LCoE) can be used. It represents the ratio between the average total cost to build and operate a power plant over its lifetime, and its energy production over the same amount of time ([1.62]). Equivalently, it can be taken as the cost at which the produced electricity must be sold to cut even.

The LCoE of serration-retrofitted blades, assuming a *zero* AEP gain, is elevated by 0.99%, while for production-installed serrations it is elevated by 0.29%. But, as discussed before, the AEP in a smart implementation of serrations will not be zero and can instead be considerably increased. By reevaluating with a 10% increase in AEP, the first case yields a *decrease* in LCoE of 7.74%, and the second case of 8.38%¹.

The balance between the cost and benefit of any proposed solution, whether it is for noise reduction or any other application, must be well founded. It might not be wise to use trailing edge serrations on every existing wind turbine, and indeed, noise regulations might render the proposal for a wind farm irremediably unsustainable, regardless of the availability of a realistic noise abatement technique. But, by employing a smart and strategic approach, such devices can in many cases improve the prospect of a wind farm development, and, by extension, ultimately benefit the overall population by providing a lower cost of energy.

1.6. OBJECTIVES AND MOTIVATION

This chapter has introduced the topic of wind turbine noise within the perspective of its source and its mitigation. The economical benefits of succeeding at this task have been laid out, and the importance of addressing it within the scope of its social significance has been discussed.

The work here presented focuses on the most industrially-promising method for reducing—what is considered—the most predominant mechanism of noise production on wind turbine blades: trailing edge serrations.

The means by which serrations reduce noise is still somewhat debated. As mentioned in section 1.4, TBL-TE noise is produced by an interaction of three components: a turbulent boundary layer, the unsteady surface pressure below it, and an edge on which the surface pressure scatters as noise. A change in any of these elements will likely result in a modification of the noise in the far field.

The change of a straight trailing edge to a serrated one may very well affect any, if not all, of those three factors. But identifying which contributes most to the noise reduction mechanism can certainly shape the direction of trailing edge serration design as one tries to harvest their potential to its maximum effect.

The work presented in this thesis will focus on identifying these contributions by

¹The AEP and LCoE numbers here shown were provided by the Greek Center for Renewable Energy Sources (KAIE/CRES) under the WINDTRUST project.

conducting unprecedented experimental research into the flow near trailing edge serrations. PIV is used to carry out the research into the flow, while acoustic beamforming arrays are used to measure the noise emissions from the airfoil.

The work is divided in three large parts:

Mean near-surface flow of flow-misaligned serrations

Serrations are installed on a NACA 0018 airfoil, and the flow near the surface is investigated using time-averaged PIV. The serrations are then misaligned with regard to the flow by means of variations in angle of attack, and in the flap angle of the serrations.

Changes in the mean flow are recorded and discussed within the scope of Howe's trailing edge serration theory ([1.59]) and the how the measured flow departs from its assumptions. Acoustic measurements are further used to compare with the analytic solution and the different degrees and sources of the flow-misalignment of the serrations.

Time-resolved boundary layer flow over serrations

Time-resolved PIV measurements of the flow, performed at 10 kHz acquisition rate, are presented over three different serration edge locations and compared between them, as well as with the flow over the straight edge of the airfoil without serrations.

This study focuses on the level of flow change as it convects over the serrations. The results are used to form a qualitative impression of the surface pressure change across the serration surface using elements of the so-called TNO-Blake model.

The results address the noise reduction mechanism from the effect that the physical presence of the serrations have on the flow when no flow-misalignment is prescribed. The findings are then weighed against the observed changes in noise emissions.

Investigation on the source of noise increase by flow-misaligned serrations

Previous research has found that serrations, when flow-misaligned, create more noise than an unserrated airfoil after a certain frequency. This study verifies this phenomenon using an acoustic beamforming array, and explores an earlier proposition that uses a Strouhal number, based on the airfoil boundary layer at its trailing edge and the mean flow velocity, to predict this frequency. The mechanism for the noise increase is further explained and localized using time-resolved PIV.

A recurring topic in this work is the effect that serration-flow misalignment has on the flow and acoustic emissions. This geometric variation is of great interest in an industrial setting, where tolerances must be established in the manufacturing and installation of these devices. Furthermore, the condition is common in wind turbine blades, where the use of cambered airfoils is the standard and operating conditions are quickly changing.

In this study, a symmetric airfoil is used with a thickness that is relatable to that used in the outboard sections of state-of-the-art wind turbines: the NACA 0018. The choice of a symmetric airfoil over a cambered one was made in order to have better control over the serration-flow misalignment, especially when flow-aligned serrations were required.

The measurements were all conducted at TU Delft's Vertical Wind Tunnel (V-Tunnel). While it provides smaller Reynolds numbers than those expected in real-life applications, the physics involved between the interaction of the tripped turbulent boundary layer and the serrations are unmodified and should scale accordingly.

BIBLIOGRAPHY

- [1.1] Global Wind Energy Council, *Global Wind Report 2015* (Global Wind Energy Council, 2015).
- [1.2] T. Price, *James Blyth Britain's first modern wind power pioneer*, *Wind Engineering* **29**, 191 (2005).
- [1.3] Anon., *Mr. Bush's Windmill Dynamo*, *Scientific American* **63**, 54 (1890).
- [1.4] H. C. Hansen, *Poul la Cour - Grundtvigianer, opfinder og folkeoplyser* (Samfundslitteratur, 1985).
- [1.5] K. Bolin, *Wind Turbine Noise and Natural Sounds: Masking, Propagation and Modeling*, *PhD Thesis*, KTH Royal Institute of Technology (2009).
- [1.6] E. Pedersen and K. Persson Waye, *Wind turbine noise, annoyance and self-reported health and well-being in different living environments*, *Occupational and Environmental Medicine* **64**, 480 (2007).
- [1.7] M. Nissenbaum, J. Aramini, and C. Hanning, *Effects of industrial wind turbine noise on sleep and health*, *Noise and Health* **14**, 237 (2012).
- [1.8] D. Shepherd, D. Welch, E. Hill, D. McBride, and K. Dirks, *Evaluating the impact of wind turbine noise on health-related quality of life*, *Noise and Health* **13**, 333 (2011).
- [1.9] E. Pedersen, F. van den Berg, R. Bakker, and J. Bouma, *Response to noise from modern wind farms in The Netherlands*, *The Journal of the Acoustical Society of America* **126**, 634 (2009).
- [1.10] D. S. Michaud, K. Feder, S. E. Keith, S. A. Voicescu, L. Marro, J. Than, M. Guay, A. Denning, D. McGuire, T. Bower, E. Lavigne, B. J. Murray, S. K. Weiss, and F. van den Berg, *Exposure to wind turbine noise: Perceptual responses and reported health effects*, *The Journal of the Acoustical Society of America* **139**, 1443 (2016).
- [1.11] E. Pedersen and P. Larsman, *The impact of visual factors on noise annoyance among people living in the vicinity of wind turbines*, *Journal of Environmental Psychology* **28**, 379 (2008).
- [1.12] N. Pierpont, *Wind Turbine Syndrome: A Report on a Natural Experiment* (K-Selected Books, 2009).
- [1.13] R. V. Harrison, *On the biological plausibility of Wind Turbine Syndrome*, *International Journal of Environmental Health Research* **25**, 960 (2015).

- [1.14] S. Oerlemans and B. Méndez López, *Acoustic Array Measurements on a Full Scale Wind Turbine*, in [11th AIAA/CEAS Aeroacoustics Conference](#), Vol. 23 (American Institute of Aeronautics and Astronautics, Monterrey, California, 2005) p. 25.
- [1.15] M. J. Lighthill, *On Sound Generated Aerodynamically. I. General Theory*, [Proceedings of the Royal Society A: Mathematical, Physical and Engineering Sciences](#) **211**, 564 (1952).
- [1.16] M. J. Lighthill, *On Sound Generated Aerodynamically. II. Turbulence as a Source of Sound*, [Proceedings of the Royal Society A: Mathematical, Physical and Engineering Sciences](#) **222**, 1 (1954).
- [1.17] S. Wagner, R. Bareiss, and G. Guidati, *Wind Turbine Noise* (Springer Science & Business Media, 2012) p. 204.
- [1.18] T. Brooks, D. Pope, and M. Marcolini, *Airfoil self-noise and prediction*, [NASA Reference Publication Number 1218](#) (1989).
- [1.19] N. Molin, M. Roger, and S. Barre, *Prediction of Aircraft High-Lift Device Noise Using Dedicated Analytical Models*, in [9th AIAA/CEAS Aeroacoustics Conference and Exhibit](#) (American Institute of Aeronautics and Astronautics, Hilton Head, South Carolina, 2003).
- [1.20] M. R. Fink and D. A. Bailey, *Airframe noise reduction studies and clean-airframe noise investigation*, [NASA-CR-159311](#), Tech. Rep. April (NASA, 1980).
- [1.21] E. Muljadi, K. Pierce, and P. Migliore, *Control strategy for variable-speed, stall-regulated wind turbines*, in [Proceedings of the 1998 American Control Conference. ACC \(IEEE Cat. No.98CH36207\)](#), June (IEEE, 1998) pp. 1710–1714 vol.3.
- [1.22] E. Muljadi and C. Butterfield, *Pitch-controlled variable-speed wind turbine generation*, [IEEE Transactions on Industry Applications](#) **37**, 240 (2001).
- [1.23] M. Smith, A. Bullmore, M. Cand, and R. Davis, *Mechanisms of amplitude modulation in wind turbine noise*, in [Acoustics 2012](#) (Société Française d'Acoustique, Nantes, France, 2012).
- [1.24] A. Laratro, M. Arjomandi, R. Kelso, and B. Cazzolato, *A discussion of wind turbine interaction and stall contributions to wind farm noise*, [Journal of Wind Engineering and Industrial Aerodynamics](#) **127**, 1 (2014).
- [1.25] G. van den Berg, *Effects of the wind profile at night on wind turbine sound*, [Journal of Sound and Vibration](#) **277**, 955 (2004).
- [1.26] D. Berg and J. Zayas, *Aerodynamic and Aeroacoustic Properties of Flatback Airfoils*, in [46th AIAA Aerospace Sciences Meeting and Exhibit](#) (American Institute of Aeronautics and Astronautics, Reno, Nevada, 2008).
- [1.27] M. Manolesos, G. Papadakis, and S. Voutsinas, *Study of Drag Reduction Devices on a Flatback Airfoil*, in [34th Wind Energy Symposium](#), January (American Institute of Aeronautics and Astronautics, San Diego, California, 2016) pp. 1–24.

- [1.28] C. P. van Dam, D. L. Kahn, and D. E. Berg, *Trailing Edge Modifications for Flatback Airfoils*, Tech. Rep. March (Sandia National Laboratories, 2008).
- [1.29] R. Amiet, *Acoustic radiation from an airfoil in a turbulent stream*, [Journal of Sound and Vibration](#) **41**, 407 (1975).
- [1.30] S. Buck, S. Oerlemans, and S. Palo, *Experimental validation of a wind turbine turbulent inflow noise prediction code*, [22nd AIAA/CEAS Aeroacoustics Conference](#) , 1 (2016).
- [1.31] J. Schepers, A. Curvers, S. Oerlemans, K. Braun, T. Lutz, A. Herrig, W. Wuerz, A. Mantesanz, M. Fischer, K. Koegler, T. Maeder, L. Garcillán, B. Méndez-López, A. Matesanz, and R. Ahrelt, *Sirocco: Silent Rotors By Acoustic Optimisation*, in [Second International Meeting on Wind Turbine Noise](#) (2007).
- [1.32] S. Oerlemans, P. Sijtsma, and B. M. López, *Location and quantification of noise sources on a wind turbine*, [Journal of sound and vibration](#) **299**, 869 (2007).
- [1.33] S. Oerlemans and J. G. Schepers, *Prediction of wind turbine noise and validation against experiment*, [International Journal of Aeroacoustics](#) **8**, 555 (2009).
- [1.34] S. Lee, S. Lee, and S. Lee, *Numerical modeling of wind turbine aerodynamic noise in the time domain*, [The Journal of the Acoustical Society of America](#) **133**, EL94 (2013).
- [1.35] J. E. Ffowcs-Williams and L. H. Hall, *Aerodynamic sound generation by turbulent flow in the vicinity of a scattering half plane*, [Journal of Fluid Mechanics](#) **40**, 657 (1970).
- [1.36] F. Hagg, N. van der Borg, and J. C. Bruggeman, *Definite Aero-Geluidonderzoek Twin*, Stork Product Engineering BV, SPE , 25 (1992).
- [1.37] T. Myck and A. Bauerdorff, [Noise Protection Regulations for Wind Turbines in Germany](#), (2014).
- [1.38] S. Oerlemans, M. Fisher, T. Maeder, and K. Kögler, *Reduction of wind turbine noise using optimized airfoils and trailing-edge serrations*, [AIAA Journal](#) **47**, 1470 (2009).
- [1.39] G. Leloudas, W. J. Zhu, J. N. Sørensen, W. Z. Shen, and S. Hjort, *Prediction and Reduction of Noise from a 2.3 MW Wind Turbine*, [Journal of Physics: Conference Series](#) **75**, 012083 (2007).
- [1.40] J. Cheng, W. Zhu, A. Fischer, N. R. García, J. Madsen, J. Chen, and W. Z. Shen, *Design and validation of the high performance and low noise CQU-DTU-LN1 airfoils*, [Wind Energy](#) **17**, 1817 (2014).
- [1.41] T. Lutz, A. Herrig, W. Würz, M. Kamruzzaman, and E. Krämer, *Design and Wind-Tunnel Verification of Low-Noise Airfoils for Wind Turbines*, [AIAA Journal](#) **45**, 779 (2007).

- [1.42] T. Kim, S. Lee, H. Kim, and S. Lee, *Design of low noise airfoil with high aerodynamic performance for use on small wind turbines*, [Science in China Series E: Technological Sciences](#) **53**, 75 (2010).
- [1.43] S. R. Koh, M. Meinke, and W. Schröder, *Impact of multi-species gas injection on trailing-edge noise*, [Computers & Fluids](#) **75**, 72 (2013).
- [1.44] J. Yu, S. R. Koh, M. H. Meinke, and W. Schroeder, *Noise Reduction via Jet Injection near the Trailing Edge*, [22nd AIAA/CEAS Aeroacoustics Conference](#) , 1 (2016).
- [1.45] D. L. Sutliff, D. L. Tweedt, E. B. Fite, and E. Envia, *Low-Speed Fan Noise Reduction With Trailing Edge Blowing*, [International Journal of Aeroacoustics](#) **1**, 275 (2002).
- [1.46] J. M. Brookfield and I. A. Waitz, *Trailing-Edge Blowing for Reduction of Turbomachinery Fan Noise*, [Journal of Propulsion and Power](#) **16**, 57 (2000).
- [1.47] E. Fite, R. Woodward, and G. Podboy, *Effect of Trailing Edge Flow Injection on Fan Noise and Aerodynamic Performance*, in [3rd AIAA Flow Control Conference](#) (American Institute of Aeronautics and Astronautics, San Francisco, California, 2006).
- [1.48] T. Geyer, E. Sarradj, and C. Fritzsche, *Porous airfoils: noise reduction and boundary layer effects*, [International Journal of Aeroacoustics](#) **9**, 787 (2010).
- [1.49] E. Sarradj and T. Geyer, *Noise Generation by Porous Airfoils*, [13th AIAA/CEAS Aeroacoustics Conference \(28th AIAA Aeroacoustics Conference\)](#) **28**, 1 (2007).
- [1.50] M. R. Khorrami and M. M. Choudhari, *Application of passive porous treatment to slat trailing edge noise*, [Langley Research Center, NASA/TM](#) **212416** (2003).
- [1.51] M. Herr, K. S. Rossignol, J. Delfs, N. Lippitz, and M. Mößner, *Specification of Porous Materials for Low-Noise Trailing-Edge Applications*, in [20th AIAA/CEAS Aeroacoustics Conference](#) (American Institute of Aeronautics and Astronautics, Atlanta, Georgia, 2014).
- [1.52] A. Finez, E. Jondeau, M. Roger, and M. C. Jacob, *Broadband Noise Reduction With Trailing Edge Brushes*, in [16th AIAA/CEAS Aeroacoustics Conference](#) (2010).
- [1.53] M. Herr and W. Dobrzynski, *Experimental Investigations in Low-Noise Trailing Edge Design*, [AIAA Journal](#) **43**, 1167 (2005).
- [1.54] M. J. Asheim, *Measurement of aeroacoustic noise generated on wind turbine blades modified by trailing edge brushes*, [Phd thesis](#), Colorado School of Mines (2014).
- [1.55] M. S. Howe, *Aerodynamic noise of a serrated trailing edge*, [Journal of Fluids and Structures](#) **5**, 33 (1991).
- [1.56] N. Fritsch-Nehring, *Trailing Edge Serrations*, [windblatt das ENERCON Magazin](#) , 19 (2015).
- [1.57] General Electric, [Introducing GE's 2.75 MW Wind Turbines](#), (2012).

- [1.58] S. Oerlemans, *Reduction of wind turbine noise using blade trailing edge devices*, [22nd AIAA/CEAS Aeroacoustics Conference](#), 1 (2016).
- [1.59] M. S. Howe, *Noise produced by a sawtooth trailing edge*, [The Journal of the Acoustical Society of America](#) **90**, 482 (1991).
- [1.60] K. A. Braun, *Serrated Trailing Edge Noise: (STENO), Final Report, Research in the Framework of the Non Nuclear Energy Programme JOULE III* (ICA, 1998).
- [1.61] LM Wind Power, *Introducing GloBlade®*, Brochure (2013).
- [1.62] International Energy Agency, *Executive Summary: Projected Costs of Generating Electricity*, (2015).

2

OVERVIEW OF AEROACOUSTICS AND AIRFOIL TRAILING EDGE NOISE

If a tree falls in a forest and no one is around to hear it, does it make a sound?

Thought philosophical experiment,
based on the discourse of George Berkeley

A brief summary of airfoil aeroacoustic models is presented in this chapter, along with a discussion of the relevant experimental research of trailing edge serrations.

THE THEORETICAL BASIS OF AEROACOUSTIC RESEARCH IS GROUNDED on the work of Sir M. James Lighthill ([2.1]). He sought to model phenomena related mostly to the noise produced by jets, providing a description for high-Mach number acoustics that are dominated by quadrupole sources in the turbulent flow volume.

In the presence of a body (although not exclusively), dipole sources appear. At lower Mach numbers, such as those found in the current application, these dominate over the quadrupole sources. They are known to scale with u^5 for compact bodies ([2.2]), and u^6 for non-compact ones ([2.3]), versus u^8 for quadrupoles ([2.1]).

The current work will therefore invest effort to research flow that is close to the surface of the airfoil, and especially its trailing edge, serrated or straight. The aforementioned source scaling rules support the argument that turbulence in the wake, or regions sufficiently far from the edge, are non-contributing.

2.1. AIRFOIL TRAILING EDGE NOISE

Trailing edge noise will be described analytically in this chapter. While the experimental research conducted in this work is unable to produce the data required for the direct implementation of these models, elements in their formulation will help to cement the discussion, and outline the relevant flow parameters for trailing edge noise evaluation in later chapters.

The more fundamental analytical solutions, such as the acoustic analogies of Lighthill ([2.1]), Curle ([2.3]) and Ffowcs-Williams Hawkins (FW-H) ([2.4]), very directly describe several families of aeroacoustic problems. More specific cases, such as those involving sharp-edged semi-infinite plates, are characterized by the approach proposed by Ffowcs-Williams and Hall [2.2] and Crighton and Leppington [2.5].

These solutions nevertheless require a level of flow field description that is, arguably, unobtainable by current experimental methods. Numerical methods are instead more often adequate for this purpose ([2.6–8] are a few examples). Their ability to retrieve the transient pressure field and surface information is of great advantage.

It is therefore desirable to formulate trailing edge noise models that are less demanding. Less expensive numerical methods, such as XFOIL or RANS, would allow a computationally cheaper, and more engineering-focused analysis of airfoil noise by reducing the turnover time. To improve the potential to utilize experimental data as an input would also be attractive.

Examples of such models are found in the work of Chase [2.9], Amiet [2.10], Howe [2.11] and Blake [2.12]. They require a reduced set of parameters, and are quicker to compute. They remain nevertheless problematic when using data directly available from state-of-the-art experimental methods.

While the entire flow field does not need to be described, that within the boundary layer does. The acquisition of volumetric data that covers at least its thickness through non-intrusive methods is still challenging, yet required to describe spanwise length scales, and convection velocity, among other parameters. The surface pressure should also be determined. Instruments that achieve this are technically unavailable for thin models, such as in the current application. It could alternatively be estimated from the pressure fluctuations in the boundary layer. This relationship is not straightforward ([2.13, 14]),

but some effort has been conducted to use particle image velocimetry (PIV) for its estimation ([2.15]). The models are nevertheless usually limited to the case of flat plates, and the relationship can depart from them in situations that deviate, such as when adverse pressure gradients are present. Chong and Vathylakis [2.16] has also provided a relationship between Reynolds stress events and high-pressure peaks on the surface.

The available acoustic models may nevertheless play a strategic role in the representation of trailing edge acoustics with experimental flow information. Dominant terms and trends can be established from them. This allows partial but relevant experimental data to be retrieved, through which trailing edge noise can be described to some degree. This approach is used in chapter 5, where elements of the TNO-Blake equation (section 2.1.3) are evaluated and used to compare flow over different streamwise locations over the edge of trailing edge serrations.

In the following sections, several of these models are described. The mathematical development is shown in order to connect with the relevant terms used later in this work. Especial focus is given to the formulation of the TNO-Blake model, and to models that describe the noise emitted from variable-shape trailing edges.

2.1.1. THE AMIET MODEL

The Amiet model requires knowledge of the wall pressure spectrum. It assumes that the presence of the wall is inconsequential to the flow, and complies with the Taylor frozen turbulence hypothesis ([2.17]). Models such as that of Corcos [2.18] can be used to approximate this information in the case of a turbulent boundary layer.

Amiet's approach is in essence a simplification of the Curle solution ([2.3]) where the volume sources—the quadrupole term—have been omitted due to the dominant nature of the dipole terms at low speed. The surface term is then used to relate the pressure discontinuity at the edge, ΔP , to the far-field pressure.

The simplified solution of the far-field sound spectrum for an observer located over the center of the airfoil span ($x_3 = 0$) is obtained by Amiet as

$$S_{pp}(x_1, x_2, x_3 = 0, \omega) = \left(\frac{\omega b x_2}{2\pi c_0 r^2} \right) \ell_3(\omega) d|\mathcal{L}|^2 S_{qq,3}(\omega, 0), \quad (2.1)$$

where x_1 , x_2 and x_3 are respectively the streamwise, wall-normal and spanwise directions, b is the semi-chord, and $S_{qq,3}(\omega, x_3)$ is the spanwise cross-spectrum of the surface pressure. The acoustic transfer function is expressed as

$$|\mathcal{L}| = \left| \int_{-2}^0 g(\xi, \omega, u_{c,1}) e^{-i\mu\xi(\text{Ma} - x_1/r)} d\xi \right|, \quad (2.2)$$

the spanwise correlation length is

$$\ell_3(\omega) = \frac{1}{S_{qq,3}(\omega, 0)} \int_0^\infty S_{qq,3}(\omega, x_3) dx_3, \quad (2.3)$$

and the distance to the observer is $r^2 = x_1^2 + \beta^2 x_2^2$ for $\beta^2 = 1 - \text{Ma}^2$. The mean freestream convection velocity in the x_0 coordinate is written as $u_{c,1}$. The function g represents the surface pressure jump at the edge, as

$$g(\bar{x}_1, \omega, u_{c,1}) = \left\{ (1 + i) E^* \left[-\bar{x}_1 (1 + \text{Ma}) \mu + \bar{K}_1 \right] - 1 \right\} e^{-i\bar{K}_1 x_1}, \quad (2.4)$$

where the overline represents a non-dimensionalized variable in terms of the semi-chord b , $\mu = \omega b \text{Ma} / U \beta^2$, $K_1 = \omega / u_{c,1}$ is the streamwise wavenumber, and

$$E^*(x_1) = \int_0^{x_1} (2\pi\xi)^{-1/2} e^{-i\xi} d\xi \quad (2.5)$$

is a combination of Fresnel integrals. While this applies for cases with zero spanwise wavenumber, $k_3 = 0$, a more general solution can be obtained.

It must be noted that the [Amiet](#) model doesn't account for leading edge effects. While this remains a valid assumption for frequencies at which the airfoil is compact, it lacks accuracy for low frequencies. A correction, obtained by considering leading edge back-scattered pressure, is provided by Roger and Moreau [2.19].

2.1.2. THE HOWE MODEL

Howe [2.11] argues that the theories based on the Lighthill analogy, while giving a correct velocity scaling for the sound under the right assumptions, do not capture the mechanism involved in noise production. In an effort to develop an alternative solution that encapsulates the models proposed by Lighthill, Amiet and others, while providing a more complete physical description, Howe develops a trailing edge model based on vortex sound theory.

The Lighthill equation can be written based in terms of a distribution of vortices—instead of quadrupoles—as

$$\left[\frac{1}{c_0^2} \left(\frac{\partial}{\partial t} + U_\infty \frac{\partial}{\partial x_1} \right)^2 - \nabla^2 \right] B = \nabla \cdot (\boldsymbol{\omega} \wedge \mathbf{U}_{c,s}) + \nabla \cdot (\overline{\boldsymbol{\omega}} \wedge \mathbf{U}_{c,w}), \quad (2.6)$$

where $\boldsymbol{\omega}$ is the vorticity vector (the overline represents the vorticity of the *shed* vortices), $\mathbf{U}_{c,s}$ is the mean convection velocity over the surface, $\mathbf{U}_{c,w}$ is the wake convection velocity, U_∞ is the freestream velocity, and

$$B = \int \frac{dp}{\rho} + \frac{\mathbf{u}^2}{2} \quad (2.7)$$

is the total or stagnation enthalpy. In essence, the two terms in the right hand side of (2.6) respectively represent the incident and shed vorticity contribution to sound.

Assuming that the convection velocity of the vortices is perpendicular to the edge, such that $k_3 = 0$, and that the observer lies in the center of the wetted span ($x_3 = 0$), the acoustic frequency spectrum density according to Howe takes the simplified form

$$S_{pp}(\omega) = \frac{\omega L}{2\pi r^2 c_0} \int_{-\infty}^{\infty} \frac{\Phi_B(k_1, 0, \omega)}{|k_1| (1 - k_1 \omega / c_0)} dk_1 \quad (2.8)$$

for $\Phi_B(\mathbf{k}, \omega)$ the so-called blocked surface pressure wavenumber-frequency spectrum.

Results obtained with Howe's theory have shown a good comparison with experimental data (as in [2.20]). It will be revisited in section 2.2.1, where it will be investigated for trailing edge of variable shapes.

2.1.3. THE TNO-BLAKE MODEL

While the Amiet approach is useful and has shown good agreement with experimental results, obtaining values for the surface pressure is not always straightforward in an experimental campaign.

Transducers for this effect have not yet reached the size requirements often necessary to properly characterize the surface pressure. The thickness of the model and the relative size of the sensors against the characteristic size of the pressure waves are important limitations that prevent obtaining data with enough precision. This topic has been addressed by Corcos [2.21] and Willmarth [2.22] among others. The surface spatial resolution obtainable with direct pressure measurements is also limited by the size of the instruments, potentially restricting the ability to measure the convection velocity of smaller-scale or short-lived surface pressure structures.

A characterization of surface pressure, based on the turbulent hydrodynamic field, is therefore desirable. It has been a well researched subject for several decades, initially motivated by applications such as sonars in ship and submarine hulls. A comprehensive overview of the research is given by Bull [2.14] and Willmarth [2.13]. Unfortunately, the connection between turbulence events in the boundary layer and the surface pressure is complex, in part due to the vertical gradient in the convection velocity of the turbulence velocity fluctuations along the boundary layer.

Efforts in overcoming this difficulty have been proposed by Farabee and Casarella [2.23] and Bull [2.24]. They suggest that a three-part division of the boundary layer is possible, wherein each layer contributes in its own way to the surface pressure. With this approach, a satisfactory collapse of the pressure spectrum to the wavenumber spectrum has been obtained. It is nevertheless sensitive to the Reynolds number ([2.25]) and unlikely to be applicable to cases more complex than a flat-plate under a zero pressure gradient.

Parchen [2.26], while at the Netherlands Organisation for Applied Scientific Research (TNO), formulated an approach based on a description of the surface pressure from turbulent boundary layer flow information as detailed in Blake [2.12]. It is now known as the TNO-Blake model.

Blake uses a Poisson equation to make this description, derived by taking the divergence of the Navier-Stokes equation and simplifying it by means of the continuity equation. After subtracting the mean flow, through Reynolds decomposition ($u = \bar{u} + u'$), it reads

$$\nabla^2 p = -2\rho \frac{\partial u'_j}{\partial x_i} \frac{\partial \bar{u}_i}{\partial x_j} - \frac{\partial^2}{\partial x_i \partial x_j} \left(u'_i u'_j - \overline{u'_i u'_j} \right), \quad (2.9)$$

where the first term on the right-hand-side represents turbulence-mean shear interactions, and the second, turbulence-turbulence interactions. This expression can be further simplified by considering that shear is only present in the wall-normal direction, x_2 , as $d\bar{u}_1/dx_2$, and by applying a rigid-wall boundary condition for u'_i , resulting in

$$\nabla^2 p = -2\rho \frac{d\bar{u}_1}{dx_2} \frac{\partial u'_2}{\partial x_1}. \quad (2.10)$$

By using the Powell [2.27] method of images, the surface pressure, p_w , can be solved over the volume using the free-field Green's function, while forcing the boundary condition $\partial p_w / \partial x_2 = 0$. Its spatial-temporal Fourier transform

$$\widetilde{p}_w(\mathbf{k}, \omega) = -2\rho \int_0^\infty \frac{\partial \overline{u}_1}{\partial x_2} \frac{k_1}{k} \widetilde{u}_2' e^{-x_2 k} dx_2 \quad (2.11)$$

is obtained. Its wavenumber-frequency spectral density is then retrieved from \widetilde{p}_w as

$$\Phi_p(\mathbf{k}, \omega) \delta(\mathbf{k} - \mathbf{k}'') \delta(\omega - \omega'') = \langle \widetilde{p}_w(\mathbf{k}, \omega) \widetilde{p}_w^*(\mathbf{k}'', \omega'') \rangle, \quad (2.12)$$

under the assumption of a spatially homogeneous and time-stationary pressure and wall-normal velocity fields.

Equally,

$$\phi_{22}(k_1, x_2, x_2'', k_3, \omega) \delta(\mathbf{k} - \mathbf{k}'') \delta(\omega - \omega'') = \langle \widetilde{u}'(k_1, x_2, k_3, \omega) \widetilde{u}'^*(k_1'', x_2'', k_3'', \omega'') \rangle \quad (2.13)$$

is the vertical fluctuation spectral density. Here $\langle \cdot \rangle$ represents the ensemble average.

The approximations of Blake [2.12] and Parchen [2.26] provide an expression for the wall pressure wavenumber-frequency spectrum

$$\Phi_p(\mathbf{k}, \omega) = 4\rho^2 \frac{k_1^2}{k^2} \int_0^\delta \Lambda_{2|22}(x_2) \left(\frac{\partial \overline{u}_1(x_2)}{\partial x_2} \right)^2 \times \overline{u_2'^2}(x_2) \phi_{22}(\mathbf{k}) \phi_m(\omega - k_1 U_c(x_2)) e^{-2|k|x_2} dx_2. \quad (2.14)$$

Here $\Lambda_{2|22}$ is the vertical integral length scale, and $\phi_m = \delta(\omega - k_1 U_c(x_2))$ is the so-called moving axis spectrum for the assumption of frozen turbulence. It is used to describe how ϕ_{22} is distorted by the generation and destruction of eddies during their convection past the trailing edge. The integration is done from the surface over the entire boundary layer of thickness δ .

Finally, the TNO-Blake far-field acoustic spectrum solution can be expressed ([2.28]) as

$$S_{pp}(x_1, x_2, x_3 = 0, \omega) = \left(\frac{C\omega x_2}{4\pi c_0 r^2} \right)^2 \frac{\pi L}{2U_c} |\mathcal{L}|^2 \Phi_p(k_1 = \omega/U_c, k_3 = 0, \omega), \quad (2.15)$$

for L the airfoil span and C its chord.

Equation (2.14) is of importance because it lets a relationship be made between the surface pressure description and hydrodynamic values in the boundary layer that are attainable with relative ease. In this way, Φ_p can be obtained, with some modifications to (2.14), from panel methods such as the XFOIL solver from Drela [2.29] or from a Reynolds averaged Navier-Stokes (RANS) simulation.

Improvements to the model, mainly focusing on accounting for turbulence anisotropy in the boundary layer, have been made by Stalnov *et al.* [2.28], Kamruzzaman *et al.* [2.30], Bertagnolio *et al.* [2.31]. A comprehensive set of experimental tests under the Benchmark Problems for Airframe Noise Computations (BANC) workshop ([2.32, 33]) have shown that TNO-Blake indeed resolves trailing edge noise within a satisfactory margin of error, but quite importantly, it does so as well with relatively low resource requirements.

Elements of the Blake [2.12] surface pressure approximation will be used later in chapter 5 to formulate a qualitative description of the pressure modification along a separation surface, based on measurements of the boundary layer flow performed with PIV.

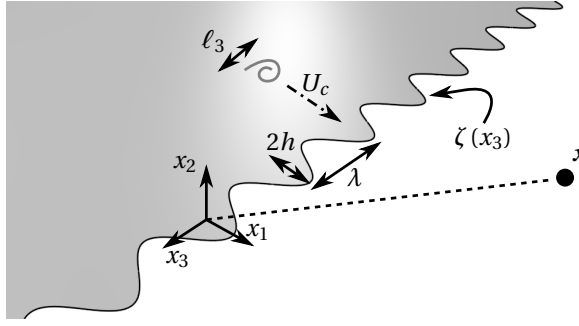


Figure 2.1: Schematic of a sinusoidal serrated trailing edge, as considered in the Howe model.

2.2. VARIABLE-SHAPE TRAILING EDGE NOISE MODELS

The discussion in this chapter has so far illustrated the development of aeroacoustic theory starting off with Lighthill and extending to advances made to correctly capture the sound of airfoil sharp trailing edges. The dominance of the dipole sound contribution has been established, and a method using boundary layer flow information to describe the far-field acoustics has been outlined.

While the research undertaken in the present work deals with trailing edge noise, the main interest is how its acoustic emission changes between straight and non-straight edges, specifically those with a sawtooth serration geometry. This section will therefore present the theoretical background of variable-shape trailing edge noise.

At this point, a distinction must be made between the concept here presented and similar devices used in jet engine applications called *chevrons*. Such geometries were first conceived by Westley and Lilley [2.34] among others, and result in the reduction of turbulent mixing noise—often dominant in such applications—through the introduction of streamwise vortex pairs ([2.35]).

Turbulent mixing noise is not present in airfoils, where the difference between the mean flow velocity over the two airfoil surfaces is relatively small. The mixing of the two layers at the wake—as discussed above—is not an efficient noise source. The high-speed jet core velocity is instead considerably larger than that of the surrounding air, resulting in an intense mixing region where quadrupole acoustic sources become significant.

2.2.1. THE HOWE MODEL

The problem of a variable-shape trailing edge is addressed by Howe [2.36], and a general solution is provided. The theory specifically targets trailing edges that are serrated, thus composed of a periodic geometric arrangement defined by $x_1 = \zeta(x_3)$. Initially it considers a sinusoidal shape (as in figure 2.1) due to its simplicity when doing the mathematical analysis. The solution was extended to a sawtooth shape soon thereafter in [2.37].

Howe argues that two scenarios exist, driven by the relative size of the turbulent eddies and the serration amplitude. When the acoustic frequency is low and is produced by eddies whose length scale greatly exceeds the amplitude of the serrations, such that $k_1 \zeta \ll 1$, the effect of the serrations would be negligible, and the acoustic pressure fre-

quency spectrum is driven by the spanwise correlation length and the frequency spectrum of the pressure fluctuations on the airfoil, as

$$S_{pp,0}(\omega, \mathbf{x}) \sim \frac{L}{r^2} \ell_3 \Phi_B(\omega), \quad (2.16)$$

where L here refers to the wetted edge length.

In the opposite case, where $k_1 \zeta \gg 1$, the diffracted pressure field

$$p_s(\mathbf{x}, \omega) = \frac{i}{2} \int_{-\infty}^{\infty} dy_3 \int_{-\infty}^0 dz_1 \int_{-\infty}^{\infty} \gamma(\mathbf{k}) [G(x, y_1, y_3, \omega)] \\ \times \tilde{p}_b(\mathbf{k}, \omega) e^{i(k_1 z_1 + k_3 y_3 + k_1 \zeta(y_3))} d^2 \mathbf{k} \quad (2.17)$$

is obtained, having introduced the variable change $z_1 = y_1 - \zeta(y_3)$.

Here $\gamma(\mathbf{k}) = i\sqrt{\kappa_0^2 - |\mathbf{k}|^2}$ for $\kappa_0 = |\omega|/c_0 > |\mathbf{k}|$ the acoustic wavenumber. The Fourier transform of the blocked pressure is $\tilde{p}_b(\mathbf{k}, \omega) = 2\tilde{p}_i(\mathbf{k}, \omega)$, for p_i the incident boundary layer pressure field that would be present if the surface was absent, and p_b the pressure resulting from p_i on a rigid and infinite plate, called the *blocked* pressure. To obtain this equality, a boundary condition at the wall, requiring the normal velocity component to vanish, has been imposed.

Based on this result, [Howe](#) states that, for smoothly varying serrations, the contribution to noise must come from sections of the trailing edge where

$$\frac{\partial \zeta(y_3)}{\partial y_3} = -\frac{U_c k_3}{\omega}, \quad (2.18)$$

or, in other words, sections where \mathbf{k} is normal to the edge. Further stating that the dominant blocked pressure fluctuations occur for $|k_3| \leq 1/\ell_3$, the contributing sources of high-frequency noise occur in regions of the trailing edge where

$$\left| \frac{\partial \zeta(y_3)}{\partial y_3} \right| \leq 1. \quad (2.19)$$

This results in an approximation of the resulting far-field acoustic spectrum as

$$S_{pp}(\omega) \approx \frac{L_e}{L} S_{pp,0}(\omega), \quad (2.20)$$

where L_e is the wetted length of the trailing edge that complies with (2.19) (or regions of the trailing edge inclined by at least 45° to the flow). For the specific case of sinusoidal serrations, such that $\zeta(y_3) = h \cos(2\pi y_3/\lambda)$ for h the peak amplitude of the serrations and λ the wavelength, it becomes approximately

$$S_{pp}(\omega) \approx \frac{S_{pp,0}(\omega)}{\pi^2 h/\lambda}. \quad (2.21)$$

As mentioned before, the extension of the theory to sawtooth serrations is given in [2.37] (other more complex geometries are further addressed by Azarpeyvand *et al.*

[2.38]). Since sawtooth geometries do not present the rounding at the tips and roots which introduce regions below the 45° suggested inclination, they are naturally preferred over sinusoidal geometries. Sawtooth geometries are more prevalent in literature and industrial applications for this reason.

For this geometry, the resulting acoustic spectrum can be approximated as

$$S_{pp}(\omega) \approx \frac{S_{pp,0}(\omega)}{1 + (4h/\lambda)^2}. \quad (2.22)$$

In summary, the theory of [Howe](#) leads to three important conclusions of the noise reduction in relation to the serration geometric parameters.

- First, it suggests that the noise reduction by serrations will only be effective after a certain frequency defined by $\omega\delta/U_c$ where the boundary layer thickness δ is related to the largest turbulent structures present, and thus the lowest frequencies encountered.
- Second, it relates the total reduction level to a ratio of the serration wavelength over its amplitude.
- And finally, it predicts an oscillatory behavior in the far-field pressure spectrum, driven by the incoherence or coherence of sources along the edge.

The arguments are based on a few assumptions, including that the boundary layer is turbulent, the flow is essentially two-dimensional (2D), and the Taylor frozen turbulence hypothesis is satisfied.

2.2.2. THE LYU MODEL

As will be discussed in section 2.3, the [Howe](#) model has been found to overestimate noise reduction. By using a Schwartzschild technique, as in [Amiet](#) [2.10], [Lyu et al.](#) [2.39] presents an alternative solution that has shown results with reduction levels closer to those observed in experiments.

The procedure adopted by [Lyu et al.](#) essentially follows that of [Amiet](#), but introduces a different trailing edge geometry. The obtained far-field spectral density solution, simplified for a very large span, becomes

$$S_{pp}(\mathbf{x}, \omega) = 2\pi L \left(\frac{\omega x_3 C}{4\pi c_0 r^2} \right)^2 \sum_{m=-\infty}^{\infty} \left| \mathcal{L}(\omega, \bar{k}_1, 2m\pi/\lambda) \right|^2 S_{qq}(\omega, 2m\pi/\lambda). \quad (2.23)$$

This is comparable to (2.1) and similar to the result obtained by [Howe](#). In fact, the zero-order solution recovers that of [Howe](#), indicating that it is the higher-order terms that help obtain a more realistic noise reduction level by the serrations.

[Lyu et al.](#) argues, as [Howe](#), that the noise reduction mechanism is due to the destructive interference of the scattered surface pressure. Two conditions are proposed, which echo those mentioned in section 2.2.1. First, that $k_1 h \gg 1$, such that an effective phase variation appears along the trailing edge in the spanwise direction. Second, that $k_1 \ell_3 (2h/\lambda) \gg 1$, such that the phase difference appears within one spanwise correlation length.

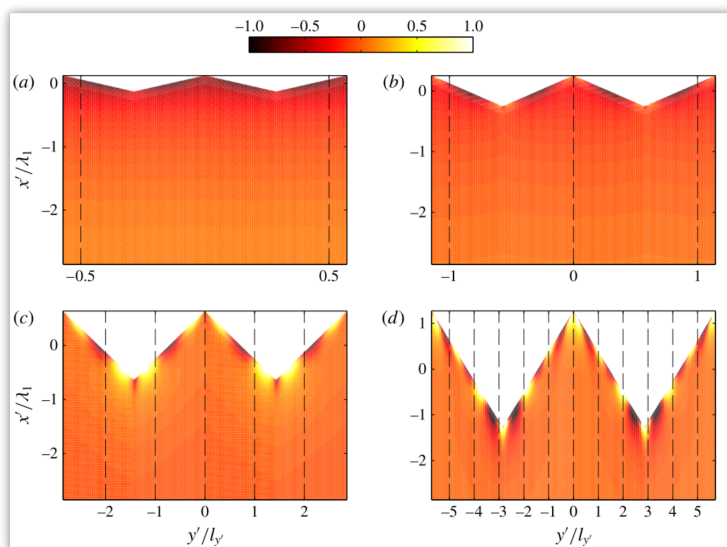


Figure 2.2: Scattered surface pressure distribution for $k_1 \ell_3 (2h/\lambda) = 7$ and four values of $k_1 h$: a) 2, b) 4 c) 10 and d) 20. Source: Lyu *et al.* [2.39].

A visual representation of results obtained by Lyu *et al.* is shown in figure 2.2. The normalized scattered surface pressure distribution (with the range $[-1, 1]$) is shown for four values of $k_1 h$ and a fixed value of $k_1 \ell_3 (2h/\lambda) = 7$. The contour maps are presented where the horizontal axis represents the spanwise correlation length-normalized x_3 coordinate (y' in the figure), and the vertical axis the streamwise coordinate x_1 (x' in the figure) normalized by the hydrodynamic wavelength $\lambda_1 = 2\pi/k_1$. The effect of $k_1 h$ on the modification of the scattered surface pressure is evident as it forces phase differences throughout the length of the edge.

2.3. OVERVIEW OF RESEARCH ON TRAILING EDGE SERRATIONS

Following the development of serration noise theory by Howe, serrations have become the object of interest in numerous studies, mainly based on wind tunnel acoustic measurements and numerical simulations. In this section, a brief overview shall be given of several such studies, summarizing the findings and the different conditions at which they have been tested¹. Although this list aims to be thorough, it does not intend to be

¹Values are reported as best understood from the text in their respective studies. As a consequence, they may not be entirely comparable with other sources. The reported angle of attack, for example, refers to the *geometric* angle of attack if specifically stated in the original text, but could otherwise also refer to the *effective* angle if it is not clear in the text. Likewise, the reported noise reduction by the serrations is the *maximum* reported reduction in the studies, whether or not it actually refers to the peak reduction in a narrowband spectrum, in the overall sound power level measured, or in any other equally plausible alternatives. The reader is referred

an exhaustive review of the entire body of research. Studies related to the mitigation of laminar boundary layer-instability noise and blunt trailing edge noise are omitted, as the topic of interest is turbulent boundary layer-trailing edge noise (TBL-TE noise).

One of the first records of acoustic measurements of serrated airfoils is found in Dassen *et al.* [2.40]. In this report, several airfoils were retrofitted with a number of serration geometries, specifically targeting design parameters such as misalignment of serrations, in the span and flapwise directions, and the effect of skewness. It uses a fixed length-to-width ratio. It is one of the few studies that addresses the issue of flapwise misalignment, concluding that it results in a loss of the noise reduction performance of the serrations. Despite its importance, very few later studies have considered this as a research parameter. Flap angles have often instead been present as a side-effect of the serration installation on airfoils, especially those with large camber. Overall, Dassen *et al.* finds that the serrations are indeed effective in reducing noise, showing a reduction of up to 10 dB.

A number of projects followed a few years later in which serrations were tested on full-scale or mid-scale rotors. Results obtained by Hagg *et al.* [2.41], Braun *et al.* [2.42] and Schepers *et al.* [2.43] successfully demonstrated the potential of serrations on prototype wind turbine rotors. It showed that reduction levels of around 3 dB were possible. Particularly, in [2.42], the issue of serration flapwise misalignment is also addressed, showing an increase in the noise in the higher frequencies. This observation is also suggested in [2.43], although not specifically investigated. Later field measurements have also obtained similar reduction levels, not ever obtaining the values observed in laboratory-controlled wind tunnel measurements. This discrepancy remains unresolved.

A great amount of wind tunnel-based research has been conducted by groups in England, namely by Gruber *et al.* [2.44], Gruber *et al.* [2.45], Chong *et al.* [2.46], Gruber *et al.* [2.47], Liu *et al.* [2.48], Chong and Vathylakis [2.16], Vathylakis *et al.* [2.49], Thomareis and Papadakis [2.50] and Vathylakis *et al.* [2.51]. Among this research, [2.16, 46, 50] have focused on serrations of cutout type, whereby wedges are cut from the airfoil such that serrations with a thick base are obtained. Others have researched flat serrations (as in the present work), attached to the otherwise unmodified airfoil geometry. Aerodynamic measurements have been conducted to a certain degree by these groups, but it has focused mainly on wake development and flow motion in the space between the serration teeth.

Chong and Vathylakis [2.16] obtained surface pressure measurements, installing the serrations on the bottom side of the wind tunnel nozzle, such that one side remained outside the flow. This allowed the necessary instrumentation to protrude from the surface without altering the flow. While this produced valuable data, relating how some flow structures are associated to surface pressure events, the conditions that this setup provides vary considerably from those experienced by serrations on airfoils, where flow is present on both sides and between them experiences a relatively small velocity difference.

Large part of the England-based research has focused on the high-camber NACA 6512-10 airfoil. Its use has implied that the tested serrations are generally misaligned with the otherwise undisturbed flow at the wake. The only variation parameter available

to the original text, should any doubt arise.

to control this has been the airfoil angle of attack.

More recently, Vathylakis *et al.* [2.51] focused on serration-flow misalignment, designing serrations with several flap angles ranging from -15° to 15° , measured against the trailing edge angle (*not* the airfoil camber). It should be noted that the sign convention used in this study is inverted from the one adopted in the present work, such that negative values angle the serrations toward the *bottom* side of the airfoil. Because of the airfoil camber, it is not straightforward to identify the neutral serration angle, namely the flap angle at which the serrations disturb the flow less. In fact, the ability to achieve zero disturbance on a cambered airfoil is debatable, as the unmodified flow at the wake would likely present a certain curvature except for a very particular airfoil- and Reynolds number-dependant angle of attack. From the aerodynamic wake measurements in the case of [2.51], it appears to lie beyond 10° .

With respect to serration design, the research of Gruber *et al.* [2.45] has produced valuable guidelines by testing a large number of serration design parameters. It has primarily focused on different lengths and widths. Its conclusions can be summarized in the following three relations,

Non-dimensional frequency

The relationship $f\delta/U_0 < St_\delta$ defines up to what frequency noise reduction is observed, for $St_\delta \approx 1$. This effect is investigated here in chapter 6.

Non-dimensional serration amplitude

The ratio between the serration length and the boundary layer thickness, $2h/\delta$, specifies what is the minimum length serrations need to have in order to provide an effective noise reduction. It has been established in [2.45] that the minimum length of the serrations needs to be around twice the thickness of the boundary layer. Physically, this relates the serration length to the larger turbulence structures convecting in the boundary layer.

Serration edge angle

An increased serration edge angle, driven by the ratio h/λ , translates to a beneficial effect in noise reduction, but it appears to also have an upper limit.

Other than the experimental research, some numerical efforts also stand out. The very detailed direct numerical simulation (DNS) of Jones and Sandberg [2.6, 54], the large eddy simulation (LES) of Arina *et al.* [2.7] and the dynamic mode decomposition (DMD) of [2.50] all offer a wealth of flow information that experimentally is unachievable. The associated acoustic results remain nevertheless difficult to validate, either because of the low Reynolds number or geometric limitations that the numerical domain needs to satisfy to avoid becoming prohibitively expensive. The number of investigated cases is usually also limited because of this reason. A more recent approach, using the lattice-Boltzmann method (LBM) is used in van der Velden *et al.* [2.8], by which a less expensive simulation is achieved for equally complicated geometries. It has also shown that a good approximation of the acoustic emissions is possible, compared to wind tunnel measurements under similar conditions.

A visualization of the research is presented in the circular dendrogram of figure 2.3. Some of the more common study criteria categories are presented with links to their respective parameters and values. This representation aims to highlight the different study

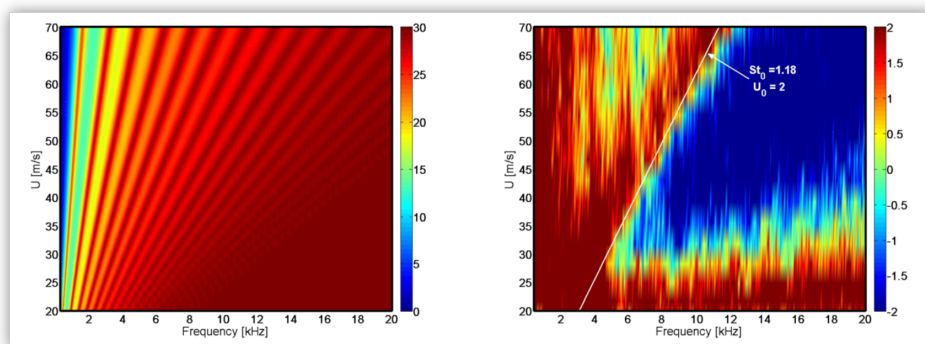


Figure 2.4: Contrast between the predicted frequency-wise noise reduction by Howe [2.37] (left) and wind tunnel-measured reduction by Gruber *et al.* [2.44] (right) over a range of flow velocities. Positive numbers indicate noise reduction. Source: Gruber *et al.* [2.44].

tion levels closer to those seen in experiments. While this is true, its spectral shape resembles that of Howe and also exhibits tip-root interference patterns which have not yet been observed in experiments. It is argued by Gruber *et al.* [2.45] that this is because in real life the turbulence is incoherent between the root and tip. The argument in Howe [2.37] where noise reduction is said to occur for $\omega h/U \gg 1$ is also not reproduced; the serrations have instead been shown to reduce noise below that given frequency, and are known to increase noise after a certain Strouhal number—a topic addressed in chapter 6.

There is no doubt that discrepancies are often unavoidable between experimental or numerical campaigns and the assumptions made in the derivation of analytic solutions. It is nevertheless clear that, although progress has been made, a comprehensive analytical approach for solving serration noise remains pending.

It is also noteworthy that the physical mechanism of noise reduction by serrations has not been satisfactorily established. Two trends can be found in literature. One considers that the modification of the flow is chiefly responsible for the noise reduction, and the second argues that the dominant reason is the loss of efficiency in the scattering by the edge due to its geometric alteration. Clearly Howe and Lyu *et al.* subscribe to the latter, as one assumption in the analytic solution is the compliance with Taylor's frozen turbulence hypothesis. A similar argument is proposed in [2.65]. Nevertheless, hydrodynamic-based reasoning is put forward in [2.6, 16, 58] and again in [2.65].

As specified before, a significant amount of work on serrations has been performed on highly cambered airfoils. In such a case, the serrations will almost unavoidably have a significant influence on the flow, which cannot therefore be assumed to be a necessary condition for noise reduction. Therefore, with the purpose of identifying the dominating cause of noise reduction, using configurations by which the serrations force a minimal effect on the flow is essential.

A cornerstone requirement to achieve this is that similar flow conditions on the upper and lower airfoil surfaces near the edge are obtained. Using a flat-plate airfoil would be one way to manage this. An example of such a setup is found in [2.56–58, 66]—the

effect there is nevertheless lost due to an asymmetry in the geometry upstream of the trailing edge. Another difficulty often encountered is that thin and long models carry an unwanted loss in rigidity. The use of symmetric airfoils is favoured, and forms the basis of the current work.

Isolating the hydrodynamic modification from the change in efficiency of the scattering mechanism remains challenging. Experimental measurements of the latter are based on the far-field acoustic emissions, but in which any effects of the former are also contained. A workaround is to focus on the serration influence on the flow and turbulence statistics, measured on a well-prepared setup. By interpretation of the results, the weight of its contribution to the modified far-field acoustics could potentially be inferred. This approach is attempted in chapter 5.

Table 2.1: List of trailing edge serration-related research relevant to the present study.

Paper	Field	Methodology	Airfoil	Type	α [deg]	$Re \times 10^6$	U_∞ [m/s]	Ma	Reduction
Howe [2.36] Howe [2.37]	Acoustics	Analytical							
Dassen <i>et al.</i> [2.40]	Acoustics	Wind tunnel	NACA 0012 NACA 630-18 NACA 636-18 NACA 4418 Flat-plate	Flat		0.71, 1.1, 1.4		0.12, 0.18, 0.22	10 dB
Braun <i>et al.</i> [2.42]	Acoustics	Field	Rotor	Flat					3.5 dB
Oerlemans <i>et al.</i> [2.52]	Acoustics	Wind tunnel	Rotor	Flat					3 dB
Schepers <i>et al.</i> [2.43] Oerlemans <i>et al.</i> [2.53]	Acoustics	Field	Rotor	Flat					3 dB
Gruber <i>et al.</i> [2.44]	Aerodynamics Acoustics	Wind tunnel	NACA 6512-10	Flat	-5, 0, 5, 10, 15	0.2, 0.4, 0.6, 0.8	20, 40, 60, 80		5 dB
Jones and Sandberg [2.6] Jones and Sandberg [2.54]	Aerodynamics Acoustics	Numerical (DNS)	NACA 0012	Flat	5	0.05		0.4	10 dB
Finez <i>et al.</i> [2.55]	Aerodynamics Acoustics	Wind tunnel	NACA 6512-10 (cascade)	Flat	16	0.55		0.23	5 dB
Gruber <i>et al.</i> [2.45]	Aerodynamics Acoustics	Wind tunnel	NACA 6512-10	Flat	0, 5	0.2, 0.4, 0.6, 0.8	20, 40, 60, 80		7 dB
Moreau <i>et al.</i> [2.56] Moreau [2.57] Moreau and Doolan [2.58] Moreau and Doolan [2.66]	Aerodynamics Acoustics	Wind tunnel	Flat-plate	Flat			[15 - 38]		7 dB
Arina <i>et al.</i> [2.7]	Aerodynamics Acoustics	Numerical (LES)	NACA 6512-10	Flat		0.6		0.17	10 dB
Chong <i>et al.</i> [2.46]	Aerodynamics Acoustics	Wind tunnel	NACA 0012	Cutout	15	[0.2 - 0.6]	[20 - 60]		8 dB

Azarpeyvand <i>et al.</i> [2.38]	Acoustics	Analytical								
Gruber <i>et al.</i> [2.47]	Aerodynamics Acoustics	Wind tunnel	NACA 6512-10	Flat	0, 5, 15	[0.2 - 0.6]	[20 - 60]			5 dB
Qiao <i>et al.</i> [2.59]	Aerodynamics Acoustics	Wind tunnel	SD2030	Cutout	[-5 - 5]	0.21, 0.25, 0.32	21, 25, 31	0.09		5 dB
Liu <i>et al.</i> [2.48]	Aerodynamics	Wind tunnel	NACA 6512-10 NACA 0012	Flat	[-5 - 20]	[0.2 - 0.6]	[20 - 60]			
Lyu <i>et al.</i> [2.39]	Acoustics	Analytical								
Vathylakis <i>et al.</i> [2.49]	Aerodynamics Acoustics	Wind tunnel	NACA 6512-10	Cutout			[20 - 60]			7 dB
Chong and Vathylakis [2.16]	Aerodynamics	Wind tunnel	Flat-plate	Cutout	0		30			
Avallone <i>et al.</i> [2.60]	Aerodynamics Acoustics	Wind tunnel	NACA 0018	Flat	0, 6, 12	0.1	10			6 dB
Clemons and Wlezién [2.61]	Aerodynamics	Wind tunnel	NACA 0012	Flat	[0 - 5]	0.8				
Thomareis and Papadakis [2.50]	Aerodynamics	Numerical (DMD)	NACA 0012	Cutout	5	0.05				
Arce León <i>et al.</i> [2.62]	Aerodynamics Acoustics	Wind tunnel	NACA 0018	Flat	0, 6, 12	0.2, 0.4	20, 40			5 dB
Arce <i>et al.</i> [2.64] Arce León <i>et al.</i> [2.62] Arce León <i>et al.</i> [2.63] Arce León <i>et al.</i> [2.67]	Aerodynamics Acoustics	Wind tunnel	NACA 0018	Flat	0, 6, 12	0.2, 0.4	20, 40			5 dB
Avallone <i>et al.</i> [2.60]	Aerodynamics Acoustics	Wind tunnel	NACA 0018	Flat	0, 6, 12	0.2, 0.4	20, 40			5 dB
van der Velden <i>et al.</i> [2.8] van der Velden and Oeflemans [2.68]	Aerodynamics Acoustics	Numerical (LBM)	NACA 0018	Flat Hybrid	0	0.2	20			6 dB

Vathylakis <i>et al.</i> [2.51]	Aerodynamics Acoustics	Wind tunnel	NACA 6512-10	Flat
Oerlemans [2.69]	Acoustics	Field	Rotor	Flat Hybrid
Fischer <i>et al.</i> [2.70] Fischer <i>et al.</i> [2.71]	Acoustics	Analytical Wind tunnel	DTU-CQN LN 118	Flat

BIBLIOGRAPHY

- [2.1] M. J. Lighthill, *On Sound Generated Aerodynamically. I. General Theory*, [Proceedings of the Royal Society A: Mathematical, Physical and Engineering Sciences](#) **211**, 564 (1952).
- [2.2] J. E. Ffowcs-Williams and L. H. Hall, *Aerodynamic sound generation by turbulent flow in the vicinity of a scattering half plane*, [Journal of Fluid Mechanics](#) **40**, 657 (1970).
- [2.3] N. Curle, *The Influence of Solid Boundaries upon Aerodynamic Sound*, [Proceedings of the Royal Society A: Mathematical, Physical and Engineering Sciences](#) **231**, 505 (1955).
- [2.4] J. E. Ffowcs-Williams and D. L. Hawkings, *Sound Generation by Turbulence and Surfaces in Arbitrary Motion*, [Philosophical Transactions of the Royal Society A: Mathematical, Physical and Engineering Sciences](#) **264**, 321 (1969).
- [2.5] D. G. Crighton and F. G. Leppington, *Scattering of aerodynamic noise by a semi-infinite compliant plate*, [Journal of Fluid Mechanics](#) **43**, 721 (1970).
- [2.6] L. Jones and R. Sandberg, *Numerical Investigation of Airfoil Self-Noise Reduction by Addition of Trailing-Edge Serrations*, in [16th AIAA/CEAS Aeroacoustics Conference](#), Vol. 2010–3703, AIAA (American Institute of Aeronautics and Astronautics, Reston, Virginia, 2010) pp. 1–23.
- [2.7] R. Arina, R. Della Ratta Rinaldi, A. Iob, and D. Torzo, *Numerical Study of Self-Noise Produced by an Airfoil with Trailing-Edge Serrations*, in [18th AIAA/CEAS Aeroacoustics Conference \(33rd AIAA Aeroacoustics Conference\)](#), June (American Institute of Aeronautics and Astronautics, Colorado Springs, CO, 2012) pp. 4–6.
- [2.8] W. C. van der Velden, A. van Zuijlen, and D. Ragni, *Flow topology and noise emission around straight, serrated and slitted trailing edges using the Lattice Boltzmann methodology*, [22nd AIAA/CEAS Aeroacoustics Conference](#), 1 (2016).
- [2.9] D. M. Chase, *Sound Radiated by Turbulent Flow off a Rigid Half-Plane as Obtained from a Wavevector Spectrum of Hydrodynamic Pressure*, [The Journal of the Acoustical Society of America](#) **52**, 1011 (1972).
- [2.10] R. Amiet, *Noise due to turbulent flow past a trailing edge*, [Journal of Sound and Vibration](#) **47**, 387 (1976).
- [2.11] M. Howe, *A review of the theory of trailing edge noise*, [Journal of Sound and Vibration](#) **61**, 437 (1978).
- [2.12] W. K. Blake, *Mechanics of Flow-Induced Sound and Vibration V2: Complex Flow-Structure Interactions, Volume 2* (Elsevier Science, 2012) p. 567.
- [2.13] W. W. Willmarth, *Pressure Fluctuations Beneath Turbulent Boundary Layers*, [Annual Review of Fluid Mechanics](#) **7**, 13 (1975).

- [2.14] M. K. Bull, *Wall-Pressure Fluctuations Beneath Turbulent Boundary Layers: Some Reflections on Forty Years of Research*, [Journal of Sound and Vibration](#) **190**, 299 (1996).
- [2.15] S. Ghaemi, D. Ragni, and F. Scarano, *PIV-based pressure fluctuations in the turbulent boundary layer*, [Experiments in Fluids](#) **53**, 1823 (2012).
- [2.16] T. P. Chong and A. Vathylakis, *On the aeroacoustic and flow structures developed on a flat plate with a serrated sawtooth trailing edge*, [Journal of Sound and Vibration](#) , 1 (2015).
- [2.17] G. I. Taylor, *The Spectrum of Turbulence*, [Proceedings of the Royal Society A: Mathematical, Physical and Engineering Sciences](#) **164**, 476 (1938).
- [2.18] G. M. Corcos, *The Structure of the Turbulent Pressure Field in Boundary-Layer Flows*, [Journal of Fluid Mechanics](#) **18**, 353 (1964).
- [2.19] M. Roger and S. Moreau, *Back-scattering correction and further extensions of Amiet's trailing-edge noise model. Part 1: theory*, [Journal of Sound and Vibration](#) **286**, 477 (2005).
- [2.20] T. Brooks, D. Pope, and M. Marcolini, *Airfoil self-noise and prediction*, [NASA Reference Publication Number 1218](#) (1989).
- [2.21] G. M. Corcos, *Resolution of Pressure in Turbulence*, [The Journal of the Acoustical Society of America](#) **35**, 192 (1963).
- [2.22] W. W. Willmarth, *Unsteady Force and Pressure Measurements*, [Annual Review of Fluid Mechanics](#) **3**, 147 (1971).
- [2.23] T. M. Farabee and M. J. Casarella, *Spectral features of wall pressure fluctuations beneath turbulent boundary layers*, [Physics of Fluids A: Fluid Dynamics](#) **3**, 2410 (1991).
- [2.24] M. K. Bull, *On the form of the wall-pressure spectrum in a turbulent boundary layer in relation to noise generation by boundary layer-surface interactions*, [In: Mechanics of sound generation in flows; Proceedings of the Joint Symposium](#) , 210 (1979).
- [2.25] W. L. Keith, D. A. Hurdis, and B. M. Abraham, *A Comparison of Turbulent Boundary Layer Wall-Pressure Spectra*, [Journal of Fluids Engineering](#) **114**, 338 (1992).
- [2.26] R. Parchen, *Progress report DRAW: A prediction scheme for trailing-edge noise based on detailed boundary-layer characteristics*, TNO Rept. HAGRPT-980023, TNO Institute of Applied Physics, The Netherlands (1998).
- [2.27] A. Powell, *On the Aerodynamic Noise of a Rigid Flat Plate Moving at Zero Incidence*, [The Journal of the Acoustical Society of America](#) **31**, 1649 (1959).
- [2.28] O. Stalnov, P. Chaitanya, and P. F. Joseph, *Towards a non-empirical trailing edge noise prediction model*, [Journal of Sound and Vibration](#) , 1 (2016).

- [2.29] M. Drela, *XFOIL: An Analysis and Design System Low Reynolds Number Aerodynamics and Transition*, edited by T. J. Mueller, Lecture Notes in Engineering (Springer Berlin Heidelberg, Berlin, 1989).
- [2.30] M. Kamruzzaman, T. Lutz, W. Würz, W. Z. Shen, W. J. Zhu, M. O. L. Hansen, F. Bertagnolio, and H. A. Madsen, *Validations and improvements of airfoil trailing-edge noise prediction models using detailed experimental data*, *Wind Energy* **15**, 45 (2012).
- [2.31] F. Bertagnolio, A. Fischer, and W. Jun Zhu, *Tuning of turbulent boundary layer anisotropy for improved surface pressure and trailing-edge noise modeling*, *Journal of Sound and Vibration* **333**, 991 (2014).
- [2.32] M. Herr and M. Kamruzzaman, *Benchmarking of Trailing-Edge Noise Computations—Outcome of the BANC-II Workshop*, *19th AIAA/CEAS Aeroacoustics Conference*, 1 (2013).
- [2.33] M. Herr, R. Ewert, C. Rautmann, M. Kamruzzaman, D. Bekiropoulos, R. Arina, A. Iob, P. Batten, S. Chakravarthy, and F. Bertagnolio, *Broadband Trailing-Edge Noise Predictions - Overview of BANC-III Results*, in *21st AIAA/CEAS Aeroacoustics Conference*, June (American Institute of Aeronautics and Astronautics, Dallas, TX, 2015) pp. 1–31.
- [2.34] R. Westley and G. M. Lilley, *An investigation of the noise field from a small jet and methods for its reduction*, Tech. Rep. (the College of Aeronautics, Cranfield, 1952).
- [2.35] K. Zaman, J. Bridges, and D. Huff, *Evolution from ‘tabs’ to ‘chevron technology’ — a review*, *International Journal of Aeroacoustics* **10**, 685 (2011).
- [2.36] M. S. Howe, *Aerodynamic noise of a serrated trailing edge*, *Journal of Fluids and Structures* **5**, 33 (1991).
- [2.37] M. S. Howe, *Noise produced by a sawtooth trailing edge*, *The Journal of the Acoustical Society of America* **90**, 482 (1991).
- [2.38] M. Azarpeyvand, M. Gruber, and P. Joseph, *An analytical investigation of trailing edge noise reduction using novel serrations*, in *19th AIAA/CEAS Aeroacoustics Conference* (2013).
- [2.39] B. Lyu, M. Azarpeyvand, and S. Sinayoko, *Prediction of noise from serrated trailing edges*, *Journal of Fluid Mechanics* **793**, 556 (2016), arXiv:1508.02276 .
- [2.40] T. Dassen, R. Parchen, J. Bruggeman, and F. Hagg, *Results of a wind tunnel study on the reduction of airfoil self-noise by the application of serrated blade trailing edges*, Tech. Rep. (National Aerospace Laboratory, NLR, 1996).
- [2.41] F. Hagg, G. van Kuik, R. Parchen, and N. van der Borg, *Noise reduction on a 1 MW size wind turbine with a serrated trailing edge*, in *Proceedings of the European Wind Energy Conference* (European Wind Energy Association, Dublin, Ireland, 1997) pp. 165–168.

- [2.42] K. Braun, N. Van der Borg, A. Dassen, F. Doorenspleet, A. Gordner, J. Ocker, and R. Parchen, *Serrated trailing edge noise (STENO)*, in *Proceedings of the European Wind Energy Conference* (European Wind Energy Association, Nice, France, 1999) pp. 180–183.
- [2.43] J. Schepers, A. Curvers, S. Oerlemans, K. Braun, T. Lutz, A. Herrig, W. Wuerz, A. Mantesanz, M. Fischer, K. Koegler, T. Maeder, L. Garcillán, B. Méndez-López, A. Matesanz, and R. Ahrelt, *Sirocco: Silent Rotors By Acoustic Optimisation*, in *Second International Meeting on Wind Turbine Noise* (2007).
- [2.44] M. Gruber, P. Joseph, and T. Chong, *Experimental investigation of airfoil self noise and turbulent wake reduction by the use of trailing edge serrations*, in *16th AIAA/CEAS Aeroacoustics Conference* (2010) pp. 1–23.
- [2.45] M. Gruber, P. Joseph, and T. Chong, *On the mechanisms of serrated airfoil trailing edge noise reduction*, in *17th AIAA/CEAS Aeroacoustics Conference (32nd AIAA Aeroacoustics Conference)*, Vol. 2781 (American Institute of Aeronautics and Astronautics, Portland, Oregon, USA, 2011) pp. 5–8.
- [2.46] T. Chong, P. Joseph, and M. Gruber, *On the airfoil self-noise reduction by trailing edge serrations of non-insertion type*, in *18th AIAA/CEAS Aeroacoustics Conference*, June (2012) pp. 4–6.
- [2.47] M. Gruber, P. Joseph, and M. Azarpeyvand, *An experimental investigation of novel trailing edge geometries on airfoil trailing edge noise reduction*, in *19th AIAA/CEAS Aeroacoustics Conference* (AIAA, Berlin, Germany, 2013).
- [2.48] X. Liu, M. Azarpeyvand, and R. Theunissen, *Aerodynamic and Aeroacoustic Performance of Serrated Airfoils*, in *21st AIAA/CEAS Aeroacoustics Conference*, June (American Institute of Aeronautics and Astronautics, Dallas, TX, 2015) pp. 1–16.
- [2.49] A. Vathylakis, T. P. Chong, and P. F. Joseph, *Poros-Serrated Trailing-Edge Devices for Airfoil Self-Noise Reduction*, *AIAA Journal*, 1 (2015).
- [2.50] N. Thomareis and G. Papadakis, *Numerical Analysis of a Trailing Edge with Triangular Serrations Using Dynamic Mode Decomposition*, in *54th AIAA Aerospace Sciences Meeting*, January (American Institute of Aeronautics and Astronautics, San Diego, California, 2016).
- [2.51] A. Vathylakis, C. C. Paruchuri, T. P. Chong, and P. Joseph, *Sensitivity of aerofoil self-noise reductions to serration flap angles*, *22nd AIAA/CEAS Aeroacoustics Conference*, 1 (2016).
- [2.52] S. Oerlemans, J. G. Schepers, G. Guidati, and S. Wagner, *Experimental demonstration of wind turbine noise reduction through optimized airfoil shape and trailing-edge serrations*, *Nationaal Lucht en Ruimtevaartlaboratorium, NLR TP* (2001).
- [2.53] S. Oerlemans, M. Fisher, T. Maeder, and K. Kögler, *Reduction of wind turbine noise using optimized airfoils and trailing-edge serrations*, *AIAA Journal* 47, 1470 (2009).

- [2.54] L. E. Jones and R. D. Sandberg, *Acoustic and hydrodynamic analysis of the flow around an aerofoil with trailing-edge serrations*, [Journal of Fluid Mechanics](#) **706**, 295 (2012).
- [2.55] A. Finez, E. Jondeau, M. Roger, and M. C. Jacob, *Broadband Noise Reduction of a Linear Cascade With Trailing Edge Serrations*, in [17th AIAA/CEAS Aeroacoustics Conference \(32nd AIAA Aeroacoustics Conference\)](#) (Portland, Oregon, USA, 2011).
- [2.56] D. Moreau, L. Brooks, and C. Doolan, *Flat plate self-noise reduction at low-to-moderate Reynolds number with trailing edge serrations*, in [Proceedings of the Annual Conference on the Australian Acoustical Society](#) (2011).
- [2.57] D. Moreau, *Experimental investigation of flat plate self-noise reduction using trailing edge serrations*, in [Congress of the International Council of the Aeronautical Sciences](#) (Brisbane, 2012) pp. 1–10.
- [2.58] D. Moreau and C. Doolan, *Noise-Reduction Mechanism of a Flat-Plate Serrated Trailing Edge*, [AIAA Journal](#) **51**, 2513 (2013).
- [2.59] W. Qiao, L. Ji, K. Xu, and W. CHENG, *An Investigation on the near-field turbulence and radiated sound for an airfoil with trailing edge serrations*, [19th AIAA/CEAS Aeroacoustics Conference](#), 1 (2013).
- [2.60] F. Avallone, C. Arce León, S. Pröbsting, K. P. Lynch, and D. Ragni, *Tomographic-PIV investigation of the flow over serrated trailing-edges*, in [54th AIAA Aerospace Sciences Meeting](#), January (American Institute of Aeronautics and Astronautics, Reston, Virginia, 2016) pp. 1–14.
- [2.61] H. Clemons and R. W. Wlezien, *Modification of Flow Structures Associated with Broadband Trailing Edge Noise*, in [46th AIAA Fluid Dynamics Conference](#) (American Institute of Aeronautics and Astronautics, Washington, D.C., 2016).
- [2.62] C. Arce León, F. Avallone, S. Pröbsting, and D. Ragni, *PIV Investigation of the Flow Past Solid and Slitted Sawtooth Serrated Trailing Edges*, in [54th AIAA Aerospace Sciences Meeting](#), January (American Institute of Aeronautics and Astronautics, San Diego, California, 2016) pp. 1–15.
- [2.63] C. Arce León, D. Ragni, S. Pröbsting, F. Scarano, and J. Madsen, *Flow topology and acoustic emissions of trailing edge serrations at incidence*, [Experiments in Fluids](#) **57**, 91 (2016).
- [2.64] C. Arce, D. Ragni, S. Pröbsting, and F. Scarano, *Flow Field Around a Serrated Trailing Edge at Incidence*, in [33rd Wind Energy Symposium](#) (American Institute of Aeronautics and Astronautics, Kissimmee, Florida, 2015).
- [2.65] M. Gruber, *Airfoil noise reduction by edge treatments*, [Ph.D. thesis](#), University of Southampton (2012).
- [2.66] D. Moreau and C. Doolan, *Tonal Noise from Trailing Edge Serrations at Low Reynolds Numbers*, [19th AIAA/CEAS Aeroacoustics Conference](#), 1 (2013).

- [2.67] C. Arce León, R. Merino-Martínez, D. Ragni, F. Avallone, and M. Snellen, *Boundary layer characterization and acoustic measurements of flow-aligned trailing edge serrations*, [Experiments in Fluids](#) **57**, 182 (2016).
- [2.68] W. C. van der Velden and S. Oerlemans, *Numerical analysis of noise reduction mechanisms on improved trailing edge serrations using the Lattice Boltzmann method*, [35th Wind Energy Symposium](#), 1 (2017).
- [2.69] S. Oerlemans, *Reduction of wind turbine noise using blade trailing edge devices*, [22nd AIAA/CEAS Aeroacoustics Conference](#), 1 (2016).
- [2.70] A. Fischer, F. Bertagnolio, W. Z. Shen, and J. Madsen, *Noise model for serrated trailing edges compared to wind tunnel measurements*, [Journal of Physics: Conference Series](#) **753**, 022053 (2016).
- [2.71] A. Fischer, F. Bertagnolio, W. Z. Shen, and J. Madsen, *Wind Tunnel Test of Trailing Edge Serrations for the Reduction of Wind Turbine Noise*, in *Inter-noise 2014* (Melbourne, Australia, 2014) pp. 1–10.

3

MEASUREMENT METHODOLOGY

... so let me begin with a parable: A man was examining the construction of a cathedral. He asked a stone mason what he was doing chipping the stones, and the mason replied, "I am making stones." He asked a stone carver what he was doing. "I am carving a gargoyle." And so it went, each person said in detail what they were doing. Finally he came to an old woman who was sweeping the ground. She said. "I am helping build a cathedral."

Richard Hamming, *Art of Doing Science and Engineering: Learning to Learn*

This chapter introduces the measurement methods that have been chosen to describe the acoustics and hydrodynamics of trailing edge serrations in the rest of this work.

THE TECHNIQUES USED in this work are experimental. All measurements were performed in a wind tunnel using an airfoil profile which allowed the retrofitting of a serrated trailing edge in place of its original straight edge. This chapter describes the facility used to conduct the measurements, and the methods used to characterize the flow and the aeroacoustic signal produced by its scattering over the airfoil trailing edge.

3.1. WIND TUNNEL FACILITY

All the measurement campaigns here presented were conducted at the vertical wind tunnel of the Delft University of Technology Aerospace Engineering Faculty, located at the Low Speed Laboratory in Delft, the Netherlands. It is known as, and will be referred to henceforth as the V-Tunnel.

It has been chosen to conduct the research here presented due to being an exceptionally quiet wind tunnel. Despite the fact that the measurement chamber is not anechoic, it remained an excellent environment to measure acoustics, even to the challenging level here required.

While the restrictions to carry out such measurements are more lenient in studies related to tonal acoustics, such as in [3.1, 2], broadband noise like that expected in the configurations here addressed, requires more advance measurement techniques, as outlined in section 3.3. At the time of writing, the V-Tunnel is undergoing an extensive overhaul which includes an anechoic retrofitting of the measurement chamber.

The operation of the tunnel is limited to flow velocities ranging from around 10 to 45 m/s. The flow is passed through a contraction between the settling chamber and the nozzle with a very high contraction ratio, around 60 : 1. A low-turbulence flow is obtained, with turbulence intensities reported in [3.3] to be under 0.02% at 10 m/s and below 1% in [3.1]. In the present study, values closer to the former were found, as will be detailed in the respective measurement campaign chapters, 4, 5 and 6. For the current case, which investigates turbulent boundary layers, the present turbulence intensity levels are sufficiently low.

A schematic of the wind tunnel is provided in figure 3.1. It is an open-jet vertical tunnel with a circular nozzle at the termination of the contraction cone, ⑥. Throughout the presented measurement campaigns, an adapter nozzle was used to convert it to a square exit. Further detail of the adapter nozzle geometry is provided by Debrouwere [3.6]. It has a resulting outlet size of $40 \times 40 \text{ cm}^2$. It is located at ① in the figure, along with the rest of the measurement apparatus and the model.

The flow is driven by a centrifugal fan, indicated in ③, after which it enters a set of sound dampeners at ⑤. The flow is then conducted through a series of pipes and enters the settling chamber at ④, moving onward through the contraction cone in ⑥ to exit towards the measurement chamber at ①. The wind tunnel can be operated as an open or closed circuit tunnel. The alteration is performed by opening an aperture at the roof (not indicated in the figure). As by opening this door lower background noise was obtained, especially at higher velocities, the tunnel was run in its open circuit configuration in most of the campaigns.

The freestream velocity was measured with a pitot tube placed upstream of the airfoil model inside the adapter nozzle. Particle image velocimetry (PIV) measurements later

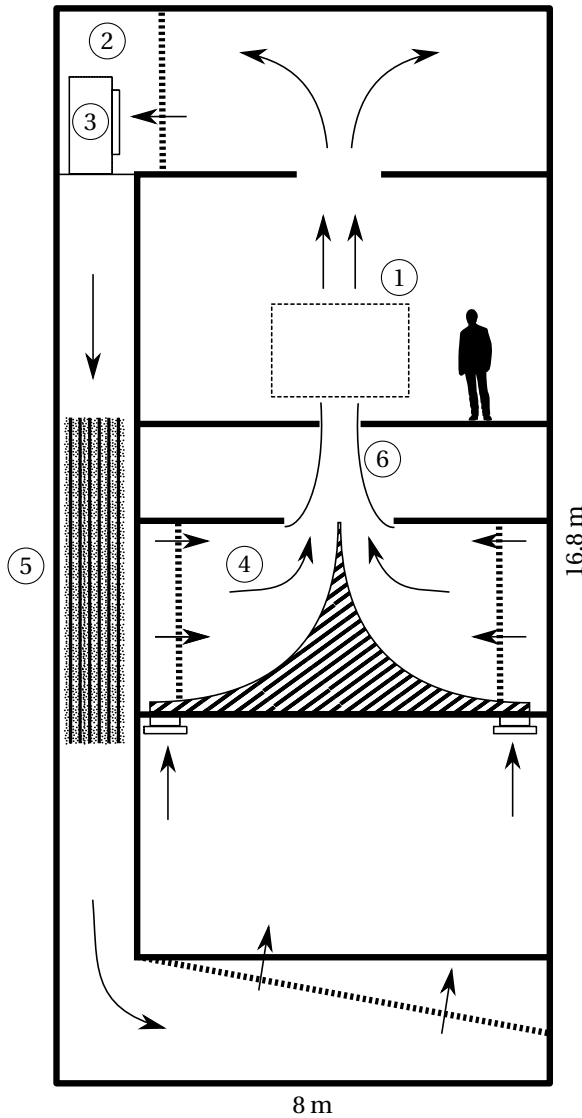


Figure 3.1: Simplified schematic of the V-Tunnel, adapted from [3.4, 5]. ① measuring chamber (approximate location of the measurement equipment and model represented by the dashed area), ② fan room, ③ centrifugal fan, ④ settling chamber, ⑤ sound dampener, ⑥ contraction.

confirmed that no effect of the pitot tube was introduced on the flow that could affect the airfoil. The dynamic pressure was determined using a Mensor digital pressure gauge, series 2100. A LabVIEW code was then used to calculate the velocity, accounting for temperature and ambient pressure. The freestream velocity was controlled by manually adjusting the fan revolutions per minute (RPM).

After the adapter nozzle, a set of modular test sections were mounted, each fulfilling the requirements of the individual measurement campaigns. More detail is therefore provided in the respective chapters.

3.2. PARTICLE IMAGE VELOCIMETRY

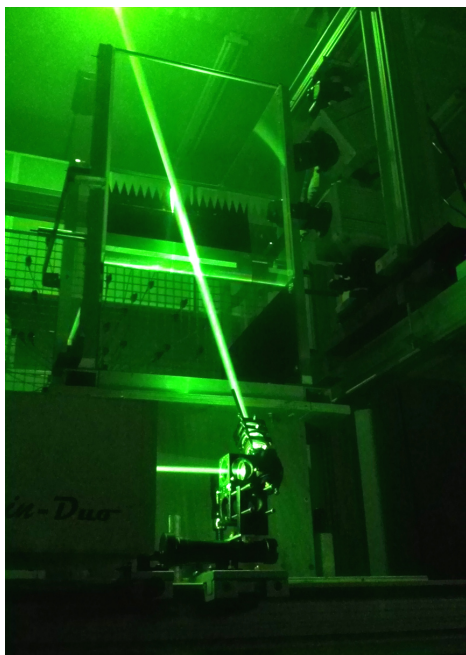


Figure 3.2: Example of an S-PIV setup used during one of the measurement campaigns.

In order to describe the flow around serrations, as presented in chapters 4, 5 and 6, particle image velocimetry (PIV) has been employed. It is an Eulerian method, capable of obtaining the average velocity within a region of the interrogated field of view (FoV). It can be assorted into different configuration types, depending on whether a two or three-dimensional space has been acquired, and whether two or three components of the velocity vectors are resolved. Within the scope of the research presented in this document, two setups have been used: planar two-component particle image velocimetry (2C-2D PIV) and stereoscopic particle image velocimetry (S-PIV). They will be described, along with their respective instrumentation setup, in the following chapters.

In essence, this method uses a set of images obtained from an illuminated stream of tracer particles in a flow to compute the velocity field of the observed re-

gion, discretized to a series of interrogation windows, and based on the observed changes between two images in quick succession. One of the large advantages of PIV is that it is an almost entirely unobtrusive measurement technique, where the particles in the flow are meant to cause a negligible effect on it by virtue of their small relative size and density similarity. This permits the simultaneous measurement of the flow in a large number of points—especially meaningful for data in the streamwise direction. Other methods, such as hot-wire anemometry, require the placement of the necessary instrumentation inside the flow, thereby affecting its behavior downstream of them. As will be seen in later chapters, the unobtrusive nature of PIV allows to obtain valuable parameters, such as the streamwise correlation and coherence, by which the convective velocity of the flow around a large region inside the FoV can be calculated.

3.2.1. WORKING PRINCIPLE OF PIV

PIV is based on a Eulerian approach, where the FoV is divided into a number of interrogation windows. The statistical change, based on the cross-correlation of particle locations

between two images taken in rapid succession, is used as the basis for the calculation of a local mean velocity vector. In describing this procedure, the derivation by Raffel *et al.* [3.7], Westerweel [3.8] is followed.

The displacement field, obtained from the image-pairs, is defined as

$$\mathbf{D}(\mathbf{x}, t) = \int_{t_i}^{t_i + \Delta t} \mathbf{u}(\mathbf{x}, t) dt \quad (3.1)$$

for $\Delta t = t_{i+1} - t_i$ the time difference between the image-pairs.

It gives information about the *average* velocity field during Δt , such that it limits information to events with a characteristic time scale longer than Δt . Furthermore, \mathbf{D} provides information only at locations where seeding is present. A displacement vector \mathbf{D} is obtained for each interrogation window in the FoV.

Care must be taken with regard to the particle density. Too many particles captured in a too small area will inhibit the ability to calculate \mathbf{D} , while using too few can lead to information loss. Ideally, the density should also match the relevant length scales one needs to resolve in \mathbf{D} .

A PIV system will consist of five major components, described below.

Tracer particles

The flow is seeded with a stream of tracer particles upstream of the region of interest. The placement of the seeder must be such that by the time the particles reach the FoV, their density is homogeneous enough.

In the research here presented, the particles were created by evaporating a glycol-based solution called SAFEX® with a fog generator. The latter was placed near ②, in figure 3.1. The resulting nominal particle size is 1 μm .

Cameras

A number of cameras is needed to record the particle location at the intended time instances. The quantity depends on the PIV setup. For a 2C-2D PIV setup, a minimum of one camera is needed. The FoV can be extended by using a series of them—as it has been accomplished in the experiment detailed in chapter 6. For a stereoscopic particle image velocimetry (S-PIV) setup, two cameras are needed in order to resolve the out-of-plane velocity component (see section 3.2.5).

Detailed information about the camera specifications is given in the sections describing the setup in the corresponding chapters (4, 5, 6, 7).

Illumination

The illumination of the scene, principally the particles, needs to be accomplished (for 2C-2D PIV and S-PIV) such that only a thin volume covering the FoV of interest is captured. Obtaining the high luminosity and exposure control necessary is well accomplished using lasers.

As with the cameras, the relevant information of the lasers used is given later in each chapter.

Synchronizer

The individual events pertaining to the acquisition of a PIV image are controlled

by a central unit. In a basic setup, these are comprised by the camera exposure and the laser Q-switch activation (figure 3.7 shows a timeline of these events). The relation between the two is addressed below in the description of the PIV working principle.

Aquisition and post-processing system

A computer is used to setup the image acquisition configuration and control the synchronizer accordingly. In the present case, the same system served to handle some initial post-processing of the images, and later, a more dedicated processing was conducted remotely to obtain the final vector field.

The photograph in figure 3.2 shows the setup used for one of the campaigns of the current research, detailed in later chapters. Several elements of the PIV system can be observed. The laser head can be seen in low light in the lower left corner, with the laser beam clearly visible. It is reflected and focused on the model with the serrations (near the center of the image) by a set of optics in the lower center of the image. As this is an S-PIV setup, the two cameras it uses can be seen near the upper right corner. The laser beam is visible due light scattering from the tracer particles, which have filled the measurement room.

3.2.2. IMAGING AND OPTICAL CONSIDERATIONS

The interrogation window I_i is the interpretation by the camera sensor of the lit scene. In such a way, luminosity peaks obtained from that signal are its interpretation of the particle locations. The diameter of these peaks on the images is highly important for the determination of the velocity field. It is comprised of two factors,

$$d_\tau = \sqrt{d_g^2 + d_{\text{diff}}^2}. \quad (3.2)$$

The term d_g is the size of the particle's geometric image. It is calculated as

$$d_g = M d_p \quad (3.3)$$

where d_p is the particle's geometric size and M is the magnification factor, defined as

$$M = z_I / Z_I \quad (3.4)$$

for z_I the distance between the image plane and the lens, and Z_I the distance between the lens and the object plane.

The second term is the diameter of the Airy disk produced by the particle. It is defined as

$$d_{\text{diff}} = 2.44 (1 + M) f_\# \lambda_p, \quad (3.5)$$

where λ_p is the light wavelength, and $f_\#$ is the lens f-number. The latter is calculated as the ratio between the focal length of the lens and its effective aperture, f/D_a . When read on a lens, the f-number is typically preceded by the symbol $f/$. This will be the preferred nomenclature in later chapters.

For particles of $d_p \lesssim 10 \mu\text{m}$, d_τ is rather independent of d_p , and d_{diff} dominates the relationship. The condition is inverted for $d_p \gtrsim 50 \mu\text{m}$ ([3.9]).

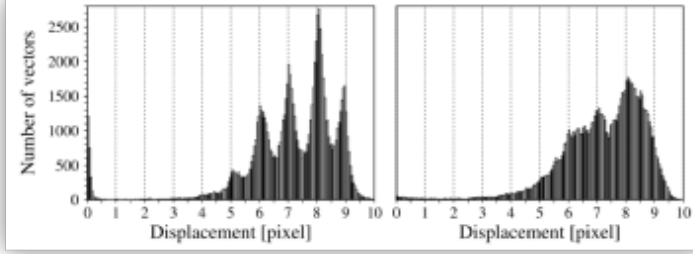


Figure 3.3: Histograms of a Monte Carlo-simulated PIV showing peak-locking (left) and a non-peak-locked case (right). Source: Raffel *et al.* [3.7].

The image obtained by the camera has a discretized coordinate system, where its resolution is determined by the pixel location on its sensor. Because the recorded particle location is performed in this space, a minimum apparent particle size is necessary to avoid unwanted effects in the measurements. According to Raffel *et al.* [3.7], Westerweel *et al.* [3.10], d_τ should occupy more than approximately 2 pixels. Following this suggestion, the sub-pixel coordinate estimation of the cross-correlation peak can be performed through interpolation methods, two of which are the peak centroid and the Gaussian peak fit. The details of these methods will not be addressed here, and the reader is referred instead to Raffel *et al.* [3.7, p160] and Westerweel [3.11, p1389].

Nevertheless, when $d_\tau < 2$ pixels, the determination of the cross-correlation peak becomes biased to discrete coordinates. This effect is called peak-locking, and it appears as a series of non-physical artifacts in the resulting velocity field. A histogram inspection of the particle count, binned by pixel displacement, will show a predisposition to integer numbers, as shown in figure 3.3. A workaround to this, if modifying the imaging parameters or particle size is not an attainable solution, is to defocus the camera lens. This effectively shifts the focal plane out of the location of the measurement volume, resulting in a growth of d_τ by about 20% of the in-focus diameter ([3.9]). A too large d_τ will nevertheless result in a proportional increase in random errors ([3.11]).

The depth of field (the width of the focal plane) is obtained from

$$\delta_Z = \frac{2f d_{\text{diff}} (M + 1)}{D_a M^2}. \quad (3.6)$$

Ideally, it should at least cover the width of the measurement volume, ΔZ_0 , in order to focus on all the particles contained therein. From (3.6), it can be seen that it is inversely proportional to the lens effective aperture. While it is therefore preferred to have a small effective aperture, there are cases in which the laser power is relatively low and it becomes necessary to increase D_a in order to capture more light. The use of high-speed PIV systems, as in some of the measurement campaigns here presented, is an example where available light becomes sparse.

3.2.3. THE SCHEIMPFLUG PRINCIPLE

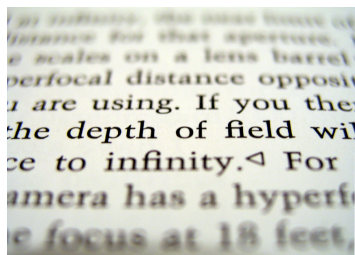


Figure 3.5: A shallow depth of field where the focal plane is misaligned with respect to the subject plane.

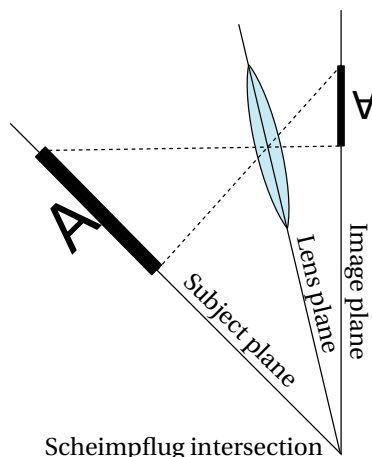


Figure 3.6: Diagram of the Scheimpflug principle.



Figure 3.4: Scheimpflug adapter used in the PIV campaigns, located between the camera body and the lens.

In order to achieve an optimal representation of all the particles inside the measurement volume, the focal plane must be parallel to it. This is readily achieved when the camera is normal to it. But sometimes, cameras will need to be rotated with respect to the measurement plane, either because the space is inaccessible due to the setup, or inevitably when using more than one camera sharing a similar FoV (as in S-PIV). In such cases, at least one focal plane will become rotated. The resulting effect is the loss of focus in parts of the subject plane—a non-PIV related example of this effect is presented in figure 3.5. In order to align it, the Scheimpflug principle is followed, as proposed by Theodore Scheimpflug and described in [3.12].

The most direct approach to visualizing this principle is through the simplified diagram on figure 3.6. It can be seen that the subject plane and the image plane are not parallel to each other. In fact, they coincide in a point in space, often called the Scheimpflug intersection. The lens plane will have a position, when rotated about this point, which will bring the focal plane into alignment with the subject plane.

In practice, this procedure carries difficulties and becomes often riddled with tedious iterations. The adjusting of a Scheimpflug adapter for a PIV measurement is more of a trial-and-error art than something that can be anticipated. Especially when the rotation of the lens needs to be done about two axes, a researcher will find that the re-focusing of cameras and re-alignment of the focal plane is an important bottleneck to be considered when deciding on a campaign test matrix.

Figure 3.4 shows the use of a Scheimpflug adapter in one of the campaign setups presented in later chapters. The device is placed between the camera body (gray, top

right) and the objective lens. The angle it applies between the two is clearly visible.

3.2.4. OPTIMAL PIV SEEDING AND TIMING GUIDELINES

As discussed in section 3.2.1, to calculate the average velocity field between two image-pairs, $I_{1,1}$ and $I_{2,1}$, these need to be taken in succession with a time separation Δt . To achieve this, in the case of a 2C-2D PIV setup, two elements need to be carefully synchronized and controlled; the camera and the laser.

A timeline of the events pertaining to the capture of two separate image-pairs, $(I_{1,1}, I_{2,1})$ and $(I_{1,2}, I_{2,2})$, is shown in figure 3.7. The laser and camera action timelines are presented here.

As the image-pair results in a single vector field, a sequence of $2N$ images produces N vector field time samples. The time separation between samples, F_1 and F_2 in the figure is ΔT , and $1/\Delta T$ is known as the acquisition frequency. This time separation should comply with the research requirements. If time-averaged data is necessary, then ΔT should be long enough as to ensure that each sample is uncorrelated. If instead time-resolved data is required, ΔT should be short, such that the time between image-pairs $I_{2,1}$ and $I_{1,2}$ is also Δt . In such a case, an intermediate time sample can also be extracted from the newly formed image-pair $I_{2,1}$ and $I_{1,2}$.

Earlier recommendations for achieving a successful PIV analysis, as proposed by Keane and Adrian [3.13], suggest guidelines for the time deltas and seeding requirements. These state that a PIV setup should be designed such that

1. within the light sheet conformed by the laser, the particles should transverse at most a distance of one fourth of its thickness in the out-of-plane direction between the capture of image-pairs,
2. around 15 particles should be contained inside each interrogation window,
3. the velocity gradient within the interrogation window should be below 5% of the mean velocity,
4. the particles should be observed to transverse around one fourth of the interrogation window dimension between image-pairs.

Modern analysis techniques have achieved a significant relaxation of these requirements, nevertheless one should remain cautious.

3.2.5. STEREOSCOPIC PARTICLE IMAGE VELOCIMETRY

The 2C-2D PIV description given up until now allows the resolution of the vector field in a two-dimensional (2D) plane, and is able to resolve the two velocity components that conform the plane. Stereoscopic particle image velocimetry (S-PIV) makes use of a second camera and an extension to the method of PIV to resolve the out-of-plane velocity component. The principle is described in detail by Arroyo and Greated [3.14] and Prasad [3.15].

The apparent particle displacement recorded by each camera is

$$\Delta \mathbf{x} = \left(-M \frac{\Delta X + X \Delta Z / Z_I}{1 - \Delta Z / Z_I}, -M \frac{\Delta Y + Y \Delta Z / Z_I}{1 - \Delta Z / Z_I} \right), \quad (3.7)$$

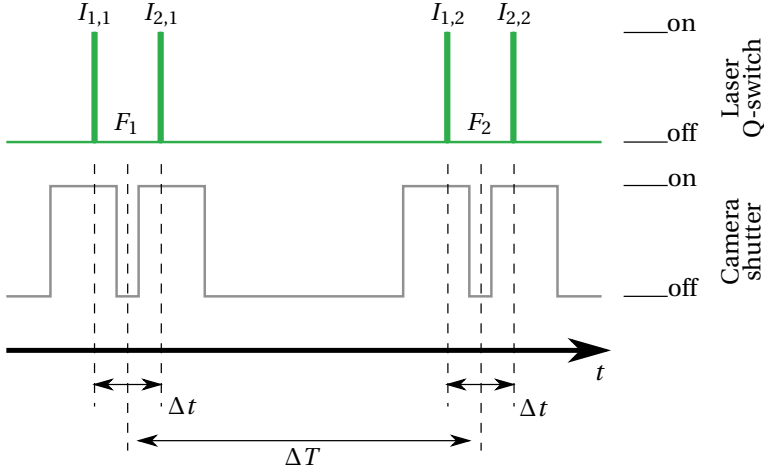


Figure 3.7: Example of a camera and laser triggering sequence for a 2C-2D PIV setup.

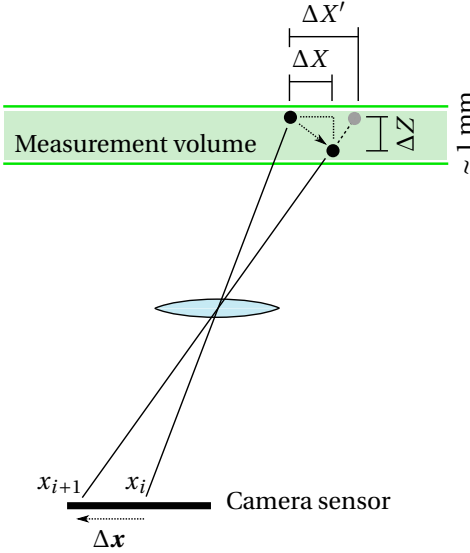


Figure 3.8: Diagram of the out-of-plane particle displacement evaluation for one camera in S-PIV.

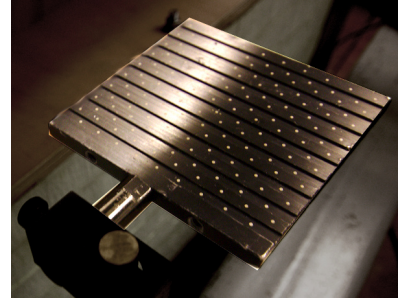


Figure 3.9: Calibration plate used for the S-PIV experiments.

where, if the particles experience out-of-plane motion, $\Delta \mathbf{x}$ maps to an apparent in-plane displacement of $\Delta \mathbf{X}' = -\Delta \mathbf{x} / M$ projected on the measurement plane, as shown in figure 3.8. The displacements measured by each camera, $\Delta \mathbf{x}_1$ and $\Delta \mathbf{x}_2$, are then recombined to recover the estimated real particle displacements, $\Delta \mathbf{X} = (\Delta X, \Delta Y, \Delta Z)$.

In order to perform this procedure, the exact location of the cameras with respect to the measurement plane needs to be established. In addition, because of the lateral shift, the perspective of each camera will be different and needs to be corrected (de-

warped into a single overlapping plane). A calibration step is thus involved, which in the current research has been conducted using a LaVision made Type 10 calibration target plate, pictured in figure 3.9. It consists of a grid of markers placed on a sequential row of steps alternating between two out-of-plane displacement levels. Tolerances between the marker spacings of around ± 0.02 mm, and of ± 0.01 mm between levels offer a convenient way to reduce error in the determination of the particle locations by accurately resolving the camera location with regard to the measurement volume.

3.2.6. ERROR QUANTIFICATION

PIV, as any measurement method, carries a set of error sources. In particular, errors pertaining to the measurement are driven by the time and displacement accuracy, quantified as

$$\varepsilon_u = u_{\text{meas}} \sqrt{\left(\frac{\varepsilon_{\Delta x}}{\Delta x}\right)^2 + \left(\frac{\varepsilon_{\Delta t}}{\Delta t}\right)^2}. \quad (3.8)$$

Thus, the error is proportional to the L^2 -norm of the spatial displacement uncertainty and the displacement, and the pulse separation error with the pulse separation. The former usually dominates the latter, with typical values in the order of 1% and 0.1%, respectively ([3.7]).

Overall, the source of errors can be classified into two categories:

Systematic errors are replicable errors as long as the instrumentation does not suffer any modifications. These happen in PIV when the calibration is off, or when peak-locking is present, for example.

Random errors instead vary between observations, and are associated in PIV with noise in the images, non-optimal seeding density, and other conditions affecting the determination of the particle displacement.

Several means of error quantification and identification are available. While some errors have a very low pixel value (below 0.1 pixels, for example), and are thus difficult to identify from the true signal, there are cases where a significant deviation exists. Such cases may stem from interrogation windows with a low particle density, or the presence of reflections. Either will affect the quality of the correlation peak, which will tend to be dominated by random peaks instead of the true displacement peak. Unlike other errors, these outliers are easy to identify and several detection methods are available ([3.16]).

An method for an *a-posteriori* error quantification has been proposed by Wieneke [3.17] as an extension, but with a different approach, to that of Sciacchitano *et al.* [3.18]. It is specifically meant to quantify random errors, and is incapable of accounting for systematic errors. Nevertheless, it offers a good estimation of the former by taking the image-pair needed to compute the displacement vectors, and dewarping the second image onto the first using the calculated displacement field, obtaining $I_{t+1}^*(\mathbf{\Gamma}) = I_{t+1}(\mathbf{\Gamma}, \mathbf{u})$. This method is implemented in the LaVision DaVis software (used to process the results in this thesis), and is applied in later chapters for the random error determination.

The evaluation of the precision obtained in the time-averaged, where a set of N samples is obtained and averaged as $\bar{p} = N^{-1} \sum_{k=1}^N p_k$, is calculated as

$$P_p < \frac{t\sigma_{\bar{p}}}{\sqrt{N}} \quad (3.9)$$

where

$$\sigma_{\bar{p}} = \left[\sum_{k=1}^N \frac{(p_k - \bar{p})^2}{N-1} \right]^{1/2} \quad (3.10)$$

is the corrected sample standard deviation of the N -result distribution, and t is a coverage factor which equals 2 if $N > 10$, according to Stern *et al.* [3.19]. Again, specific quantities will be addressed later regarding each respective experimental campaign in chapters 4, 5 and 6.

3

3.3. ACOUSTIC BEAMFORMING

In the research on serrated trailing edges that will be presented in later chapters, a large part has been dedicated to describing the flow characteristics near the edges and surfaces. The objective has been to supplement the body of knowledge on serrations with information that has been up until today missing. The findings are complemented with acoustic measurements, both to confirm the noise-reduction effects of serrations, and to isolate modifications that the serrations exact on the acoustic emissions, as in the case of serration-flow misalignment in the flapwise direction (chapters 4 and 6).

The method chosen to acquire and process the acoustic emissions of the airfoil with straight and serrated trailing edges was *acoustic beamforming*, also known as acoustic imaging.

By applying a beamforming algorithm to the acoustic data recorded by an array of microphones, one can obtain the approximate position and strength of sound sources. This ability is of great value to the application at hand, as it allows a preliminary inspection of the results. It allows, for example, an evaluation of the adequateness of the setup, and the opportunity to improve it. The capacity to observe the different sound sources in the acoustic FoV of the array also means that spurious sources (such as sidelobes) and background noise can be more clearly identified and omitted from the acoustic evaluation.

The wind tunnel facility used (section 3.1) is quiet, but not anechoically treated. The benefits of acoustic beamforming therefore enhanced the ability of correctly determining the noise emissions from the different airfoil configurations. This is especially important in the present study, as it requires differences below 1 dB to be adequately resolved.

Throughout the different campaigns, the same acoustic array configuration was implemented. It consisted of 64 electret-condenser omni-directional microphones (PUI AUDIO 665-POM-2735P-R). They have a sensitivity of -35 ± 2 dB (for a reference of 1 V/Pa) between 0.2 and 25 kHz. The arrangement of the microphones approximated a multi-arm logarithmic spiral configuration ([3.20, 21]). This configuration was chosen with the attempt to minimize the presence of sidelobes below -12 dB. The array has an effective diameter of 0.9 m and was optimized for a frequency range between 1 and 5 kHz. A schematic describing the microphone locations over the array plane can be seen in figure 3.10.

For the acoustic measurements, a specific test section was used and placed over the wind tunnel nozzle. It was designed to be open, with two long side-plates used to support the model and allow a quasi-2D flow over most of its span. This configuration permitted a direct line of sight to the trailing edge, while maximizing the separation of po-

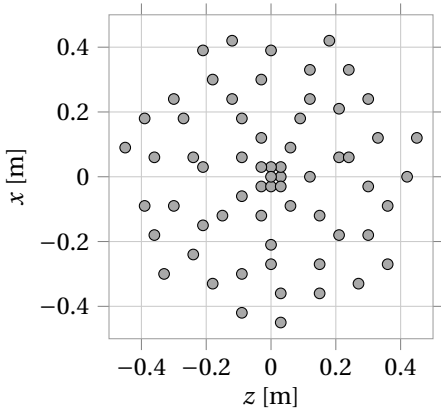


Figure 3.10: Microphone organization in the acoustic array.

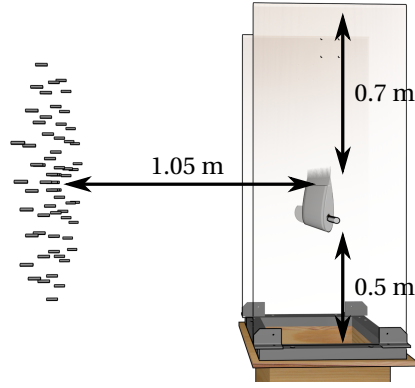


Figure 3.11: Perspective projection diagram of the acoustic setup used, showing the location of the array with respect to the open test section and the model.

tentially unwanted sound sources coming from both the wind tunnel nozzle (located 0.5 m upstream of the airfoil leading edge) and the side-plate edges (0.7 m downstream of the airfoil trailing edge), from the area of interest. A diagram of the test section can be seen in figure 3.11. Here the wind tunnel nozzle is depicted at the bottom, and the side-plates are rendered semi-transparent to show the location of the model. The distance between the array and the model is 1.05 m.

The microphones were calibrated with a pistonphone, and the performance of the array was evaluated with sound from a known source at several discrete frequencies, and with white noise. The sound pressure level (SPL) values at the array center were also measured using a calibrated TENMA 72-947 sound level meter. This procedure results in an effective source location and strength calibration of the array.

Data for all the measurements was acquired at a sampling frequency of 50 kHz over a period of $T_{ac} = 60$ s. The acoustic data was later used to average the cross-spectral matrix over different time blocks of 2048 samples, or a duration of $\Delta t_{ac} = 40.96 \mu s$, evaluated in frequency-space using a fast Fourier transform (FFT) and windowed by a Hanning weighting function with 50 % data overlap, preferred because of its low aliasing and the conservation of the signal energy.

The chosen beamforming method to process the data is called *conventional frequency-domain beamforming* ([3.22]). It has been preferred over other methods due to its simplicity and robustness, and its low computational cost. As discussed by Dougherty [3.23], it carries the additional benefit of being able to resolve continuous sources, as what is expected from trailing edge noise. The implementation considers a medium with uniform flow ([3.24]).

For the flow velocities tested, the shear layer correction, as detailed by Amiet [3.25], is considered to be negligible and has thus been omitted ([3.26]). This argument is further supported by the sufficiently small angle between the array center and the edges of the measurement domain (below 10°).

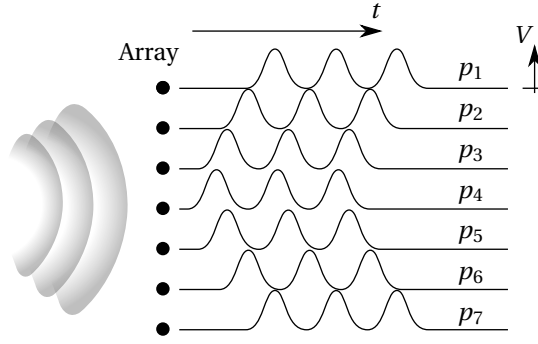


Figure 3.12: Diagram showing the time delay between the signal recorded by an array, outlining the principle behind beamforming.

The acoustic source maps are obtained from the beamforming method through its application over a discrete scan grid. It formed a rectangle covering the airfoil in the spanwise and chordwise directions. The domain details are provided in the respective campaign sections in chapters 4, 5 and 6.

The maximum obtainable resolution of the source maps is a function of frequency, given by Rayleigh's criterion, [3.27]. For the highest frequency considered, 5 kHz, and $c = 340$ m/s, it is 0.1 m.

The results obtained from the beamforming source maps are integrated ([3.28]) over a region centered the airfoil trailing edge and covering ± 0.1 m in the spanwise direction, and ± 0.06 m in the streamwise direction. The selection of this area was motivated by efforts to exclude spurious noise sources. These were observed to be located principally at the wind tunnel nozzle, the side-plates' trailing edge and, to a lesser degree near the airfoil sides, as it contacts the side-plates. The latter source is presumed to come from either small separations between the airfoil and the side-plates, or from the interaction of the side-plate boundary layer and the airfoil surface.

Once obtained, the acoustic sources over the evaluated area were normalized by the integral of a simulated unitary point source located at its center, and considered within the same spatial domain ([3.24]). In order to obtain the final noise spectrum, this process was repeated for each selected frequency.

3.3.1. WORKING PRINCIPLE OF CONVENTIONAL BEAMFORMING

In essence, conventional beamforming relies on the comparison of acoustic signals, as captured by the different microphones in an array (see figure 3.12), to a reference pressure source. By evaluating the phase delays between the signals, the localization of the source is possible. The derivation of the method here presented follows that of Sijtsma [3.22], using his notation.

The description of the pressure source can be taken as a monopole in the frequency domain,

$$p(\mathbf{x}, \omega) = \frac{e^{-i\omega\Delta t_e}}{4\pi\|\mathbf{r}\|} a(\omega), \quad (3.11)$$

where Δt_e is the time delay between the emission and the reception of the signal, $a(\omega) =$

$\tilde{\sigma}(\omega)$ the acoustic source amplitude (for $\sigma(\omega)$ the source signal), and the vector $\mathbf{r} = \mathbf{x} - \boldsymbol{\xi}$ represents the distance between the observer, \mathbf{x} , and the monopole locations, $\boldsymbol{\xi}$. The terms in the fraction are called the steering function and are contracted as $g(\mathbf{x}, \omega)$. This particular expression refers to a case with no freestream, which, if present, expands the steering vector expression to

$$g(\mathbf{x}, \omega) = \frac{e^{-i\omega\Delta t_e}}{4\pi\sqrt{(\mathbf{Ma} \cdot \mathbf{r})^2 + (1 - \text{Ma})^2 \|\mathbf{r}\|^2}}, \quad (3.12)$$

where $\mathbf{Ma} = \mathbf{U}_\infty / c$ is the Mach number vector.

Given a set of signals $\mathbf{p}(\omega) = (p_1(\omega), p_2(\omega), \dots, p_N(\omega))$ in the frequency domain, recorded by the N -microphone array, the approach used to evaluate the amplitude at a particular location $\boldsymbol{\xi}$ is to minimize the cost function

$$J = \|\mathbf{p} - a_{\text{est}}\mathbf{g}\|, \quad (3.13)$$

for $\mathbf{g} = (g_1, g_2, \dots, g_N)$ a set of steering vectors and a_{est} the estimated source signal. The estimation of the source is then obtained as a result of a least squares optimization as

$$A_{\text{est}} = \frac{1}{2} a_{\text{est}} a_{\text{est}}^* = \frac{\mathbf{g}^* \mathbf{C} \mathbf{g}}{\|\mathbf{g}\|^4} \quad (3.14)$$

where $\mathbf{C}(\omega_k) = \frac{1}{2} \mathbf{p}(\omega_k) \mathbf{p}^*(\omega_k)$ is the k -th frequency cross-spectral matrix, given by

$$\mathbf{C} = \frac{1}{2} \begin{pmatrix} p_1 p_1^* & p_1 p_2^* & \cdots & p_1 p_N^* \\ p_2 p_1^* & p_2 p_2^* & \cdots & p_2 p_N^* \\ \vdots & \vdots & \ddots & \vdots \\ p_N p_1^* & p_N p_2^* & \cdots & p_N p_N^* \end{pmatrix}. \quad (3.15)$$

In the time-domain, the signal p can be split into M samples of length Δt_{ac} and windowed in order to perform the FFT. In the present research, a Hanning window was applied ([3.29]).

This approach is valid for signals that are relatively stationary with respect to the array (as in the present case), and has been extended to several derivatives that offer improved results in some specific applications, such as functional beamforming ([3.30]), DAMAS ([3.31]), CLEAN-SC ([3.32]), among others. For the purpose of this research, conventional beamforming has proven to be an adequate approach.

BIBLIOGRAPHY

- [3.1] S. Pröbsting, J. Serpieri, and F. Scarano, *Experimental investigation of aerofoil tonal noise generation*, [Journal of Fluid Mechanics](#) **747**, 656 (2014).
- [3.2] A. T. de Jong and H. Bijl, *Investigation of higher spanwise Helmholtz resonance modes in slender covered cavities*, [The Journal of the Acoustical Society of America](#) **128**, 1668 (2010).
- [3.3] S. Ghaemi, D. Ragni, and F. Scarano, *PIV-based pressure fluctuations in the turbulent boundary layer*, [Experiments in Fluids](#) **53**, 1823 (2012).

- [3.4] E. Dobbinga, *Over de stroming door VILEDON-filterdekens voor toepassing in windtunnels*, Tech. Rep. (Delft University of Technology, Delft, the Netherlands, 1987).
- [3.5] P. Skare, *Flow measurements for an afterbody in a vertical wind tunnel*, Tech. Rep. (Delft University of Technology, Delft, the Netherlands, 1995).
- [3.6] M. Debrouwere, *An Assessment of Acoustically Transparent Wind Tunnel Walls for Improving Aero-acoustic Measurements*, *M.Sc. Thesis*, Delft University of Technology (2013).
- [3.7] M. Raffel, C. E. Willert, and J. Kompenhans, *Particle Image Velocimetry* (Springer Berlin Heidelberg, Berlin, Heidelberg, 1998) p. 448.
- [3.8] J. Westerweel, *Digital particle image velocimetry: Theory and application*, *PhD Thesis*, Delft University of Technology (1993).
- [3.9] R. J. Adrian, *Particle-Imaging Techniques for Experimental Fluid Mechanics*, *Annual Review of Fluid Mechanics* **23**, 261 (1991).
- [3.10] J. Westerweel, D. Dabiri, and M. Gharib, *The effect of a discrete window offset on the accuracy of cross-correlation analysis of digital PIV recordings*, *Experiments in Fluids* **23**, 20 (1997).
- [3.11] J. Westerweel, *Fundamentals of digital particle image velocimetry*, *Measurement Science and Technology* **8**, 1379 (1997).
- [3.12] T. Scheimpflug, *Method of distorting plane images by means of lenses or mirrors*, (1904).
- [3.13] R. D. Keane and R. J. Adrian, *Optimization of particle image velocimeters. I. Double pulsed systems*, *Measurement Science and Technology* **1**, 1202 (1990).
- [3.14] M. P. Arroyo and C. A. Greated, *Stereoscopic particle image velocimetry*, *Measurement Science and Technology* **2**, 1181 (1991).
- [3.15] A. K. Prasad, *Stereoscopic particle image velocimetry*, *Experiments in Fluids* **29**, 103 (2000).
- [3.16] A. Sciacchitano, *Uncertainty quantification in particle image velocimetry and advances in time-resolved image and data analysis*, *PhD thesis*, Delft University of Technology (2014).
- [3.17] B. Wieneke, *PIV uncertainty quantification from correlation statistics*, *Measurement Science and Technology* **26** (2015), 10.1088/0957-0233/26/7/074002.
- [3.18] A. Sciacchitano, B. Wieneke, and F. Scarano, *PIV uncertainty quantification by image matching*, *Measurement Science and Technology* **24**, 045302 (2013).

- [3.19] F. Stern, M. Muste, M. Beninati, and W. Eichinger, *Summary of experimental uncertainty assessment methodology with example*, Tech. Rep. (Iowa Institute of Hydraulic Research, College of Engineering, The University of Iowa, Iowa City, USA, 1999).
- [3.20] T. Mueller, *Aeroacoustic Measurements* (Springer Science & Business Media, 2002) p. 313.
- [3.21] R. Dougherty and R. Stoker, *Sidelobe suppression for phased array aeroacoustic measurements*, in *4th AIAA/CEAS Aeroacoustics Conference* (American Institute of Aeronautics and Astronautics, Reston, Virginia, 1998).
- [3.22] P. Sijtsma, *Experimental techniques for identification and characterisation of noise sources*, Tech. Rep. NLR-TP-2004-165 (National Aerospace Laboratory (NLR), Anthony Fokkerweg 2, 1059 CM Amsterdam, P.O. Box 90502, 1006 BM Amsterdam, The Netherlands, 2004).
- [3.23] R. P. Dougherty, *Functional Beamforming for Aeroacoustic Source Distributions*, in *20th AIAA/CEAS Aeroacoustics Conference* (American Institute of Aeronautics and Astronautics, Reston, Virginia, 2014).
- [3.24] P. Sijtsma, *SAE Technical Paper*, Tech. Rep. October (National Aerospace Laboratory (NLR), Anthony Fokkerweg 2, 1059 CM Amsterdam, P.O. Box 90502, 1006 BM Amsterdam, The Netherlands, 2010).
- [3.25] R. Amiet, *Correction of open jet wind tunnel measurements for shear layer refraction*, in *2nd Aeroacoustics Conference* (American Institute of Aeronautics and Astronautics, Hampton, Virginia, 1975).
- [3.26] P. Salas and S. Moreau, *Noise Prediction of a Simplified High-Lift Device*, in *22nd AIAA/CEAS Aeroacoustics Conference* (American Institute of Aeronautics and Astronautics, Reston, Virginia, 2016).
- [3.27] Rayleigh, XXXI. *Investigations in optics, with special reference to the spectroscope*, *Philosophical Magazine Series 5* **8**, 261 (1879).
- [3.28] C. C. Pagani, D. S. Souza, and M. A. F. Medeiros, *Slat Noise: Aeroacoustic Beamforming in Closed-Section Wind Tunnel with Numerical Comparison*, *AIAA Journal* **54**, 2100 (2016).
- [3.29] F. Harris, *On the use of windows for harmonic analysis with the discrete Fourier transform*, *Proceedings of the IEEE* **66**, 51 (1978).
- [3.30] R. P. Dougherty, *Functional Beamforming*, in *5th Berlin Beamforming Conference, February 19-20 2014, Berlin, Germany*. (GFaI, e.V., Berlin, 2014).
- [3.31] T. F. Brooks and W. M. Humphreys, *A deconvolution approach for the mapping of acoustic sources (DAMAS) determined from phased microphone arrays*, *Journal of Sound and Vibration* **294**, 856 (2006).
- [3.32] P. Sijtsma, *CLEAN based on spatial source coherence*, *International Journal of Aeroacoustics* **6**, 357 (2007).

4

MEAN-FLOW AND ACOUSTICS OF SERRATIONS, AND THEIR DEPARTURE FROM THE ANALYTICAL APPROACH

Don't fight forces; use them

R. Buckminster Fuller, *Shelter*

Use the force, Harry

Gandalf

The mean flow and boundary layer statistics over trailing edge serrations are investigated. Several degrees of flow-misalignment are prescribed through airfoil incidence and serration flap angle. The obtained results are discussed within the scope of the achieved noise reduction, and its departure from both the analytic noise reduction prediction and its hydrodynamic assumptions.

The contents of this chapter have been adapted from Arce León *et al.* [4.1].

BROADBAND AIRFOIL NOISE EMISSIONS that originate due to the interaction of the airfoil turbulent boundary layer with the sharp trailing edge ([4.2]) have been shown to be effectively reduced using trailing edge serrations. Evidence of this has been observed in acoustic measurements performed in both wind tunnel experiments ([4.3–5]), and on full scale wind turbines ([4.6, 7]). For the latter, airfoil self-noise reduction is relevant in relation to the observance of noise limits established by local regulations. Furthermore, experimental studies related to the flow around serrations and surface pressure characterization have also been previously performed ([4.8–10]).

Flow near serrated trailing edge has so far been investigated experimentally by Gruber *et al.* [4.11, 12], Finez *et al.* [4.9], and Moreau and Doolan [4.4]. Out of these studies, the first three have used a highly cambered NACA 6512-10 airfoil on which the serrations have been installed following the trailing edge. This will result in an inevitable misalignment with respect to the otherwise undisturbed flow (the mean direction that the flow would follow if the serrations were absent). It is therefore expected that the serrations will modify the flow to a certain degree, which is a measure which was not addressed exhaustively. In the study of Moreau and Doolan [4.4], the serrations were installed on the trailing edge of a flat-plate profile. While this will reduce the interference of the serrations on the flow, an absence in symmetry is still present due to the thickness of the plate with respect to the serrations, and the latter not being installed in the center of the former.

The lack of research directed towards the effect that serration-flow misalignment has on the mean flow, and on its turbulence statistics, therefore highlights a need to fill the void in knowledge of this parameter. As serrations become increasingly prevalent in wind turbine applications ([4.13–15]), it becomes desirable to establish the operational envelope of this device with regard to their flap angle and the airfoil angle of attack.

Furthermore, as the analytical models of Howe [4.16] and Lyu *et al.* [4.17] fail to satisfactorily predict the noise reduction observed otherwise in wind tunnel measurements (see the discussion in section 2.3), additional insight on the effect of serration-flow misalignment can shed light on the departure of flow properties in experiments from those assumed in the formulation of the analytical models.

The research presented in this chapter combines stereoscopic particle image velocimetry (S-PIV) and acoustic phased array measurements of sawtooth trailing edge serrations on a NACA 0018 airfoil. The experiments are conducted comparing the serrated trailing edge with the unmodified straight-edge airfoil.

In addition to testing the serrations aligned to the mean stream direction of the non-incident airfoil, several degrees of serration-flow misalignment are also investigated. The pressure unbalance between the serration upper and lower surfaces is varied by placing the airfoil at several degrees of incidence, and accentuated when the inclination of the serrations is also varied.

The time-averaged flow topology is first characterized to determine the streamline distortion with respect to the flow-aligned serrations. The analysis of the turbulent velocity fluctuations yields the properties of the boundary layer along the serrations.

The noise emitted by the serrated trailing edge is monitored with a microphone array, yielding the power spectral density of the acoustic pressure fluctuations in the relevant

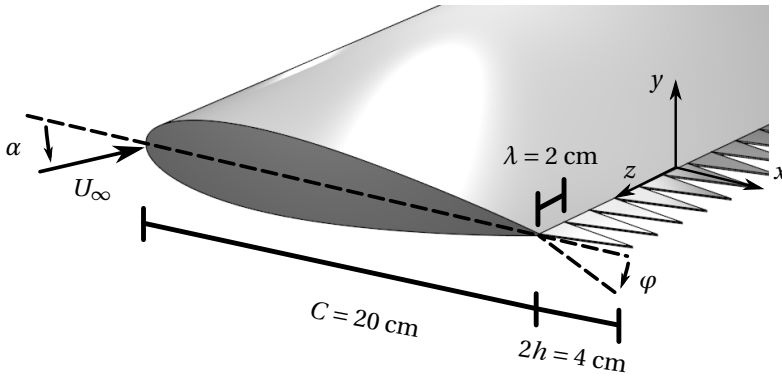


Figure 4.1: Schematic showing the dimensions of the airfoil and serrations, and the angle convention used for α and φ .

frequency range.

4.1. EXPERIMENTAL SETUP

Experiments were conducted in the V-Tunnel, as detailed in section 3.1. The NACA 0018 airfoil profile has been computer numerical control (CNC)-machined into an aluminum model with removable trailing edge inserts, a chord $C = 20$ cm and a span of 40 cm. The length of the serrations is $2h = 4.0$ cm with $2h/\lambda = 2$, such that $\lambda = 2.0$ cm is the serration wavelength (see figure 4.1). The serration panel thickness is 1.0 mm, and is the same as the thickness of the unmodified straight trailing edge of the airfoil, which is the baseline configuration used for comparison. The serration panel was installed at the trailing edge of the airfoil using a modular section, allowing to switch between the unmodified geometry and the installation of one of several serration designs. A detail of this can be seen in 4.2.

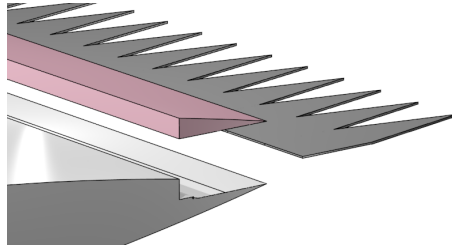


Figure 4.2: Removable trailing edge section allowing to vary the setup between the straight and the serrated trailing edge models.

The relevant parameters inducing an unbalance in the pressure between the serration upper and lower surfaces are the airfoil angle of attack, α , and the serration flap angle, φ . Figure 4.1 shows the convention used, where a positive value of φ indicates an inclination of the flap angle toward the airfoil pressure side.

The boundary layer was forced to turbulent transition with randomly distributed roughness elements. The trip tape was constructed by an appropriate density of dispersed carborundum elements of 0.6 mm nominal size, placed on a thin double-sided tape of 1 cm width. The guidelines of Braslow *et al.* [4.18] were followed for this purpose. The tape was streamwise-centered at $0.2C$, and spans the entirety of the airfoil. A stethoscope probe was used in order to verify that the boundary layer was successfully tripped,

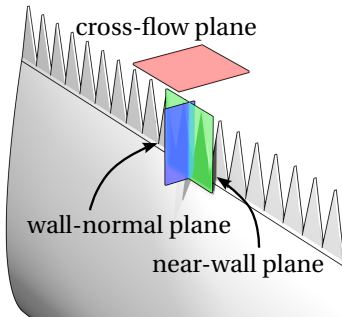


Figure 4.3: Locations of the particle image velocimetry (PIV) measurement planes used in this campaign.

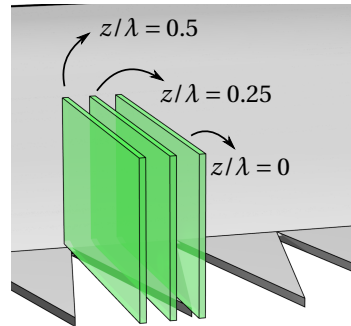


Figure 4.4: Spanwise locations of the wall-normal plane measurements.

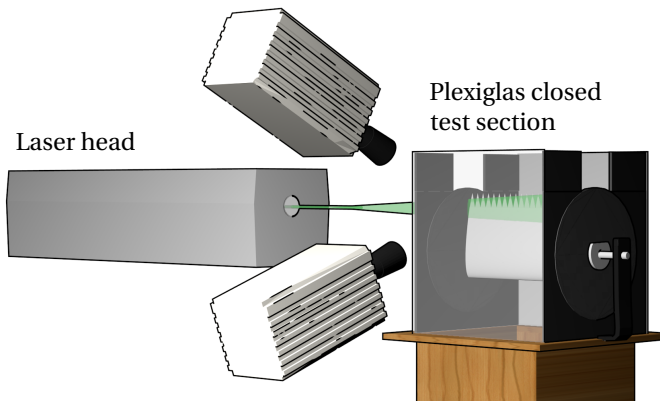


Figure 4.5: Setup used in the near-wall plane measurement; laser and camera positions shown with respect to the closed test section and the model.

and that it remained turbulent downstream until the trailing edge.

4.1.1. STEREOSCOPIC PIV

The airfoil was placed at the exit of the wind tunnel and held by means of side plates. Three experimental configurations were needed to measure the flow at three different plane locations. These are shown in figure 4.3 and will be referred to as: the near-wall plane, the cross-flow plane, and wall-normal plane. The wall-normal plane setup consisted of three separate spanwise locations, as indicated in figure 4.4. A sketch of the setup used to capture the near-wall plane measurements can be observed in figure 4.5.

The coordinate system is defined with x , y and z along the freestream, vertical and spanwise directions respectively, as indicated in figure 4.1. The origin is located at the trailing edge of the airfoil, and at the serration tooth centerline. The velocity vector is

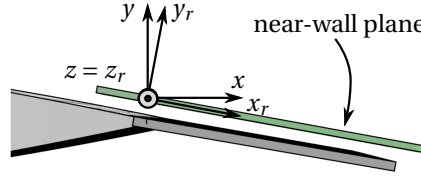


Figure 4.6: Schematic showing the rotated coordinate system used for the near-wall plane measurements.

represented by the components u , v and w , in the x , y , and z coordinate directions respectively.

For the near-wall plane measurements, located at $y = 2$ mm, the laser sheet is maintained parallel to the surface of the serrations, as indicated in figure 4.6. As the serration-parallel plane rotates about the z axis for different configurations of α and φ , the results will be later presented based on a surface-parallel coordinate system, indicated with (x_r, y_r, z_r) .

This measurement location will enable a quantification of the streamline distortion, and to study the near-wall flow topology. The cross-flow plane, at $x = 60$ mm ($1.5 \times 2h$) inspects the streamwise vortices emanating from the serrated trailing edge. And the three wall-normal planes, at $z = 0, \lambda/4$ and $\lambda/2$, determine the properties of the turbulent boundary layer upstream and spanwise across the trailing edge.

The S-PIV experiments were conducted at a freestream velocity of $U_\infty = 20$ m/s, corresponding to a chord-based Reynolds number of 2.6×10^5 . The illumination is obtained with a Quantronix Darwin Duo, Nd:YLF laser (2×25 mJ at 1 kHz) and laser optics is used to form a sheet of approximately 1.5 mm thickness.

Time-averaged results were obtained from image pairs acquired with a time separation of $50 \mu\text{s}$ at a rate of 250 Hz for a total of 1500 instantaneous measurements (6 seconds). Image interrogation is performed with LaVision DaVis 8 software using a multi-pass stereo cross-correlation with a final window size of 16×16 px ($0.8 \times 0.8 \text{ mm}^2$). An overlap factor of 75% between adjacent windows is applied, leading to a vector spacing of 0.2 mm.

The imaging system is composed of two Photron Fastcam SA1 CMOS cameras (1024×1024 px, with a pixel pitch of $20 \mu\text{m}/\text{px}$, and 5.4 frames per second) equipped with Nikon NIKKOR macro objective lenses and Scheimpflug adapters to correct for the misalignment between the object and sensor plane. With about 50 cm distance from the object and an angle of 40° between the two cameras, the field of view covers an area of approximately $5 \times 5 \text{ cm}^2$, resulting in a digital imaging resolution of 20 px/mm.

The typical measurement uncertainty is estimated by a linear propagation approach ([4.19]) and verified *a-posteriori* using the statistical analysis method introduced by [4.20]. The random and bias components are considered.

Bias errors due to peak-locking ([4.21]) are associated to the large imaging aperture ($f/5.6$) yielding a diffraction spot of only half pixel diameter. This effect is mitigated by slightly defocusing the images ([4.22]), bringing the particle image diameter to approximately 1.5 px. The verification is performed inspecting the histogram of particles image displacement, which in this case gives no evidence of peak-locking.

The error due to finite spatial resolution depends on the characteristic length to be accurately measured in the PIV velocity fields. With a multi-pass cross-correlation algorithm with window deformation the amplitude of the fluctuation is measured with less than 5% modulation when the window size is smaller than 0.6 times the length of the scale to be measured ([4.23]). Therefore, with 0.8 mm window size, flow structures down to 1.2 mm (0.13% of the boundary layer) can be measured within 95% precision.

Other systematic sources of uncertainty, including calibration errors and lens distortion, are alleviated by iterative steps of a self-calibration procedure with a polynomial mapping of the images. This is performed via the DaVis software. A disparity vector smaller than 1 px is reached for the stereo calibration ([4.22]).

The random components of the uncertainty have been evaluated with a technique following the work of Wieneke [4.20], where the degree of particle images matching is quantified with the analysis of the correlation peak width. Random errors vary along the measurement domain with less than 1% and approximately 3% in the freestream and in the inner boundary layer regions respectively. The uncertainty of the mean of the velocity, and the root mean square (rms) of its fluctuations, also depends upon the size of the measured ensemble to form the statistics. In the present case, the uncertainty on the mean velocity is 0.01% and 2% on its rms.

4

4.1.2. ACOUSTIC MEASUREMENTS

A beamforming technique is applied by means of a phased microphone array as discussed in section 3.3. The airfoil is installed in the wind tunnel open test section. A view of the experimental arrangement can be seen in figure 3.11, and sample acoustic source maps are shown later in figure 5.26.

The beamforming technique follows Sijtsma [4.24]. The resulting source power distribution is integrated over a region around the trailing edge to obtain the source power. This integration region was centered on the trailing edge and is 20 cm long in the spanwise direction, while it scales with the frequency dependent beamwidth in the chordwise direction.

4.1.3. ANGLE OF ATTACK CORRECTION

For the acoustic measurements, an open test section is necessary in order to allow an unobstructed direct line of sight for the acoustic emissions. This setup was also used for the wall-normal plane PIV measurements due to practical reasons—these two campaigns were conducted jointly and at a later date than the near-surface and cross-flow PIV campaigns, which used the closed test section.

In order to compare the results acquired from both test sections, a correction in the angle of attack is necessary. It follows the empiric relation from Brooks *et al.* [4.25], where the effective angle of attack, α^* , is related with the geometric one, α_g , as

$$\alpha^* = \alpha_g \frac{1 + 2\sigma}{(1 + 2\sigma)^2 + \sqrt{12}\sigma}. \quad (4.1)$$

Here $\sigma = \pi^2 C^2 / 48 H^2$ for H the wind tunnel nozzle height.

Applying the corrections on the geometric values used in the experiments gives $\alpha_g = 12.0^\circ \rightarrow \alpha^* = 6.6^\circ$, and $\alpha_g = 6.0^\circ \rightarrow \alpha^* = 3.3^\circ$. While the approximation given by Brooks

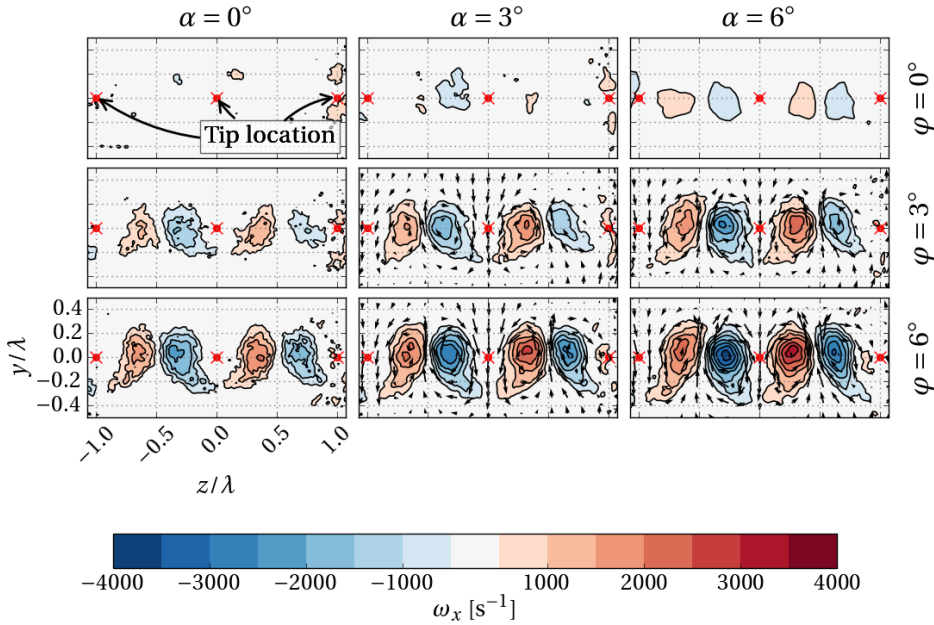


Figure 4.7: Cross-flow measurements showing streamwise vorticity for different permutations of α and φ and $U_\infty = 20 \text{ m/s}$. Mean flow direction in v and w is indicated with arrows in the four bottom right frames.

et al. [4.25] is based on a slightly thinner airfoil, the error involved is expected to be small and non-consequential for the fair comparison of the results later on. For the closed test section, the necessary correction is considered to be small, such that $\alpha^* \approx \alpha_g$.

In the remainder of the discussion, α will refer to α_g .

4.2. RESULTS AND DISCUSSION

4.2.1. MEAN FLOW TOPOLOGY

Results of the cross-flow plane measurements are presented in figure 4.7, where the vorticity component, ω_x , is shown for different configurations of flap angle and airfoil incidence. The position of the serration tip is projected on the measurement plane.

The presence of streamwise, counter-rotating vortex pairs, emanating from the serrations is evident from these results. It is also shown that the circulation pertaining to these vortices is also more strongly correlated with the serrations flap angle, rather than with the incidence of the whole airfoil. An increase in φ by 3° for $\alpha = 0^\circ$, increases the vorticity maximum by over 1000 s^{-1} . Incrementing α by 3° , keeping φ constant at 0° , increases the vorticity by just half the amount.

The vortex pairs produce a vigorous upwash motion in between the serrations and a downwash directly behind the serration tips, resulting from the pressure difference established between the two sides of the serrations once they are placed at an angle with

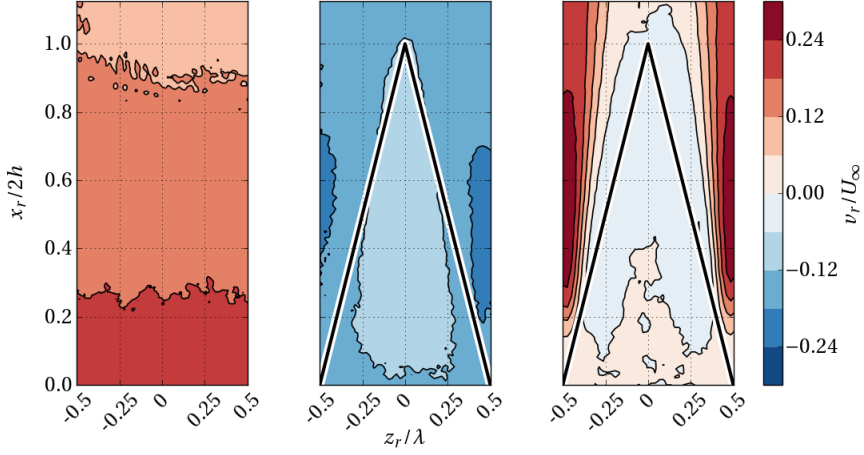


Figure 4.8: Color contours of time-averaged wall-normal velocity distribution for $\alpha = 6^\circ$ and $\phi = 6^\circ$. Straight trailing edge (left), serrated pressure side (middle), and serrated suction side (right).

respect to the airfoil chord. Similar flow behavior, with a transverse motion between the teeth towards the suction side, has been reported by Arina *et al.* [4.26].

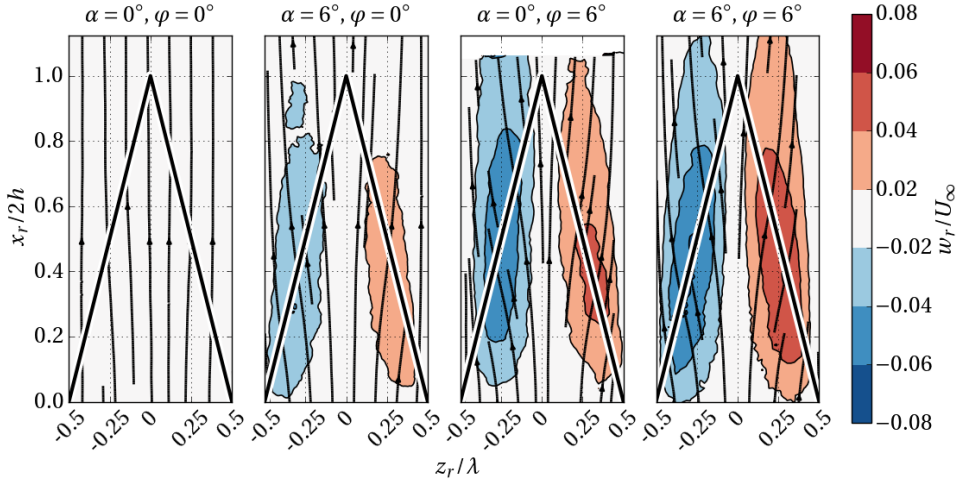
The streamwise vortices give an indication of secondary motions in the wake, in turn associated with the streamline distortion close to the surface of the trailing edge. These observations suggest consequently that the angle by which turbulent fluctuations are advected across the edge will depart from that of the serrations (defined below as θ_0).

The result for the normalized wall-normal flow component, v_r/U_∞ , for the case where $\alpha = 6^\circ$ and $\phi = 6^\circ$, can be seen in figure 4.8. The measurement of the straight trailing edge (located at $x = 0$) is also shown for comparison. The outline of the serrated trailing edge is indicated.

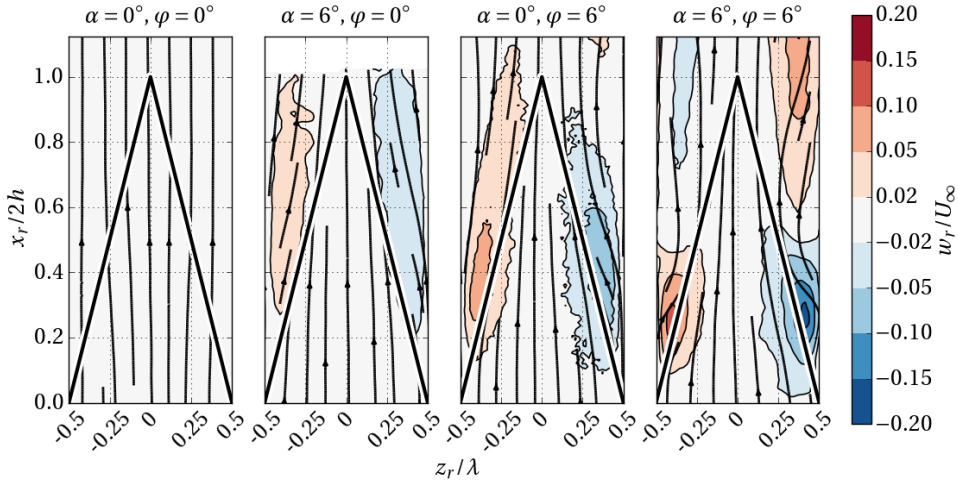
On the pressure side (figure 4.8, middle), the flow is directed into the measurement plane over the entirety of the domain. This indicates that flow passes through it with regions of higher velocity in between adjacent serrations at around half a serration length. The velocity on the suction side (figure 4.8, right) exhibits two streamwise elongated regions with positive wall-normal velocity. These regions are consistent with the formation of streamwise vortices observed in the wake.

The near surface flow distortion is better observed in the measurement of w_r/U_∞ (figure 4.9). The streamlines are affected to a different extent when airfoil angle of attack or serration flap angle are increased. The w_r component of the streamlines has been scaled by a factor of four to clarify the direction to which the streamlines point. The effect of flap angle is again more pronounced than that of the airfoil angle of attack.

The near surface flow at the pressure side (figure 4.9a), exhibits deflection away from the serration centerline, $z_r/\lambda = 0$. Instead, the streamlines on the suction side (figure 4.9b) appear to converge towards the tip of the serration tooth. This result indicates that the serration trailing edge angle apparent to the mean flow streamlines is being modified by the secondary flow pattern established as a result of a pressure difference. The most direct implication is a discrepancy to the prediction obtained from the model of Howe



(a) pressure side



(b) suction side

Figure 4.9: Near surface spanwise velocity (color contours) and a qualitative streamline pattern for varying α and φ .

[4.16].

In the analytical formulation of [4.16], it is argued that flow properties around a distance δ from the serration edge are relevant to its noise reduction mechanism. When no airfoil incidence or serration flap angle is applied, the mean flow behavior near the serrations has been shown in figure 4.9 to adhere closely to the above assumption. The most notable modification due to serrations remains the change in the effective angle at

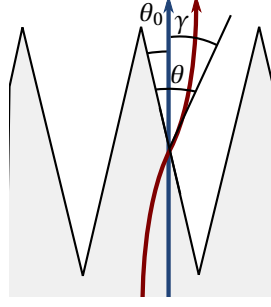


Figure 4.10: Definition of the flow curvature angle, θ , with respect to the serration trailing edge. Schematic situation on the airfoil pressure side.

4

which the turbulent flow structures convect over the trailing edge. The latter are responsible for noise generation, with the most effective condition for noise production given by streamlines being orthogonal to the edge.

On the suction side the streamlines tend to align even more with the edge, while on the pressure side the behavior is opposite and the streamlines tend to become normal to the edge. Even under these conditions, the serrations have been shown in multiple studies ([4.27, 28]) to be effective at reducing noise. This further suggests that, although the main working principle hypothesized by Howe [4.16] (to change the effective angle at which the noise generating flow structures convect over the trailing edge) remains true, the validity of frozen flow properties does not hold true.

The angle formed by the streamlines and the trailing edge plays a primary role in Howe's model (as discussed in section 2.2.1),

$$S_{pp}(\omega) \approx \frac{S_{pp,0}(\omega)}{1 + (4h/\lambda)^2}. \quad (4.2)$$

Therefore, understanding how airfoil incidence or serration flap angle modify the flow behavior and the noise reduction is the relevant question addressed. The actual streamline topology obtained from the PIV analysis explains part of this phenomenon.

The angle at which the local streamline passes over the serration trailing edge will be referred to as θ and is illustrated in figure 4.10. Here θ_0 represents the angle between the undisturbed streamline and the serration trailing edge, and γ is the local flow deflection over the trailing edge, such that $\theta = \theta_0 + \gamma$. The angle γ is positive by a deflection that increases the total angle θ .

The serration geometric parameters in equation (4.2) can be rewritten such that it becomes a function of the trailing edge angle. Since

$$\cot \theta_0 = 4h/\lambda, \quad (4.3)$$

then, from equation (4.2),

$$S_{pp} \approx \frac{S_{pp,0}}{1 + \cot^2 \theta_0} = S_{pp,0} \sin^2 \theta_0. \quad (4.4)$$

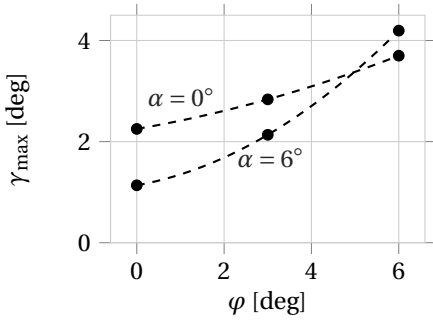


Figure 4.11: Values of γ_{\max} for different cases measured over the serration trailing edge.

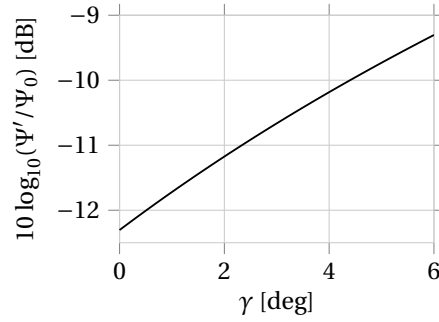


Figure 4.12: Expected influence of γ on equation (4.4).

Correcting for the streamline deflection yields $S_{pp} \approx S_{pp,0} \sin^2(\theta_0 + \gamma)$.

The maximum observed value of γ is charted in figure 4.11 for the pressure side. For $\phi = 6^\circ$, γ approaches 4° . Figure 4.12 shows the difference in decibels between the predicted noise of the serrated trailing edge and that of a straight trailing edge. When the value of γ increases, the serration is expected to become less effective in reducing the trailing edge noise. For the cases studied here, the serrations are expected to lose approximately 2 dB in noise reduction performance at the highest observed deflection only on the pressure side. A simplifying hypothesis is made here that the boundary layer properties (thickness and shape factor) along with the flow turbulence are unaltered by the presence of the serrations at varying values of ϕ .

From the suction side, instead, following Howe's approach, one expects an additional reduction of noise emission since the streamline deflection tends to reduce θ even further, with the flow becoming more parallel to the trailing edge.

There is evidence (see [4.29, 30]) that the contribution of noise between the pressure and suction sides is not equal and the peak noise level is likely to be strongly driven by the boundary layer thickness. This suggests that, for a straight trailing edge airfoil the suction side is the dominant source of noise. Based on the observations made regarding the beneficial direction in which the flow is deflected on the suction side, this leads to the conclusion that the observed streamline distortion would further increase the overall noise reduction. This is not observed, and serration misalignment has instead been linked to an increase in noise in the higher frequencies while maintaining similar levels of reduction in the lower and mid-frequency ranges ([4.12]).

Admittedly, it must be retained in mind that the value of γ is not constant over the serration trailing edge, which should be considered for a quantitative measurement of it. Considering a correction based on the maximum deflection of streamlines, the result does not come to agree with the large differences (approximately 6 dB) reported between the analytical solution of the serrated trailing edge noise, and the results current and previous of wind tunnel experiments ([4.3, 4]).

Therefore, further elements are taken in consideration below, first of all the boundary layer thickness, shape factor and the turbulent fluctuations.

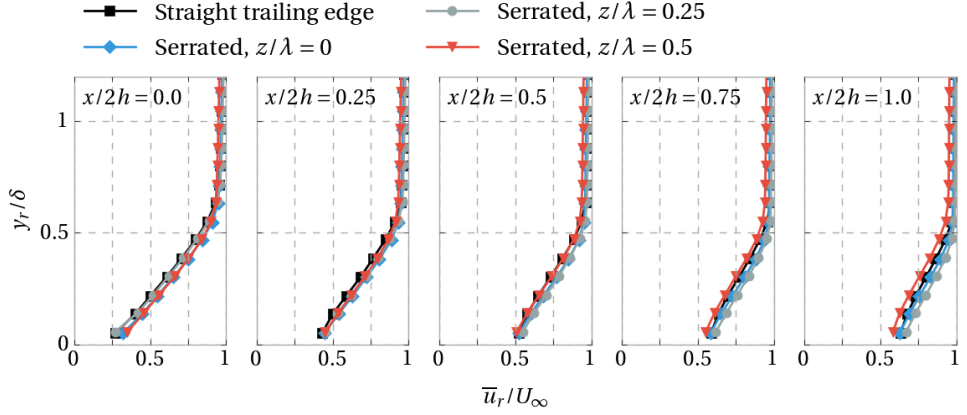


Figure 4.13: Profiles over the wall-normal coordinate direction of \bar{u}_r for the straight trailing edge and three spanwise locations of the serrated edge for $\alpha = 0^\circ$ and $\varphi = 0^\circ$.

4.2.2. BOUNDARY LAYER ACROSS SERRATIONS

The properties of the flow across the serrations are inspected in three planes spanning one serration element. These measurements were taken with the open test section setup, and as discussed above, the correction of the presented geometric angle of attack must be considered. The wall-normal distance, y_r , is normalized with the boundary layer thickness, δ , measured at the straight trailing edge at $\alpha = 0^\circ$.

When the airfoil is at zero incidence and with zero flap angle, no significant difference is found between the straight edge and the cases with serrations (figure 4.13). At higher angles of attack, namely $\alpha = 12^\circ$ ($\alpha^* \approx 6.6^\circ$), as shown in figure 4.14, clear differences emerge between the straight and serrated trailing edges. The former shows flow with a lower velocity region in the wake location, which is replicated by the $z/\lambda = 0.5$ location of the serrated edge after $x/2h = 0.5$, and slightly by the $z/\lambda = 0.25$ spanwise location further downstream.

The time-averaged streamwise velocity field is presented in figure 4.15. The value of α is 12° , and the serrations are placed at $\varphi = 6^\circ$. The three spanwise measurement locations are presented for the serrated case. Contours of \bar{u}/U_∞ are shown along with the projection of streamlines onto the examined planes.

Regions of lower velocity are observed close to the serration for the locations $z/\lambda = 0$ and 0.5 . These two planes also exhibit a similar shape in the flow topology close to the serration surface and in its near wake. The flow in the measurement plane between adjacent serrations, $z/\lambda = 0.5$, shows notable differences. Here the flow passing through adjacent serration teeth is evident, as seen previously in figure 4.8, as well as its influence on the shape, location, and thickness of the wake region.

4.2.3. TURBULENCE STATISTICS

The mean flow topology near the serrations has been presented in the previous section and related to the discussion on serrated trailing edge noise in [4.16, 31]. A look into the

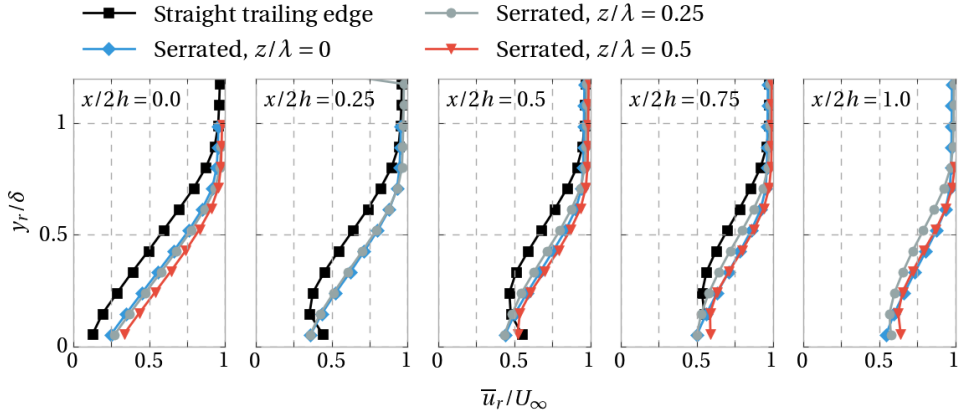


Figure 4.14: Profiles over the wall-normal coordinate direction of \bar{u}_r for straight and serrated trailing edge for $\alpha = 12^\circ$ and $\varphi = 0^\circ$. Suction side.

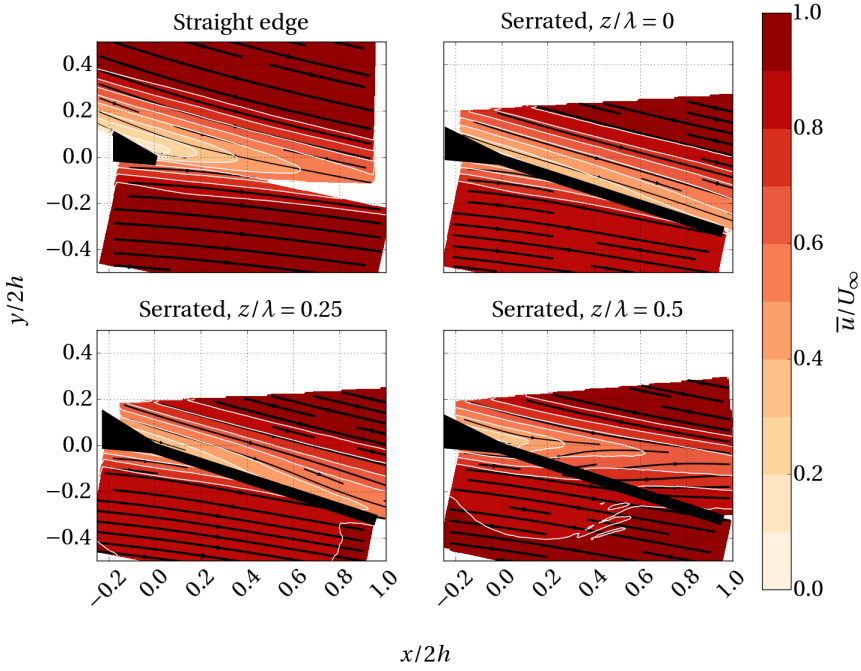


Figure 4.15: Time-averaged streamlines and contours of streamwise velocity component, \bar{u} . Straight trailing edge on the upper left, and varying spanwise positions of the serrated edge ($\varphi = 0^\circ$).

flow behavior from a turbulence statistics point of view will be given here.

The wall-normal profiles of $u_{r,rms}$ are given in figure 4.16. No large differences are evident between the straight or serrated edges, nor for spanwise variations in the latter.

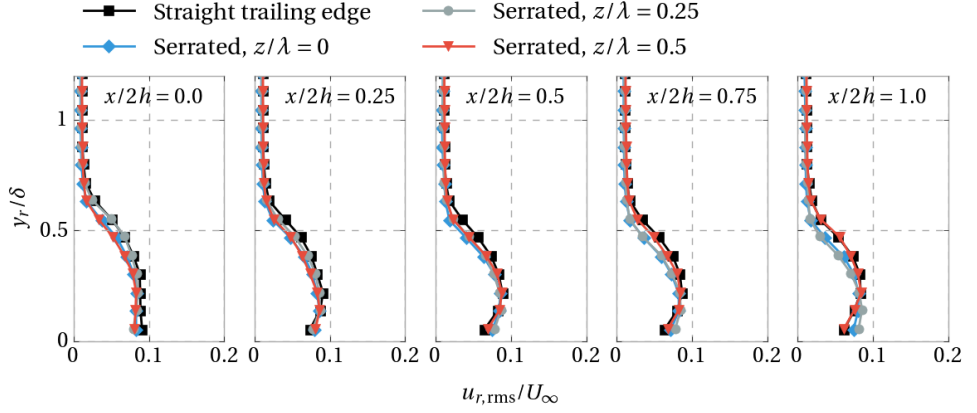


Figure 4.16: Wall-normal profiles of $u_{r,rms}/U_{\infty}$ for the straight and serrated trailing edges at different spanwise locations, $\alpha = 0^\circ$, $\varphi = 0^\circ$.

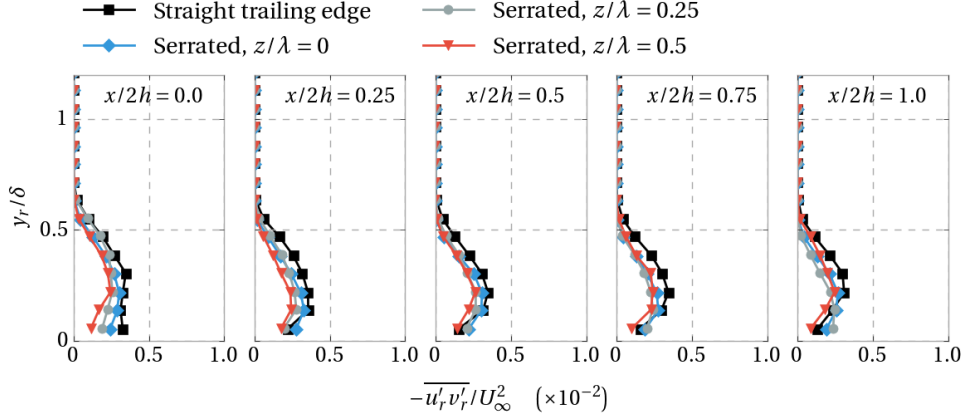
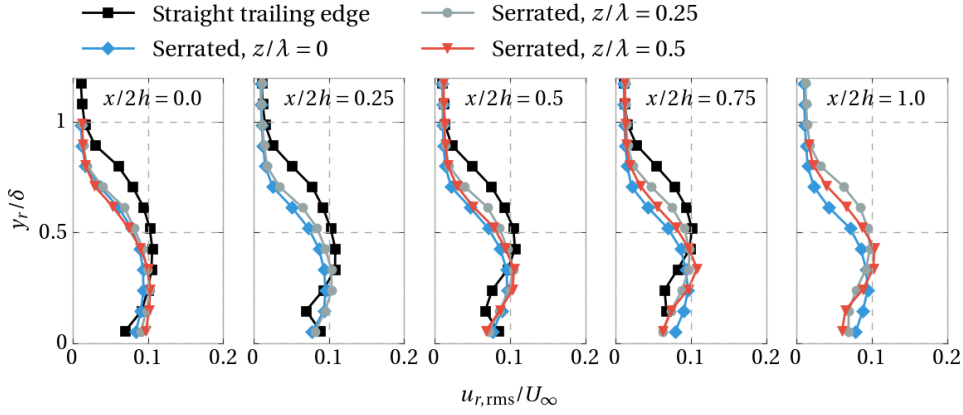


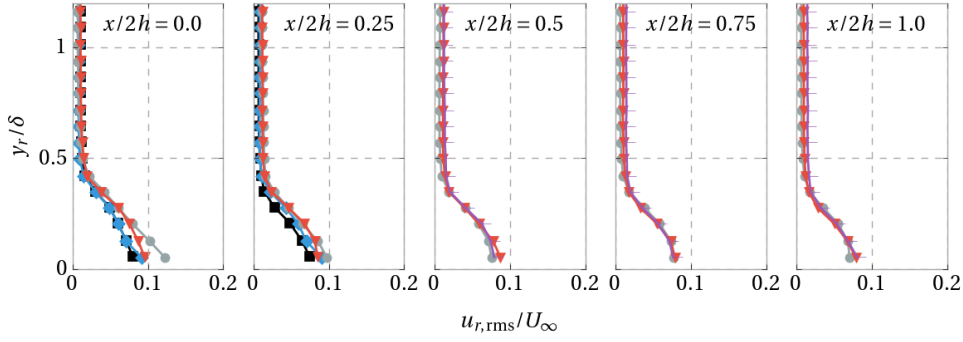
Figure 4.17: Wall-normal values of $-\overline{u'v'}/U_{\infty}^2$ for the straight and serrated trailing edges at different spanwise locations, $\alpha = 0^\circ$, $\varphi = 0^\circ$.

The straight and the serrated edge at $z/\lambda = 0.5$ do exhibit similar behavior, with higher fluctuations seen further from $y/\delta = 0$, and lower values closer to it. These similarities become more evident further downstream. The measured Reynolds stress, $-\overline{u'v'}$, shown in figure 4.17 show a similar trend, with overall little significant differences between the cases, but with the straight edge departing slightly from the serrated edge, which shows almost no spanwise variation.

Measurements of $u_{r,rms}$ for an airfoil incidence of 12° (figure 4.18) show notable differences between straight and serrated trailing edges, and also along different spanwise locations of the latter. When $z/\lambda = 0$, a behavior similar to what was seen for $\alpha = 0^\circ$ for all streamwise locations is experienced. Measurements at $z/\lambda = 0.25$ and 0.5 show a dis-



(a) suction side



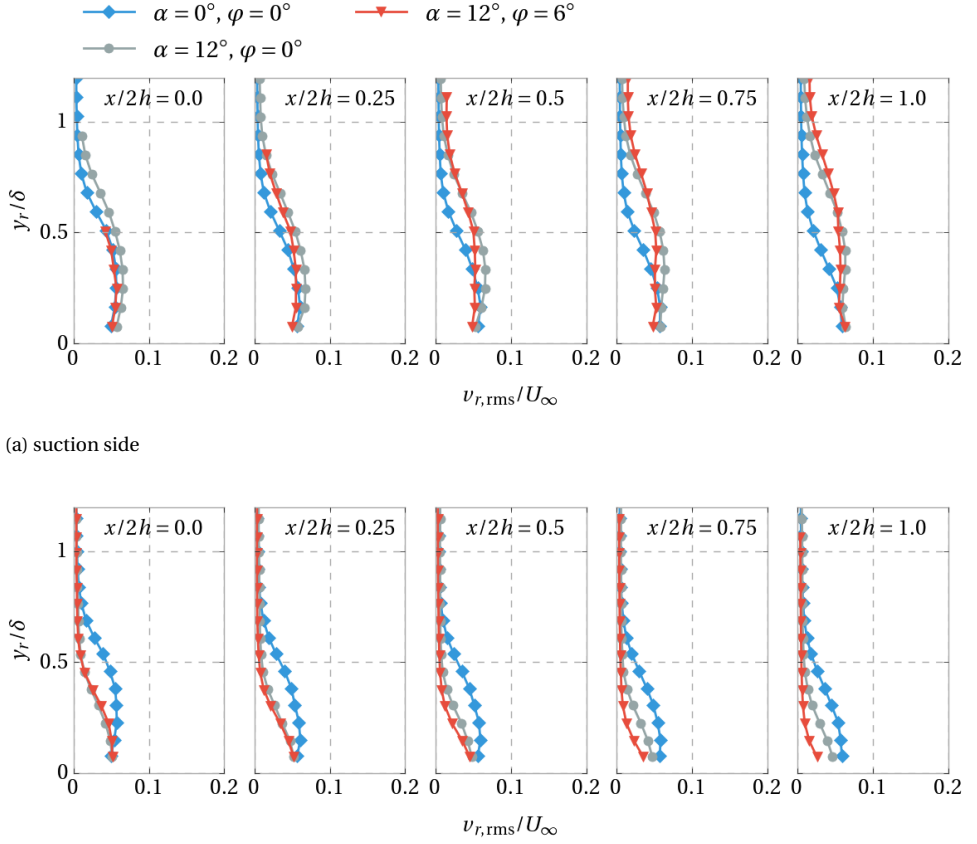
(b) pressure side

Figure 4.18: Values of $u_{r,rms}/U_{\infty}$ for the straight and serrated trailing edges for different spanwise locations, $\alpha = 12^\circ$, $\varphi = 0^\circ$.

tinctly stronger decrease in fluctuation intensity around the wake centerline, an effect which is more apparent for locations further downstream.

Values for the off-center spanwise locations are higher than for the $\alpha = 0^\circ$ case for regions downstream of $x/2h = 0.25$, but remain similar for the $z/\lambda = 0$ location.

Measurements of $v_{r,rms}$ for different values of α and φ are taken for $z/\lambda = 0.25$ and shown in figure 4.19. At the suction side (figure 4.19a), cases at incidence or with flap deflection show higher values of $v_{r,rms}$ than for $\alpha = 0^\circ$, $\varphi = 0^\circ$. At $x/2h = 0.5$, the serration trailing edge intersects the measurement plane, which reveals a change in the flow structure from this point onwards. Beyond $x/2h = 0.5$, the cases with incidence and flap angle exhibit more pronounced differences. In particular the $v_{r,rms}$ values are significantly higher above $y_r/\delta \approx 0.25$, reaching maximum values of around $v_{r,rms} \approx 0.07$ close to $y_r/\delta \approx 0.4$, and exhibiting a similar profile between them. The $\alpha = 0^\circ$, $\varphi = 0^\circ$ case has instead its maximum closer to $y_r/\delta = 0$, and remains largely unchanged for the different



(a) suction side

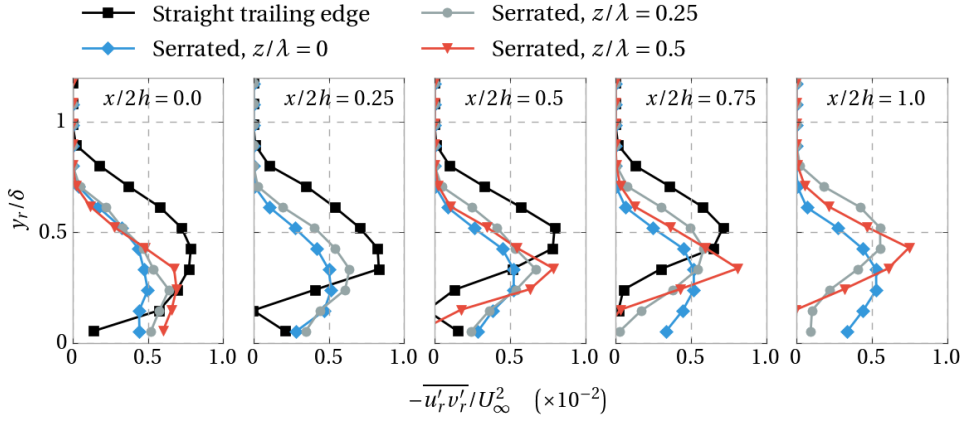
(b) pressure side

Figure 4.19: Values of the serrated trailing edge $v_{r,rms}$ for different values of α and φ .

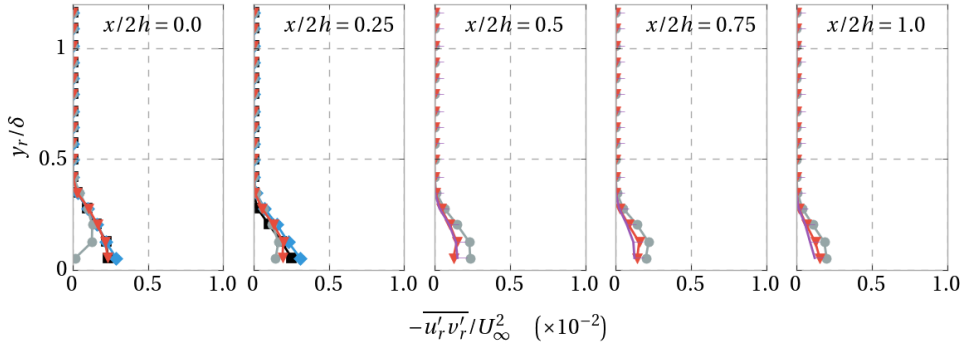
streamwise locations.

At the pressure side (figure 4.19b), measurement of $v_{r,rms}$ for cases at incidence or with flap angle, show higher values than for $\alpha = 0^\circ, \varphi = 0^\circ$. For the former, values of $v_{r,rms}$ also cover a smaller y_r extent before dropping to zero. Translating the above observations in terms of noise generation by the trailing edge requires the evaluation of the intensity and spectrum of the hydrodynamic surface pressure fluctuations that are scattered by it (see [4.32–34]). In the present experiments, the measured amplitude of wall-normal rms fluctuations and their closeness to the sharp edge is used to infer a trend in the expected sound level that is produced. The higher values seen here for the cases with airfoil incidence or serration flap angle are found to be well in line with the increase of noise emissions that are measured by the serrations at these configurations with respect to the case at $\alpha = 0^\circ, \varphi = 0^\circ$. This result is recalled in the discussion of section 4.2.4.

The Reynolds stress $-\overline{u'_r v'_r}$ of figure 4.20 shows overall higher values than for the zero



(a) suction side



(b) pressure side

Figure 4.20: Values of $-\overline{u'_r v'_r}$ for the straight and serrated trailing edges at different spanwise locations, $\alpha = 12^\circ$, and $\varphi = 0^\circ$.

incidence measurements. The $z/\lambda = 0.5$ case approaches the profile of the straight edge for downstream locations, and $z/\lambda = 0.25$ follows with less intensity but a similar shape. The serration centerline plane measurements remain distinctly different and follow the shape seen earlier for $\alpha = 0^\circ$, but with higher values.

The spatial distribution of $-\overline{u'_r v'_r}$ is illustrated in figure 4.21 at the spanwise location of $z/\lambda = 0.25$, where the measurement plane intersects the serration edge at $x/2h = 0.5$. Values of $-\overline{u'_r v'_r}$ over the suction side (figure 4.21a) attain a minimum for $\alpha = 0^\circ$, $\varphi = 0^\circ$. Instead, the cases with airfoil incidence and serration flap angle exhibit Reynolds shear stresses approximately three times higher, with the case $\alpha = 12^\circ$, $\varphi = 6^\circ$ showing the highest. The location of the maxima varies as well between cases, where for $\alpha = 0^\circ$, $\varphi = 0^\circ$ it is approximately at $y_r / \delta = 0.25$, and for the other cases it increases from around $y_r / \delta = 0.25$ at $x/2h = 0$ to $y_r / \delta = 0.7$ and 0.5 for $x/2h = 1$. At the pressure side

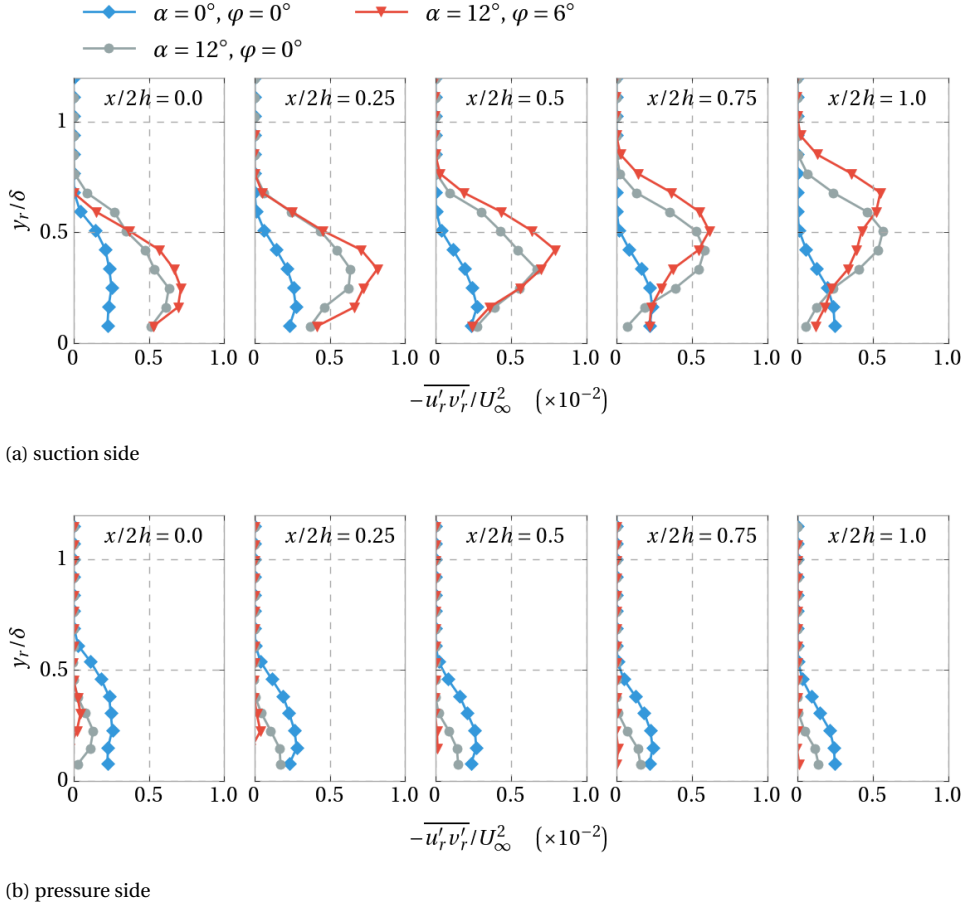
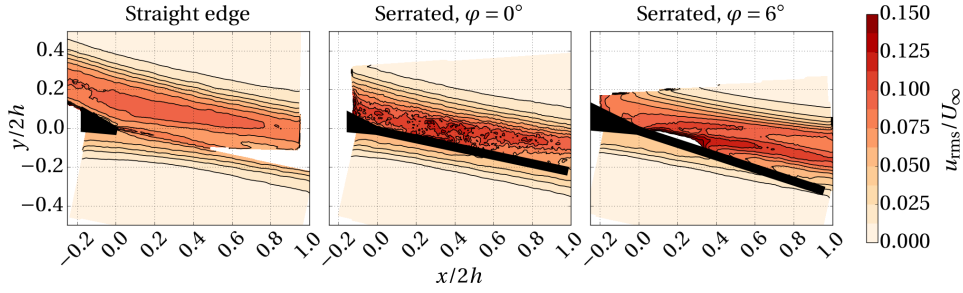


Figure 4.21: Values of $-\overline{u'_r v'_r}$ at different values of α and φ for the serrated trailing edge.

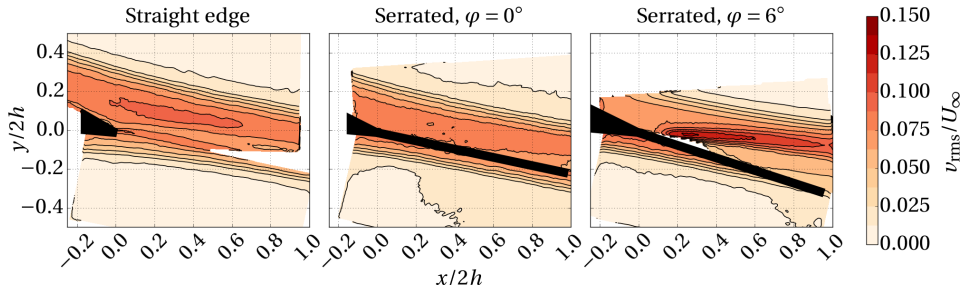
(figure 4.21b), the situation is similar to that observed for the wall-normal fluctuations, with the case $\alpha = 0^\circ, \varphi = 0^\circ$ yielding the highest values of $-\overline{u'_r v'_r}$, and also spanning a larger extent of y_r before dropping to zero.

The amplitude of Reynolds shear stresses is associated to the importance of turbulent activity at relatively small scales in the boundary layer (see [4.35, 36]). In the present context, higher values of $-\overline{u'_r v'_r}$ are therefore associated to a potential increase of sound production in the high-frequency range of the spectrum. The acoustic measurements of serrated edges presented in section 4.2.4 reveal indeed that cases with larger values of α and φ are louder than the case at $\alpha = 0^\circ, \varphi = 0^\circ$, and even than the straight trailing edge. This is particularly evident at higher frequencies, which could be explained by the behavior of $-\overline{u'_r v'_r}$ and v_{rms} . This topic will be addressed in detail in chapter 6.

To visualize the location of regions with high u_{rms} and v_{rms} for different cases with $\alpha = 12^\circ$, figure 4.22 shows the contour plots for the $z/\lambda = 0.5$ plane. The straight trailing



(a) streamwise component rms



(b) wall-normal component rms

Figure 4.22: Velocity fluctuations of components u_{rms} and v_{rms} , for the straight edge (left), and the serrated edge (with $\varphi = 0^\circ$ and 6°) at the spanwise location $z/\lambda = 0.5$ and $\alpha = 12^\circ$.

edge shows higher u_{rms} and v_{rms} on the suction side which continues downstream while another region of higher rms is seen to originate from the trailing edge. This behavior was previously observed in the PIV measurements conducted by Finez *et al.* [4.9]. The serrated trailing edge with $\varphi = 6^\circ$ shows this effect as well, and this region of increased fluctuations is seen to originate from the root of the serrations. The presence of this pattern is not evident in the serrated case with $\varphi = 0^\circ$.

Trailing edge noise is mainly produced by the more effective scattering mechanism related to dipole noise sources than by quadrupole sources in the turbulent wake ([4.37]). Nevertheless, studies such as [4.12], in which the increased turbulence of this region has been measured with hot-wire, have implicated the latter with the observed increase of noise. The present work will refer to this topic in 6, wherein a different origin, dipole related, is discussed.

Further evidence of the effect of serration misalignment and the increase in turbulence intensity can be seen in the cross-flow plane measurements at the wake of the serrations, figures 4.23 and 4.24. Higher levels of turbulence intensity can be seen for the u component than for the v component, supporting the observations made in the wall-normal plane. The u component exhibits periodic and alternating up/down facing horseshoe-shaped regions of increased fluctuations behind the tips (\cup shaped), and the

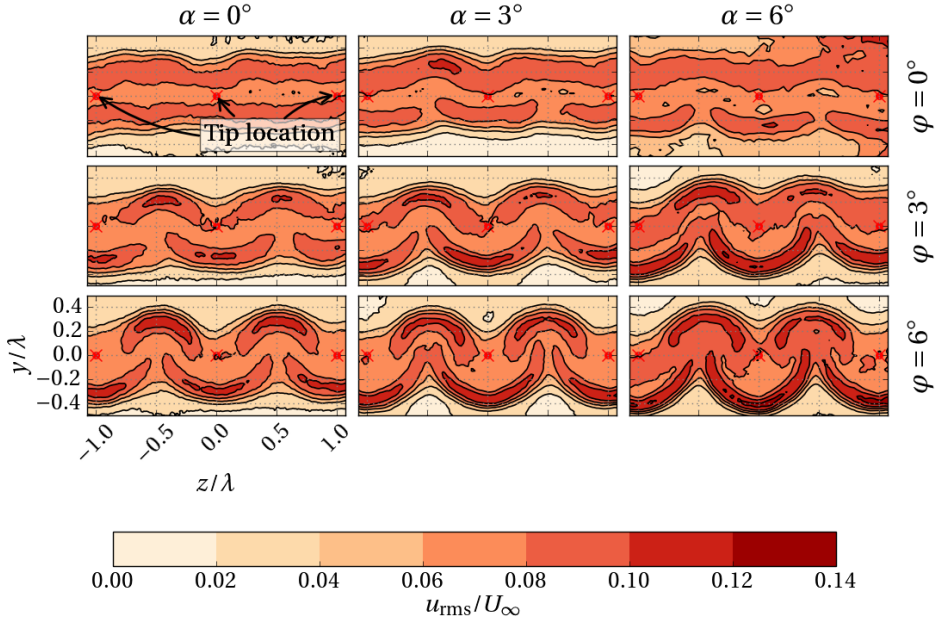


Figure 4.23: Velocity fluctuations of the u component in the cross-flow plane.

roots of the serrations (\cap shaped), with slightly higher u_{rms} from the tip regions. The fluctuation intensity of the v component (figure 4.24) shows similar patterns but is instead dominant in the region behind the serration root. This region is also where opposing streamwise vortices are in close proximity (see figure 4.7).

The $\alpha = 0^\circ$ and $\varphi = 0^\circ$ case shows no significant modulation along the spanwise direction. Increasing φ causes a rapid increment of velocity fluctuations, which indicates that serrations at incidence cause an increase of turbulent fluctuations, in addition to altering the time-averaged streamlines patterns.

It is notable therefore that, despite of the above conditions, the overall effect of serrations remains that of reducing the noise emissions (near 7 dB for some frequencies), as will be seen in the next section.

Observations in the cross-flow plane downstream of the serrations enable to visualize the spanwise distribution of the Reynolds shear stresses (figure 4.25). The airfoil incidence and the flap deflection introduce a significant increase of $-\overline{u'_r v'_r}$ with respect to the $\alpha = 0^\circ$, $\varphi = 0^\circ$ case. Positive maxima are formed trailing the serration teeth center, whereas negative-valued maxima emanate from the serration valleys. The value of these maxima is two to three times higher than that measured at zero incidence, with a slightly higher peak value originating from the pressure side shear layer. The overall pattern of Reynolds shear stresses is highly correlated to that of the vorticity distribution in figure 4.7, indicating an increase of turbulent kinetic energy production at airfoil incidence and

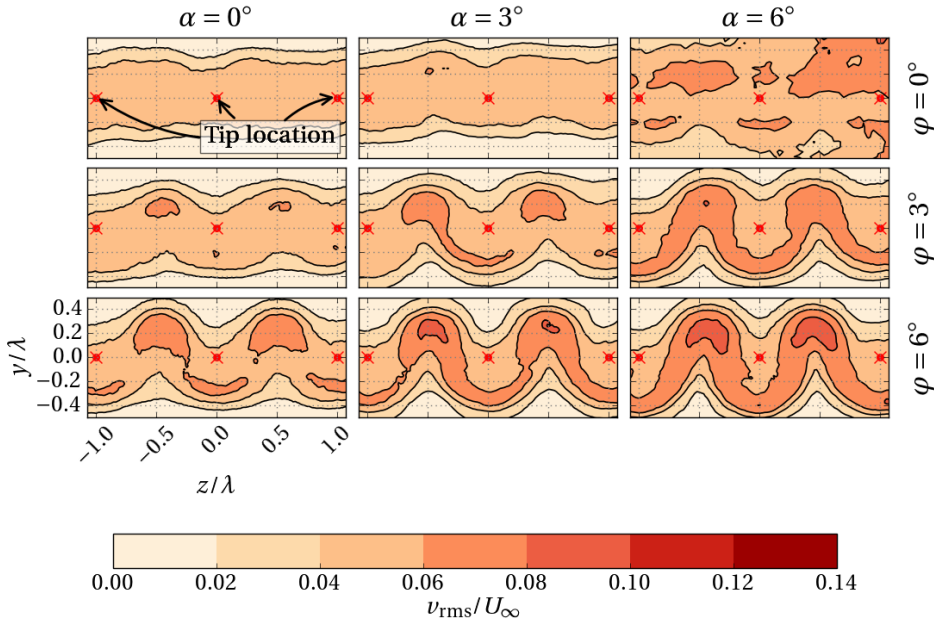


Figure 4.24: Velocity fluctuations of the ν component in the cross-flow plane.

flap deflection.

The overall conclusion is that the Reynolds shear stress increase is more pronounced than that of u' (approximately 30% to 50%) and ν' (50% to 70%), which preludes to an increase of sound production at the high frequency side of the spectrum.

4.2.4. NOISE EMISSIONS

The third-octave band sound pressure level (SPL) of the straight trailing edge airfoil and the serrated airfoil can be seen in figure 4.26 for $\alpha = 0^\circ$ and $U_\infty = 35$ m/s. The serrations are shown to be effective at reducing the noise emitted by the airfoil trailing edge. Also, there is a marked difference between the noise measured using the serrations with $\varphi = 0^\circ$ and those with $\varphi = 6^\circ$.

Results of the measured noise for the serrations, relative to the straight edge, are shown in figure 4.27. The three airfoil incidence cases and the two serration flap angles are presented for a freestream velocity of 35 m/s. The vertical axis represents the measured sound pressure level difference in decibels with respect to the straight trailing edge, where a positive number indicates a reduction in noise and a negative value represents an increase in noise.

At $\varphi = 0^\circ$ (figure 4.27, top), the serrations offer a reduction of up to 7 dB for the frequency band between 1 kHz and 3 kHz. Beyond this upper limit, the reduction vanishes when approaching 5 kHz. At $\varphi = 0^\circ$ the change in angle of attack has only a small effect

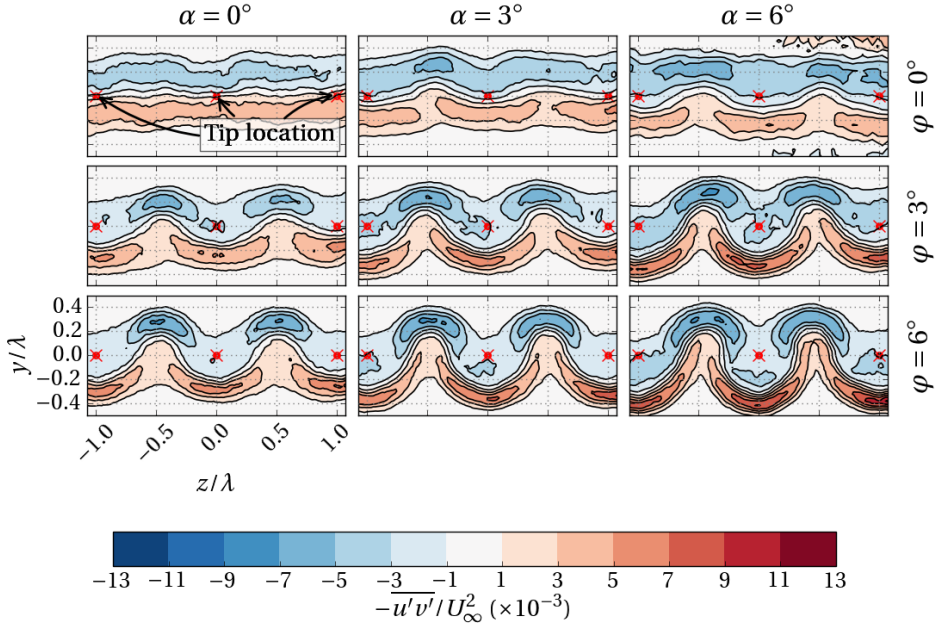


Figure 4.25: Values of the Reynolds stress $-\overline{u'_r v'_r}$ in the cross-flow plane.

on the noise reduction.

When the serrations are placed at $\varphi = 6^\circ$ (figure 4.27, bottom), the noise reduction is less pronounced, to the point that, depending on airfoil incidence, an increase of noise is measured in the higher frequency range. This increase may relate to the presence of high rms in the flow caused by these high flap or airfoil incidence angles, as discussed in the previous section. The frequency where such inversion occurs is denoted as crossover frequency, f_c , and has been reported in detail by Gruber *et al.* [4.38] and chapter 6.

The approximation of Howe [4.16] for the noise of a similar serration geometry on the trailing edge of an infinitely thin flat-plate under the same flow conditions, without incidence, is also presented in figure 4.27 (dashed line). The differences observed with the experimentally measured noise from the serrated airfoil are notable. A variation regarding the spectrum shape is persistent, where the present case shows higher reduction at the lower and mid-frequency range presented, and less reduction in the higher frequencies. Instead, the prediction indicates an opposite behavior. This contrast has also been reported by Gruber *et al.* [4.12]. Alternatively, a simplistic application of equation (4.4) based on the spectrum of the straight edge in figure 4.27, would be approximated as a constant reduction for all frequencies, thus represented as a straight line, at the same predicted constant reduction discussed above in figure 4.12, indicating an overestimation of at least 5 dB over the reduction levels here observed. Its inclusion is omitted for conciseness.

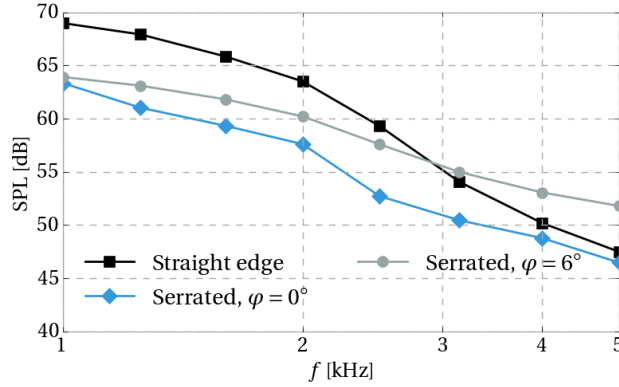


Figure 4.26: Third-octave sound pressure levels for the straight, and two serrated trailing edges ($\varphi = 0^\circ$ and 6°), with $\alpha = 0^\circ$ and $U_\infty = 35$ m/s.

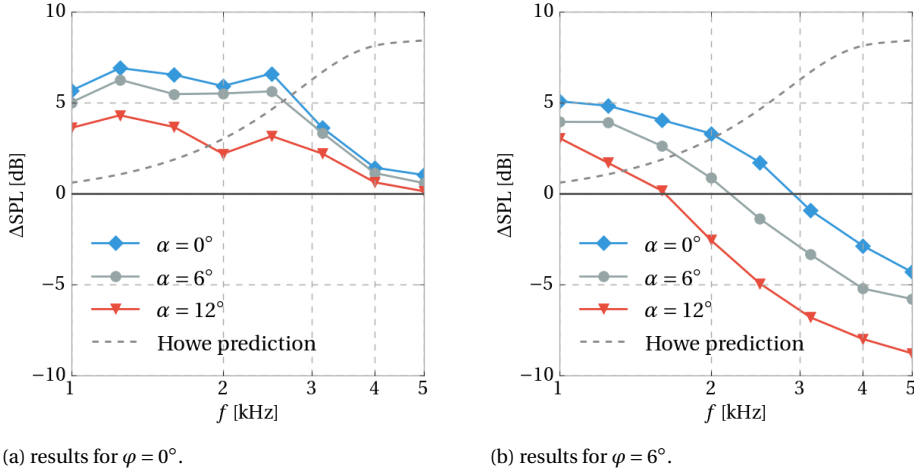


Figure 4.27: Measured noise differences in third-octave band SPL of serrations relative to the straight trailing edge for $U_\infty = 35$ m/s, for $\varphi = 0^\circ$ and 6° . The noise of the serrated trailing edge of a flat-plate according to Howe [4.16] is also presented, relating to the $\alpha = 0^\circ$, $\varphi = 0^\circ$ case.

Although the authors have determined that the degree of serration-flow misalignment significantly affects the efficiency at which the serrations reduce noise, the fact that the discrepancies between the predicted and measured levels of reduction are present for the $\alpha = 0^\circ$, $\varphi = 0^\circ$ case, indicates that misalignment by itself cannot be used to explain them. A comprehensive study of the boundary layer flow properties, especially using time-resolved information, could help identify further reasons for this discrepancy. This analysis demands a dedicated scrutiny and is reserved for an separate study.

4.3. CONCLUSIONS

The mean topology and the turbulence statistics of the flow near trailing edge serrations have been studied using PIV under different degrees of airfoil incidence and serration flap angle. The PIV measurements yield the pattern of streamlines close to the surface of serrations enabling to quantify their departure from the freestream direction. Measurements in the cross-flow plane indicate the presence of streamwise vortices emanating from the serrated edge, with their strength primarily influenced by the serration flap angle. The results of the mean flow measurements are input to a simplified version of the model of Howe [4.16] that estimates relative noise reduction on the basis of the local angle between the flow and the trailing edge.

The study is complimented with acoustic measurements, by which it is shown that the serrated trailing edge effectively reduces the turbulent boundary layer trailing edge noise of the airfoil, although to a lesser extent than that which the prediction suggests. This is consistent with experimental findings reported in literature. The PIV survey further reveals that, in the $\alpha_g = 0^\circ$, $\varphi = 0^\circ$ case, the mean flow and turbulence statistics do not exhibit significant changes, yet a noticeable noise reduction is achieved. When serration–flow misalignment is prescribed, the flow undergoes important changes in various mean flow and turbulence statistic measures. Despite this significant departure from the assumed conditions in the Howe model, the noise is still reduced in the lower frequencies of the range measured. At higher frequencies, the noise is instead increased. Changes in turbulence statistics between serration–flow misaligned cases and the $\alpha = 0^\circ$, $\varphi = 0^\circ$ case serve to explain the observed change in acoustic emissions.

BIBLIOGRAPHY

- [4.1] C. Arce León, D. Ragni, S. Pröbsting, F. Scarano, and J. Madsen, *Flow topology and acoustic emissions of trailing edge serrations at incidence*, [Experiments in Fluids](#) **57**, 91 (2016).
- [4.2] T. Brooks, D. Pope, and M. Marcolini, *Airfoil self-noise and prediction*, [NASA Reference Publication Number 1218](#) (1989).
- [4.3] M. Gruber, P. Joseph, and M. Azarpeyvand, *An experimental investigation of novel trailing edge geometries on airfoil trailing edge noise reduction*, in [19th AIAA/CEAS Aeroacoustics Conference](#) (AIAA, Berlin, Germany, 2013).
- [4.4] D. Moreau and C. Doolan, *Noise-Reduction Mechanism of a Flat-Plate Serrated Trailing Edge*, [AIAA Journal](#) **51**, 2513 (2013).
- [4.5] T. Dassen, R. Parchen, J. Bruggeman, and F. Hagg, *Results of a wind tunnel study on the reduction of airfoil self-noise by the application of serrated blade trailing edges*, Tech. Rep. (National Aerospace Laboratory, NLR, 1996).
- [4.6] J. Schepers, A. Curvers, S. Oerlemans, K. Braun, T. Lutz, A. Herrig, W. Wuerz, A. Mantesanz, M. Fischer, K. Kogler, T. Maeder, L. Garcillán, B. Méndez-López, A. Matesanz, and R. Ahrelt, *Sirocco: Silent Rotors By Acoustic Optimisation*, in [Second International Meeting on Wind Turbine Noise](#) (2007).

- [4.7] S. Oerlemans, M. Fisher, T. Maeder, and K. Kögler, *Reduction of wind turbine noise using optimized airfoils and trailing-edge serrations*, *AIAA Journal* **47**, 1470 (2009).
- [4.8] T. P. Chong and A. Vathylakis, *On the aeroacoustic and flow structures developed on a flat plate with a serrated sawtooth trailing edge*, *Journal of Sound and Vibration* , **1** (2015).
- [4.9] A. Finez, E. Jondeau, M. Roger, and M. C. Jacob, *Broadband Noise Reduction of a Linear Cascade With Trailing Edge Serrations*, in *17th AIAA/CEAS Aeroacoustics Conference (32nd AIAA Aeroacoustics Conference)* (Portland, Oregon, USA, 2011).
- [4.10] C. Arce, D. Ragni, S. Pröbsting, and F. Scarano, *Flow Field Around a Serrated Trailing Edge at Incidence*, in *33rd Wind Energy Symposium* (American Institute of Aeronautics and Astronautics, Kissimmee, Florida, 2015).
- [4.11] M. Gruber, P. Joseph, and T. Chong, *Experimental investigation of airfoil self noise and turbulent wake reduction by the use of trailing edge serrations*, in *16th AIAA/CEAS Aeroacoustics Conference* (2010) pp. 1–23.
- [4.12] M. Gruber, P. Joseph, and T. Chong, *On the mechanisms of serrated airfoil trailing edge noise reduction*, in *17th AIAA/CEAS Aeroacoustics Conference (32nd AIAA Aeroacoustics Conference)*, Vol. 2781 (American Institute of Aeronautics and Astronautics, Portland, Oregon, USA, 2011) pp. 5–8.
- [4.13] N. Fritsch-Nehring, *Trailing Edge Serrations*, *windblatt das ENERCON Magazin* , **19** (2015).
- [4.14] General Electric, *Introducing GE's 2.75 MW Wind Turbines*, (2012).
- [4.15] S. Oerlemans, *Reduction of wind turbine noise using blade trailing edge devices*, *22nd AIAA/CEAS Aeroacoustics Conference* , **1** (2016).
- [4.16] M. S. Howe, *Noise produced by a sawtooth trailing edge*, *The Journal of the Acoustical Society of America* **90**, 482 (1991).
- [4.17] B. Lyu, M. Azarpeyvand, and S. Sinayoko, *Prediction of noise from serrated trailing edges*, *Journal of Fluid Mechanics* **793**, 556 (2016), [arXiv:1508.02276](https://arxiv.org/abs/1508.02276) .
- [4.18] A. L. Braslow, R. M. Hicks, and R. V. Harris Jr., *Use of grit-type boundary-layer transition trips on wind-tunnel models*, *NASA Technical Note* (1966).
- [4.19] F. Stern, M. Muste, M. Beninati, and W. Eichinger, *Summary of experimental uncertainty assessment methodology with example*, Tech. Rep. (Iowa Institute of Hydraulic Research, College of Engineering, The University of Iowa, Iowa City, USA, 1999).
- [4.20] B. Wieneke, *PIV uncertainty quantification from correlation statistics*, *Measurement Science and Technology* **26** (2015), [10.1088/0957-0233/26/7/074002](https://doi.org/10.1088/0957-0233/26/7/074002).
- [4.21] J. Westerweel, *Fundamentals of digital particle image velocimetry*, *Measurement Science and Technology* **8**, 1379 (1997).

- [4.22] M. Raffel, C. Willert, and J. Kompenhans, *Springer*, Experimental Fluid Mechanics (Springer, Berlin, Heidelberg, 2007).
- [4.23] F. F. J. Schrijer and F. Scarano, *Effect of predictorcorrector filtering on the stability and spatial resolution of iterative PIV interrogation*, *Experiments in Fluids* **45**, 927 (2008).
- [4.24] P. Sijtsma, *SAE Technical Paper*, Tech. Rep. October (National Aerospace Laboratory (NLR), Anthony Fokkerweg 2, 1059 CM Amsterdam, P.O. Box 90502, 1006 BM Amsterdam, The Netherlands, 2010).
- [4.25] T. Brooks, M. Marcolini, and D. Pope, *Airfoil trailing edge flow measurements and comparison with theory, incorporating open wind tunnel corrections*, in *9th Aeroacoustics Conference* (AIAA, Williamsburg, Virginia, 1984).
- [4.26] R. Arina, R. Della Ratta Rinaldi, A. Iob, and D. Torzo, *Numerical Study of Self-Noise Produced by an Airfoil with Trailing-Edge Serrations*, in *18th AIAA/CEAS Aeroacoustics Conference (33rd AIAA Aeroacoustics Conference)*, June (American Institute of Aeronautics and Astronautics, Colorado Springs, CO, 2012) pp. 4–6.
- [4.27] M. Gruber, *Airfoil noise reduction by edge treatments*, *Ph.D. thesis*, University of Southampton (2012).
- [4.28] D. Moreau, L. Brooks, and C. Doolan, *Flat plate self-noise reduction at low-to-moderate Reynolds number with trailing edge serrations*, in *Proceedings of the Annual Conference on the Australian Acoustical Society* (2011).
- [4.29] W. K. Blake, *Mechanics of Flow-Induced Sound and Vibration V2: Complex Flow-Structure Interactions, Volume 2* (Elsevier Science, 2012) p. 567.
- [4.30] F. Bertagnolio, A. Fischer, and W. Jun Zhu, *Tuning of turbulent boundary layer anisotropy for improved surface pressure and trailing-edge noise modeling*, *Journal of Sound and Vibration* **333**, 991 (2014).
- [4.31] M. S. Howe, *Aerodynamic noise of a serrated trailing edge*, *Journal of Fluids and Structures* **5**, 33 (1991).
- [4.32] S. Pröbsting, M. Tuinstra, and F. Scarano, *Trailing edge noise estimation by tomographic Particle Image Velocimetry*, *Journal of Sound and Vibration* **346**, 117 (2015).
- [4.33] M. K. Bull, *On the form of the wall-pressure spectrum in a turbulent boundary layer in relation to noise generation by boundary layer-surface interactions*, In: *Mechanics of sound generation in flows; Proceedings of the Joint Symposium*, 210 (1979).
- [4.34] T. Brooks and T. Hodgson, *Trailing edge noise prediction from measured surface pressures*, *Journal of Sound and Vibration* **78**, 69 (1981).
- [4.35] B. Ganapathisubramani, E. K. Longmire, and I. Marusic, *Characteristics of vortex packets in turbulent boundary layers*, *Journal of Fluid Mechanics* **478**, 35 (2003).

- [4.36] S. Ghaemi and F. Scarano, *Turbulent structure of high-amplitude pressure peaks within the turbulent boundary layer*, [Journal of Fluid Mechanics](#) **735**, 381 (2013).
- [4.37] M. Howe, *Trailing Edge Noise at Low Mach Numbers*, [Journal of Sound and Vibration](#) **225**, 211 (1999).
- [4.38] M. Gruber, M. Azarpeyvand, and P. F. Joseph, *Airfoil trailing edge noise reduction by the introduction of sawtooth and slitted trailing edge geometries*, [Proceedings of 20th International Congress on Acoustics, ICA](#) **10**, 1 (2010).

5

BOUNDARY LAYER AND ACOUSTIC EMISSION CHARACTERIZATION OF FLOW-ALIGNED SERRATIONS

When life becomes too complicated and we feel overwhelmed, it's often useful just to stand back and remind ourselves of our overall purpose, our overall goal. When faced with a feeling of stagnation and confusion, it may be helpful to take an hour, an afternoon, or even several days to simply reflect on what it is that will truly bring us happiness, and then reset our priorities on the basis of that. This can put our life back in proper context, allow a fresh perspective, and enable us to see which direction to take.

Dalai Lama XIV, *The Art of Happiness: A Handbook for Living*

42

Deep Thought¹

The question of the noise reduction mechanism of serrations is investigated from a hydro-dynamic perspective. The condition of flow-alignment of the serrations is ensured by using a symmetric airfoil, zero incidence and no flap angle. Time-resolved and time-averaged flow statistics are presented, with a TNO-Blake approach to the qualitative description of surface pressure modification in the streamwise direction.

¹Douglas Adams, *The Hitchhiker's Guide to the Galaxy*

The contents of this chapter have been adapted from Arce León *et al.* [5.1].

SERRATIONS ARE AN EFFECTIVE DEVICE FOR AIRFOIL NOISE REDUCTION. The measurements presented in chapter 4 confirm this, along with results found in multiple other studies—as discussed in section 2.3.

Nevertheless, the mechanism behind this effect has not been clearly identified. Two proposed alternatives remain plausible. The first argues that serrations beneficially modify the flow such that its contribution to the generated noise is reduced (supported in [5.2–4]). The second proposes that the scattering at the sharp trailing edge is reduced by avoiding the more efficient straight geometry ([5.5, 6]).

In the current application, either is likely to be present and thus somehow be responsible for a certain level of modification to the airfoil's noise emissions. Their separation is therefore not straightforward and it remains unclear which dominates. Solving this dichotomy is desired as it may have an effect on the direction of future serration design philosophies.

The problem is aggravated by trailing edge scattering not being quantifiable through flow or pressure measurements alone, and it is only indirectly observable through acoustic measurements. Furthermore, modifications to the flow are by themselves difficult to equate to changes in the acoustic emissions.

An alternative analysis is therefore proposed. An accurate measurement of key flow parameters in the boundary layer near the trailing edge should be obtained. The absence of significant flow changes will infer the dominance of the geometry as an acoustic emission modifier. An observed level of modification, if not considered negligible, will nevertheless not help to resolve the problem.

Obtaining a sufficiently accurate flow description requires a carefully designed experimental setup where no flow modification is induced by anything other than the physical presence of the serrations in their most baseline configuration—procuring the same flow conditions over the upper and lower sides of the serrations is the most essential requirement.

Historically, experimental research on serrations has been done primarily through the measurement of the acoustics emissions. It has been possible to test different conditions and geometries, and form guidelines on which work best ([5.7]). But a relatively limited description of the flow has been collected so far. Even more critically, most research has been performed at significant levels of serration-flow misalignment. This condition makes the experimental approach outline above impossible to realize. This state-of-the-art admittedly came as a surprise—and then a concern—to the author at the commencement of his research.

Gruber *et al.* [5.8], for example, investigated serrations without a detailed focus on the level of flow-misalignment. A highly cambered airfoil was used, and serrations protruded straight from the angled trailing edge. It is clear that such a setup cannot meet the proposed condition of equal flow over the upper and lower serration surfaces. Flow visualization using smoke was used to confirm to some level the effects of misalignment in [5.7]. A similar setup is also employed in [5.9], and other derivative studies.

In [5.3], the condition of flow-alignment is better achieved, as serrations are installed at the trailing edge of a flat plate. Nevertheless, the relatively large angle (12°) on the upper side of the flat plate as it narrows to form the sharp trailing edge does not ensure

that a similar flow condition over the upper and lower serration sides is obtained. The study furthermore focuses on the reduction of tonal noise components due mainly to vortex shedding, thus a different mechanism than the turbulent boundary layer-trailing edge noise (TBL-TE noise) here addressed.

In the pursuit of describing the noise reduction mechanism, serration-flow misalignment can be considered a source of measurement data contamination. As serrations have been shown to work even when flow-misaligned ([5.10]), the sufficient conditions for noise reduction may be misinterpreted. Even a small deviation from the baseline case can lead to the discovery of misleading flow features that may be falsely attributed as necessary to achieve noise reduction. The effects of flow-misalignment instead lead to a different modification of the airfoil acoustic footprint. Its description is addressed in chapter 6.

So, in order to better understand the noise reduction mechanism of serrations, a detailed flow-based research on serrations (wherein achieving serration-flow alignment is observed) is critical, but remains missing.

The work presented in this chapter attempts to fill this research gap by examining the level of flow modification at zero serration-flow misalignment in detail. Special emphasis is given on the description of the boundary layer flow at locations near the serration edge. A comparison with the flow in the boundary layer over the straight edge is provided.

While the turbulent boundary layer is ultimately responsible for TBL-TE noise, it is the resulting unsteady surface pressure which scatters at the edge, radiating into the far-field as sound. Therefore, along with the obtained flow observations, a description of the surface pressure along the edges would improve the identification of the serration noise reduction mechanism.

Unfortunately, obtaining direct measurements on the surface pressure is technically unachievable in the present implementation. This is due in part to instrumentation requirements. State-of-the-art pressure transducers and their connections demand model thicknesses larger than the required serration panel thickness in wind tunnel measurements of this size (1 mm in the present model). So, while numerical methods allow the retrieval of such information ([5.2, 11–13]) a direct experimental measurement remains out of reach.

Workarounds have been attempted in research on serrations. In [5.4] and [5.5], serrations have been cut into a flat plate and used as an extension to one side of a wind tunnel nozzle. The instrumented side forms the wall below the turbulent boundary layer. The opposite side—from which the measurement instruments (transducers, tubes and so forth) protrude—remains in a quiescent state. Although valuable information has been retrieved in this manner, the method violates the proposed same-flow-condition over the two serration sides.

In an attempt to describe the surface pressure, the present investigation proposes a different approach. Particle image velocimetry (PIV) is used to form an accurate and time-resolved description of the flow. It is used in turn as an input to a modified implementation of the TNO-Blake TBL-TE noise prediction model (see section 2.1.3). A qualitative approximation to the surface pressure near the edges is then achievable.

While an extension of the method to serrated edges has been proposed by Fischer

et al. [5.14] by approximating some parameters, their direct evaluation, necessary for the full TNO-Blake implementation, is unobtainable in the present approach. Only a qualitative approximation of the pressure is therefore attempted, as described in section 5.2.2.

The flow vector field is retrieved with its three components using time-resolved stereoscopic particle image velocimetry (S-PIV) ([5.15]). As in the work presented in chapter 4, thin trailing edge serrations were retrofitted on a NACA 0018 airfoil. No incidence has been prescribed, in order to maintain a balance in the mean pressure between the serration sides, and the tests are performed at a Reynolds number of 263 000. The flow measurements are complimented with microphone array measurements to characterize the noise reduction of the serrations.

5.1. EXPERIMENTAL SETUP

The experiments were conducted at the Delft University of Technology vertical wind tunnel (V-Tunnel), described in section 3.1. The airfoil and serration model used is described in detail in section 4.1. It is a NACA 0018 airfoil of chord $C = 20$ cm that spans the 40 cm width of the test section. A modular trailing edge design allows the serrations to be installed at the trailing edge while keeping the surface free from irregularities and allowing to revert to the straight-edge geometry. The model has been installed in an *ad-hoc* prepared open test section with two long side plates to approximate the two-dimensional flow condition over most of the wing span. Two versions of the test section were used, one optimized for the PIV measurements (figure 5.2), and the other for the acoustic measurements (figure 3.11).

All measurements were conducted at $\alpha = 0^\circ$ angle of attack and zero serration flap angle, $\varphi = 0^\circ$. A freestream velocity of 20 m/s was chosen for the PIV measurements, resulting in a chord-based Reynolds number of 263 000. This velocity was selected as it is the highest with which time-resolved flow information can be gathered with the current high-speed PIV system. The acoustic measurements were conducted at speeds of 30, 35 and 40 m/s. In this case, higher velocities were needed in order to distinguish the trailing edge noise from the background noise, especially for the reduced levels obtained when serrations were applied. The reconciliation between the PIV and acoustic measurement velocity differences is addressed in section 5.2.3.

At the tested velocities, the boundary layer is forced to turbulent transition with randomly distributed roughness elements. The trip tape was constructed by an appropriate density of dispersed carborundum elements of 0.6 mm nominal size, placed on a thin double sided tape of 1 cm width, following guidelines outlined in [5.16]. The tape, streamwise-centered at $0.2C$, spans the entirety of the airfoil. A stethoscope probe has been used to verify that the boundary layer was tripped and that it remains turbulent downstream until the trailing edge.

5.1.1. STEREOSCOPIC PIV

S-PIV ([5.15]) has been employed to obtain measurements of the three velocity components in a plane aligned with the flow field. The flow was seeded with tracer particles of evaporated SAFEX®, as described in section 3.2. Their illumination was pro-

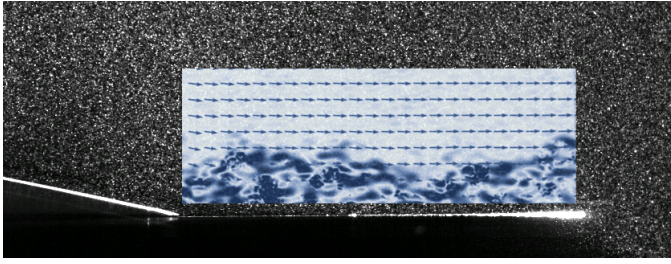


Figure 5.1: Single camera capture of the airfoil trailing edge side (left), serrations and the tracer particles, illuminated by the laser. The flow goes from left to right. An instantaneous vorticity field from the PIV cross-correlation result is overlaid for illustration purposes.

vided by a Quantronix Darwin Duo double cavity Nd:YLF laser. It has an energy of 2×25 mJ at 1 kHz. Two high-speed Photron Fastcam SA1 cameras were used, equipped with 1024×1024 px resolution CMOS sensors with a pixel-pitch of $20 \mu\text{m}/\text{px}$, and a digital resolution of 12 bit. Nikon NIKKOR macro objective lenses of 105 mm focal length at an aperture of $f/5.6$ were fitted on the cameras. One perpendicular to was mounted perpendicular to the flow field, and the second one was mounted at a relative angle of 35° with respect to the first. With an overall distance of about 40 cm, the resulting magnification factor is about 0.40, entailing that the particle image on the sensor is limited by diffraction to about $10 \mu\text{m}$ ([5.17]).

To avoid the problem of peak-locking, potentially present for the available $20 \mu\text{m}/\text{px}$ pixel pitch of the cameras, defocusing is applied to the raw images by slightly displacing the focus plane from the laser one ([5.18]). The procedure allows keeping the particle images in the range between 1 and 1.5 px and to obtain a stochastic distribution of round-off errors in the computed velocity field.

Since the S-PIV method requires the cameras to be at an angle with respect to the measurement plane, a Scheimpflug adapter was used to correct the sensor measurement plane misalignment. The final field of view is the calibrated and dewarped combination of the images of both cameras. A resulting area of $2 \times 5 \text{ cm}^2$ was obtained by cropping the sensor to 512×1024 px, permitting the same field of view for both time-resolved data and statistics, with a digital imaging resolution of about $20 \text{ px}/\text{mm}$. A sample capture of one of the cameras can be seen in figure 5.1.

The triggering of the camera shutter and the firing of the laser pulse was controlled by a LaVision HighSpeed Controller. The capture sequence command and data acquisition, along with the data processing, was performed using the LaVision software DaVis 8. Two acquisition setups were used to capture either time-resolved or uncorrelated flow samples for averaging. Their respective configurations are detailed in the following two subsections. For both, a multi-pass stereo cross-correlation was applied with a final window size of 16×16 px (or $0.8 \times 0.8 \text{ mm}^2$). The adjacent windows were overlapped by 75% such that the flow is sampled with a spatial resolution of 0.8 mm and a vector spacing of 0.2 mm.

A schematic of the S-PIV setup can be seen in figure 5.2. The cameras are located on the side of the airfoil, one perpendicular to the laser sheet and another above it, as

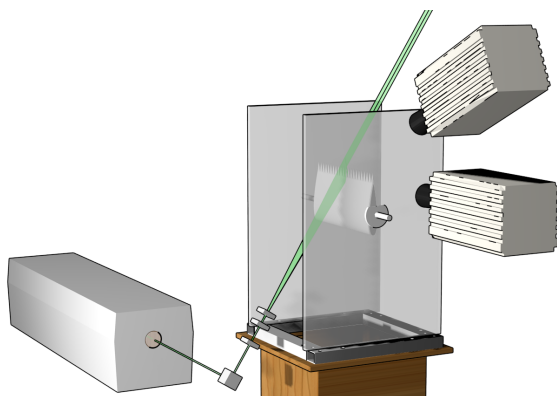


Figure 5.2: PIV setup indicating the two camera locations and laser sheet formation with respect to the wind tunnel open test section and the airfoil.

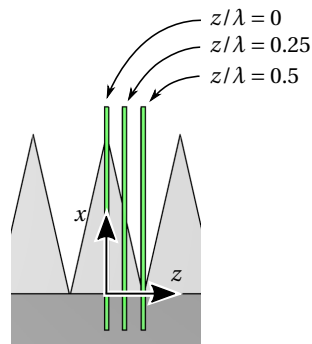


Figure 5.3: Wall-normal measurement plane locations over the serration surface. The y axis is positive out-of-plane.

5

previously mentioned. The laser is fired from the side and oriented perpendicular to the airfoil surface by means of a mirror. It is formed into a sheet of about 1 mm thickness in the field of view region using optical lenses. Figure 3.2 shows a picture of this setup.

For the serrated edge, three spanwise locations were measured at planes normal to the z axis. A schematic of these locations can be seen in figure 5.3, along with the orientation of the coordinate system and the location of its origin. The x axis is oriented parallel to the airfoil chord in the streamwise direction and located at the serration median line of the serration and its root. The z axis is oriented in the spanwise direction, and the y axis is in the wall-normal direction. An auxiliary definition for the orientation of the x and y axes will be given below in section 5.2.1 for wall-normal measurements over the airfoil surface. This becomes necessary to correct for the difference in angle between the airfoil and the serration surfaces, and adhere to the definition for the boundary layer measurements. The measurement planes are located spanwise in the serration-width normalized locations $z/\lambda = 0, 0.25$ and 0.5 .

ACQUISITION OF THE UNCORRELATED DATASET

For simplicity this setup will be referred to as the time-averaged measurement for the remainder of the chapter. The time separation between image pairs was chosen to be $\Delta t = 50 \mu\text{s}$, yielding a particle image displacement of approximately 15 pixels in the freestream. A minimum distance to the wall of around $y^+ \approx 10$ was achieved, limited mainly by the finite digital resolution obtained with the setup, as discussed in the results section 5.2.1. An acquisition frequency of 250 Hz was chosen, ensuring that all vector fields are uncorrelated at this flow speed. In total, 2000 time instances were captured per case, for a total of 8 s of measurement time.

TIME-RESOLVED SAMPLE ACQUISITION

For the time-resolved sample acquisition, a continuous set of images is captured for which each individual image serves as the cross-correlation pair for the following time

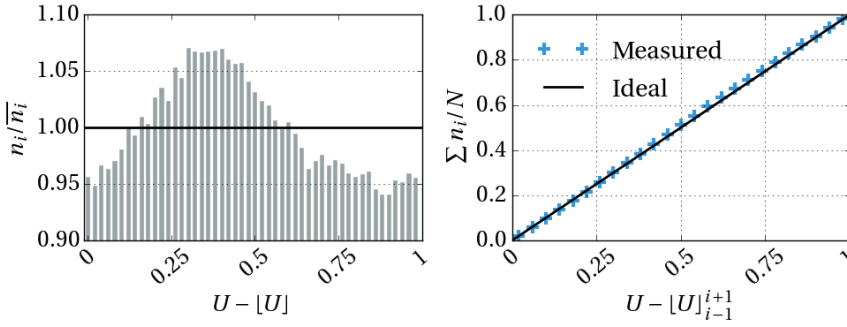


Figure 5.4: Evaluation of the presence peak-locking error by means of a decimal distribution histogram (left) and a cumulative distribution of binned decimal counts (right, only each second point is shown).

instance. For this purpose, the repetition rate of each of the laser cavities was set to 5000 Hz while the pulse separation time was set to 100 μ s. Being the pulse separation time half with respect to the repetition rate, the raw images can be re-shuffled in order to obtain a time-series of about 10 100 particle images at 10 000 Hz. With this acquisition frequency, a particle displacement of around 24 px in the freestream was achieved for the 20 m/s flow velocity (about double the one used for statistics).

UNCERTAINTY ANALYSIS FOR THE PIV METHOD

A linear propagation approach ([5.19]) was used to estimate the typical measurement uncertainty. It was verified *a-posteriori* using the statistical method introduced in [5.20].

Bias errors occurring to peak-locking ([5.18]) happen when the particle diffraction spots are imaged with less than a pixel on the camera sensor. As mentioned in the experimental setup paragraph, the source is thus alleviated by following the technique proposed in [5.21], wherein it is suggested that a slight de-focusing of the images by the lens can bring the apparent particle size to above 1 px. A histogram of the particle displacement is provided in figure 5.4 and shows the success of this approach, giving no evidence of peak-locking. Here the decimals of the measured velocity magnitudes, $U - [U]$, where $[\cdot]$ is the floor function, are binned into a histogram, which would show a large deviation towards one or more values, if a peak-locking error would dominate. The line plot represents the cumulative distribution of the binned decimal occurrences, showing a very close approximation to the ideal result.

Further, the finite spatial resolution of the resulting velocity fields may limit the capture of flow structures. With the applied multi-pass cross-correlation algorithm, and the application of window deformation, the amplitude of the fluctuations is measured with less than 5% modulation, for window sizes smaller than 0.6 times the characteristic structure length scale ([5.22]). Having a window size of $0.8 \times 0.8 \text{ mm}^2$, as specified earlier, flow structures down to 1.2 mm can thus be measured within 95% accuracy.

An iterative self-calibration procedure was applied to further improve the fitting of the captured planes from the initial location based calibration, which is based on a known three-dimensional target. The application of the two calibration procedures helps alleviate further aspects such as the lens distortion. A final polynomial fitting used for the

mapping of the images is implemented within DaVis and iterated on the raw images, yielding a disparity vector of less than 0.10 px after self calibration, considered satisfactory to carry out the stereo cross-correlation ([5.21]).

The random errors in the measurement domain have been found to vary with less than 1% in the freestream and around 3% in the inner boundary layer region. The method used to approximate these numbers has been based on the work of [5.20].

The mean velocity and velocity root mean square, or rms, of the fluctuations carry uncertainties that are dependent on the size of the statistical sample. For the present case the error in the mean velocity reduces to 0.05% of \bar{U} , and 2% of U_{rms} .

5.1.2. MICROPHONE ARRAY

For this experiment, microphone array measurements have been employed to quantify the noise reduction capabilities of the adopted serrations. An array with 64 microphones and of an effective diameter, D , of 0.9 m was used, arranged in a multi-arm logarithmic spiral configuration ([5.23, 24]), as shown in figure 3.10 and 3.11, with the distinction that the array was placed 1.26 m away from the airfoil. The center of the array was aligned in the streamwise direction with the root of the serrations at the trailing edge.

The test section was modified from that described in the PIV setup in order to have longer side plates, terminating 0.7 m downstream of the airfoil trailing edge. Furthermore, the airfoil leading edge is separated 0.5 m from the nozzle exit. These measures helped to separate the extraneous noise sources coming from the nozzle and the downstream edges of the side plates from the airfoil trailing-edge noise source.

The sampling frequency used was 50 kHz and the selected sound frequency range of interest extended from 1 to 5 kHz. For each measurement, a recording time of 60 s was employed. The acoustic data was averaged using time blocks of 2048 samples ($\Delta t = 40.96$ ms) for each Fourier transform and windowed using a Hanning weighting function with 50% data overlap. With these values, the frequency resolution for the source maps is 24.41 Hz. The averaged cross-spectral matrix required for beamforming was obtained after cross-correlating the microphones signals. The expected error ([5.25]) in the estimate for the cross-spectrum is, therefore:

$$\varepsilon_r = \sqrt{\frac{\Delta t}{T_{\text{meas}}}} = 2.6\%. \quad (5.1)$$

Considering a normal Gaussian distribution for the measurements ([5.25]), the spectral estimate 95% confidence interval is:

$$\hat{G}_{xx}(1 - 2\varepsilon_r) \leq G_{xx} \leq \hat{G}_{xx}(1 + 2\varepsilon_r). \quad (5.2)$$

With the normalized random error calculated in equation 5.1, we obtain:

$$0.948 \hat{G}_{xx} \leq G_{xx} \leq 1.052 \hat{G}_{xx},$$

where G_{xx} and \hat{G}_{xx} are the true and the measured values of the cross spectrum, respectively.

The rectangular scan grid used for beamforming covered the expected area of noise generation, ranging from $z = -0.22$ m to $z = 0.22$ m in the spanwise direction and from

$x = -0.7$ m to $x = 0.3$ m in the streamwise direction. The distance between grid points is 1 mm. The scan grid covered the whole airfoil and went from the nozzle exit until 0.3 m after the trailing edge using 441×1001 grid points.

The lower boundary of the minimum angular distance at which two different sources can be separated using an array of circular aperture of diameter D can be estimated using the Rayleigh criterion ([5.26]):

$$\varphi = 1.22 \frac{c}{fD}. \quad (5.3)$$

For the current experimental setup, the minimum angular distance for the highest frequency considered in this analysis (5 kHz), considering $c = 340$ m/s, is $\varphi = 0.092$ rad. Thus, the minimum resolvable distance, R , at a distance from the array r of 1.26 m is $R = r \tan \varphi \approx 0.12$ m. Therefore, the selected spacing between grid points is approximately 120 times smaller than the Rayleigh's limit distance at that frequency.

Because trailing-edge noise is supposed to be a distributed sound source, the source maps were integrated over an area extending from $z = -0.1$ m to $z = 0.1$ m and from $x = -0.06$ m to $x = 0.06$ m (see figure 5.26). This section was chosen to minimize the contribution from extraneous sound sources, while still containing a representative part of the trailing edge ([5.27]). The beamforming results in that area were normalized by the value of the integral of a simulated point source of unitary strength placed at the center of the area of integration, evaluated within the same spatial boundaries ([5.28]). This process was then repeated for each frequency of interest to obtain the acoustic frequency spectra of the trailing edge.

Each microphone was previously calibrated using a pistonphone which generates a 250 Hz signal of known amplitude. Moreover, the performance of the array itself was assessed and calibrated by using tonal sound generated with a speaker at a known position emitting at several single frequencies: 500, 1000, 2000, 3000, 4000 and 5000 Hz. The SPLs at the center of the array were also measured with a calibrated TENMA 72-947 sound level meter. Therefore, the microphone array was calibrated in both source position and strength detection.

The effect of the shear layer in the acoustic measurements ([5.29]) was neglected due to the small angle ($< 10^\circ$) between the center of the array and the scan area of interest and the considerably low flow velocities employed in this experiment ([5.30]).

5.2. RESULTS

To discuss the results, a characterization of the boundary layer is shown first, based on the time-averaged PIV measurements. Its purpose is to identify both the effect that the serrations have on the flow directly upstream of the trailing edge, and on the mean flow and turbulence parameters pertaining to the flow as it convects over downstream locations of the serration edge.

The statistical description of the flow field in terms of average velocity and Reynolds stresses indicates which regions, within the boundary layer, exhibit larger levels of turbulence intensity. Nevertheless, the correlation between a change in the latter and the pressure fluctuations at the object surface remains complex, as discussed in the introduction of this chapter.

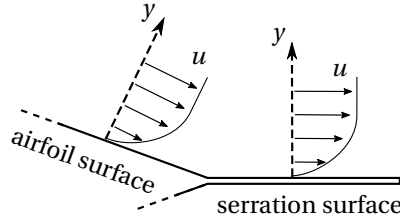


Figure 5.5: Schematic of the boundary layer definition over the airfoil and the serration surfaces.

To study this link, the discussion turns its focus on the elements of the TNO-Blake model based on results obtained from the time-resolved PIV measurements. Its objective is to provide a qualitative comparison between the flow at three different locations over the serrated edge, and over the straight edge.

Lastly, the results of the acoustic measurements are presented with the purpose of confirming and quantifying the noise reduction effects that this serration design offers when retrofitted on the used airfoil profile.

5

5.2.1. MEAN FLOW CHARACTERIZATION OF THE TURBULENT BOUNDARY LAYER

Time-averaged measurements are taken with S-PIV. Data are presented in the wall-normal direction at different streamwise locations over the surface of the airfoil and the serration tooth. Adherence to the definition of the boundary layer results in an intersection between the wall-normal lines over the airfoil surface and over the serration surface (due to the angle present between the two). For simplicity, the defined coordinate system will also be rotated accordingly, as indicated in the schematic of figure 5.5, such that y always points in the local wall-normal direction, and $u = \bar{u} + u'$, is the local wall-parallel component of U , where \bar{u} and u' are the time average and fluctuating parts of the flow according to the Reynolds decomposition.

The streamwise locations are picked 1 mm ($0.025 x/2h$) upstream of the respective trailing edge, mainly to avoid the directional ambiguity carried by the vertex between the airfoil and the serration tooth at $x/2h = 0$. This choice of translation in x is kept in all locations for consistency. For simplicity, the $x/2h = -0.025$ will still be referred to as the airfoil trailing edge, and written as $x/2h = 0$ in the rest of this chapter. The locations $x/2h = -0.025$, 0.475 and 0.975, along the serration trailing edge, will be referred to as the serration trailing edge, and noted as $x/2h = 0$, 0.5 and 1.0.

To analyze the boundary thickness, the surface-parallel edge velocity, u_e , is taken as the velocity at the wall-normal location y_δ at which the spanwise vorticity, integrated from the closest available wall-normal location, y_{\min} to y_δ , $-\int_{y_{\min}}^{y_\delta} \omega_z(y) dy$, stabilizes. This method offers an accurate way to determine the boundary layer edge by virtue of the values of ω_z being negligibly small beyond it (see [5.31, 32]). The establishment of u_e in this way is preferable over assuming the freestream velocity from the wind tunnel Pitot tube measurements, as small deviations ($\pm 1\%$) are expected in the mean flow freestream velocity between different runs, causing variations in the boundary layer locations.

First, wall-normal results at $x/2h = 0$ are presented for the straight edge and the 3 spanwise locations for the serrated edge: $z/\lambda = 0$, 0.25 and 0.5. The objective is to es-

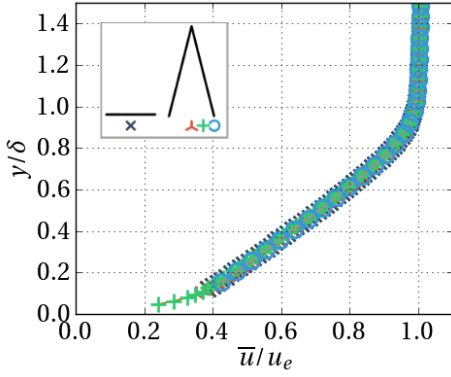


Figure 5.6: Wall-normal boundary layer profiles of \bar{u}/u_e at $x/2h = 0$.

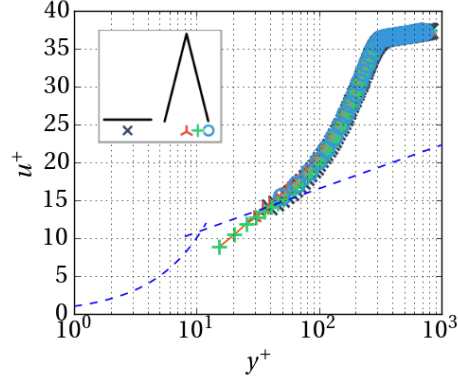


Figure 5.7: Non-dimensional boundary layer profile at $x/2h = 0$. The dashed lines show the law of the wall and log-law.

Table 5.1: Measures of boundary layer thickness at $x/2h = 0$.

Trailing edge	z/λ	δ_{99} [mm]	δ^* [mm]	θ [mm]
Serrated	0	8.9	2.1	1.2
Serrated	0.25	9.3	2.2	1.3
Serrated	0.5	9.2	2.2	1.3
Straight	.	9.4	2.1	1.3
XFOIL	.	.	1.7	1.0

establish whether the serration has any measurable effect on the flow close upstream to it. Figure 5.6 shows the results obtained for the mean streamwise velocity, \bar{u} . Differences along the wall-normal profile between the straight edge and the serration, or spanwise locations of the latter, are practically absent.

The resulting boundary layer thickness values are given in table 5.1 for the different serrated edge spanwise locations and for the straight edge, along with the results from the XFOIL ([5.33]) simulation on the latter. The values found from the PIV measurements on the straight edge airfoil show a good approximation to the ones reported by XFOIL. As expected from figure 5.6 and the discussed similarity of the \bar{u} wall-normal profiles, the values of δ_{99} , δ^* and θ (respectively the boundary layer thickness at 99% of the edge velocity, u_e , the displacement thickness, and the momentum thickness) are also similar for all measurements, with δ_{99} having a variation range of ± 0.25 mm, δ^* of ± 0.05 mm, and θ also of ± 0.05 mm. In the remainder of the article, if not explicitly indicated, δ will refer to δ_{99} .

The non-dimensional boundary layer profile is shown in figure 5.7 for the resolved vector field above the wall, $y^+ > 10$. It shows a departure from the log-law expected from a flat plate boundary layer measurement, and instead follows the trend expected for a boundary layer in an adverse pressure gradient ([5.34, 35]), which is the case at this

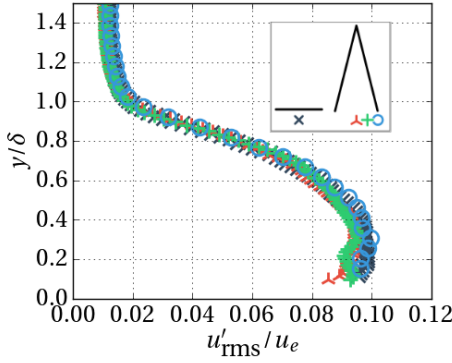


Figure 5.8: Wall-normal profiles of u'_{rms}/u_e at $x/2h = 0$.

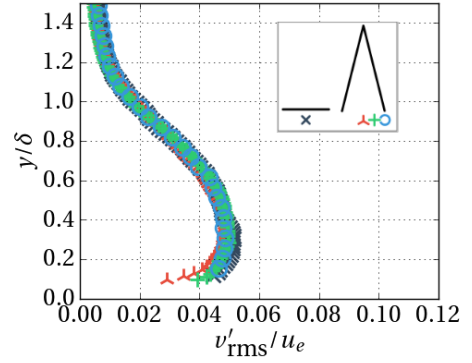


Figure 5.9: Wall-normal profiles of v'_{rms}/u_e at $x/2h = 0$.

5

location over the airfoil surface.

The skin friction coefficient, defined as $C_f = \mu(\partial u/\partial y)_{y=0}$, where μ is the fluid dynamic viscosity, is a guide to the general shape of the boundary layer. It will be discussed later (section 5.2.2) that the intensity of the mean pressure at the surface is found to be especially sensitive to the shear experienced in the boundary layer, for which C_f is an indicator. The direct calculation of C_f is impossible due to the absence of flow data close enough to the wall. Instead, the results presented in figure 5.7 use an estimation of C_f based on a best fit of the data against the log-law. The value found that best collapses the data (allowing for an expected deviation due to the adverse pressure gradient) is found to be approximately $C_f = 1.5 \times 10^{-2}$. An XFOIL simulation of the same setup yields a value of $C_f = 1.87 \times 10^{-2}$ at the same streamwise location, $x/2h = -0.025$ (or $x/C = -0.05$). The C_f value of 1.5×10^{-2} in the XFOIL simulation is reached instead slightly downstream at a streamwise location of $x/2h = -0.14$ (or $x/C = -0.028$). This represents a small deviation of around $0.03 C$ or $0.11 2h$. The approximation of the friction coefficient is thus considered satisfactory and will be examined later to evaluate its downstream evolution.

The wall-normal profiles of u_{rms} and v_{rms} at $x/h = 0$ are presented in figures 5.8 and 5.9. Only slight differences are observed between the different locations of the serrated edge and the straight edge. The u_{rms} shows higher values, slightly above or around $0.09 u_e$, at locations near the surface, at around $y/\delta = 0.2$ to 0.3 . The values of u_{rms} rapidly decline, reaching an asymptote of around $0.01 u_e$ by $y \approx 1.1\delta$.

Values of v_{rms} show the same trend as u_{rms} , but with a lower maxima of around $0.05 u_e$. The maxima happen at around the same wall-normal location as for u_{rms} , and the decline is seen to reach minima slightly above that for u_{rms} , in this case being closer to $y \approx 1.2\delta$.

Having discussed the mean flow properties of the wall-normal data at the $x/2h = 0$ location, it is established that the serrations have a negligible effect on the flow immediately upstream. The same analysis will now be applied to the 3 streamwise trailing edge locations of the serrations, at $x/2h = 0, 0.5$ and 1.0 .

The measured \bar{u} is shown in figure 5.10. Contrary to what was discussed for $x/2h = 0$

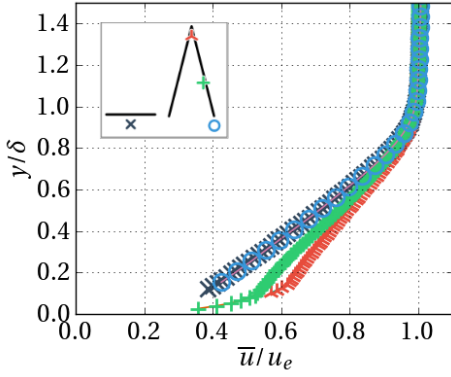


Figure 5.10: Wall-normal profiles of \bar{u}/u_e at different spanwise trailing edge locations of the serration, and the straight edge.

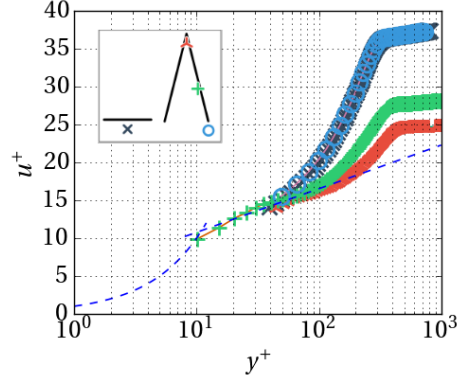


Figure 5.11: Non-dimensional boundary layer profile measured at different spanwise trailing edge locations of the serration, and the straight edge. The dashed lines show the law of the wall and log-law.

in figure 5.6, the velocity profiles seen here for the different cases vary significantly. The straight edge case, and the serration at $x/2h = 0$, are at the same locations as presented before and are included here to facilitate the comparison to the locations further downstream. As the boundary layer develops, the \bar{u} profile exhibits an increase in velocity.

Figure 5.11 provides evidence that the two downstream locations agree more closely with the log-law than the previously discussed measurements at $x/2h = 0$. A good fit is found between $20 < y^+ < 100$ for $x/2h = 0.5$, and between $50 < y^+ < 150$ for $x/2h = 0$. These two profiles also fit closer to non-adverse pressure gradient conditions, from which the measurements at $x/2h = 0$ deviate considerably, as was discussed above. The approximation of C_f for $x/2h = 0.5$ yields a value of $C_f = 2.6 \times 10^{-2}$, and for $x/2h = 1$, $C_f = 3.3 \times 10^{-2}$. Again, for both the serrated and straight edge at $x/2h = 0$, C_f was established earlier to be 1.5×10^{-2} .

It can be concluded that the skin friction coefficient increases for downstream locations of the serration edge, and is larger than that of the straight edged airfoil, approximately doubling by the time the flow reaches the tip of the serration. This directly relates to an increase in the boundary layer shear observed near the wall. The velocity shear is later reduced after $y/\delta \approx 0.1$, as confirmed by the mean flow profiles in figure 5.10. This reduced shear in the middle and upper boundary layer, thanks to the lower skin friction of the lower boundary layer which has allowed a larger velocity compared to the same wall-normal locations of the $x/2h = 0$ measurements, spans a larger extent of the boundary layer. It will be shown later that, according to equation (5.4), this change ascribes to an expected beneficial change in the qualitative mean pressure values at the surface.

The measured boundary layer thickness parameters for these trailing edge locations are shown in table 5.2. The δ_{99} values appear to shrink downstream, becoming 10% thinner when measured over the tip of the serration at $x/2h = 1$ than when done so over $x/2h = 0$, but it is very similar between the former and $x/2h = 0.5$. The values of δ^* and θ show only small differences downstream.

Table 5.2: Measures of boundary layer thickness at the trailing edge of the specified spanwise locations.

Trailing edge	z/λ	$x/2h$	δ_{99} [mm]	δ^* [mm]	θ [mm]
Serrated	0	1	8.3	1.1	0.8
Serrated	0.25	0.5	8.4	1.3	0.9
Serrated	0.5	0	9.2	2.2	1.3
Straight	.	0	9.4	2.2	1.3

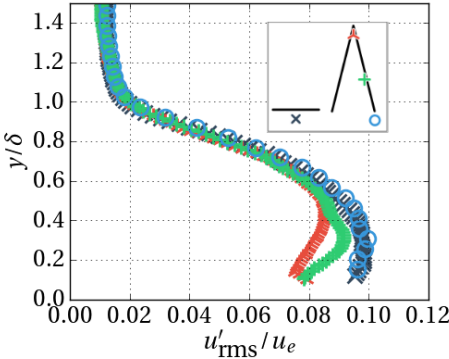


Figure 5.12: Wall-normal profiles of u'_{rms}/u_e at different spanwise trailing edge locations of the serration, and the straight edge.

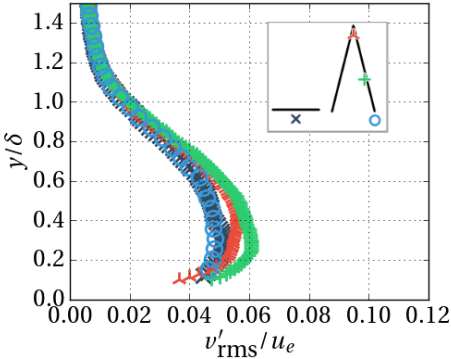
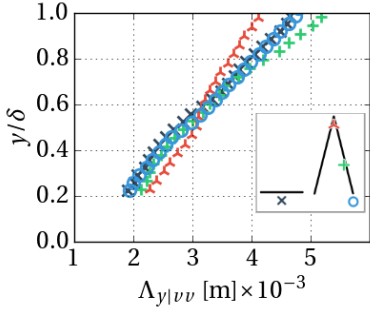
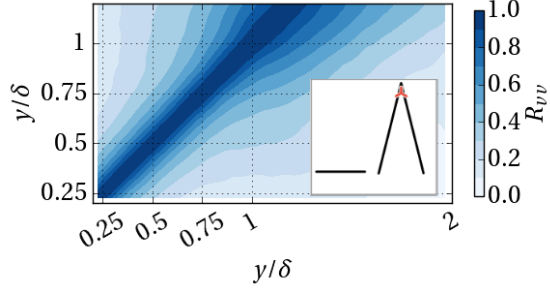


Figure 5.13: Wall-normal profiles of v'_{rms}/u_e at different spanwise trailing edge locations of the serration, and the straight edge.

The rms measurements of u' and v' are shown in figures 5.12 and 5.13. For u'_{rms} , the maxima decrease at trailing edge locations downstream of $x/2h = 0$, from around $u'_{\text{rms}}/u_e = 0.095$ to $u'_{\text{rms}}/u_e = 0.085$. The locations of the maxima of $x/2h = 1$ are higher than for the rest of the locations, and stand around $y/\delta \approx 0.4$ instead of between $y/\delta \approx 0.2$ and 0.3 . The lower values of u'_{rms} for $x/2h = 1$ and 0.5 persist at the same wall-normal locations up to around $y/\delta = 1.2$, showing differences of around $u'_{\text{rms}}/u_e = 0.02$ compared to the serrated edge at $x/2h = 0$ and the straight edge. The measurement of v'_{rms} shows the trailing edge location at $x/2h = 0.5$ to have a larger rms than the rest of the presented locations, which is unexpected based on the evolution of the boundary layer downstream of the airfoil.

5.2.2. TURBULENCE STATISTICS AND QUALITATIVE ANALYSIS OF SURFACE PRESSURE

In order to establish the effect that the observed boundary layer properties have on the surface pressure, the time-resolved PIV dataset is used here to characterize the different

Figure 5.14: Wall-normal values of $\Lambda_{y|vv}$.Figure 5.15: Values of R_{vv} for the serrated case streamwise location $x/2h = 1$.

elements of the TNO-Blake surface pressure approximation ([5.36]),

$$\Pi_p(\omega) = \frac{4\pi\rho^2}{\Lambda_{p|z}(\omega)} \int_0^\delta \Lambda_{y|vv}(y) U_c(y) \left[\frac{\partial u(y)}{\partial y} \right]^2 \times \frac{\bar{v}^2(y)}{U_c^2(y)} \Phi_{vv}(k_x, k_z=0) e^{-2|k|y} dy. \quad (5.4)$$

Here ρ refers to the fluid density, $\Lambda_{y|vv}$ refers to the wall-normal integral length scale taken over the flow component v , U_c refers to the wall-normal-dependent convection velocity magnitude, $\Phi_{vv}(k_x = \omega/U_c(y), k_z = 0)$ refers to the wavenumber spectral density of the v flow component where k is the flow component-dependent wavenumber. An analysis of the wall-normal and streamwise dependence of these values will be given below and the results will be summarized in section 5.2.2. The term $\Lambda_{p|z}$ is the spanwise surface pressure integral length scale, and is relevant to get a final approximation to Π_p . Unfortunately, as discussed in the introduction, $\Lambda_{p|z}$ is technically impossible to quantify in this case due to the unavailability of transducers thin enough for these serrations, and is therefore left out of this discussion.

VERTICAL INTEGRAL LENGTH SCALE

The vertical integral length scale results, shown in figure 5.14, are calculated as ([5.37])

$$\Lambda_{y|vv}(y) = \int_{0.2\delta}^{2\delta} R_{vv}(y, \xi_y) d\xi_y, \quad (5.5)$$

where

$$R_{vv} = \frac{\overline{v(y) v(y + \xi_y)}}{\sqrt{\overline{v(y) v(y + \xi_y)}}} \quad (5.6)$$

is the correlation coefficient between the signal of v at the wall-normal location y , and that separated by ξ_y in the wall-normal direction. The resulting R_{vv} values for the serrated streamwise location $x/2h = 1$ are presented in figure 5.15 for reference. This results

in a more complex prediction of the constructive and destructive interference of the local scattered pressure waves along the edges.

Overall, a wall-normal variation in $\Lambda_{y|vv}$ of around 3 mm is experienced for all cases, showing similar values between the streamwise measurement locations and an overall increase in integral length scale at locations further from the wall, indicating an increase in turbulent structure size as expected. A similar trend has been observed in [5.38]. There is a difference of values between the cases along the same wall-normal location of no more than 0.5 mm, with the downstream location initially showing lower values, and exhibiting a crossover at $y/\delta = 0.6$. The $x/2h = 0.5$ location follows the upstream location, either serrated or unserrated, more closely. This similarity suggests that streamwise surface pressure variations are weakly driven by this factor.

CONVECTION VELOCITY AND MEAN VELOCITY SHEAR

A wide variety of methods have been proposed to approximate the convection velocity, a good summary of which is given in [5.39]. In the present study a spectral approach is taken based on [5.40] and used in [5.4] to obtain the surface pressure convection velocity. It is obtained using the streamwise cross-spectral density results and evaluating the slope of the phase spectrum over a two-point measurement separation ξ_x , as

$$u_c(y) = 2\pi\xi_x \frac{df}{d\phi(y, f, \xi_x)}, \quad (5.7)$$

where $\phi \equiv \arctan \left[\text{Im}(P_{u|12}) \text{Re}(P_{u|12})^{-1} \right]$ and $P_{u|12}$ the streamwise velocity component cross-spectral density between streamwise locations x_1 and $x_2 = x_1 + \xi_x$. Traditionally, it has been troublesome to obtain the velocity information at x_2 since velocity probes located at x_1 disturb the flow downstream. Since a non-intrusive measurement technique is adopted in the current study, a wide range of ξ_x is attainable, allowing a deeper evaluation of its dependence on ϕ .

Since ξ_x is wall-parallel, the streamwise component of the convection velocity, u_c , is evaluated instead of the convection velocity magnitude, U_c . Since at the chosen locations the wall-parallel component is largely dominant, the wall-normal and spanwise component contributions to the convection velocity are considered negligible, and $u_c \rightarrow U_c$. Though for the sake of rigorousness, u_c is indicated.

The phase, $\phi = \phi(y, f, \xi_x)$ is dependent on the streamwise location, the frequency and the two-point measurement separation. Having a frequency dependence suggests that turbulent structures of different size might convect at different velocities if $df/d\phi$ is not constant. It has nevertheless been previously observed that in similar applications the relation between convection velocity and frequency appears to be negligible ([5.4, 41]). This is confirmed in figure 5.16, which shows a measure of ϕ for $x/2h = 1$ and $y/\delta = 0.9$, and where it is evident that $\phi(y/\delta = 0.9, f, \xi_x)$ varies linearly over f , with a slope that increases with larger ξ_x . Only one case is presented for conciseness, but the linearity of ϕ with respect to the measured range of f has been separately confirmed for other streamwise and wall-normal locations.

Being the result of an arctangent, the phase result varies as $-\pi \leq \phi \leq \pi$. A selective procedure has been applied to remove the discontinuities in ϕ over the presented

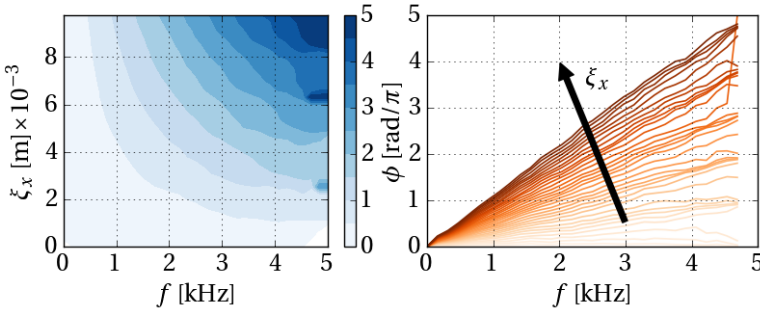


Figure 5.16: Contours of ϕ (left) as a function of frequency and ξ_x . A line plot representation (right) is shown the linear nature of ϕ . Measurement taken at $x/2h = 1$ and $y/\delta = 0.9$.

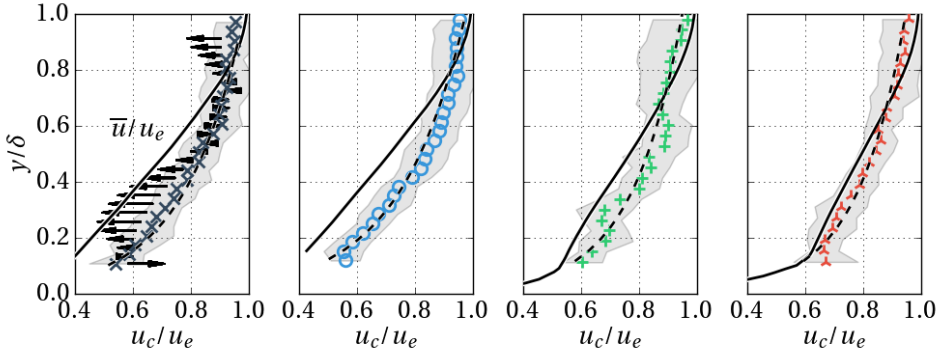


Figure 5.17: Wall-normal convection velocity. From left to right: straight edge (\times), and serrated edge at locations $x/2h = 0$ (\circ), $x/2h = 0.5$ ($+$) and $x/2h = 1$ (\times). Mean u is presented ($-$), as is the log-fitted curve from the convection velocity results ($- -$).

frequency range. The signal coherence is seen to break down first at higher frequencies, and more rapidly for locations nearer the wall and for smaller ξ_x . Once this has happened, naturally the value of ϕ becomes erratic and affects the calculation of u_c by means of its slope. To account for this and keep an accurate calculation of $df/d\phi$, a procedure was applied by which the values of $f(\phi)$ are linearly interpolated starting at $f = 0$ until the coefficient of determination drops below 0.97. The slope is then calculated from the result of the linear interpolation. Cases for which the coherence was so poor that not enough samples over f were employable (less than 25% of those available) were discarded.

The resulting convection velocity, calculated from equation (5.7), is shown in figure 5.17. The marker locations represent the mean of $df/d\phi$ for the different values of ξ_x tested. The standard deviation of the sample per wall-normal location is represented by the gray region around the mean location.

The dashed line represents the mean convection velocity variation over the boundary layer, fitted with least-squares to the boundary layer log-law equation. The convec-

tion velocity is seen to depart slightly from the log-law fit, fact which is highlighted in the left-most plot with horizontal arrows, scaled with the magnitude of the difference between the two values. This difference has a negative maximum at around $y/\delta = 0.3$ and a small positive one at around $y/\delta = 0.7$, becoming negative again at the uppermost region of the boundary layer. A similar behavior is replicated for the rest of the locations. Having established the presented u_c as the mean over a wide range of eddy sizes and events occurring throughout the boundary layer, this departure from the log-law fit might suggest that a tendency for ejection events is experienced at around $y/\delta = 0.3$, and of sweep events for $y/\delta = 0.7$, a discussion of which is presented in [5.40, 42, 43], and is expanded here in section 5.2.2.

The mean flow profile, \bar{u} , is indicated as a solid line in the plots. The convection velocity is greater than \bar{u} below a certain crossover point in the boundary layer. This crossover is located at $y/\delta = 0.8$ over $x/2h = 0$ for both the serrated and straight edge cases, and around $y/\delta = 0.7$ further downstream at $x/2h = 1$. A similar trend of $u_c > \bar{u}$ has been observed in [5.44] for a turbulent boundary layer over a flat plate, and [5.45] for a turbulent mixing layer. The degree of difference seen here is larger than that observed by [5.44], and may be attributed to conditional differences between the two cases, possibly driven by the adverse pressure gradient in the present one. This assumption is supported by the closer match in the downstream location, where, as it was previously discussed, the boundary layer shows a better fit to the log-law.

A direct comparison of the convection velocity for the measured streamwise locations for the serrated edge and that of the straight edge is presented in figure 5.18. It can be seen that the trend follows the one observed for the mean velocity in section 5.2.1, where the velocity near the wall exhibits an increasing as it moves downstream.

The square of the mean velocity vertical shear factor of equation (5.4) is presented in figure 5.19, where the most downstream measurement location $x/2h = 1$ exhibits the lowest values throughout the boundary layer, followed by $x/2h = 0.5$. A decrease of about 1 s^{-2} in the maximum value is observed moving downstream between the different measurement stations.

The last remaining velocity dependent factor in equation (5.4) is $[\bar{v}/u_c]^2$, which is presented in figure 5.20. A significant difference is observed between the measurements at $x/2h = 0$ and the other streamwise locations. This is due to the wall-parallel flow at the location $x/2h = 0$ encountering either the surface of the serrations at approximately an angle of 11° or the flow convecting from the opposite side of the airfoil (with a similar effect). This interaction causes the flow to gain upward momentum relative to the direction parallel to the airfoil surface, increasing the value of \bar{v} . At the downstream measurement locations, the flow at the edge remains instead relatively invariant in the v component, and thus the value of $[\bar{v}/u_c]^2$ becomes driven by the denominator, which is also several times larger than \bar{v} . The measurement of this factor at $x/2h = 1$ is less than half than that of the measurement at $x/2h = 0.5$. As expected, at $x/2h = 0$ the measurement is similar for both the serrated and unserrated cases.

REYNOLDS STRESSES, AND SWEEP AND EJECTION EVENTS

The Reynolds stress, evaluated from a quadrant analysis, can give valuable information on turbulent structures that convect in the boundary layer. This information is also rel-

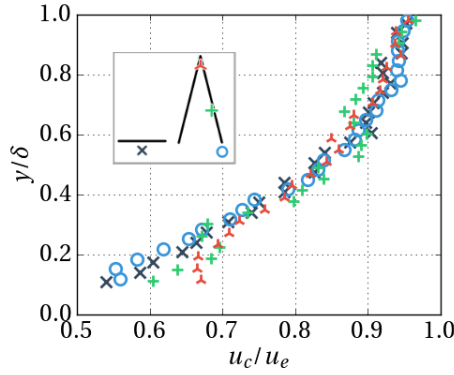


Figure 5.18: Comparison of the convection velocity for the straight edge and the streamwise measurement locations of the serrated case.

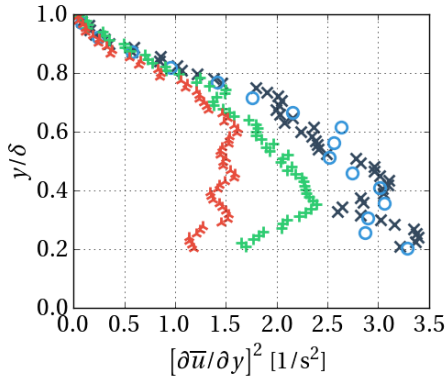


Figure 5.19: The square of the vertical shear of the mean velocity.

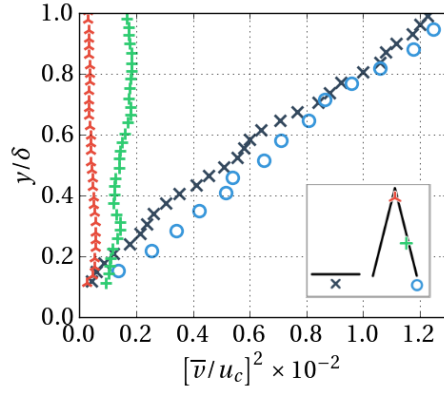


Figure 5.20: The $[\bar{v}/u_c]^2$ factor of equation (5.4).

event as it may provide further understanding of surface pressure peak events. In [5.4], a relational approach between simultaneous pressure peak measurements on the surface is made along with turbulence fluctuation measurements in the boundary layer. Conclusions in their observations indicate that, near the wall, events occurring in the IV quadrant are strongly correlated to surface pressure peaks, and at regions further away from it (near or beyond δ) the II quadrant events appear to contribute more. Separately, [5.43] find that sweep events are correlated with positive pressure peaks on the surface, and conversely, ejection events are correlated with negative pressure pressure peaks. In a quadrant plot, the II quadrant is associated to ejection events, and the IV quadrant to sweep events.

For the purpose of evaluating the Reynolds stress variation over the boundary layer, figure 5.21 shows the values of $-u'v'$ for the measured locations. The Reynolds stress values for all streamwise locations reduce quite well to zero at the measured y/δ location.

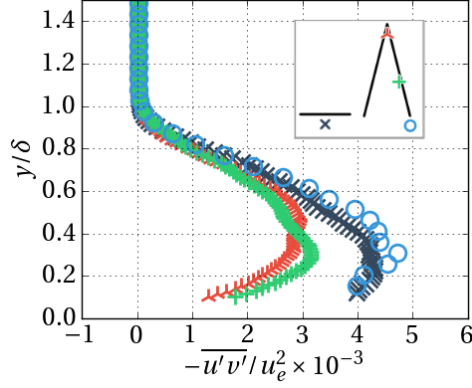


Figure 5.21: Wall-normal profiles of $-\overline{u'v'}$ at trailing edge locations.

5

The downstream serration locations at $z/\lambda = 0$ and 0.25 show a noticeably different behavior than for $x/2h = 0$, exhibiting much lower values at their maxima, reaching about $-\overline{u'v'}/u_e^2 \approx 3 \times 10^{-3}$, or about two-thirds of that which is measured at $x/2h = 0$. A similar observation has been made in [5.5].

In order to inspect the correlation of the velocity component fluctuations and perform a relational analysis to the expected surface pressure events, a series of quadrant analysis plots are shown in figure 5.22. Kernel density estimation (kde) contours for the entire time series are shown to more clearly indicate the relational trends observed between the two component fluctuations over the four quadrants. The hyperbola lines $|u'v'| = -6\overline{u'v'}$ are presented, above which are $u'v'$ events that are 6 times larger than the mean Reynolds shear stress ([5.46, 47]). The choice of the factor 6 is made to match that used in [5.4]. In order to avoid overpopulating the plots, only events occurring outside of the $-6\overline{u'v'}$ limit are shown. The measurements over the straight edge are omitted for brevity, but are separately confirmed to be very similar to the measurements of the serrated case at $x/2h = 0$.

As is expected from the observations made on figure 5.21, away from the wall, at $y/\delta = 0.9$, the magnitude of both u' and v' is reduced. The events are also less correlated, indicated by the kde exhibiting a more circular footprint.

At $y/\delta = 0.6$ and below, the fluctuation components show an anticorrelation between u' and v' , indicated by an elongated kernel density distribution towards the II and IV quadrants. A larger range in the u' direction is present, evidenced by the kde being generally more slanted towards the u' axis. This pattern was also observed in [5.4], and is supported by the larger u_{rms} magnitude observed above. There is additionally a marked existence of events having a magnitude bias towards the II quadrant. Most events are nevertheless seen clustered in low values at the IV quadrant, as suggested by the location of the kde peak.

The fluctuations at $y/\delta = 0.3$, remain more evenly concentrated between quadrants II and IV, both in the location of the kde peak, and in its distribution. A slightly larger range for u' and v' is exhibited. This is expected, as this is the rough location where the

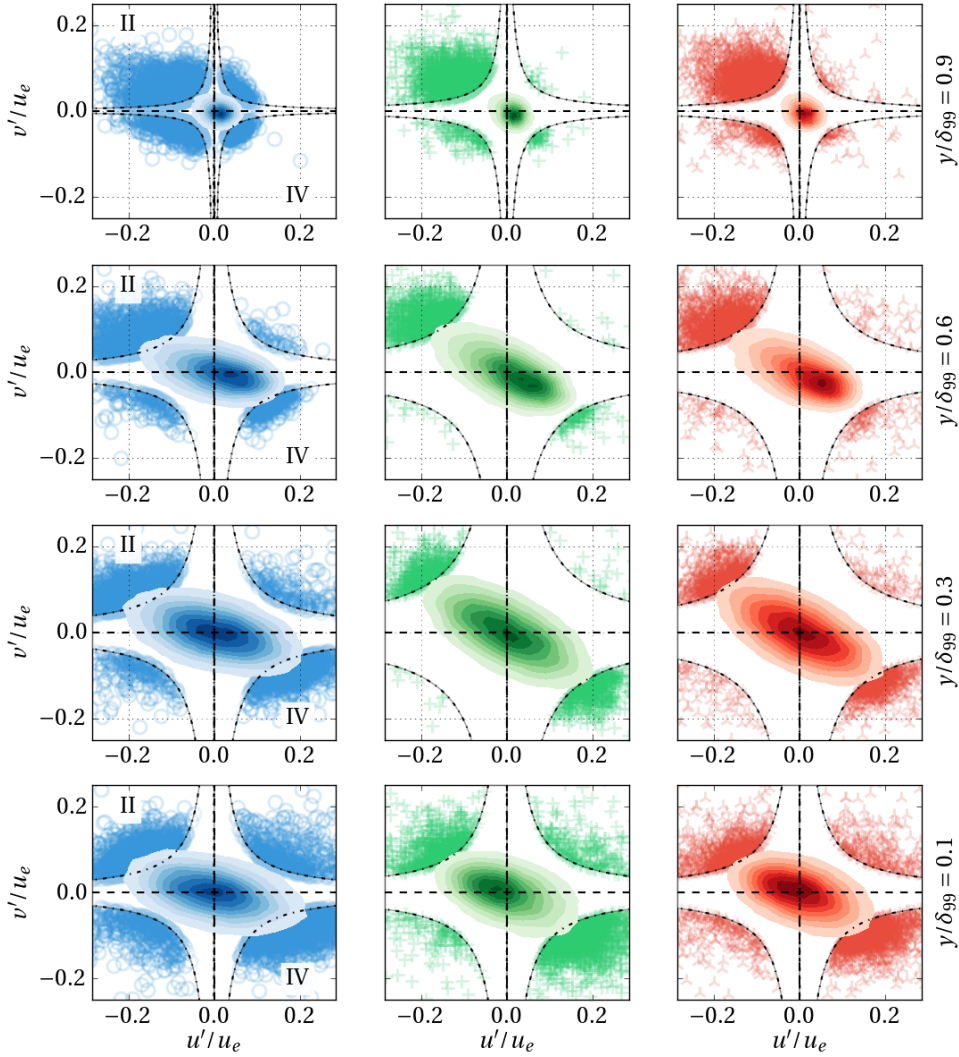


Figure 5.22: Distribution of u' and v' for different wall-normal locations. A kde contours are shown. The hyperbolas correspond to $|u'v'| = -6\overline{u'v'}$ and only events that are larger than this limit are shown to avoid clutter. From left to right, \circ : serration vertex at $x/2h = 0$; $+$: serration edge at $x/2h = 0.5$; \wedge : serration tip at $x/2h = 1.0$.

rms maxima were observed in section 5.2.1, as well as from the observations made of figure 5.21.

The measurements nearest to the wall show slightly decreased activity with respect to the mid-boundary layer locations, especially in the wall-normal direction. This is again expected from the observed rms results discussed before. A slight shift in the most-likely event location for $x/2h = 0.5$ is observed, indicated by a bias in the kde peak towards the

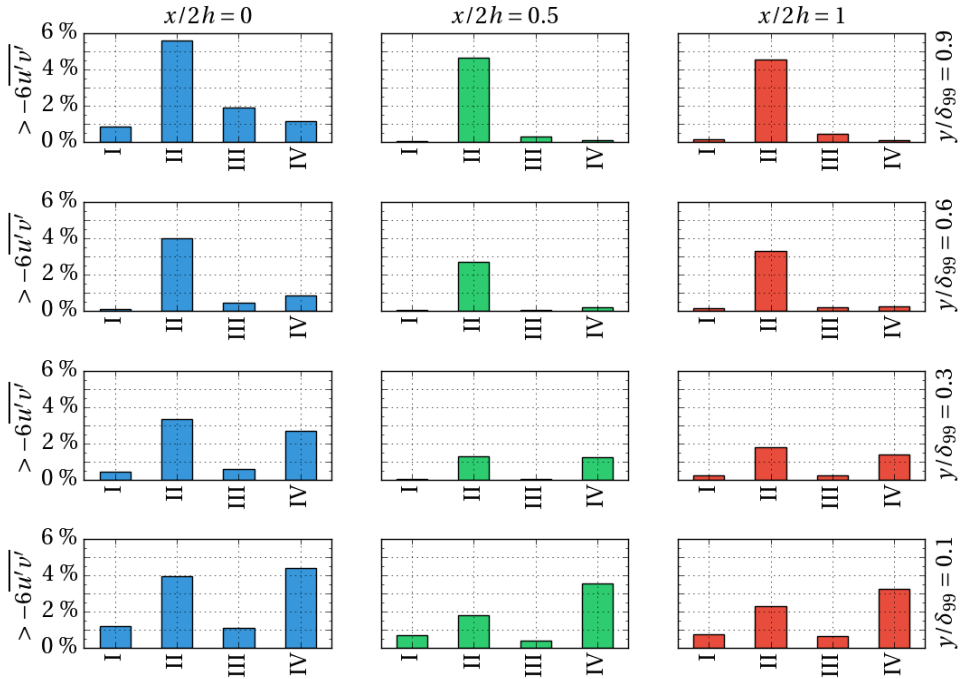


Figure 5.23: Percentage of events with $|u'v'| > -6u'v'$ occurring at each quadrant, for the different streamwise and wall-normal locations.

II quadrant. At $x/2h = 1$ this behavior is also present but more moderate, and at $x/2h = 0$ the peak remains instead centered at the origin.

To simplify the observation of high intensity events, figure 5.23 is provided, showing the percentage of the total events that comply with $|u'v'| > -6u'v'$. In the current results, such events are present for all wall-normal locations, but at $y/\delta > 0.6$ they are significantly biased towards the II quadrant, thus contributing to both high and low pressure peaks at the surface. Closer to the wall, events are more evenly distributed between quadrants II and IV. Overall, there is a decrease of high intensity events by up to around 2% moving downstream, which is beneficial for noise reduction as it indicates the convection of less intense surface pressure events at locations close to most of the serration edge. This further implies that each location of the serration edge will contribute differently to noise reduction.

In relation to the observed variance in the convection velocity of figure 5.17, the measurements at $y/\delta = 0.6$ indicate that most events happen in the IV quadrant, suggesting a larger number of sweep events (although events are of lower intensity than events in the II quadrant). This goes in line with the higher convection velocity observed at around this height with respect to the log-law behavior. At around $y/\delta = 0.3$, where the convection velocity is lower than the log-law fit, the peak of the kde is well centered, indicating no event bias to either the II or IV quadrants. This is also true for the predom-

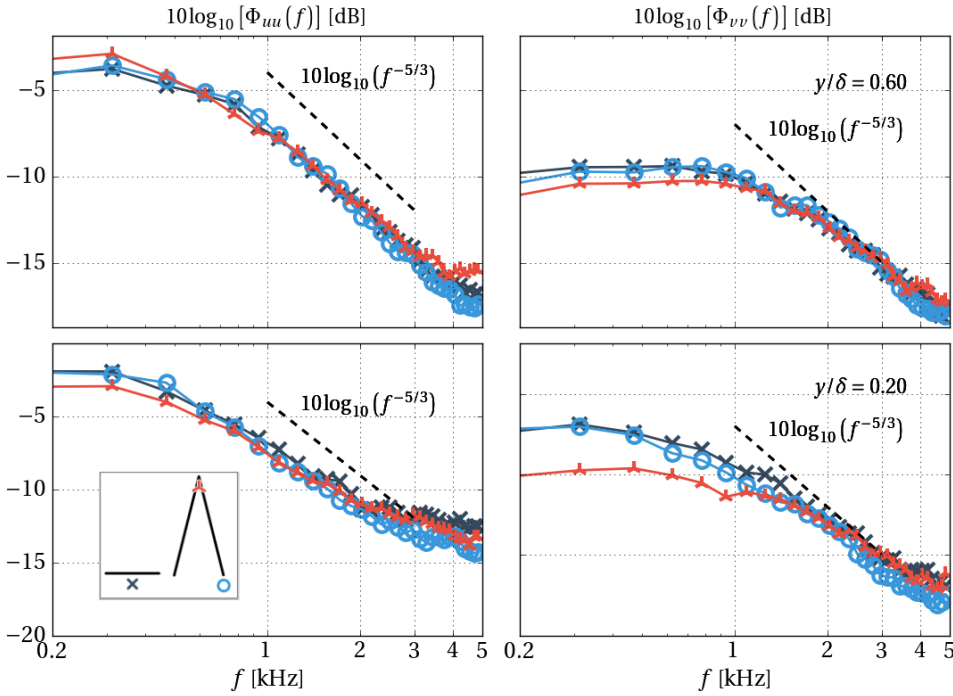


Figure 5.24: The flow frequency dependent auto-spectra of the wall-parallel component (left) and wall-normal component (right) at two wall-normal locations.

inance of high intensity events, which are also well distributed between the II and IV quadrants. This symmetry inhibits an explanation of the observed convection velocity anomaly based on the Reynolds shear measurements, requiring further investigation.

TURBULENT FLOW SPECTRA

The final factor of equation (5.4) that is evaluated is the wavenumber auto-spectra. To evaluate the results, the frequency dependent auto-spectra is provided in figure 5.24 for both the streamwise and wall-normal components. As observed in the quadrant analysis above, the fluctuations over u have a larger range, behavior which is reflected here, evidenced by the larger energy of Φ_{uu} compared to Φ_{vv} , which is about 7 dB higher at the lowest frequencies presented. Both spectra follow the Kolmogorov $-5/3$ decay well until higher frequencies are reached. This is expected because of limitations in the temporal resolution achieved by the PIV signal-to-noise ratio between the instantaneous flow fields, which settles the maximum measurable frequency to about $3/4$ of the Nyquist frequency ([5.43]). It appears to be more sensitive at lower boundary layer location presented, $y/\delta = 0.2$, reaching a plateau at around $f = 3$ kHz for Φ_{uu} . Overall, the results between the streamwise cases are very similar. The most downstream location does present lower energies in frequencies below 1 kHz for both components, with Φ_{vv} showing up to a 3 dB loss.

The pre-multiplied wavenumber spectra is presented in figure 5.25. Large overall

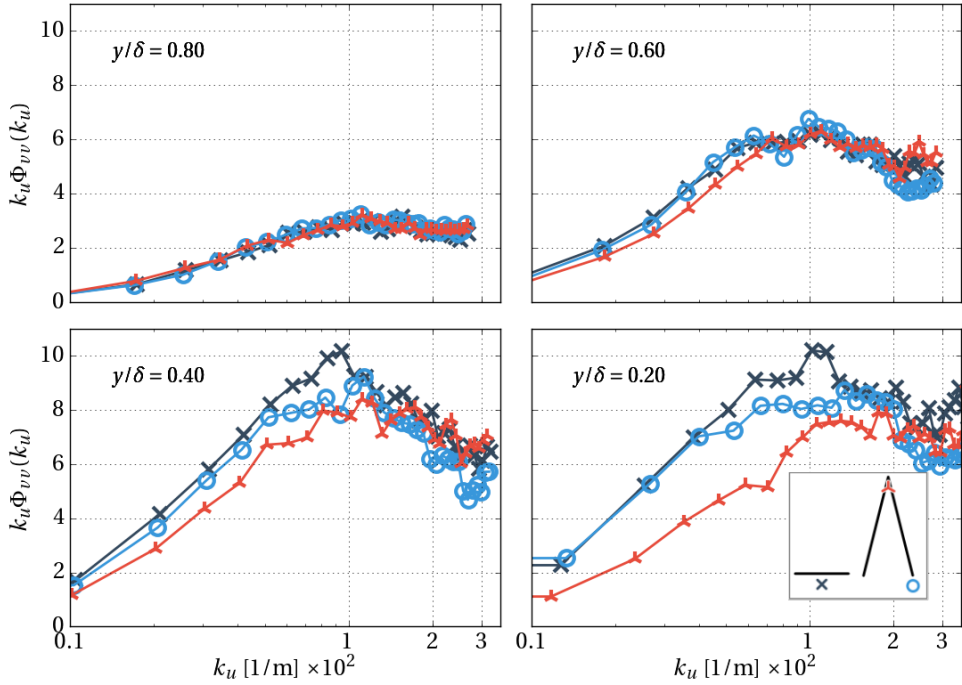


Figure 5.25: The flow wavenumber dependent pre-multiplied auto-spectra of the wall-normal component at four wall-normal locations.

level differences are seen between the different wall-normal locations, reducing greatly for regions in the upper boundary layer. All the streamwise locations exhibit peaks located close to $k_u \approx 100 \text{ m}^{-1}$. As expected from the frequency dependent auto-spectra of figure 5.25, the downstream location of the serrated edge shows lower levels, especially evident at around $y/\delta = 0.4$ and below for wavenumbers under $k_u \approx 200 \text{ m}^{-1}$. The k_u location of the peak for the downstream measurement appears to suffer a slight increase to around 150 m^{-1} . A variation in the wavenumber suggests changes in the intensity and spectral shape of the acoustic emissions due to modifications in the turbulent structure size and convection velocity. In the present case the most contributing change appears to be in the intensity, with small variations in k_e across the serration edge.

SUMMARY OF THE FLOW PARAMETER OBSERVATIONS

The different elements of equation 5.4 that are attainable from the hydrodynamic measurements have been considered in the previous sections. Observations clearly indicate that the flow in the boundary layer changes as it convects past the different edge locations of the serration.

In summary, the following findings have been discussed:

- the overall thickness of the boundary layer is reduced as the flow evolves beyond the adverse pressure gradient that is present between the end of the airfoil and the

serration surface,

- the vertical integral length remains similar along the boundary layer height between downstream locations,
- the convection and mean velocity suffer changes, mostly seen below $y/\delta = 0.4$, with downstream locations exhibiting higher velocity,
- the shear is reduced downstream as a consequence of this,
- the factor \bar{v}/u_c becomes is hard to evaluate, given the relatively large downward motion of the flow with respect to the boundary layer line at $x/2h = 0$, but the downstream location $x/2h = 1$ shows slightly reduced levels with comparison to $x/2h = 0.5$,
- the quadrant analysis reveals the presence of turbulent structures in the boundary layer that lead to high pressure peaks on the surface, but suggests a reduction of these events downstream,
- the auto-spectra of the flow indicates that below a certain frequency the downstream location over the serration tip exhibits less energy than the upstream location for both the serrated case and the straight edge case,
- peaks in the wavenumber auto-spectra are present around 100 m^{-1} , with a slight increase seen for the tip location near the surface to about 150 m^{-1} .

The boundary layer integrated results for the different factors are calculated in table 5.3 for the different streamwise locations. The product of these factors is also presented, excluding the \bar{v}^2/u_c^2 factor due to the the previously discussed discrepancy in conditions between the $x/2h = 0$ and other streamwise locations that is unclear how to account for. There is a noticeable reduction in the levels between the streamwise locations, driven primarily by the shear factor and modified throughout by the thinning boundary layer. This implies a change in the surface pressure intensity, driven by the convecting flow over it. At the same time, this fact suggests that an accurate calculation of the noise emitted at the serration edges requires a streamwise dependent input of the surface pressure. This limits the direct applicability of Green's function as it is done in [5.6] in the case of serration-retrofitted airfoils. The downstream change in the surface pressure appears nevertheless to be beneficial for the pursuit of lower noise emissions.

Proof that the serrations used in the current setup reduce noise when compared to the unmodified airfoil is provided in the next section. Although the hydrodynamic investigation shows that beneficial changes in the flow and surface pressure are prescribed by the introduction of the serrations, their modification of the scattering efficiency remains a credible and additional driver in the mechanism of noise reduction.

5.2.3. BEAMFORMING RESULTS

In order to assess the influence of the presence of serrations and the flow velocity on the emitted noise levels, the acoustic data from the microphone array was utilized. A set of flow speeds between 30 m/s and 40 m/s was used for the acoustic measurements, within

Table 5.3: Boundary layer integrated values for the different elements of equation (5.4)

Tailing edge	$x/2h$	$\Lambda_{y vv}$ [mm]	u_c [m/s]	$(\partial u / \partial y)^2$ [s ⁻²]	\bar{v}^2 / u_c^2 $\times 10^{-2}$	Product ¹
Straight	0.0	23.3	6.6	15.1	2.1	2.3
Serrated	0.0	23.8	6.7	14.6	1.3	2.3
Serrated	0.5	21.6	6.0	10.1	0.29	1.3
Serrated	1.0	19.2	5.8	7.4	0.06	0.8

¹ Ommitts \bar{v}^2 / u_c^2

which the airfoil self-noise was well distinguishable from the background noise. While these flow velocities are too high to capture the time-resolved flow data with the current PIV system, it will be shown that the trends recorded between the serrated and the unserrated airfoils are consistent within the 10 m/s flow velocity range that was tested, and an extension of the conclusions here obtained to 20 m/s is, thus, achievable.

The source plots for the aforementioned flow velocities and frequencies between 1 to 5 kHz are gathered in figure 5.26, for both the airfoil with straight trailing edge and the one including serrations. It can be observed that the strongest noise sources are located at the trailing edge in all cases, as expected. In these acoustic images it can readily be noted that higher velocities produce higher noise levels and that the serrations offer quieter results for all cases with respect to the straight trailing edge case in this frequency range.

The frequency spectra obtained from the beamforming source plots for $U_\infty = 30, 35$ and 40 m/s are depicted in figure 5.27. The results are shown in third-octave bands to better distinguish relevant differences between the two cases. The largest noise reductions were observed between 1 to 2 kHz.

The noise emission differences observed between the straight and serrated edges reflect those in literature, although none have used the same serration geometry, flow settings and airfoil combination. Results in [5.3] show frequency-dependent reductions ranging from 3 dB to 13 dB on a serrated flat plate which experienced vortex shedding. This flow situation was not present in the current case. In [5.8], a maximum 5 dB reduction is observed for a case with a highly cambered airfoil and serrations with a flap angle towards its bottom side. The same reduction level is observed in [5.48] and [5.9]. These studies have used single microphones or linear arrays. Acoustic beamforming is used in [5.49], where serrations also reduced noise by approximately 5 dB.

The relation between the SPL and the flow velocity, and serration noise reduction can be observed more clearly in figure 5.28, where the integrated noise levels (for frequencies between 1 and 5 kHz) obtained in the acoustic images in figure 5.26 are plotted against the flow velocity for both cases. An approximately constant SPL difference of around 6 dB is present in all cases. Given the characteristic length of the airfoil tested and the dominance of low frequency noise in the spectra, the noise source can be considered as compact [5.50]. The expected 5th power law dependence of the acoustic power with the flow speed ([5.50–52]) is also included in figure 5.28, showing a close agreement with both cases. These observations suggest that the noise reduction trend remains signifi-

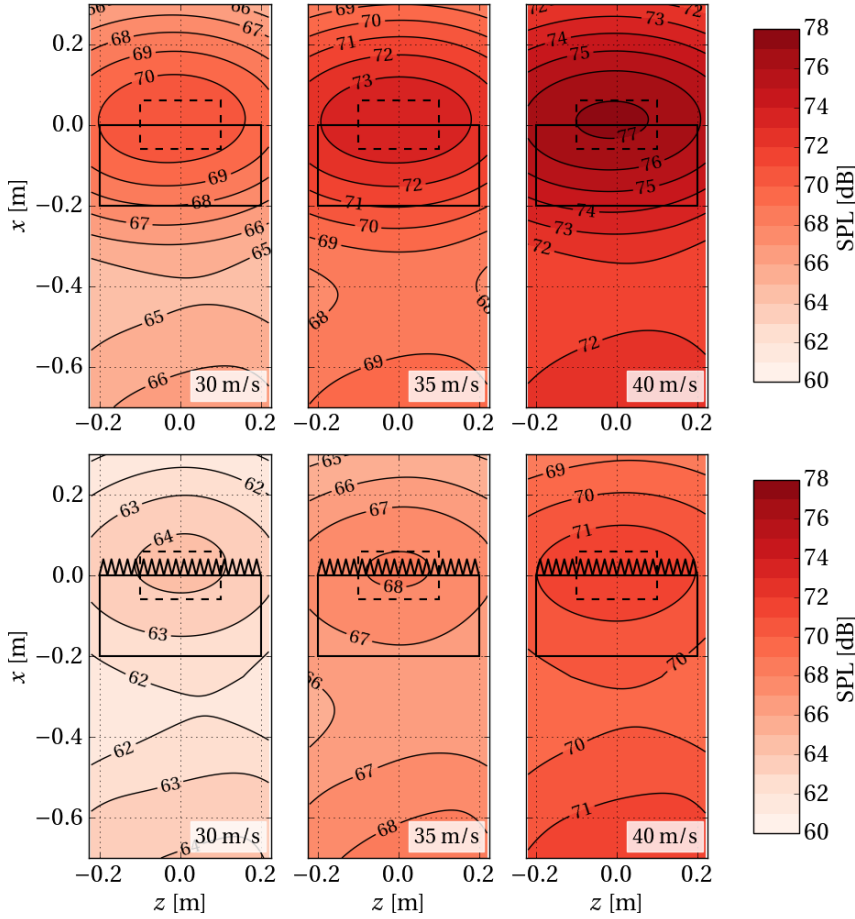


Figure 5.26: Acoustic source maps obtained for the airfoil with the straight edge (top) and with the serrated edge (bottom) at the freestream velocities indicated in the figures and frequencies between 1 and 5 kHz. The airfoil location is marked by the solid rectangle and the integration area by the dashed rectangle.

cant at the 20 m/s flow speed.

5.3. CONCLUSIONS

Time-resolved flow data was acquired with PIV over the unmodified and serration-retrofitted trailing edges of a NACA 0018 airfoil at zero-lift. Acoustic measurements were further performed to characterize the noise emissions from both trailing edges, by which the noise reduction benefits of the retrofitted serrations were confirmed, showing reductions of up to 6 dB with respect to the unmodified configuration.

In order to evaluate the role of the flow in this reduction, statistics have been presented for both configurations and, by means of the TNO-Blake model, were used to

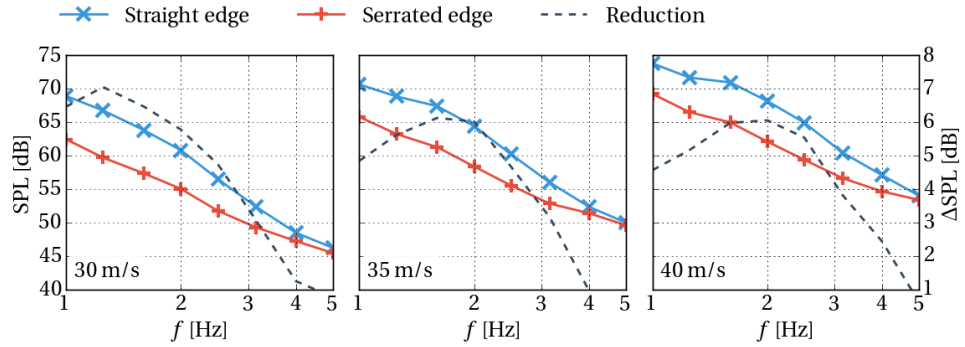


Figure 5.27: Acoustic frequency spectra of the airfoil with straight and serrated edges. The freestream velocity is indicated in the plots. The obtained SPL reduction in decibels is presented in the right vertical axis and plotted with the discontinuous line.

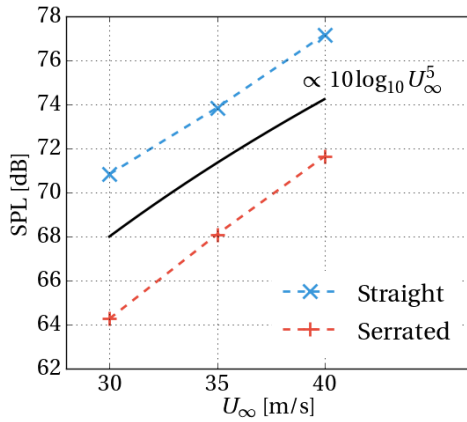


Figure 5.28: Velocity dependence law (—) for trailing edge noise emissions compared to the measured noise from the airfoil with straight and serrated edges.

form a qualitative approximation of the unsteady surface pressure near the edges. This approach has been favored, as a technical mean by which to directly evaluate the latter on thin serrations is absent.

While at the root of the serrations the flow remains unmodified, considerable changes are experienced as it convects downstream. Parameters of the TNO-Blake model were evaluated, and results indicate that changes in the flow, as it convects downstream, lead to lower intensities in the unsteady surface fluctuations. It is found that these changes were mostly driven by the shear and the boundary layer thickness, which becomes thinner at downstream locations. Additionally, the spectra of the wall-normal component showed a decrease in energy in the lower frequencies and wavenumbers for the location furthest downstream over the serration tooth. A quadrant analysis was further presented, and events known to be related to high intensity surface pressure peaks were

shown to be less prominent downstream.

These findings reveal that, at least when retrofitted on an airfoil, the mechanism of noise reduction by serrations is aided by beneficial changes in the flow that convects over its edges. The variation of the pressure fluctuations in the streamwise direction, and of the flow parameters reported, is such that the local scattered pressure waves might vary along the serration edges. While [5.53] suggests a geometric dependence of the constructive and destructive interference of the local scattered pressure waves along the edges, this variation would make the prediction more complex.

BIBLIOGRAPHY

- [5.1] C. Arce León, R. Merino-Martínez, D. Ragni, F. Avallone, and M. Snellen, *Boundary layer characterization and acoustic measurements of flow-aligned trailing edge serrations*, *Experiments in Fluids* **57**, 182 (2016).
- [5.2] L. E. Jones, N. D. Sandham, and R. D. Sandberg, *Acoustic Source Identification for Transitional Airfoil Flows Using Cross Correlations*, *AIAA Journal* **48**, 2299 (2010).
- [5.3] D. Moreau and C. Doolan, *Noise-Reduction Mechanism of a Flat-Plate Serrated Trailing Edge*, *AIAA Journal* **51**, 2513 (2013).
- [5.4] T. P. Chong and A. Vathylakis, *On the aeroacoustic and flow structures developed on a flat plate with a serrated sawtooth trailing edge*, *Journal of Sound and Vibration*, **1** (2015).
- [5.5] M. Gruber, *Airfoil noise reduction by edge treatments*, *Ph.D. thesis*, University of Southampton (2012).
- [5.6] M. S. Howe, *Noise produced by a sawtooth trailing edge*, *The Journal of the Acoustical Society of America* **90**, 482 (1991).
- [5.7] M. Gruber, P. Joseph, and T. Chong, *On the mechanisms of serrated airfoil trailing edge noise reduction*, in *17th AIAA/CEAS Aeroacoustics Conference (32nd AIAA Aeroacoustics Conference)*, Vol. 2781 (American Institute of Aeronautics and Astronautics, Portland, Oregon, USA, 2011) pp. 5–8.
- [5.8] M. Gruber, P. Joseph, and T. Chong, *Experimental investigation of airfoil self noise and turbulent wake reduction by the use of trailing edge serrations*, in *16th AIAA/CEAS Aeroacoustics Conference* (2010) pp. 1–23.
- [5.9] A. Finez, E. Jondeau, M. Roger, and M. C. Jacob, *Broadband Noise Reduction of a Linear Cascade With Trailing Edge Serrations*, in *17th AIAA/CEAS Aeroacoustics Conference (32nd AIAA Aeroacoustics Conference)* (Portland, Oregon, USA, 2011).
- [5.10] C. Arce León, D. Ragni, S. Pröbsting, F. Scarano, and J. Madsen, *Flow topology and acoustic emissions of trailing edge serrations at incidence*, *Experiments in Fluids* **57**, 91 (2016).

- [5.11] R. D. Sandberg and L. E. Jones, *Direct numerical simulations of low Reynolds number flow over airfoils with trailing-edge serrations*, [Journal of Sound and Vibration](#) **330**, 3818 (2011).
- [5.12] L. E. Jones and R. D. Sandberg, *Acoustic and hydrodynamic analysis of the flow around an aerofoil with trailing-edge serrations*, [Journal of Fluid Mechanics](#) **706**, 295 (2012).
- [5.13] R. Arina, R. Della Ratta Rinaldi, A. Iob, and D. Torzo, *Numerical Study of Self-Noise Produced by an Airfoil with Trailing-Edge Serrations*, in *18th AIAA/CEAS Aeroacoustics Conference (33rd AIAA Aeroacoustics Conference)*, June (American Institute of Aeronautics and Astronautics, Colorado Springs, CO, 2012) pp. 4–6.
- [5.14] A. Fischer, F. Bertagnolio, W. Z. Shen, and J. Madsen, *Noise model for serrated trailing edges compared to wind tunnel measurements*, [Journal of Physics: Conference Series](#) **753**, 022053 (2016).
- [5.15] M. P. Arroyo and C. A. Greated, *Stereoscopic particle image velocimetry*, [Measurement Science and Technology](#) **2**, 1181 (1991).
- [5.16] A. L. Braslow, R. M. Hicks, and R. V. Harris Jr., *Use of grit-type boundary-layer transition trips on wind-tunnel models*, [NASA Technical Note](#) (1966).
- [5.17] C. D. Meinhart and S. T. Wereley, *The theory of diffraction-limited resolution in microparticle image velocimetry*, [Measurement Science and Technology](#) **14**, 1047 (2003).
- [5.18] J. Westerweel, *Fundamentals of digital particle image velocimetry*, [Measurement Science and Technology](#) **8**, 1379 (1997).
- [5.19] F. Stern, M. Muste, M. Beninati, and W. Eichinger, *Summary of experimental uncertainty assessment methodology with example*, Tech. Rep. (Iowa Institute of Hydraulic Research, College of Engineering, The University of Iowa, Iowa City, USA, 1999).
- [5.20] B. Wieneke, *PIV uncertainty quantification from correlation statistics*, [Measurement Science and Technology](#) **26** (2015), 10.1088/0957-0233/26/7/074002.
- [5.21] M. Raffel, C. Willert, and J. Kompenhans, [Springer](#), Experimental Fluid Mechanics (Springer, Berlin, Heidelberg, 2007).
- [5.22] F. F. J. Schrijer and F. Scarano, *Effect of predictorcorrector filtering on the stability and spatial resolution of iterative PIV interrogation*, [Experiments in Fluids](#) **45**, 927 (2008).
- [5.23] T. Mueller, [Aeroacoustic Measurements](#) (Springer Science & Business Media, 2002) p. 313.
- [5.24] S. Pröbsting, M. Zamponi, S. Ronconi, Y. Guan, S. C. Morris, and F. Scarano, *Vortex shedding noise from a beveled trailing edge*, [International Journal of Aeroacoustics](#) **15**, 712 (2016).

- [5.25] A. Brandt, *Noise and vibration analysis: signal analysis and experimental procedures*, second series (John Wiley & Sons, 2011).
- [5.26] Rayleigh, XXXI. *Investigations in optics, with special reference to the spectroscope*, *Philosophical Magazine Series 5* **8**, 261 (1879).
- [5.27] C. C. Pagani, D. S. Souza, and M. A. F. Medeiros, *Slat Noise: Aeroacoustic Beam-forming in Closed-Section Wind Tunnel with Numerical Comparison*, *AIAA Journal* **54**, 2100 (2016).
- [5.28] P. Sijtsma, *SAE Technical Paper*, Tech. Rep. October (National Aerospace Laboratory (NLR), Anthony Fokkerweg 2, 1059 CM Amsterdam, P.O. Box 90502, 1006 BM Amsterdam, The Netherlands, 2010).
- [5.29] R. Amiet, *Correction of open jet wind tunnel measurements for shear layer refraction*, in *2nd Aeroacoustics Conference* (American Institute of Aeronautics and Astronautics, Hampton, Virginia, 1975).
- [5.30] P. Salas and S. Moreau, *Noise Prediction of a Simplified High-Lift Device*, in *22nd AIAA/CEAS Aeroacoustics Conference* (American Institute of Aeronautics and Astronautics, Reston, Virginia, 2016).
- [5.31] P. R. Spalart and J. H. Watmuff, *Experimental and numerical study of a turbulent boundary layer with pressure gradients*, *Journal of Fluid Mechanics* **249**, 337 (1993).
- [5.32] J.-L. Balint, J. M. Wallace, and P. Vukoslavcevic, *The velocity and vorticity vector fields of a turbulent boundary layer. Part 2. Statistical properties*, *Journal of Fluid Mechanics* **228**, 53 (1991).
- [5.33] M. Drela, *XFOIL: An Analysis and Design System Low Reynolds Number Aerodynamics and Transition*, edited by T. J. Mueller, Lecture Notes in Engineering (Springer Berlin Heidelberg, Berlin, 1989).
- [5.34] Y. Nagano, T. Tsuji, and T. Houra, *Structure of turbulent boundary layer subjected to adverse pressure gradient*, *International Journal of Heat and Fluid Flow* **19**, 563 (1998).
- [5.35] J.-H. Lee and H. J. Sung, *Effects of an adverse pressure gradient on a turbulent boundary layer*, *International Journal of Heat and Fluid Flow* **29**, 568 (2008).
- [5.36] W. K. Blake, *Mechanics of Flow-Induced Sound and Vibration V2: Complex Flow-Structure Interactions, Volume 2* (Elsevier Science, 2012) p. 567.
- [5.37] M. Kamruzzaman and T. Lutz, *On the Length Scales of Turbulence for Aeroacoustic Applications*, AIAA Conference , 05 (2011).
- [5.38] M. Kamruzzaman, T. Lutz, A. Ivanov, A. Herrig, W. Wuerz, E. Kraemer, W. Würz, and E. Krämer, *Evaluation of Measured Anisotropic Turbulent Two-Point Correlation Data for the Accurate Prediction of the Turbulence Noise Sources*, *15th*

- AIAA/CEAS Aeroacoustics Conference (30th AIAA Aeroacoustics Conference) , 11 (2009).
- [5.39] N. Renard and S. Deck, *On the scale-dependent turbulent convection velocity in a spatially developing flat plate turbulent boundary layer at Reynolds number*, *Journal of Fluid Mechanics* **775**, 105 (2015).
 - [5.40] G. Romano, *Analysis of two-point velocity measurements in near-wall flows*, *Experiments in Fluids* **20**, 68 (1995).
 - [5.41] O. Stalnov, P. Chaitanya, and P. F. Joseph, *Towards a non-empirical trailing edge noise prediction model*, *Journal of Sound and Vibration* , 1 (2016).
 - [5.42] P. Krogstad, J. H. Kaspersen, and S. Rimestad, *Convection velocities in a turbulent boundary layer*, *Physics of Fluids* **10**, 949 (1998).
 - [5.43] S. Ghaemi and F. Scarano, *Turbulent structure of high-amplitude pressure peaks within the turbulent boundary layer*, *Journal of Fluid Mechanics* **735**, 381 (2013).
 - [5.44] C. Atkinson, N. A. Buchmann, and J. Soria, *An Experimental Investigation of Turbulent Convection Velocities in a Turbulent Boundary Layer*, *Flow, Turbulence and Combustion* **94**, 79 (2015).
 - [5.45] O. R. H. Buxton and B. Ganapathisubramani, *PIV measurements of convection velocities in a turbulent mixing layer*, *Journal of Physics: Conference Series* **318**, 052038 (2011).
 - [5.46] J. Kim, P. Moin, and R. Moser, *Turbulence statistics in fully developed channel flow at low Reynolds number*, *Journal of Fluid Mechanics* **177**, 133 (1987).
 - [5.47] S. S. Lu and W. W. Willmarth, *Measurements of the structure of the Reynolds stress in a turbulent boundary layer*, *Journal of Fluid Mechanics* **60**, 481 (1973).
 - [5.48] W. Qiao, L. Ji, K. Xu, and W. CHENG, *An Investigation on the near-field turbulence and radiated sound for an airfoil with trailing edge serrations*, *19th AIAA/CEAS Aeroacoustics Conference* , 1 (2013).
 - [5.49] A. Fischer, F. Bertagnolio, W. Z. Shen, and J. Madsen, *Wind Tunnel Test of Trailing Edge Serrations for the Reduction of Wind Turbine Noise*, in *Inter-noise 2014* (Melbourne, Australia, 2014) pp. 1–10.
 - [5.50] N. Curle, *The Influence of Solid Boundaries upon Aerodynamic Sound*, *Proceedings of the Royal Society A: Mathematical, Physical and Engineering Sciences* **231**, 505 (1955).
 - [5.51] J. E. F. Williams and L. H. Hall, *Aerodynamic sound generation by turbulent flow in the vicinity of a scattering half plane*, *Journal of Fluid Mechanics* **40**, 657 (1970).
 - [5.52] M. R. Fink, *Noise Component Method for Airframe Noise*, in *Journal of Aircraft*, Vol. 16 (1979) pp. 659–665.
 - [5.53] B. Lyu, M. Azarpeyvand, and S. Sinayoko, *A Trailing-Edge Noise Model for Serrated Edges*, in *21st AIAA/CEAS Aeroacoustics Conference* (AIAA, Dallas, Texas, 2015).

6

EFFECT OF TRAILING EDGE SERRATION-FLOW MISALIGNMENT ON AIRFOIL NOISE EMISSIONS

When the well's dry, we know the worth of water

Benjamin Franklin, *Poor Richard's Almanac*

*It isn't pollution that's harming the environment.
It's the impurities in our air and water that are doing it.*

Dan Quayle

An increase in noise beyond a certain frequency has been hypothesized to be caused by the misalignment of the serrations with the flow. This assumption is here investigated by observing the near-edge boundary layer and correlating it with the measured noise increase. The acoustic crossover frequency is analyzed with regard to a Strouhal number, and its relationship to airfoil incidence and freestream velocity is described.

The contents of this chapter have been adapted from Arce León *et al.* [6.1].

WHILE IT HAS BEEN DEMONSTRATED consistently that trailing edge serrations are able to reduce turbulent boundary layer-trailing edge noise (TBL-TE noise) in wind tunnel measurements, as discussed in previous chapters, an increase in noise beyond a certain frequency, called the crossover frequency, has also been observed ([6.2–6]). This departure is not foreseen in the analytical models proposed by Howe [6.7], Azarpeyvand *et al.* [6.8], Lyu *et al.* [6.9], and has been ascribed to the increased turbulence intensity observed in the regions between serration teeth ([6.10]).

The increase is particularly evident when the serrations are not aligned with the undisturbed wake flow ([6.4]), given a rotation about the z axis (see figure 6.1). This condition occurs when the airfoil is at incidence, or the serration has a flap angle. The latter has been found to have a more pronounced effect ([6.11], chapter 4), although it can happen at zero values of both, if the airfoil has a camber that results in a downwash at the near-trailing edge wake.

The condition in which the serrated trailing edge is not aligned with the undisturbed wake flow of the unserrated airfoil will be referred to as serration-flow misalignment. In the present work, the degree of misalignment is given in terms of the angle of attack of the airfoil and the flap angle of the serrations.

In the industrial use of trailing edge serrations, such as in wind turbine blades, a certain level of misalignment is expected to occur frequently. Situations such as the wide range of angles of attack at which blade sections are operated, departures from the serration installation or manufacturing tolerances, and the prevalent use of cambered airfoils are a few examples that would lead to serration-flow misalignment. An investigation into how this condition causes an undesired increase in noise is therefore essential.

The frequency above which noise is increased is defined here as the crossover frequency, f_c , following Gruber *et al.* [6.4]. It has been found to be correlated to the boundary layer thickness δ_{99} (for simplicity contracted to δ) and the inflow velocity, U_∞ , by a constant Strouhal number

$$St_c = \frac{f_c \delta}{U_\infty}. \quad (6.1)$$

Gruber *et al.* [6.4] proposed a value of $St_c \approx 1$, found empirically from measurements of several serration geometries, retrofitted on a NACA 6512-10 airfoil, and run at flow velocities ranging from 20 to 70 m/s. Different angles of attack were also tested during this research, ranging from 0° to 15° , but it is not evident in [6.4] at which the results of the Strouhal number are discussed. In [6.12], results are presented for $\alpha = 0^\circ$ and 5° . The experimental measurements of St_c for the different cases collapse around $St_c = 1$ with an uncertainty of 30%. The variance was attributed to the accuracy of the boundary layer estimation, which was not measured for all flow velocities, but was instead calculated using XFOIL. The authors further suggested that the collapse of St_c is expected to improve if spanwise variations of the boundary layer, introduced by the irregularity of the serrated edge, were to be considered.

Besides the pioneering work in [6.10, 13], and later [6.6], no other studies have tried to link the effect of serration misalignment to the important noise increase at high frequencies, despite its critical importance for the effective application of these devices in

industrial settings. Moreover, detailed flow field measurements in addition to acoustic measurements are needed to provide insight into the origin of this effect.

Therefore, in order to confirm the observations in [6.10, 13] regarding the Strouhal number, and to further explore the relation between the hydrodynamic flow behavior and the noise increase, the present study employs a combination of acoustic microphone array measurements and flow field data obtained via particle image velocimetry (PIV).

A NACA 0018 airfoil, with its original straight trailing edge, and fitted with serrations, is experimentally tested at different freestream velocities. Multiple serration flap angles, φ , and angles of attack, α , are prescribed as sources of serration-flow misalignment. Time-averaged flow information is obtained with stereoscopic particle image velocimetry (S-PIV), [6.14], by which the boundary layer near the edge is studied. Its thickness is measured from the straight-edge airfoil and, with the acoustic measurements of f_c , the crossover Strouhal values, St_c , are calculated.

Time-resolved PIV is then employed to inspect the flow dynamic behavior and reveal the link between the turbulent flow in the boundary layer and the far-field acoustic spectra. In particular, parameters such as the streamwise length scales and most energy-bearing eddies are compared near the edge between the straight-edge and the serrated-edge airfoils. The turbulence frequency spectra are then used, in conjunction with the Strouhal number, to identify and locate the source of the high frequency noise increase.

6.1. EXPERIMENTAL SETUP

6.1.1. FLOW FACILITY, MODEL, AND FLOW CONDITIONS

Delft University of Technology's vertical wind tunnel (V-Tunnel), described in 3.1, was used to carry out the experiments.

A NACA 0018 airfoil profile with a chord length $C = 20$ cm and span 40 cm, covering the full width of the test section, was chosen to conduct the study. At the trailing edge, sawtooth serrations produced from a sheet of metal were attached. As in the research outlined in chapters 4 and 5, the tooth length was $2h = 4.0$ cm ($0.2C$), the spanwise width was $\lambda = 2.0$ cm ($\lambda = h$), and the thickness was equal to 1 mm. The airfoil and serration dimensions, along with the definition of α and φ , and the location of the coordinate system, were described earlier in figure 4.1. The chosen dimensions of the serrations follow the recommendations in [6.10], where it is suggested that $2h \gtrsim \delta$, for δ the boundary layer thickness. In the present case $2h \approx 4\delta$ at $\alpha = 0^\circ$, $\varphi = 0^\circ$.

Laminar-to-turbulent transition was forced with a strip of carborundum (nominal size of 0.6 mm) placed at $0.2C$, following guidelines given in [6.15], on both sides of the airfoil. The effectiveness of the device was verified using a remote microphone probe, which indicated a broadband spectrum in the turbulent boundary layer after transition.

Due to the change in slope at the junction between the airfoil and the serrated attachment, two coordinate systems are defined based on the wall-normal of the airfoil surface at the trailing edge and that of the serration surface. Figure 6.1 shows the coordinate system for the serrated attachment at $\varphi = 0^\circ$ (x, y, z) and for the airfoil (x', y', z). For simplicity, the prime will be omitted in the results section and is implicit for the straight edged airfoil case. The velocity components corresponding to these coordinate systems

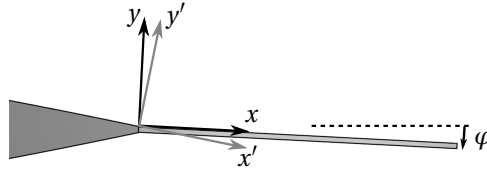


Figure 6.1: Convention used for the coordinate system rotation over the airfoil and serration surfaces.

will be indicated as (u, v, w) , respectively, and are implied to be (u', v', w) for the airfoil measurements.

To investigate different levels of serration-flow misalignment, two serration flap angles and three angles of attack of the airfoil were selected. The flap angles tested were $\varphi = 0^\circ$ and 6° , while the geometric values of the chosen angles of attack were $\alpha_g = 0^\circ, 6^\circ$, and 12° .

Both acoustic phased array and statistical flow field measurements with PIV were conducted spanning the range of flow velocities, 30, 35, and 40 m/s. The resulting chord-based Reynolds number is approximately 400 000, at the lowest velocity. This velocity range yields a sufficient signal-to-noise ratio for the trailing edge noise source above the laboratory background acoustic noise. The flow field measurements were conducted at a freestream velocity of 20 m/s, limited by the PIV system acquisition frequency and the temporal resolution necessary to obtain time-resolved flow information.

6

6.1.2. ACOUSTIC MEASUREMENTS

Acoustic phased array measurements, as outlined in section 3.3, were recorded to estimate the noise modification due to the serrations. The microphone array (figure 3.10), placed at a distance of 1.05 m is also described in section 3.3, and is illustrated in figure 3.11. The test section was designed in such a way that it helped reduce unwanted parasitic noise sources originating from the nozzle and the downstream edges of the side plates.

For applying beamforming to the data from acoustic phased array measurements, a scan grid of potential sound sources is defined. The shear layer effect in the acoustic measurements ([6.16]) was assumed to be negligible due to the small angle ($< 10^\circ$) between the array center and the limits of the scanned area of interest, and the considerably low flow speeds used ([6.17]). Source maps, also known as acoustic images, are obtained by applying the beamforming procedure for all the points in the scan grid. The scan grid covered a rectangle from $z = -0.22$ m to $z = 0.22$ m in the spanwise direction and from $x = -0.3$ m to $x = 0.3$ m in the streamwise direction, relative to the axes in figure 4.1. A distance between grid points of 1 mm is used. The scan grid therefore contained the entire airfoil and was composed of 441×601 grid points. Based on Rayleigh's criterion ([6.18]), the minimum resolvable distance for the highest frequency considered

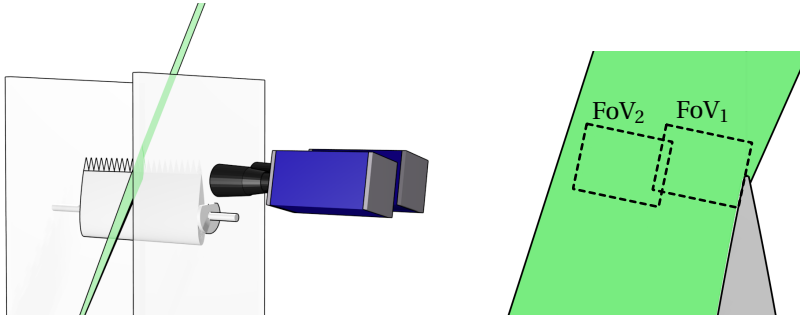


Figure 6.2: Planar PIV measurement setup (left) and resulting FoVs (right).

in this analysis (5 kHz), and considering $c = 340$ m/s, is 0.10 m. The considered spacing between grid points is approximately 100 times smaller than Rayleigh's limit at 5 kHz.

Since trailing edge noise is expected to be a distributed sound source, the beamforming results were integrated over an area extending from $z = -0.1$ m to $z = 0.1$ m and from $x = -0.06$ m to $x = 0.06$ m (see figure 6.4). This area was selected to reduce the noise contribution from extraneous sources, while including a representative part of the trailing edge ([6.19]). The beamforming results in that area were normalized by the integral of a simulated unitary point source located at the center of the integration area evaluated within the same spatial domain ([6.20]). This process was repeated for each frequency of interest in order to obtain the trailing edge noise spectra.

6.1.3. VELOCITY MEASUREMENTS

BOUNDARY LAYER CHARACTERIZATION

Boundary layer profiles and integral parameters for the straight trailing edge airfoil were obtained with low-repetition-rate planar two-component particle image velocimetry (2C-2D PIV). A Quantel Twin BSL 200 laser (Nd:YAG, 200 mJ/pulse) was used for the illumination of the tracer particles (section 3.2) in the measurement plane, which was oriented perpendicular to the airfoil surface and near mid-span (x - y plane).

Two PCO Sensicam QE CCD cameras with sensors of size 1376×1040 px and a pixel-pitch of $6.7 \mu\text{m}/\text{px}$ were used. Both cameras were equipped with Nikon NIKKOR macro objectives of 105 mm focal length and operated at an f-number of $f/8$. Their combined field of view (FoV) of $36 \times 16 \text{ mm}^2$ enclosed the boundary layer at the trailing edge at $\alpha = 12^\circ$. The resulting digital imaging resolution was approximately $S = 65 \text{ px}/\text{mm}$. Figure 6.2 shows a schematic of the setup.

Sets of 300 uncorrelated image pairs were acquired per test case and camera at a frequency of 5 Hz with a laser pulse separation time of $\Delta t = 15 \mu\text{s}$. At a freestream velocity of 20 m/s, this pulse separation is equivalent to a freestream particle displacement of about $\Delta x = 0.31 \text{ mm}$, or $S\Delta x = 20 \text{ px}$.

The acquired image pairs were processed with the LaVision DaVis 8 software using a multi-pass, multi-grid algorithm with window deformation ([6.21]). The final interrogation windows size was set to $16 \times 16 \text{ px}$ and 50% overlap resulting in a physical interrogation window size of $0.24 \times 0.24 \text{ mm}^2$ and vector spacing of $0.12 \times 0.12 \text{ mm}^2$. Uncertainty

Table 6.1: Parameters for the boundary layer characterization PIV measurements.

Parameter	Symbol	Value
Sensor size		1376×1040 px
Single field of view	SFoV	20×16 mm ²
Combined field of view	FoV	36×16 mm ²
F-number	$f/$	8
Focal length		105 mm
Magnification		0.44
Imaging resolution	S	65 px/mm
Laser pulse separation	Δt	15 μ s
Freestream displacement	Δx	≈ 0.31 mm
	$S\Delta x$	≈ 20 px
Light sheet thickness		1.5 mm
Acquisition frequency	f_s	5 Hz
Number of samples		300
Interrogation window size		16×16 px
		0.24×0.24 mm ²
Vector spacing (overlap 50%)		0.12×0.12 mm ²

in the vector fields, at this magnification and flow conditions, is typically driven by cross-correlation uncertainty and peak-locking. With a relatively high magnification of 0.44 and a pixel-pitch of $6.7 \mu\text{m}/\text{px}$, peak-locking is unlikely since the particle image diameter exceeds one pixel ([6.22]). Uncertainty of the cross-correlation between the image pairs is the most critical source of random errors for the current setup. For 2C-2D PIV, this error is typically estimated to be 0.1 px ([6.23]). Following this approach and with a freestream particle displacement of $S\Delta x = 20$ px, the random error on the instantaneous velocity fields is estimated at 0.5% of the freestream velocity. For the given experimental setup and number of samples, the error on the mean velocity reduces to below 0.1% of the freestream velocity. Table 6.1 provides an overview of the experimental parameters for the statistical boundary layer measurements.

TIME-RESOLVED STEREOSCOPIC PIV

For the time-resolved flow field measurements, an S-PIV setup was employed to measure the temporal evolution and statistics of the three velocity components in the x - y plane around the serrations. The flow was seeded as described in the previous section. For illumination, a Quantronix Darwin Duo dual-cavity Nd:YLF high-speed laser was used (2×25 mJ at 1 kHz). Two high-speed Photron Fastcam SA1.1 CMOS high-speed cameras (1024×1024 px, $20 \mu\text{m}/\text{px}$ pixel-pitch, 12 bit resolution) were equipped with 105 mm Nikon NIKKOR macro objectives set at an f -number of $f/5.6$. The cameras were placed such that the optical axis of the first camera was perpendicular to the measurement plane, while that of the second camera pointed upstream at a relative angle of 35° with respect to the first. This setup was also utilized in the research discussed in chapter 5. A schematic of it is shown in figure 5.2. With a field of view of 26×50 mm² (imaged

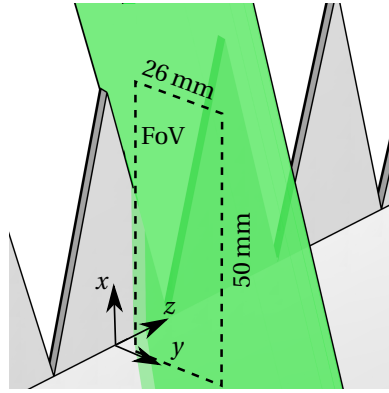


Figure 6.3: Location of the field of view for the stereoscopic PIV measurements in the $z/\lambda = 0.25$ measurement plane.

with half the sensor: 512×1024 px) centered on the serrated trailing edge (see figure 6.3), the digital image resolution was $S = 20$ px/mm at a magnification of 0.4.

10 100 images were acquired at an effective repetition rate of 10 kHz (image pairs acquired at 5 kHz with $\Delta t = 100$ μ s, corresponding to 10 kHz in single frame mode), resulting in a particle displacement of $\Delta x = 1.25$ mm or $S\Delta x = 25$ px. Additionally, 2000 image-pairs of particle images were acquired at 250 Hz in order to obtain time-uncorrelated statistics. The pulse separation was $\Delta t = 50$ μ s, corresponding to a freestream particle displacement of $\Delta x = 0.6$ mm or $S\Delta x = 12.5$ px.

LaVision DaVis 8 was used for image acquisition and processing. For both configurations, a multi-pass stereoscopic cross-correlation was applied with a final interrogation window size of 16×16 px and an overlap factor of 75%, resulting in a spatial resolution of 0.8 mm and a vector spacing of 0.2 mm. Conventional stereoscopic calibration and self-calibration alleviated aspects such as lens distortion and resulted in a disparity vector of less than 0.1 px. This is considered sufficient for stereoscopic cross-correlation ([6.23]). Table 6.2 provides an overview of the experimental parameters for the boundary layer measurements.

At the given magnification factor of about 0.4, the particle image diameter is about 10 μ m ([6.22]). Mitigation of the peak-locking effect by defocusing was verified by considering the histogram of the particle displacements. All measured velocity values, $n_i = U_i - \lfloor U_i \rfloor$, with the floor function $\lfloor \cdot \rfloor$, were distributed within 0.95 and 1.07 of n_i/\bar{n}_i , confirming the small effect of peak-locking in the measurement uncertainty. More important is the filtering effect due to the spatial resolution. With the application of the aforementioned multi-pass cross-correlation algorithm and window deformation, it has been established by Schrijer and Scarano [6.24] that the velocity amplitude modulation will vary with less than 5% for windows smaller than 0.6 times the characteristic wavelength. In the present case, a window size of 0.8×0.8 mm² was obtained, therefore allowing the measurement of flow structures down to 1.2 mm with 95% accuracy. In order to quantify random errors encountered in the present PIV setup, an *a-posteriori* statistical

Table 6.2: Parameters for the time-averaged and time-resolved stereoscopic PIV measurements.

Parameter	Symbol	Acquisition	
		Statistical	Time-resolved
Sensor size		512×1024 px	512×1024 px
Field of view	FoV	26×51 mm ²	26×51 mm ²
F-number	f/l	5.6	5.6
Focal length		105 mm	105 mm
Magnification		≈ 0.4	≈ 0.4
Imaging resolution	S	20 px/mm	20 px/mm
Interrogation window size		16×16 px	16×16 px
		0.8×0.8 mm ²	0.8×0.8 mm ²
Vector spacing (overlap 75%)		0.2×0.2 mm ²	0.2×0.2 mm ²
Laser pulse separation	Δt	50 μ s	100 μ s
Freestream displacement	Δx	≈ 0.6 mm	≈ 1.25 mm
	$S\Delta x$	≈ 12 px	≈ 25 px
Light sheet thickness		1.5 mm	1.5 mm
Acquisition frequency	f_s	250 Hz	5 kHz (10 kHz) ¹
Number of samples		2000	10,100

¹ Single frame

method, introduced by Wieneke [6.25], was used. Following Wieneke [6.25], the random error in each velocity field is approximately 1% in the freestream, and around 3% in the inner boundary layer. As a consequence, for the acquired number of samples (2000), the resulting error in the mean velocity is within 0.05% and 2% for the root mean square (rms) value.

6.2. RESULTS

6.2.1. ACOUSTIC EMISSIONS

The acoustic measurements yield the difference in the acoustic frequency spectra between the original and the serration-retrofitted trailing edge. Figure 6.4 shows the acoustic source maps for the baseline configuration and the serrated trailing edges, with $\varphi = 0^\circ$ and 6° , at a third-octave band center frequency of 4 kHz. The data shown was acquired at $U_\infty = 35$ m/s and $\alpha = 0^\circ$. The trailing edge of the airfoil (indicated by the thin line) poses the primary sound source in all three cases. The flow-aligned serrations provide a noise reduction of about 2 dB, while the flow-misaligned serrations ($\varphi = 6^\circ$) have an adverse effect.

The plots in figure 6.5 show the integrated third-octave band sound pressure level (SPL) with α varying between 0° and 12° , and for $\varphi = 0^\circ$ and 6° , respectively. The serrations are seen to effectively lower the noise emission when compared to the original edge geometry, as also observed in [6.5, 10, 26]. The fact that the reduction is also present at low frequency is consistent with the aforementioned studies. Cases with $\varphi = 0^\circ$ exhibit a noise reduction of about 7 dB at $f \approx 1$ kHz. At higher frequency, the noise reduction de-

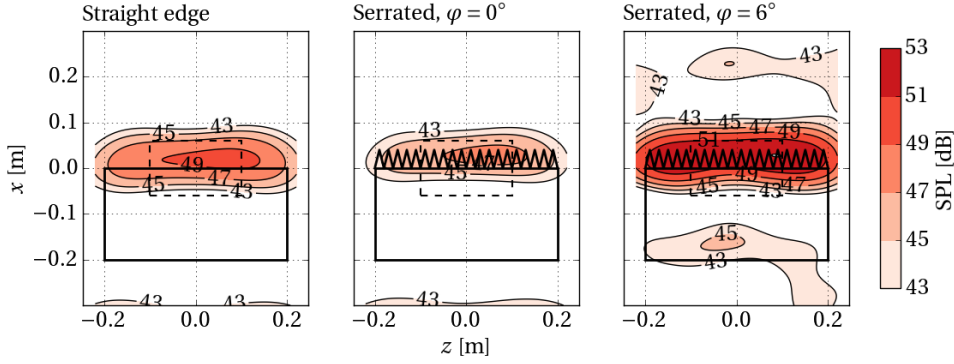


Figure 6.4: Acoustic source maps for a third-octave band center frequency of 4 kHz. Airfoil with straight trailing edge (left), serrated trailing edge with $\varphi = 0^\circ$ (center), and $\varphi = 6^\circ$ (right). Solid lines indicate the airfoil and the serrations, and dashed lines indicate the integration region. $U_\infty = 35$ m/s, $\alpha = 0^\circ$.

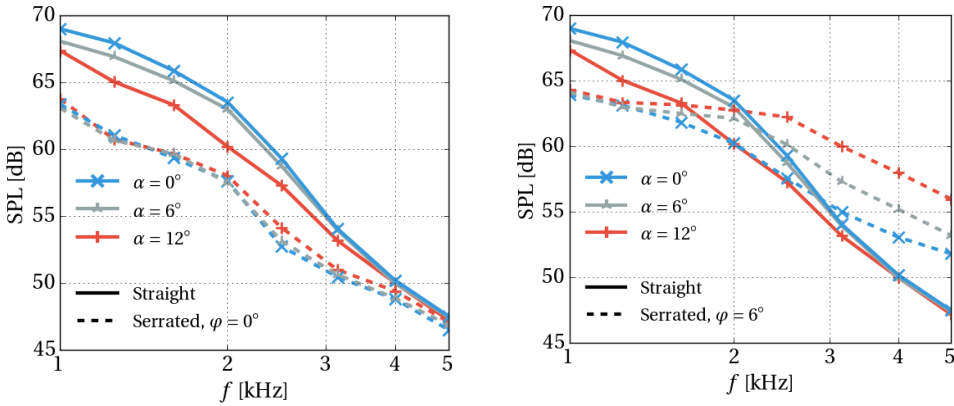


Figure 6.5: Third-octave band SPL for the straight and serrated trailing edges for various α . $U_\infty = 35$ m/s, $\varphi = 0^\circ$ (left) and $\varphi = 6^\circ$ (right).

creases, resulting in very similar levels for both configurations at 5 kHz. Serrations with $\varphi = 6^\circ$ also reduce the noise by about 5 dB at the low frequency, but the flatter spectrum leads to its intersection with that of the baseline trailing edge at about $f_c = 3.0$ kHz. The frequency where the crossover takes place varies with the airfoil incidence: $f_c = 3.0$ kHz, 2.2 kHz, and 1.6 kHz, respectively for the cases $\alpha = 0^\circ$, 6° and 12° .

As shown for $U_\infty = 35$ m/s in figure 6.5, crossover frequencies are only observed for $\varphi = 6^\circ$, but regardless of α . The same holds for the tests conducted at $U_\infty = 30$ and 40 m/s, which are omitted for the sake of conciseness. This behavior is ascribed to the effect of the near-surface mean flow deflection and the formation of streamwise coherent structures. In [6.11] it is argued that changes in the angle of attack induce a global deformation of the flow field around the airfoil and shows that a flap angle induces instead a localized effect, along with a change of the local pressure gradient and turbulence

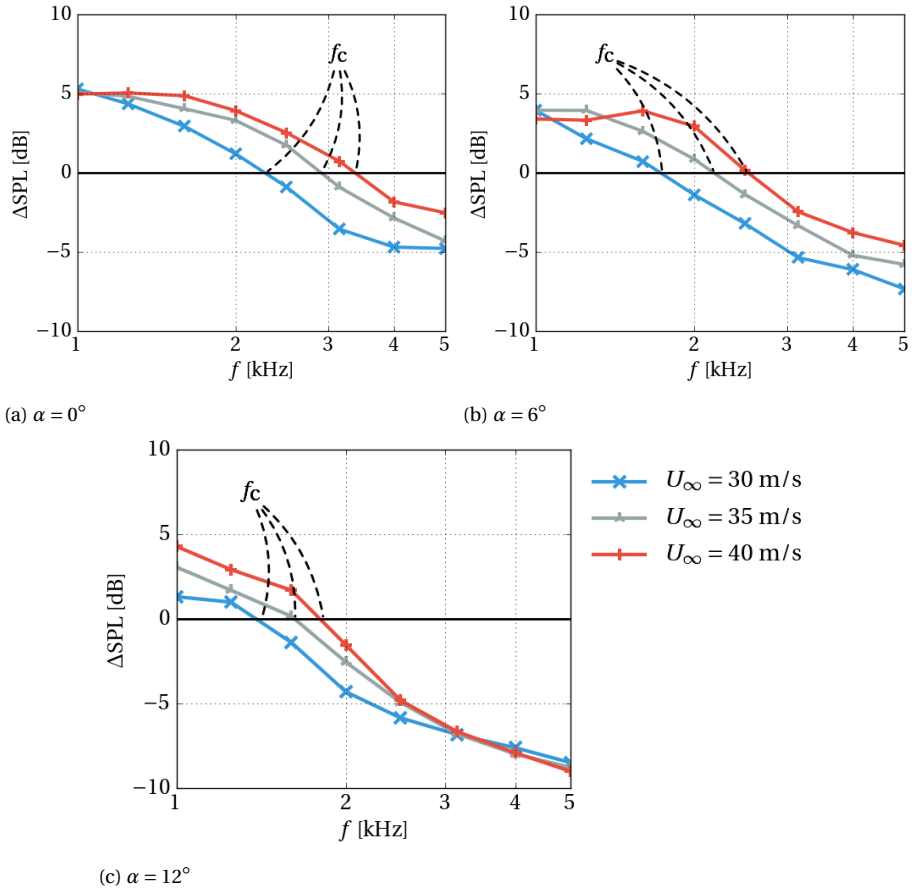


Figure 6.6: Noise reduction for the serrated trailing edge relative to the baseline airfoil for different α values and $\varphi = 6^\circ$. The crossover frequency f_c is indicated for each U_∞ .

intensity. This supports the hypothesis that the noise increase is due to the serration misalignment with the flow, leading to an increase in turbulence levels near the edge.

To facilitate the comparison between the emissions from the serrated edge and the baseline configuration for the representative case $\varphi = 6^\circ$, differences in SPL are presented in figures 6.6a, 6.6b, and 6.6c for $\alpha = 0^\circ$, 6° , and 12° , respectively. Positive values indicate a reduction in noise. The crossover frequency is estimated by linear interpolation of the third-octave band data.

Figure 6.6a shows the results for $\alpha = 0^\circ$, where the serrations exhibit a similar reduction in noise between the three measured velocities, at around $f = 1$ kHz ($\Delta \text{SPL} = 5$ dB). The amount of reduction quickly decreases as the frequency increases, which occurs earlier for lower velocities. At the highest frequencies measured and $U_\infty = 30$ m/s, serrations attain a noise level 5 dB louder than the straight trailing edge. For $\alpha = 6^\circ$, as discussed above (figure 6.6b), the crossover frequency is lower than for $\alpha = 0^\circ$ at all mea-

sured velocities. The difference in SPL at the lower frequency is between 4 and 5 dB, while at $f = 5$ kHz the increase in SPL reaches 7.5 dB. A similar result is seen for $\alpha = 12^\circ$, where crossovers occur at even lower frequencies, between $f_c = 1.5$ kHz and 1.8 kHz. In this case, the increase in SPL at the highest measured frequency, $f = 5$ kHz, reaches a value of around 8 dB.

6.2.2. CROSSOVER FREQUENCY SCALING

Different boundary layer thickness parameters were investigated in order to evaluate their effect on St_c (Eq. (6.1)) and its collapse: the wall-normal location of the $0.99 u_e$ velocity (where u_e is the edge velocity of the boundary layer), δ_{99} , the displacement thickness, δ^* , and the momentum thickness, θ . In contrast to [6.10], the edge velocity u_e was considered as the velocity scale instead of the freestream velocity U_∞ .

The boundary layer parameters were evaluated over the straight airfoil trailing edge, following the aforementioned study. Figure 6.7 shows the different boundary layer parameters for various angles of attack and freestream velocities. The parameters generally show an increasing trend with angle of attack on the suction side and a decreasing trend on the pressure side, as expected. A larger variation between the different velocities is observed with increasing angle of attack, especially noticeable on the suction side. It is worth to note that δ^* shows a larger relative increase with an increase in angle of attack.

Based on the boundary layer parameters in figure 6.7, St_c was evaluated using the crossover frequencies for the serrated edge at $\varphi = 6^\circ$ discussed in section 6.2.1. Figures 6.8 and 6.9 show St_c obtained using the suction and pressure side boundary layer parameters, respectively. In both cases, the crossover frequency St_c generally collapses well within 10% varying the freestream velocity.

When considering different angles of attack, a constant Strouhal number cannot be identified. This suggests that St_c , as hypothesized in [6.4], is valid for changes in the freestream velocity at an identical level of airfoil incidence. A linear trend in St_c is nevertheless found for different angles of attack, indicated by the linear regression applied to the measured data in figures 6.8 and 6.9 (dashed line). In order to quantify the predictability of the data with the given linear trend over the three velocities presented, the coefficient of determination, r^2 , is indicated in figures 6.8 and 6.9.

With δ_{99} as the characteristic length scale over the suction side (figure 6.8, left), St_c on one hand shows a decreasing trend with increasing α . On the other hand, the values exhibit a large spread for the different velocities. With δ^* (figure 6.8, center), St_c instead shows an increase for increasing α . This results in the aforementioned larger relative increase in δ^* (figure 6.7, center). Overall, the collapse of St_c with respect to the fit is very good when different values of the freestream velocity are considered (maximum 10% deviation for the suction side with δ_{99}). The variation of St_c with θ (figure 6.7, right) is similar to that with δ_{99} and shows a downward trend with increasing α . In conclusion, the scaling with the displacement thickness, δ^* , offers a more systematic fit with the data.

In general, the results suggest that a universal collapse of St_c for all angles of attack and Reynolds numbers is not possible with the set of scaling parameters investigated here. On the pressure side, St_c appears to vary with near-linear behavior with angle of attack, exhibiting consistently high values of r^2 over the three boundary layer thickness

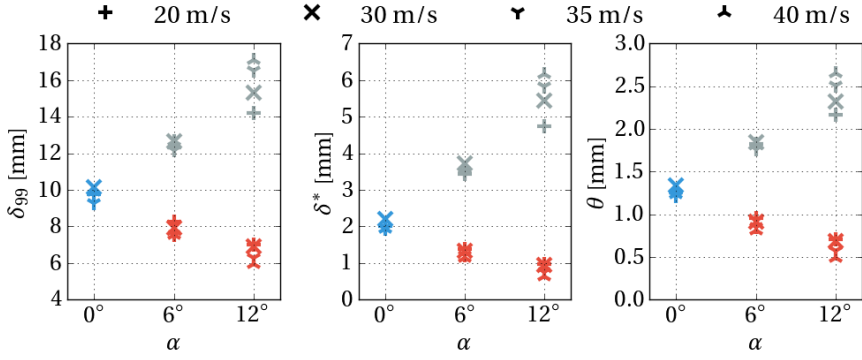


Figure 6.7: δ_{99} , δ^* and θ , at the trailing edge of the baseline airfoil. $U_\infty = 20$ m/s: +, $U_\infty = 30$ m/s: ×, $U_\infty = 35$ m/s: ∇, $U_\infty = 40$ m/s: ⋈. Pressure side (red), suction side (gray), and measurements at $\alpha = 0^\circ$ (blue).

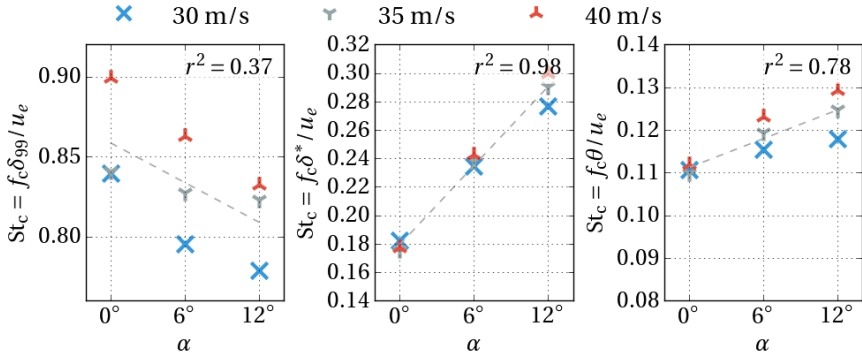


Figure 6.8: St_c for different boundary layer thickness parameters measured on the suction side. $U_\infty = 30$ m/s: ×, $U_\infty = 35$ m/s: ∇, $U_\infty = 40$ m/s: ⋈.

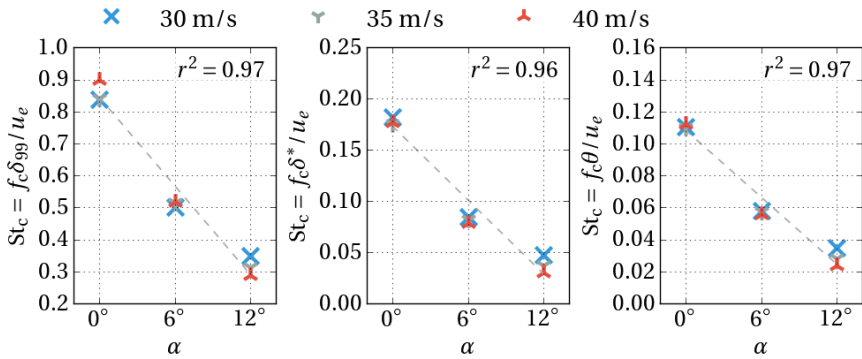


Figure 6.9: St_c for different boundary layer thickness parameters measured on the pressure side. $U_\infty = 30$ m/s: ×, $U_\infty = 35$ m/s: ∇, $U_\infty = 40$ m/s: ⋈.

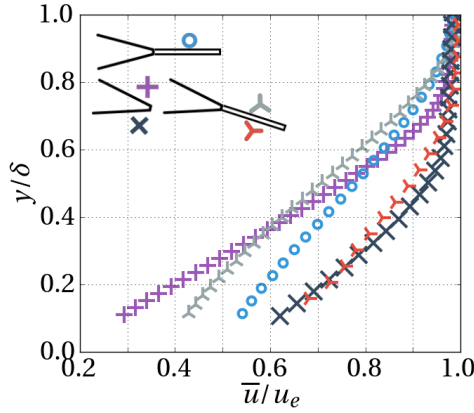


Figure 6.10: Streamwise mean flow component, \bar{u} .

parameters. The suction side, on the other hand, has a less predictable behavior, exhibiting r^2 of 0.37, 0.91 and 0.62. While the parameters used for scaling of the crossover Strouhal number were measured on the baseline airfoil, they are indicative of the condition when the serration is applied.

6.2.3. NEAR-EDGE FLOW CHARACTERIZATION

PIV measurements in the x - y plane are used to characterize the mean flow and turbulence intensity in the near-edge boundary layer. The analysis will compare key parameters between the straight edge and the serrated edge.

The angle of attack and serration flap angle used are $\alpha = 12^\circ$, $\varphi = 6^\circ$, at a freestream velocity of $U_\infty = 20$ m/s. As stated in section 6.1, this is the upper velocity limit at which good-quality time-resolved flow information was obtainable with the current PIV system. The $\alpha = 0^\circ$, $\varphi = 0^\circ$ case is additionally shown for comparison. This configuration was chosen based on the predicted value of f_c for this case, which is expected to occur well below the upper frequency limit of the time-resolved flow data. Its approximation is discussed further below.

The analysis is performed by comparing the flow at the serration edge at the plane crossing $z/\lambda = 0.25$ (as indicated in section 6.1.3 and figure 6.3) and $x/2h = 0.5$, with the flow over the straight edge of the unserrated airfoil at $x/2h = 0$. The choice of this location has been made based on results from [6.11]. It is established there that, at this location over the serrated edge, the flow experiences the largest degree of spanwise flow deflection near the edge when serration-flow misalignment is prescribed.

The mean flow component in the streamwise direction, \bar{u} , is presented in figure 6.10. Suction and pressure side measurements are shown for the straight and the serrated edges at $\alpha = 12^\circ$, with $\varphi = 6^\circ$ for the latter. Additionally, the serrated edge in the flow-aligned configuration, $\alpha = 0^\circ$, $\varphi = 0^\circ$, is shown for reference.

On the pressure side trailing edge, both the straight and serrated airfoil edges exhibit higher velocity than at the suction side. Values of \bar{u} for $\alpha = 0^\circ$, $\varphi = 0^\circ$ are found between

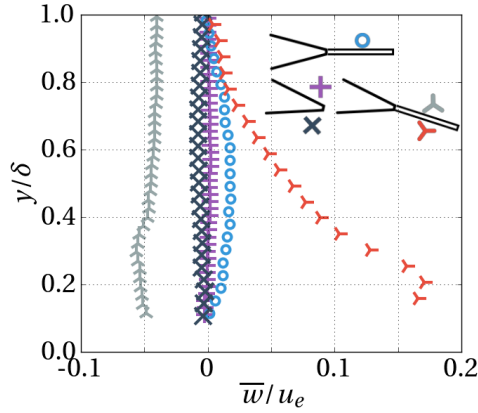


Figure 6.11: Spanwise mean flow component, \bar{w} .

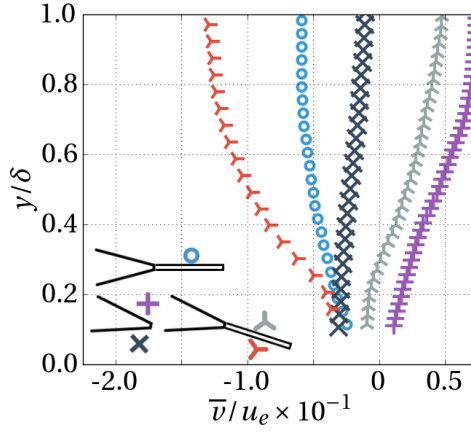
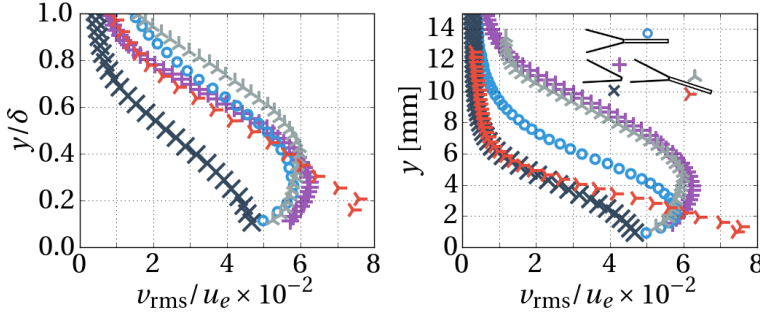
those observed for the suction and pressure sides for the serrated $\alpha = 12^\circ$, $\varphi = 6^\circ$ case. The lower speed over the suction side is due to the adverse pressure developing with the airfoil incidence. These results also confirm that no region of reverse flow is formed at the suction side.

As mentioned above, the largest degree of flow deflection is experienced at this edge location for the flow-misaligned serrations ($z/\lambda = 0.25$, $x/2h = 0.5$). To quantify this, figure 6.11 presents the profile of the spanwise mean velocity component, \bar{w} . When the mean flow is not significantly modified, such as in the case of the straight edge, and when the serrations are flow-aligned, \bar{w} is close to zero.

Misaligned serrations instead exhibit a significant spanwise velocity of $\bar{w} \approx 0.15 u_e$. The highest level of deflection occurs on the pressure side, at around $y/\delta \approx 0.2$, with a quick decrease away from the wall, and reaches $\bar{w} = 0$ the edge of the boundary layer. Therefore, the spanwise flow deflection is determined to have an effect on the entire boundary layer flow. On the suction side, the deflection is about a third of that of the pressure side, $\bar{w} \approx 0.05 u_e$, with opposite direction (towards the center of the serration tooth). It has a rather uniform value due to the effect of the streamwise vortex formed behind the serration, as discussed in [6.11, 27], and chapter 4.

The mean wall-normal flow component, \bar{v} , is shown in figure 6.12. Here, negative values represent flow that is oriented towards the surface (it is reminded that the y axis is chosen such that it is always wall-normal). As expected, the surface at the pressure side of the flow-misaligned serration experiences a considerable degree of flow directed towards the wall. This suggests that an efficient transfer of energy from the turbulent eddies to the unsteady surface pressure is expected in this region. This likely results in a significant contribution to the noise produced by the edge.

The same measurement over the suction side shows instead flow being directed away from the wall, a consequence of the flow passing through the serration teeth. Due to the nature of the serration geometry, with its angled edge, the streamwise vortex that is being formed behind it fails to impinge on its suction side surface, contrary to what is usually observed in flap edges ([6.28]).

Figure 6.12: Wall-normal mean flow component, \bar{v} .Figure 6.13: Wall-normal fluctuations, ν_{rms} .

As the wall-normal component fluctuations, ν_{rms} , are related to the increase in acoustic emissions by the edge (see the trailing edge noise prediction equations in [6.7, 29, 30] and the discussion in chapter 2), they will be here investigated.

Figure 6.13 (left) shows similar behavior and levels for the suction side measurements, reaching maxima at about $y/\delta = 0.3$. While the pressure side measurement of the straight edge airfoil shows the lowest values of ν_{rms} , the measurement of the serrated edge airfoil exhibits instead a large increase near the surface, about a third larger than the maxima of the suction side measurements, and twice of the straight edge airfoil pressure side measurement. The results suggest a correlation between \bar{w} and ν_{rms} , likely driven by the wall-normal transport of turbulent fluctuations as the streamwise vortex formation occurs.

The maximum of wall-normal fluctuations is observed at $y/\delta = 0.2$ on the pressure side, which is considerably close to the wall (1.5 mm), noting that the boundary layer is significantly thinner here than on the suction side. The maxima for the suction side

measurements occurs instead at around $y = 5$ mm.

6.2.4. CHARACTERIZATION OF THE NEAR-EDGE TIME-RESOLVED FLOW

The boundary layer thickness differences between the pressure and suction sides indicates a contraction of the integral length scale of the turbulent structures at the pressure side. This suggests that increased wall-normal fluctuations at the pressure side are due to smaller structures, contributing to the higher end of the noise frequency spectrum.

To evaluate this, the streamwise integral length scale is investigated, defined in [6.31] as

$$\Lambda_{x|uu} = \int_0^\infty R_{uu}(\xi_x) d\xi_x, \quad (6.2)$$

where ξ_x is the separation distance in the x direction between signals for the calculation of the spatial two-point correlation coefficient,

$$R_{uu} = \frac{\overline{u(x) \cdot u(x + \xi_x)}}{u^2(x)}. \quad (6.3)$$

As the upper boundary of the integral is limited by the field of view available, a fixed value is chosen for all the presented cases, such that $\xi_{x,\max} = 0.5h$. The choice of $\Lambda_{x|uu}$ over other scales comes from the ability to accurately describe it with the implemented measuring methodology. It scales linearly with $\Lambda_{x|vv}$, as shown by results in [6.31].

Due to the angle of the serration surface against the mean flow direction, the latter is not necessarily parallel to the wall or the coordinate system arrangement used so far. A rotation in the axes has, therefore, been prescribed, such that the x direction is aligned with the local mean flow, \bar{u} (calculated *a-posteriori*), and the definition of $\Lambda_{x|uu}$ is preserved. Some of the extent of $\xi_{x,\max}$ is nevertheless lost due to this rotation, and the data is presented only for y locations where the limit $0.5h$ is obtainable. The rotation is applied throughout the results in this section.

The values of $\Lambda_{x|uu}$ are shown in figure 6.14, in terms of the absolute wall distance. Alongside are the values for the wavenumber of the most energy-bearing eddies, approximated empirically ([6.32]) as

$$k_e = \frac{\sqrt{\pi}}{\Lambda_{x|uu}} \frac{\Gamma(5/6)}{\Gamma(1/3)}, \quad (6.4)$$

where Γ is the gamma function. The application of this approximation nevertheless requires isotropic turbulence to be assumed, as considered in [6.32–34], and for which tuning procedures have been introduced ([6.35]).

A notable difference in the integral length scales between the pressure and suction side measurements is observed. The minimum wavelength on the pressure side is approximately 1.5 mm at around 5 mm distance from the wall. On the suction side, the minimum wavelength is 2.5 mm, detected at 11 mm from the upper surface. These observations support the argument that the pressure side contributes to the noise emission in the higher end of its frequency spectrum.

A slightly higher wavenumber ($k_e = 450 \text{ m}^{-1}$) is exhibited on the pressure side serrated case compared to the straight edge case ($k_e = 370 \text{ m}^{-1}$), indicating a slight additional contraction of the boundary layer with the serration.

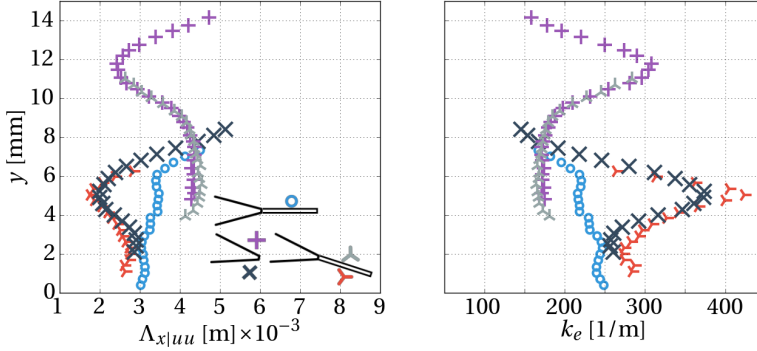


Figure 6.14: Streamwise turbulence length scale, $\Lambda_{x|uu}$ (left), and most energetic streamwise wavenumbers (right).

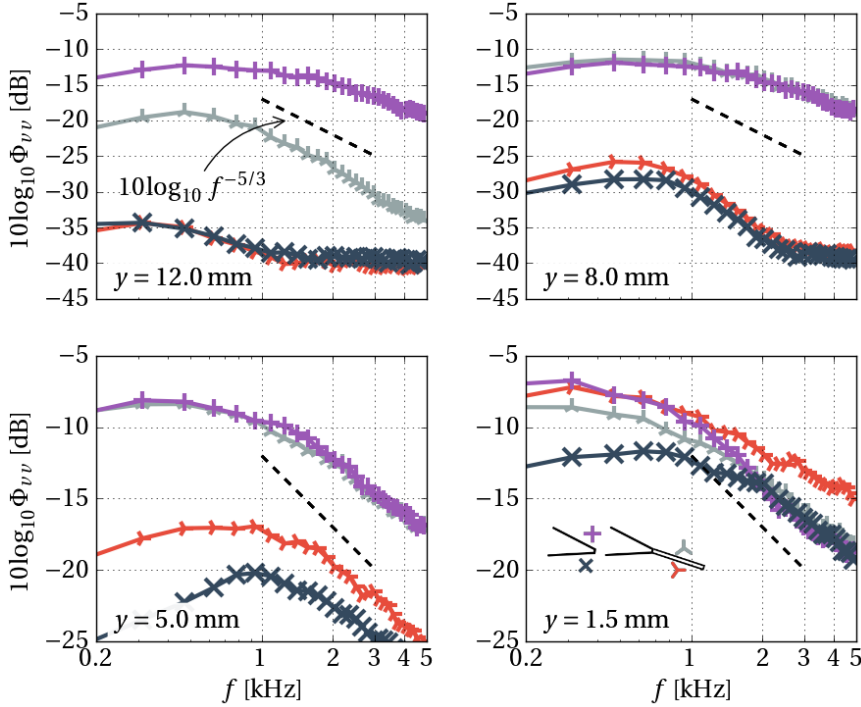


Figure 6.15: Spectrum of the wall-normal velocity component for different wall-normal locations.

To illustrate the relation between the observed v_{rms} over the boundary layer and the energy in the turbulent flow eddies, the wall-normal flow component spectra, Φ_{vv} , are presented in figure 6.15. The suction and pressure sides of the straight and serrated edges are shown for $\alpha = 12^\circ$, $\varphi = 6^\circ$. The absolute wall-normal distance is used to compare various locations in the boundary layer of each case, while maintaining the same

wall distance scale. The Kolmogorov law is shown in the plots for reference. The signal floor due to noise is reached at about -40 dB, as is evident from the plateau of the pressure side measurement.

The spectral results agree with the ν_{rms} levels of the different cases. Larger values are observed over the straight edge at the location furthest from the wall, $y = 12$ mm. The levels and spectral shape for the straight and serrated cases at $y = 8$ mm are the same, as observed for ν_{rms} at this location.

Nearer the wall, the pressure side cases exhibit increasing levels, by about 10 dB between $y = 8$ and 5 mm. The most notable feature is found at $y = 1.5$ mm, where the Φ_{vv} levels of the pressure side reach those of the suction side. Most importantly, the levels for the pressure side of the serrated case exceed any other above roughly 1.1 kHz. A difference of around 5 dB is observed at the top limit of the observed frequency range.

The relation between this turbulence spectra crossover frequency and the acoustic spectrum one, f_c , will be here established. For this purpose, the value of f_c for this case, $\alpha = 12^\circ$, $\varphi = 6^\circ$ at 20 m/s, will be obtained with the St_c model, as discussed in section 6.2.2.

Each choice of δ showed a dependence of St_c on u_e . Therefore, an estimation of f_c on u_e must take this into account. The results obtained in section 6.2.2 are linearly extrapolated to obtain the acoustic f_c for a 20 m/s freestream velocity. The result of

$$f_c = \text{St}_c u_e / \delta. \quad (6.5)$$

is shown in figure 6.16 for the freestream velocities of the acoustic measurements, as presented in section 6.2.1, and the extrapolated result at 20 m/s PIV freestream velocity. The mean between the results of the different boundary layer thickness parameter results is indicated at 1.14 kHz, which correlates well to the observed crossover in the spectra of the turbulence, ≈ 1.1 kHz.

These results confirm that the pressure side flow near the edge is the source of the high frequency noise increase, exhibiting a crossover value in the turbulence spectrum similar to that expected in the acoustic emissions.

6.3. CONCLUSIONS

The increase in high frequency noise by trailing edge serrations has been confirmed using acoustic beamforming and ascribed to the misalignment of the serrations with regard to the otherwise undisturbed mean wake flow.

A Strouhal number, proposed by Gruber *et al.* [6.10], relating the crossover frequency of the serration noise increase with the boundary layer thickness and its edge velocity, has been investigated. Contrary to a single-number collapse, it exhibits a linear modification with changes in angle of attack, and varies slightly for different freestream velocities. A better fit is furthermore found by taking the pressure, and not the suction side boundary layer thickness. As the thinner pressure side boundary layer carries smaller turbulent eddies, and in turn these relate to the production of higher frequency noise, its use in the Strouhal number calculation is more representative.

PIV measurements determine the boundary layer flow properties over the serration and straight trailing edge. A sharp increase in ν_{rms} on the pressure side of the serrated

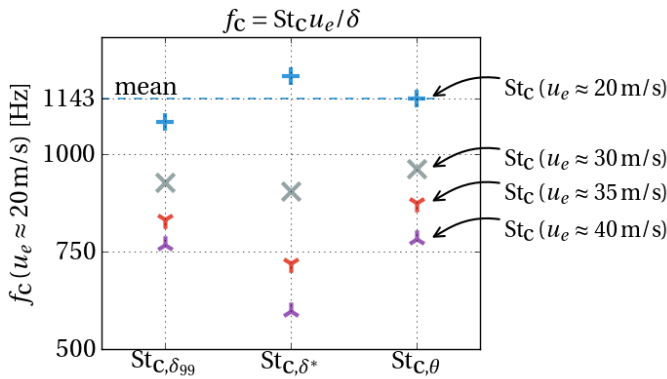


Figure 6.16: Predicted value of f_c based on the pressure side measurements of St_c based on $U_\infty = 30$ m/s (\times), $U_\infty = 35$ m/s (γ), $U_\infty = 40$ m/s (Δ), and the linear extrapolation to $U_\infty = 20$ m/s (+).

case with a significant increase of spanwise velocity is observed. The integral length scale of the turbulence is retrieved, identified on the pressure side to be around half the size of the suction side values. This corresponds approximately to the pressure and suction side boundary layer thickness ratio.

The turbulence frequency spectrum exhibits an increase in energy corresponding to that of the estimated acoustic crossover. This increase is observed at the pressure side, where v_{rms} is seen to sharply increase, and coincides with the highest spanwise flow deflection.

The latter suggests that the source of the high frequency noise leading to the crossover phenomenon is due to interactions taking place at the pressure side.

BIBLIOGRAPHY

- [6.1] C. Arce León, R. Merino-Martínez, D. Ragni, F. Avallone, F. Scarano, S. Pröbsting, M. Snellen, D. G. Simons, and J. Madsen, *Effect of trailing edge serration-flow misalignment on airfoil noise emissions*, [Journal of Sound and Vibration](#) **405**, 19 (2017).
- [6.2] T. Dassen, R. Parchen, J. Bruggeman, and F. Hagg, *Results of a wind tunnel study on the reduction of airfoil self-noise by the application of serrated blade trailing edges*, Tech. Rep. (National Aerospace Laboratory, NLR, 1996).
- [6.3] S. Oerlemans, M. Fisher, T. Maeder, and K. Kögler, *Reduction of wind turbine noise using optimized airfoils and trailing-edge serrations*, [AIAA Journal](#) **47**, 1470 (2009).
- [6.4] M. Gruber, P. Joseph, and T. Chong, *Experimental investigation of airfoil self noise and turbulent wake reduction by the use of trailing edge serrations*, in [16th AIAA/CEAS Aeroacoustics Conference](#) (2010) pp. 1–23.
- [6.5] A. Finez, E. Jondeau, M. Roger, and M. C. Jacob, *Broadband Noise Reduction of*

- a Linear Cascade With Trailing Edge Serrations*, in *17th AIAA/CEAS Aeroacoustics Conference (32nd AIAA Aeroacoustics Conference)* (Portland, Oregon, USA, 2011).
- [6.6] A. Vathylakis, C. C. Paruchuri, T. P. Chong, and P. Joseph, *Sensitivity of aerofoil self-noise reductions to serration flap angles*, *22nd AIAA/CEAS Aeroacoustics Conference*, 1 (2016).
- [6.7] M. S. Howe, *Noise produced by a sawtooth trailing edge*, *The Journal of the Acoustical Society of America* **90**, 482 (1991).
- [6.8] M. Azarpeyvand, M. Gruber, and P. Joseph, *An analytical investigation of trailing edge noise reduction using novel serrations*, in *19th AIAA/CEAS Aeroacoustics Conference* (2013).
- [6.9] B. Lyu, M. Azarpeyvand, and S. Sinayoko, *A Trailing-Edge Noise Model for Serrated Edges*, in *21st AIAA/CEAS Aeroacoustics Conference* (AIAA, Dallas, Texas, 2015).
- [6.10] M. Gruber, P. Joseph, and T. Chong, *On the mechanisms of serrated airfoil trailing edge noise reduction*, in *17th AIAA/CEAS Aeroacoustics Conference (32nd AIAA Aeroacoustics Conference)*, Vol. 2781 (American Institute of Aeronautics and Astronautics, Portland, Oregon, USA, 2011) pp. 5–8.
- [6.11] C. Arce León, D. Ragni, S. Pröbsting, F. Scarano, and J. Madsen, *Flow topology and acoustic emissions of trailing edge serrations at incidence*, *Experiments in Fluids* **57**, 91 (2016).
- [6.12] M. Gruber, *Airfoil noise reduction by edge treatments*, *Ph.D. thesis*, University of Southampton (2012).
- [6.13] M. Gruber, M. Azarpeyvand, and P. F. Joseph, *Airfoil trailing edge noise reduction by the introduction of sawtooth and slitted trailing edge geometries*, *Proceedings of 20th International Congress on Acoustics, ICA* **10**, 1 (2010).
- [6.14] M. P. Arroyo and C. A. Greated, *Stereoscopic particle image velocimetry*, *Measurement Science and Technology* **2**, 1181 (1991).
- [6.15] A. L. Braslow, R. M. Hicks, and R. V. Harris Jr., *Use of grit-type boundary-layer transition trips on wind-tunnel models*, *NASA Technical Note* (1966).
- [6.16] R. Amiet, *Correction of Open Jet Wind Tunnel Measurements For Shear Layer Refraction*, in *2nd AIAA Aeroacoustics Conference, March 24-26, Hampton, VA, USA* (1975).
- [6.17] P. Salas and S. Moreau, *Noise prediction of a simplified high-lift device*, in *22nd AIAA/CEAS Aeroacoustics Conference. May 30 - June 1 2016. Lyon, France.* (2016) AIAA paper 2016-2962.
- [6.18] F. R. S. Lord Rayleigh, XXXI. *Investigations in Optics with special reference to the Spectroscope*, *The London, Edinburgh and Dublin Philosophical Magazine and Journal of Science* **8**, 261 (1879).

- [6.19] C. C. J. Pagani, D. S. Souza, and M. A. F. Medeiros, *Slat noise: Aeroacoustic beamforming in closed-section wind tunnel with numerical comparison*, [AIAA Journal](#) **54**, 2100 (2016).
- [6.20] P. Sijtsma, *Phased array beamforming applied to wind tunnel and fly-over tests*, Tech. Rep. NLR-TP-2010-549 (National Aerospace Laboratory (NLR), Anthony Fokkerweg 2, 1059 CM Amsterdam, P.O. Box 90502, 1006 BM Amsterdam, The Netherlands, 2010).
- [6.21] F. Scarano, *Iterative image deformation methods in PIV*, [Measurement Science and Technology](#) **13**, R1 (2002).
- [6.22] C. D. Meinhart and S. T. Wereley, *The theory of diffraction-limited resolution in microparticle image velocimetry*, [Measurement Science and Technology](#) **14**, 1047 (2003).
- [6.23] M. Raffel, C. Willert, and J. Kompenhans, [Springer](#), Experimental Fluid Mechanics (Springer, Berlin, Heidelberg, 2007).
- [6.24] F. F. J. Schrijer and F. Scarano, *Effect of predictorcorrector filtering on the stability and spatial resolution of iterative PIV interrogation*, [Experiments in Fluids](#) **45**, 927 (2008).
- [6.25] B. Wieneke, *PIV uncertainty quantification from correlation statistics*, [Measurement Science and Technology](#) **26** (2015), 10.1088/0957-0233/26/7/074002.
- [6.26] D. Moreau and C. Doolan, *Noise-Reduction Mechanism of a Flat-Plate Serrated Trailing Edge*, [AIAA Journal](#) **51**, 2513 (2013).
- [6.27] C. Arce León, F. Avallone, S. Pröbsting, and D. Ragni, *PIV Investigation of the Flow Past Solid and Slitted Sawtooth Serrated Trailing Edges*, in [54th AIAA Aerospace Sciences Meeting](#), January (American Institute of Aeronautics and Astronautics, San Diego, California, 2016) pp. 1–15.
- [6.28] Y. Guo, *Aircraft Flap Side Edge Noise Modeling and Prediction*, [AIAA/CEAS Aeroacoustics Conference](#), 1 (2011).
- [6.29] R. Amiet, *Noise due to turbulent flow past a trailing edge*, [Journal of Sound and Vibration](#) **47**, 387 (1976).
- [6.30] R. Parchen, *Progress report DRAW: A prediction scheme for trailing-edge noise based on detailed boundary-layer characteristics*, TNO Rept. HAGRPT-980023, TNO Institute of Applied Physics, The Netherlands (1998).
- [6.31] M. Kamruzzaman and T. Lutz, *On the Length Scales of Turbulence for Aeroacoustic Applications*, AIAA Conference, 05 (2011).
- [6.32] O. Stalnov, P. Chaitanya, and P. F. Joseph, *Towards a non-empirical trailing edge noise prediction model*, [Journal of Sound and Vibration](#), 1 (2016).

- [6.33] T. Lutz, A. Herrig, W. Würz, M. Kamruzzaman, and E. Krämer, *Design and Wind-Tunnel Verification of Low-Noise Airfoils for Wind Turbines*, [AIAA Journal](#) **45**, 779 (2007).
- [6.34] S. Lee, *Source Characterization of Turbulent Boundary Layer Trailing Edge Noise Using an Improved TNO Model*, [22nd AIAA/CEAS Aeroacoustics Conference](#) , 1 (2016).
- [6.35] F. Bertagnolio, A. Fischer, and W. Jun Zhu, *Tuning of turbulent boundary layer anisotropy for improved surface pressure and trailing-edge noise modeling*, [Journal of Sound and Vibration](#) **333**, 991 (2014).

7

ACOUSTIC EMISSIONS OF SEMI-PERMEABLE TRAILING EDGE SERRATIONS

*If you haven't found something strange during the day,
it hasn't been much of a day.*

John Archibald Wheeler

*There is a theory which states that if ever anyone discovers exactly what the Universe is for
and why it is here, it will instantly disappear and be replaced by something even more
bizarre and inexplicable. There is another theory which states that this has already
happened.*

Douglas Adams, *The Restaurant at the End of the Universe*

Several serration geometries are investigated, two of which are semi-permeable. This feature is achieved by using a slitted surface rather than one which is solid. The acoustic emissions of these serrations when attached to a symmetric airfoil are compared both at incidence and zero lift. The results are discussed and used to undertake the formulation of a hypothesis to explain the noise reduction mechanism of the serrations.

The contents of this chapter have been adapted from Arce León *et al.* [7.1].

AS TRAILING EDGE SERRATIONS have become the predominant device for noise reduction in industrial wind turbine blade applications ([7.2–4]), they have adopted a design philosophy that traditionally consists of thin, triangle-shaped panels with an otherwise solid and non-permeable surface—a design which is reflected by the serrations used in previous chapters.

Designs that incorporate some level and type of surface permeability have nevertheless been present in some research. Gruber *et al.* [7.5] presents a detailed evaluation of a range of such design options, prescribing surface permeability by the introduction of holes or slits in the material.

While the traditional solid (nonpermeable) serrations have been found to reduce noise, they have also been known to increase it beyond a certain frequency ([7.6, 7], chapter 6). This unwanted effect can lead to the degradation of the overall noise reduction performance of serrations, or limit their application to a reduced range of conditions in industrial applications.

This effects seems nevertheless to be quite well averted by one particular design in [7.5]. By cutting the surface streamwise in a repeated pattern such as to create a series of slits, the increase in high frequency noise showed to be mitigated. Such a step in design might in fact indicate that a promising new direction towards improved serrations alternatives could be be achievable.

Being an interesting proposal, the work here presented attempts to replicate this result, and compare its noise emissions against two solid serration geometries. In addition, a new hybrid design that mixes both the slitted and solid serrations is explored.

The serrations were mounted on a NACA 0018 airfoil. This symmetric airfoil has been preferred, as equal flow conditions are obtained on the upper and lower sides at $\alpha = 0^\circ$, allowing noise reduction to be tested based on this premise. The choice of airfoil differs from [7.5], where a non-symmetric NACA 6512-10 airfoil was used, and as a consequence pressure differences over the two serration sides are expected almost regardless of conditions.

The present study investigates turbulent boundary layer-trailing edge noise (TBL-TE noise) of the four serrations by means of acoustic beamforming¹, using a microphone array, for three freestream velocities, 30, 35 and 40 m/s (the highest corresponding to a Reynolds number of around 526 000), and two angles of attack, $\alpha = 0^\circ$ and $\alpha = 12^\circ$ (the *geometric* angle of attack is indicated).

7.1. EXPERIMENTAL SETUP

The experiments were conducted at the Delft University of Technology Vertical Wind Tunnel (V-Tunnel), described in section 3.1. The setup used to perform the acoustic measurements has been further described in section 3.3.

As in the research detailed in previous chapters, a $C = 20$ cm chord length NACA 0018 airfoil was used (figure 4.1). To ensure that the noise source observed was TBL-TE noise, the boundary layer was tripped at $0.2 \cdot C$ using three-dimensional roughness elements following the recommendations in [7.8]. It was confirmed to remain turbulent up to the

¹Gruber *et al.* [7.5], used single uncorrelated microphones to obtain the noise levels.

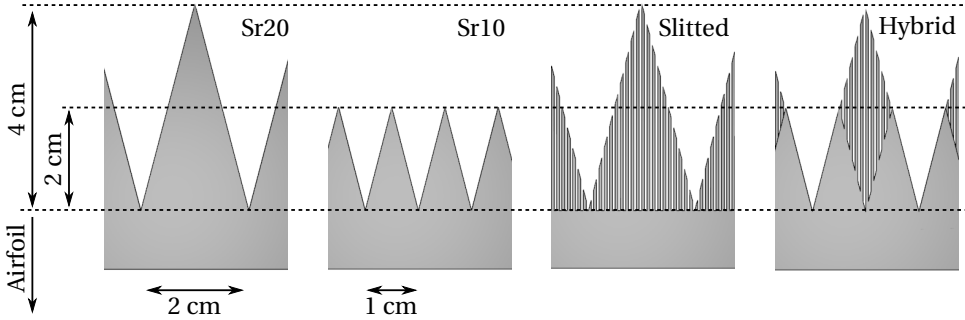


Figure 7.1: Serration model schematic.

trailing edge using a microphone probe.

The serrations were inserted in the trailing edge using a modular system, as shown in figure 4.2. The straight edge refers to the unmodified trailing edge of the airfoil.

Two traditional solid-surface serrations, and two semi-permeable serrations were tested. The length of the solid serrations (labeled Sr20 and Sr10) is established as a ratio of the airfoil chord length, such that the Sr20 serrations are $0.2 \cdot C = 4$ cm in length, and the Sr10 serrations are $0.1 \cdot C = 2$ cm long. The semi-permeable designs, labeled Slitted and Hybrid, along with the solid serrations, can be observed in figure 7.1. The solid area of the Hybrid design is the same as Sr10, while the length of the semi-permeable area in both designs is the same as for Sr20. The serration root of all the designs aligns with the original trailing edge of the airfoil.

The serration lengths were chosen following the design guidelines presented in [7.6], where it is recommended that they be at least twice the boundary layer thickness, δ . For the current setup, δ was measured using particle image velocimetry (PIV) and reported in [7.9] and chapter 5. The serration length was confirmed to satisfy this recommendation using those results.

The design of the Slitted serrations followed that of [7.5]. 0.5 mm cutouts were made in the material, leaving 0.5 mm slits. The cutouts end at the base of the serration. The same slit widths are used in the Hybrid design.

7.2. MEASUREMENT METHODOLOGY

Delay-and-sum beamforming, also known as conventional frequency domain beamforming ([7.10, 11]) was applied to the acoustic data, as in the previous chapters.

Recordings with a sampling frequency of 50 kHz and a measurement time of 60 s were employed. To calculate the ensemble-average of the cross-spectral matrix, the acoustic data was averaged using time blocks of 2048 samples ($\Delta t = 40.96$ ms) for each Fourier transform, and a Hanning window with 50 % data overlap. With these parameters values, the frequency resolution is 24.41 Hz and the expected error ([7.12]) in the estimate for the cross-spectrum was 2.6%.

For beamforming, a scan grid covering the expected area of noise generation was selected, ranging from $z = -0.22$ m to $z = 0.22$ m in the spanwise direction and from

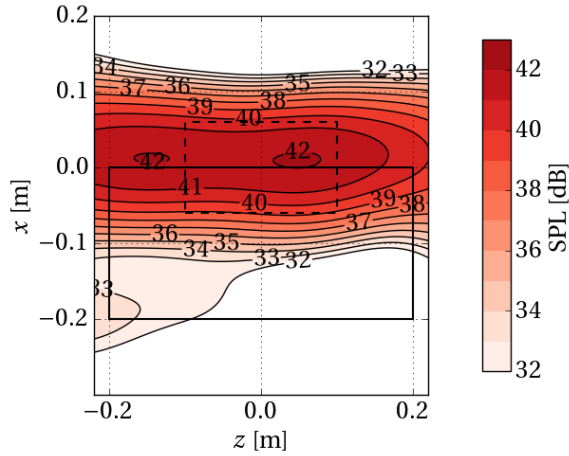


Figure 7.2: One-third octave band (3150 Hz) beamforming source plot for the straight edge airfoil with $U_\infty = 40$ m/s and $\alpha = 0^\circ$. The solid black line represents the airfoil position, and the dashed black line the integration region.

$x = -0.3$ m to $x = 0.2$ m in the streamwise direction, according to the axes defined in figure 3.10, with a distance between grid points of 1 mm. Thus the resulting grid size is 441×501 .

Since TBL-TE noise is assumed to be a distributed sound source, the source maps were integrated over an area extending from $z = -0.1$ m to $z = 0.1$ m and from $x = -0.06$ m to $x = 0.06$ m. This region was selected to reduce the contribution from extraneous sound sources, while still containing a representative part of the trailing edge noise ([7.13]). A source map sample, indicating the airfoil and integration region (dashed line), is shown in figure 7.2.

The beamforming results in that region were normalized by the value of the integral of a simulated line source of monopoles of unitary strength placed horizontally at the trailing-edge position ($x = 0$ and from $z = -0.1$ m to $z = 0.1$ m), evaluated within the same area. This method was proposed by Sijtsma ([7.14]) and it is a similar approach as the Covariance Matrix Fitting algorithm ([7.15, 16]) applied to the Source Power Integration technique ([7.11]). This method was proven to provide very accurate results in the array methods benchmark ([7.17]) for a simulated line-source heavily contaminated with background noise. In addition, for this chapter, the main diagonal of the cross-spectral matrix was deleted to reduce the influence of incoherent background noise.

This integration process was then repeated for each frequency of interest to obtain the acoustic frequency spectra of the trailing edge for the different serrations configurations.

7.3. RESULTS

The integrated sound pressure level (SPL) at a reference distance of 1 m of the four serrated geometries and the straight edge is observed in figure 7.3. The three investigated

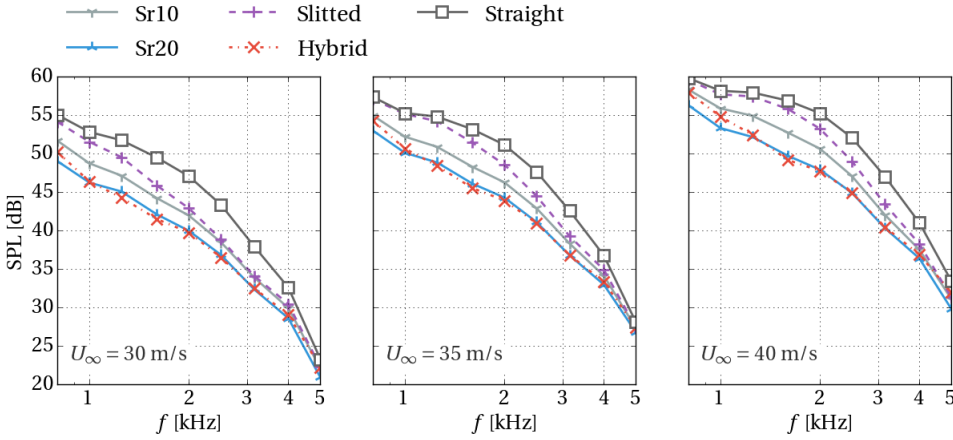


Figure 7.3: Absolute integrated SPL for the four serrated geometries and the straight edge at $\alpha = 0^\circ$.

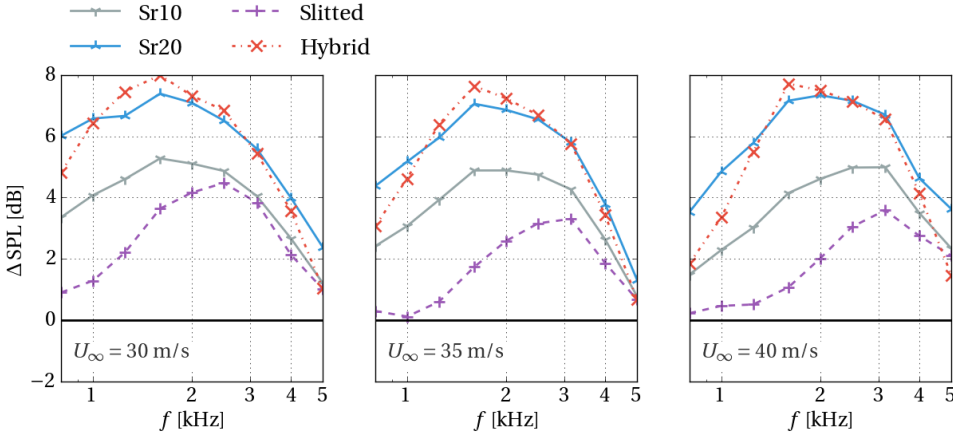


Figure 7.4: Relative integrated SPL for the four serrated geometries with respect to the straight edge at $\alpha = 0^\circ$.

freestream velocities are shown for $\alpha = 0^\circ$. The noise reduction by all four serrations is evident.

To better illustrate the levels of noise reduction obtained, the same data is presented relative to the straight edge in figure 7.4. A positive ΔSPL represents a reduction in noise.

Reduction levels of up to 8 dB are achieved by the Hybrid serrations. Serrations Sr20 perform similar, exhibiting only slightly lower reduction levels. The short serrations, Sr10, perform about 2 dB worse across the observed spectrum. The Slitted design prove to be most inefficient, especially at frequencies below 2.5 kHz. This result disagrees with what has been observed in [7.5], where this design performed similar or better than the equivalent solid serration design. It again should be noted that the airfoil used in [7.5] was not symmetric, nevertheless the slit and serration geometries are comparable.

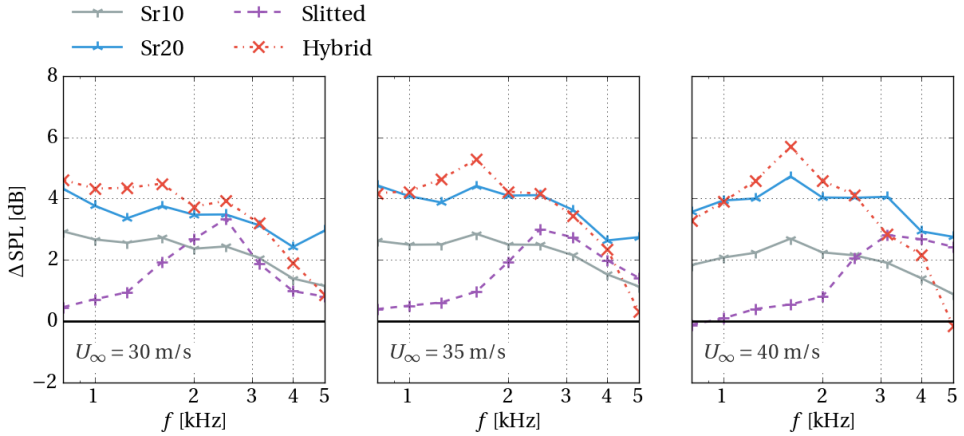


Figure 7.5: Relative integrated SPL for the four serrated geometries with respect to the straight edge at $\alpha = 12^\circ$.

The reduction level trends vary moderately across the investigated velocities, showing some slight degradation at lower frequencies.

The results at $\alpha = 12^\circ$, shown in figure 7.5, exhibit a weakened noise reduction performance for all the serration designs. Sr20 and Hybrid remain as the designs that reduce most noise, topping almost at 6 dB. Negligible trend differences are again observed with increasing velocity, suggesting that the noise reduction performance is only weakly affected by it.

7

7.4. DISCUSSION

All investigated serration designs provided a reduction of the noise compared to the straight edge. Differences between them were nevertheless observed.

In the current experiment, the serrations were investigated at a zero flow incidence, in the $\alpha = 0^\circ$ case. This was achieved by using a symmetric airfoil and no serration flap angle. The same flow conditions were thereby attained over the upper and lower serration sides.

Under these conditions, only small or negligible differences have been found in the mean boundary layers features over the Sr20 and the Slitted serrations ([7.18]). It is suggested therefore that the poor noise reduction achieved with the Slitted serrations, compared to Sr20, is likely explained from a standpoint of the scattering efficiency reduction by the geometrically modified edge.

An argued intent of the serrations is indeed to avert a trailing edge design which is perpendicular to the flow direction, thereby alleviating the impedance discontinuity at the edge ([7.19–21]). The Slitted serration design nevertheless retains a strong impedance change at the location where the slits originate, where it preserves 50% of the wetted edge of the straight trailing edge. It has been furthermore shown that at this location the intensity of the acoustic source term is larger ([7.22]), possibly having a more critical effect on noise. It is therefore likely that this feature fails to achieve the intended

relaxation of the impedance discontinuity. The Hybrid serrations instead successfully recover the alleviation of that discontinuity, even instead outperforming Sr20 in noise reduction at around 1.8 kHz.

The performance of the Hybrid design suggests that the slits are indeed not an unwanted feature, but they need to be carefully integrated into a proper design. It is further interesting to note that, despite that the Hybrid design has the same solid serration contour as Sr10 (see figure 7.1), it consistently reduces more noise than the former, especially in the central frequency range that has been observed.

At $\alpha = 12^\circ$ the relative noise reduction trends of the different designs remain similar, with the Sr20 and Hybrid serrations being most effective, although by a lesser degree.

It is worth noting that the mean flow in the boundary layer is known to be heavily modified by the solid serration when serration-flow misalignment is prescribed ([7.7, 23]). Strong streamwise vortical structures have been observed originating from the serration edges, and increased turbulence activity has been measured at the pressure side near them ([7.24], chapter 6). The turbulent structures near the edges are therefore significantly modified and are vastly different on the upper and lower serration sides. Despite of this, noise reduction is still observed by up to 4 dB, reinforcing the hypothesis that a crucial factor to achieve noise reduction remains the alleviation of the impedance discontinuity, which is still obtained despite the introduction of serration-flow misalignment and important modifications to the flow.

Slitted serrations, on the other hand, have been shown to exhibit less large-scale mean flow modification ([7.18]), likely due to its permeability, allowing an alleviation of the pressure difference between the upper and lower sides of the serrations. Avoiding the observed flow modification of the solid serrations does not appear therefore to be an advantage for improving noise reduction, without an effective relief of the impedance discontinuity.

Instead, the Hybrid serrations, which already appeared to have a more efficient modification of this discontinuity in the $\alpha = 0^\circ$ case, recover again the levels of noise reduction of Sr20. Improvement is observed between around 1 and 2 kHz, while the effect appears to lose effectiveness for frequencies close to 5 kHz. A detailed flow study may reveal the reason for this, but remains otherwise unexplained at this point.

7.5. CONCLUSIONS

The noise reduction of several serration designs has been investigated with respect to the unmodified trailing edge of a NACA 0018 airfoil. Several flow velocities and angles of attack were prescribed, and a reduction in the noise was confirmed for all the serrations.

Differences in the reduction levels were nevertheless observed. The Slitted serrations exhibit the lowest reduction, while the Hybrid and Sr20 designs the highest.

The observations imply that the design of serrations should focus on the alleviation of the impedance discontinuity at the trailing edge, which is suggested to be the primary mechanism to obtain noise reduction. Further benefits may be obtained from beneficially modifying the flow or pressure properties near the edge.

Designs such as the Hybrid serrations might be an interesting alternative to the traditional serration design. The significant reduction of TBL-TE noise is supplemented by a smaller wetted surface, compared to solid serrations with a similar noise reduction

(Sr20, in this case). This is likely to have a lower impact to the aerodynamic performance of the airfoil on which the serrations are installed, a desirable feature for their use in some industrial wind turbine applications.

BIBLIOGRAPHY

- [7.1] C. Arce León, R. Merino-Martínez, S. Pröbsting, D. Ragni, and F. Avallone, *Acoustic Emissions of Semi-Permeable Trailing Edge Serrations*, [Acoustics Australia](#) , 1 (2017).
- [7.2] J. Hurault, A. Gupta, E. Sloth, N. C. Nielsen, A. Borgoltz, and P. Ravetta, *Aeroacoustic wind tunnel experiment for serration design optimisation and its application to a wind turbine rotor*, in *6th International Meeting on Wind Turbine Noise* (Glasgow, 2015).
- [7.3] J. Mathew, A. Singh, J. Madsen, and C. Arce León, *Serration Design Methodology for Wind Turbine Noise Reduction*, [Journal of Physics: Conference Series](#) **753**, 022019 (2016).
- [7.4] S. Oerlemans, *Reduction of wind turbine noise using blade trailing edge devices*, [22nd AIAA/CEAS Aeroacoustics Conference](#) , 1 (2016).
- [7.5] M. Gruber, P. Joseph, and M. Azarpeyvand, *An experimental investigation of novel trailing edge geometries on airfoil trailing edge noise reduction*, in [19th AIAA/CEAS Aeroacoustics Conference](#) (AIAA, Berlin, Germany, 2013).
- [7.6] M. Gruber, P. Joseph, and T. Chong, *On the mechanisms of serrated airfoil trailing edge noise reduction*, in [17th AIAA/CEAS Aeroacoustics Conference \(32nd AIAA Aeroacoustics Conference\)](#), Vol. 2781 (American Institute of Aeronautics and Astronautics, Portland, Oregon, USA, 2011) pp. 5–8.
- [7.7] C. Arce León, D. Ragni, S. Pröbsting, F. Scarano, and J. Madsen, *Flow topology and acoustic emissions of trailing edge serrations at incidence*, [Experiments in Fluids](#) **57**, 91 (2016).
- [7.8] A. L. Braslow, R. M. Hicks, and R. V. Harris Jr., *Use of grit-type boundary-layer transition trips on wind-tunnel models*, [NASA Technical Note](#) (1966).
- [7.9] C. Arce León, R. Merino-Martínez, D. Ragni, F. Avallone, and M. Snellen, *Boundary layer characterization and acoustic measurements of flow-aligned trailing edge serrations*, [Experiments in Fluids](#) **57**, 182 (2016).
- [7.10] D. H. Johnson and D. E. Dudgeon, *Array Signal Processing, Concepts and Techniques* (P T R Prentice Hall, Englewood Cliffs, 1993) ISBN: 9780130485137.
- [7.11] P. Sijtsma, *Phased array beamforming applied to wind tunnel and fly-over tests*, Tech. Rep. NLR-TP-2010-549 (National Aerospace Laboratory (NLR), Anthony Fokkerweg 2, 1059 CM Amsterdam, P.O. Box 90502, 1006 BM Amsterdam, The Netherlands, 2010).

- [7.12] A. Brandt, *Noise and vibration analysis: signal analysis and experimental procedures*, Second (John Wiley & Sons, 2011) ISBN 978-0-470-74644-8.
- [7.13] C. C. J. Pagani, D. S. Souza, and M. A. F. Medeiros, *Slat Noise: Aeroacoustic Beam-forming in Closed-Section Wind Tunnel with Numerical Comparison*, *AIAA Journal* **54**, 2100 (2016).
- [7.14] P. Sijtsma, *Analytical Benchmark 1*, in 22nd AIAA/CEAS Aeroacoustics Conference. May 30 - June 1 2016. Lyon, France. (2016) Presentation in Microphone Array Methods Discussion Panel.
- [7.15] T. Yardibi, J. Li, P. Stoica, N. S. Zawodny, and L. N. Cattafesta III, *A covariance fitting approach for correlated acoustic source mapping*, *Journal of the Acoustical Society of America* **127**, 2920 (2010).
- [7.16] B. J. Tester, *Engine noise source breakdowns from an improved inverse method (AFINDS) of processing phased array measurements*, in 20th AIAA/CEAS Aeroacoustics Conference. June 16-20 2014. Atlanta GA, USA. (2014) AIAA paper 2014-3067.
- [7.17] E. Sarradj, G. Herold, P. Sijtsma, R. Merino-Martinez, T. F. Geyer, C. J. Bahr, R. Porteous, D. J. Moreau, and C. J. Doolan, *A microphone array method benchmarking exercise using synthesized input data*, in 23rd AIAA/CEAS Aeroacoustics Conference. June 5-9 2017. Denver, CO, USA. (2017) abstract submitted for the conference.
- [7.18] C. Arce León, F. Avallone, S. Pröbsting, and D. Ragni, *PIV Investigation of the Flow Past Solid and Slitted Sawtooth Serrated Trailing Edges*, in 54th AIAA Aerospace Sciences Meeting, January (American Institute of Aeronautics and Astronautics, San Diego, California, 2016) pp. 1–15.
- [7.19] M. S. Howe, *Noise produced by a sawtooth trailing edge*, *The Journal of the Acoustical Society of America* **90**, 482 (1991).
- [7.20] M. Azarpeyvand, M. Gruber, and P. Joseph, *An analytical investigation of trailing edge noise reduction using novel serrations*, in 19th AIAA/CEAS Aeroacoustics Conference (2013).
- [7.21] B. Lyu, M. Azarpeyvand, and S. Sinayoko, *Noise Prediction for Serrated Leading-edges*, 22nd AIAA/CEAS Aeroacoustics Conference (2016), 10.2514/6.2016-2740.
- [7.22] F. Avallone, S. Pröbsting, and D. Ragni, *Three-dimensional flow field over a trailing-edge serration and implications on broadband noise*, *Physics of Fluids* **28**, 117101 (2016).
- [7.23] C. Arce, D. Ragni, S. Pröbsting, and F. Scarano, *Flow Field Around a Serrated Trailing Edge at Incidence*, in 33rd Wind Energy Symposium (American Institute of Aeronautics and Astronautics, Kissimmee, Florida, 2015).
- [7.24] C. Arce León, R. Merino-Martínez, D. Ragni, F. Avallone, F. Scarano, S. Pröbsting, M. Snellen, D. G. Simons, and J. Madsen, *Effect of trailing edge serration-flow misalignment on airfoil noise emissions*, *Journal of Sound and Vibration* **405**, 19 (2017).

8

CONCLUSION

The work presented here has investigated the effect that trailing edge serrations have on the flow near their surface, and how they modify the acoustic emissions of an airfoil compared to its original trailing edge geometry.

Serrations have been widely adopted by the wind industry in recent years, and represent a cost effective and relatively simple means of achieving a reduction of the overall rotor noise by reducing TBL-TE noise, hence their relevance. But some even fundamental questions on how they work remain unanswered.

Most serration-related research has traditionally leaned towards the evaluation of their acoustic emission ([8.1–4]), and some focus has been put on the parametric assessment of designs. Essential guidelines have been thus established, and the general form that a serration should have to function as an aeroacoustic device has been proposed ([8.5]).

While some level of flow characterization has been conducted before, an unfavorable circumstance afflicts a significant portion of it: the lack of flow symmetry between the upper and lower serration surfaces, brought on by a prevalent use of cambered airfoils, airfoils at incidence, serrations with flap angles, and otherwise flat plates with non-symmetric trailing edge fairings. These configurations make it difficult or outright impossible to ensure similar flow over both serration sides.

The flow-alignment of serrations—that is, when the serrations follow the direction that the mean flow streamlines have without them being present—is argued in this thesis to be a critical criterion to investigate the mechanism that makes serrations reduce noise.

An infinitely thin (mean flow-aligned) flat plate with a serrated trailing edge is expected to be effective at reducing noise. This situation is in fact the baseline assumption in the analytic solution of variable-shape trailing edge aeroacoustics ([8.6–8]). The flow-misalignment of serrations, for the purpose of understanding their noise reduction mechanism, is therefore considered in the present work as an introduction of contamination to the measurements.

Such a condition would create flow structures that are not present in the flow-aligned

case, and which may therefore be unnecessary to achieve noise reduction. This is not to say that, through the beneficial modification of flow, serrations *may enhance* the amount of noise reduced, which may be an entirely likely situation in some cases, as presented in chapter 5.

It is in fact very interesting and worth noting again that, even when significantly flow-misaligned, serrations retain their noise reduction feature. To a large degree, when flow-misaligned is induced, the noise modification compared to a flow-aligned case is instead ascribed to the introduction of *new* aeroacoustic noise sources (as detailed in chapter 6) and, arguably to a lesser degree, the loss of noise reduction capability.

Serration-flow misalignment therefore conforms a cornerstone and recurrent topic in this thesis and the research that supports it. It is concluded from the extensive analysis of flow and aeroacoustic measurements performed on serrations that the purposeful prescription of flow misalignment on the serrations can indeed be used to improve our knowledge on the mechanism behind noise reduction.

Mindful of this proposition, the learnings of the research presented in chapters 4, 5, 6 and 7, are here summarized.

1. On the serration-flow misalignment by flap angle or airfoil incidence

Misalignment in this work was prescribed by modifying (either, or in combination) the angle of attack and the flap angle of the serrations.

It was observed that the mean flow is notably more sensitive to a flap angle modification rather than that of the angle of attack (chapter 4).

This conclusion becomes intuitive if the angle of attack is thought of as having a wider modification on the flow around the entire airfoil, while the flap angle has a more local and more sudden effect in the immediate vicinity of the serrations.

2. On the near-surface flow deflection induced by serration-flow misalignment

When flow-misalignment is prescribed on the serrations, PIV-measured mean flow data over the near surface of the serrations shows significant deflection. Over the pressure side, outwards curvature (away from the serration center) is observed over the surface, while over the suction side it curves inwards, with maxima found after crossing the trailing edge, and some deflection seen outwards further downstream (section 4.2.1).

3. Regarding the upstream mean flow modification by serrations

For flow-aligned serrations, none or negligible modifications are made to the boundary layer flow over the joint between the airfoil and the serrations, compared to that of the unserrated straight edge at the same location. There is also no indication that meaningful spanwise alteration of the flow exists at the root. When flow-misaligned, some level of modification is instead observed. Detailed results are found in section 4.2.2.

4. On the formation of streamwise vorticity by serration-flow misalignment

Serration-flow misalignment has been related to the formation of strong, steady and counter-rotating streamwise vortices that originate from opposing serration tooth sides (section 4.2.1). Upwash between serration teeth correlates to the mean flow deflection observed near the surface.

These structures nevertheless reside in the wake, and aren't seen to directly interact with the surface or edges. They are thus not believed to contribute to the far-field noise, given the low Mach number and therefore dominance of dipole sources of noise.

5. Spectral shapes and levels of experimental and theoretical noise reduction

The research here presented echoes the observations in [8.1, 3, 4], where the levels of noise reduction measured (regardless of flow-alignment) are overpredicted by the theory in [8.6] (and on which [8.7] is based). The overall levels are more accurately predicted in [8.9], but the spectral shape of the reduction remains underpredicted in the lower frequencies and overpredicted in the higher frequencies by all analytic solutions (section 4.2.4).

6. Regarding the departure of the mean flow from the analytical assumptions

Having noted this significant deviation between the measured and predicted noise reduction, flow departure from the assumptions made in the theory might suggest an explanation.

An important assumption made in the theory regarding the mean flow is that it should follow Taylor's frozen turbulence hypothesis. With respect to the geometry, it is assumed that the serrations extend from a semi-infinite (infinitesimally thin) flat plate without incidence.

Chapters 4 and 5 address the streamwise alteration over the serration surface for the flow-aligned case, and some level of it is indeed found. Nevertheless, the setup used here undeniably fails to resemble a semi-infinite flat plate. Despite conceiving a configuration where the serrations achieve mean flow symmetry over their two sides, a relatively thick airfoil (a NACA 0018) has been used. This makes the presence of an adverse pressure gradient around the transition between the airfoil and the serrations quite unavoidable. The angle present between them at their joint may in fact also be a source of flow modification.

Therefore, while streamwise flow modification was observed, it cannot be inferred that the same would be present in the case of a semi-infinite, infinitesimally thin flat plate with a serrated trailing edge. It is perfectly plausible that in such a case it would be near or entirely negligible.

Furthermore, it must be observed that the level of streamwise flow modification is relatively small. It would be therefore unanticipated that the significant differences seen between the measured and predicted noise reductions could be explained entirely by this modest change and its departure from the analytical assumptions.

While this statement is contemplated, this work will not venture a source of error to the analytic approaches that are today available.

7. On the streamwise flow modification of the boundary layer of flow-aligned serrations

As mentioned in the previous point, the flow was seen to exhibit some level of flow modification in the streamwise direction as it convects over the serrations. The question of whether this plays a role in the noise reduction mechanism was therefore investigated.

Chapter 5 addresses this subject by examining relevant boundary layer parameters. These have been chosen based on terms used in the TNO-Blake model for trailing edge noise modeling (the backscattered pressure and unobtainable pressure features were omitted), and previous findings regarding the correlation between high surface pressure peaks and Reynolds stress events are considered.

The inspection suggests that, as the flow convects over the serrations, it experiences beneficial changes that may culminate in less noise being emitted to the far-field. Based on the TNO-Blake model, alterations in the boundary layer shear factor and its overall thickness appear to be dominating factors. Some modification observed in the turbulence spectrum also suggests that a level of energy loss occurs in the lower-frequency as the flow approximates the serration tip.

As serrations are placed misaligned to the flow, these observations may nevertheless change. Furthermore, they may be case-dependent, conditioned for example to which airfoil is used, its camber and its thickness.

8. Flow misalignment of serrations and its role increasing noise

Assumptions as to whether the flow-misalignment of serrations lead to a loss of noise reduction performance, or indeed a noticeable increase in noise, have been raised before ([8.1–3, 10, 11]).

The research presented in chapter 6 looks more deeply into the acoustic consequences of misaligning serrations, both by an increase in angle of attack, and flap angle.

Reiterating the observations made on the flow impact of either of these changes, a substantial change in acoustic emissions was observed when a change in flap angle was prescribed. A noise increase of around 8 dB was measured at the higher frequencies. A change in angle of attack resulted instead only in a modest modification of the emitted noise.

It was confirmed therefore that serration-flow misalignment results in a significant increase in noise, and that this noise is of a high frequency character, manifested as an increase above a particular crossover frequency, compared to the noise of the unserrated trailing edge. Previous observations were thus confirmed.

9. On the relation of the crossover frequency to a Strouhal number

In [8.10] it is proposed that the crossover frequency mentioned in the previous point can be related to a constant Strouhal number ($St_c \approx 1$), associating it with the boundary layer thickness and free-stream velocity.

In chapter 6 this question was addressed by performing acoustic and boundary layer measurements at several degrees of serration-flow misalignment and free-stream velocities.

The findings indicate that, to consider the crossover Strouhal number as a constant value, would only approximate the situation over a range of free-stream velocities, under which a small but consistent change is nevertheless still observed.

For a change in angle of attack, the crossover Strouhal number displays instead a considerable variation. A linear correlation between the two was proposed.

It is concluded therefore that the Strouhal number is far from being constant. It seems rather dependant on the angle of attack and the flap angle (which is in fact not accounted for in the Strouhal number equation). To a lesser degree, but still significantly so, it appears to vary linearly for the free-stream velocity. And it is furthermore conceivable that it could be affected by airfoil shape.

While the situation is clearly more complicated than that suggested in [8.10], its findings and the more detailed observations made here suggest that the proposed Strouhal number behavior remains a useful parameter for serration design. The crossover frequency can be thereby anticipated for a range of angles of attack and free-stream velocities, given a particular airfoil and serration design for which it has been established *ab initio* for a small set of conditions.

10. The source of high frequency noise increase from serration-flow misalignment

While this research confirmed the previously observed increase in noise by flow-misaligned serrations, it also aimed at resolving the issue of what causes it (chapter 6). Earlier studies have proposed that it is the increase in turbulence in the region between serration teeth ([8.5]).

High-speed stereoscopic particle image velocimetry (S-PIV) measurements were performed, and the flow at the near-edge regions of the serrations and straight trailing edges was compared. It was determined that a significant increase in the root mean square (rms) of the flow is induced on the pressure side (around double that of the straight edge), correlated to regions where the most mean flow spanwise deflection was observed.

Further inspection of the turbulence spectra at this location showed a noticeable increase in high frequency energy (by about 5 dB) for the misaligned serration case, with respect to the straight edge. The location in the turbulence spectrum where the turbulence crossover frequency is observed correlates well with the spectral location of the acoustic crossover frequency.

It is concluded therefore that the high frequency noise increase is due to an increase in the energy of smaller scale turbulence structures near the pressure side edge of the serrations.

11. Regarding the noise reduction performance of slitted serration designs

Research presented in [8.12] suggests that the addition of surface permeability to the serration design, in the form of slits, offers added benefits to noise reduction,

and in fact may lead to the prevention of the high frequency noise increase mentioned earlier.

In the work discussed in chapter 7 it was attempted to replicate this finding. The slitted serration design was compared acoustically to conventional solid serrations, and a hybrid mix between the two.

It was not possible to reproduce the benefits of the slitted serrations, which showed only a relatively small noise reduction, around 3 dB at its maximum. The hybrid design provided instead similar reduction levels as the best-performing solid serration, around 8 dB at its maximum. They surpassed every other serration design in certain cases or frequencies.

The observed differences in noise reduction efficiency by the different serration designs at zero serration-flow misalignment are of particular interest. As none or only small differences in the mean flow and its statistics were previously reported ([8.13]), the significant deviations in noise reduction suggest that the flow modification by serrations is likely but a secondary contributor to the noise reduction mechanism, as argued before, and discussed further in the following point.

12. Towards a hypothesis for the noise reduction mechanism of trailing edge serrations

Broadly speaking, two trends of thought exist on how serrations may reduce noise. The generation of beneficial flow changes by the presence of the serrations (for example, but not exclusively supported in [8.14, 15]), and a reduction of the acoustic scattering efficiency provided by the serrated edge (equally not exclusively in [8.4, 6, 9, 16]) have been proposed as the mechanism drivers¹.

The establishment of the dominating process is scheduled to be of consequence to the formulation of a sensible serration design philosophy, hence its value within an industrial standpoint. Its relevance as a research question is thereby asserted, and the carefulness by which it should be addressed is highlighted.

As indicated in the beginning of this chapter, the present work considers serration-flow misalignment as a source of potentially unwanted hydrodynamic modification. This condition could lead to the observation of flow structures that are not essential to the attainment of noise reduction, but which could affect the interpretation of the results.

These effects should therefore be contemplated when surveying research where serration-flow misalignment is present (for example [8.10, 14, 15, 17]). Even in cases where flow-alignment is attempted (such as the current one and [8.18, 19]), results should be carefully interpreted. As mentioned above, the airfoil geometry used here is expected to induce an adverse pressure gradient near the trailing edge which can potentially lead to changes as the flow convects downstream over the serrations.

The presence of the serrations may thus correlate with flow modification in some cases, but it is not necessarily its source. The corollary can equivalently be made

¹Whether both mechanisms contribute to noise reduction is likely; the answer sought is which dominates.

where flow may well be modified, but correspondingly, it is not necessarily the cause of the pursued acoustic alteration.

With the intention of committing a hypothesis on the working mechanism of serrations, the research presented in chapter 7 is recalled. The acoustic emission differences observed there between the flow-aligned solid (Sr10 and Sr20), Slitted and Hybrid serrations, are suggested to be pivotal to the determination of the noise reduction mechanism driver.

The investigation in [8.13] supports the assumption that the flow modification is considered minimal in the flow-aligned case between the different designs. The geometric similarity between the Hybrid and Slitted serrations, and the Hybrid and solid serrations further strengthens this assertion. It would be therefore implausible that the significant differences of about 7 dB in reduction observed in the acoustic emissions are a reflection of such modest flow modification.

When approaching the question from a perspective of edge scattering efficiency, a far more compelling argument is raised.

The Slitted serrations approach more closely the geometry of the original trailing edge of the airfoil, sharing 50% of its wetted edge. They also exhibit the worst noise reduction achieved (around 3 dB versus 8 dB for the Hybrid serrations, as mentioned above). It is argued that this loss of performance is due to their failure to significantly alleviate the large impedance jump suffered as the flow convects past the straight edge.

This feature is nevertheless recovered by the solid serrations, where a piecewise (but otherwise uninterrupted) slanted edge is introduced to the airfoil trailing edge geometry. As originally proposed in [8.6], this is what accomplishes noise reduction. It is further replicated again with the Hybrid serration design, whereby the slitted component is complimented with a solid serrated edge, and where a significant noise reduction is again observed.

This finding, in addition to the flow and acoustic measurements reported earlier in this work, allows to reach a conclusion on the ultimate purpose of serrations as a noise reduction device: to moderate the impedance discontinuity at the trailing edge by slanting it and thus avoiding edges that are perpendicular to the flow convection.

As proposed in [8.6], sawtooth shaped trailing edge serrations remain the most basic geometry that effectively achieves noise reduction, and by following the recommendations in [8.5], a designer can very well accomplish a successful device.

But as one undertakes the challenge of creating a mass-produced component that is expected to endure the harsh and changing conditions as it remains attached to a wind turbine blade, complications are bound to arise. A resourceful blend between the right material, a sturdy construction, and the right shape should be realized. Considering all of these factors, and the noise reduction performance we observe today in blades out in the field, we find ourselves far from closing this chapter, and the work of an aeroacoustician remains essential.

BIBLIOGRAPHY

- [8.1] T. Dassen, R. Parchen, J. Bruggeman, and F. Hagg, *Results of a wind tunnel study on the reduction of airfoil self-noise by the application of serrated blade trailing edges*, Tech. Rep. (National Aerospace Laboratory, NLR, 1996).
- [8.2] S. Oerlemans, M. Fisher, T. Maeder, and K. Kögler, *Reduction of wind turbine noise using optimized airfoils and trailing-edge serrations*, *AIAA Journal* **47**, 1470 (2009).
- [8.3] A. Finez, E. Jondeau, M. Roger, and M. C. Jacob, *Broadband Noise Reduction of a Linear Cascade With Trailing Edge Serrations*, in *17th AIAA/CEAS Aeroacoustics Conference (32nd AIAA Aeroacoustics Conference)* (Portland, Oregon, USA, 2011).
- [8.4] M. Gruber, *Airfoil noise reduction by edge treatments*, *Ph.D. thesis*, University of Southampton (2012).
- [8.5] M. Gruber, P. Joseph, and T. Chong, *On the mechanisms of serrated airfoil trailing edge noise reduction*, in *17th AIAA/CEAS Aeroacoustics Conference (32nd AIAA Aeroacoustics Conference)*, Vol. 2781 (American Institute of Aeronautics and Astronautics, Portland, Oregon, USA, 2011) pp. 5–8.
- [8.6] M. S. Howe, *Noise produced by a sawtooth trailing edge*, *The Journal of the Acoustical Society of America* **90**, 482 (1991).
- [8.7] M. Azarpeyvand, M. Gruber, and P. Joseph, *An analytical investigation of trailing edge noise reduction using novel serrations*, in *19th AIAA/CEAS Aeroacoustics Conference* (2013).
- [8.8] B. Lyu, M. Azarpeyvand, and S. Sinayoko, *A Trailing-Edge Noise Model for Serrated Edges*, in *21st AIAA/CEAS Aeroacoustics Conference* (AIAA, Dallas, Texas, 2015).
- [8.9] B. Lyu, M. Azarpeyvand, and S. Sinayoko, *Prediction of noise from serrated trailing edges*, *Journal of Fluid Mechanics* **793**, 556 (2016), [arXiv:1508.02276](https://arxiv.org/abs/1508.02276).
- [8.10] M. Gruber, P. Joseph, and T. Chong, *Experimental investigation of airfoil self noise and turbulent wake reduction by the use of trailing edge serrations*, in *16th AIAA/CEAS Aeroacoustics Conference* (2010) pp. 1–23.
- [8.11] A. Vathylakis, C. C. Paruchuri, T. P. Chong, and P. Joseph, *Sensitivity of aerofoil self-noise reductions to serration flap angles*, *22nd AIAA/CEAS Aeroacoustics Conference*, 1 (2016).
- [8.12] M. Gruber, P. Joseph, and M. Azarpeyvand, *An experimental investigation of novel trailing edge geometries on airfoil trailing edge noise reduction*, in *19th AIAA/CEAS Aeroacoustics Conference* (AIAA, Berlin, Germany, 2013).
- [8.13] C. Arce León, F. Avallone, S. Pröbsting, and D. Ragni, *PIV Investigation of the Flow Past Solid and Slitted Sawtooth Serrated Trailing Edges*, in *54th AIAA Aerospace Sciences Meeting*, January (American Institute of Aeronautics and Astronautics, San Diego, California, 2016) pp. 1–15.

- [8.14] R. Arina, R. Della Ratta Rinaldi, A. Iob, and D. Torzo, *Numerical Study of Self-Noise Produced by an Airfoil with Trailing-Edge Serrations*, in [18th AIAA/CEAS Aeroacoustics Conference \(33rd AIAA Aeroacoustics Conference\)](#), June (American Institute of Aeronautics and Astronautics, Colorado Springs, CO, 2012) pp. 4–6.
- [8.15] T. P. Chong and A. Vathylakis, *On the aeroacoustic and flow structures developed on a flat plate with a serrated sawtooth trailing edge*, [Journal of Sound and Vibration](#), **1** (2015).
- [8.16] L. Jones and R. Sandberg, *Numerical Investigation of Airfoil Self-Noise Reduction by Addition of Trailing-Edge Serrations*, in [16th AIAA/CEAS Aeroacoustics Conference](#), Vol. 2010–3703, AIAA (American Institute of Aeronautics and Astronautics, Reston, Virginia, 2010) pp. 1–23.
- [8.17] F. Avallone, S. Pröbsting, and D. Ragni, *Three-dimensional flow field over a trailing-edge serration and implications on broadband noise*, [Physics of Fluids](#) **28**, 117101 (2016).
- [8.18] W. C. van der Velden, A. van Zuijlen, and D. Ragni, *Flow topology and noise emission around straight, serrated and slitted trailing edges using the Lattice Boltzmann methodology*, [22nd AIAA/CEAS Aeroacoustics Conference](#), **1** (2016).
- [8.19] W. C. van der Velden and S. Oerlemans, *Numerical analysis of noise reduction mechanisms on improved trailing edge serrations using the Lattice Boltzmann method*, [35th Wind Energy Symposium](#), **1** (2017).

EPILOGUE

The fundamental importance of the serration-flow alignment parameter has been repeatedly stated throughout this work. While it was known from the beginning that it was a feature that required deeper investigation, its relevance became better understood later on.

Trailing edge serration knowledge, both experimental and numerical, has previously been cultivated using airfoil and serration models which overwhelmingly overlook a careful consideration of this parameter (see section 2.3 for a discussion on this). While from an airfoil performance point of view it might be tempting to consider the $\alpha = 0^\circ$, $\varphi = 0^\circ$ setup as uninteresting, the research presented here adopts it instead as the most fundamental and revealing case for the study of noise reduction.

The desired baseline condition of flow-alignment can be more generally understood as the attainment of equivalent flow conditions over the upper and lower serration sides. For this purpose, the use of a symmetric airfoil is thus preferred. It may in fact be necessary; working with camber severely complicates—or makes it straight out impossible to realize the flow equivalency objective.

Ultimately, the purpose of this objective is to achieve better control over the flow, and thus avoid unnecessary complexities when investigating noise reduction. It avoids the introduction of flow modifications by the serrations that would otherwise not exist in a serration-flow aligned setup. This is critical to describe the noise reduction mechanism through the separation of the hydrodynamic and scattering effects. Flow misalignment, as stated in chapter 8, would effectively construe the introduction of contamination to the experiment, thereby risking the false ascription of flow features as being necessary for noise reduction.

Nevertheless, avoiding such potentially misleading features remains challenging in an experimental setting. As it is proposed in the discussion of chapter 5, even the selection of a symmetric airfoil as a platform to study serrations still has the potential to introduce streamwise flow variations where the serrations would be located. This effect could for example be induced by its thickness and the ensuing adverse pressure gradient in the region around its trailing edge.

Ideally, but quite unrealistically, serrations should be installed at the trailing edge of a semi-infinite plate, approximating the theoretical models used by Howe. This would allow one further degree of control by attempting to avoid an induced departure from Taylor's frozen turbulence hypothesis. It would thus provide a *cleaner* flow and a better condition within which the noise reduction mechanisms of serrations can be investigated. The ideal setup would help to more confidently attribute flow modifications directly to the presence of the serrations.

In a real setting, such a configuration remains quite evidently a challenge. One reason is that the flat plate should be only as thick as the serrations (1 mm was the thickness

of the serrations used here). This naturally presents practical complications. Ensuring a long, yet even and rigid surface would be difficult.

The work here presented therefore naturally recognizes that much remains to be done. Through the use of a set of carefully designed experiments, and the ensuing discussions and observations presented in this and other work published elsewhere, it is the author's hope that a renewed basis for the advancement of the research has been laid. In its current state, a conclusion on the noise reduction mechanism has been put forward, and while the evidence endorses it, its assessment and scrutiny by other efforts is certainly encouraged.

The author believes that numerical simulations would offer a fitting approach to do this. A setup such as that described, wherein an infinitesimally thin, semi-infinite flat plate with a serrated trailing edge is far more realizable in that manner. A transient description of the surface pressure would be readily available, as would volumetric flow information. The flow and pressure modification by the serrations could thus be better investigated. Its absence, and confirmation that noise reduction is still attainable, would rule it out as a requirement for noise reduction.

Such an effort would then hopefully render a better description of this mechanism. The introduction of complexities to the system could then be conducted more assuredly. Beneficial and deliberate flow modification could be more accurately understood and controlled. And ultimately, better serration designs could be proposed.

ACKNOWLEDGEMENTS

It is said that to earn a PhD is to demonstrate that one is capable of conducting independent research. While I've always understood the spirit of that concept, I had to go through one to realize that it absolutely cannot be done alone.

Instead, the time spent on this PhD has been when I've needed most of the people around me. Whether for cleaning up a PIV run, a coffee under the stern watch of a scribbled whiteboard, a beer at one of Delft's finest, or, very simply, a hug.

To my parents, who have been there literally since day one, thanks for letting me attempt to find my own way, however stubborn that sometimes might have felt. It has been thanks to your teachings and example that it has led to such interesting and good places. But I am merely following your steps, trying to reach the very high-standard bar that you've set.

Inga, it has been six years of happiness. Your company and love have shone bright, through even the more darker days of this project. You gave me that much needed push, without which I don't know if I had been able to make it to this point. A few years ago you might have not thought you'd end up with some nerdy physicist, much less surviving a PhD by his side. But today you've earned this achievement as much as I have. You are amazing in ways I only wish I was, and it has been a pleasure to have been witness to these years of your life. I'm excited to spend the rest of our time making new memories and reliving some. Thanks for taking those many leaps of faith with me.

To my oldest friends from back home, Jason, Marcello, Henry and Daniel S.C., thanks for being an inspiration in your own right, in such different ways. The perseverance and passion in what you do and love is something I always try to reflect.

Thanks to Los Fuegos, Julián and Amila, for being an incredibly efficient distraction for so many years. You helped me get to places (and stages) I never thought I'd be, and form memories that I'll always treasure. Mario, thanks especially to you, for your unconditional and constant friendship during my time in Denmark, for the many things (good and bad) that we lived together, and for having a sense of humor and way of seeing the world of which I still have a lot to learn.

To those who made Kolding an unexpected hive of fun and a place to miss, Paul, Mario V., Mathilde, Mohammed, Aanchal, Agata, Anne-Cecilie, Elsa, Emil, Heidi, Rosemary, Kim, Martin D., Anne, thanks for the friendship and laughs.

To those who brought the best out of Delft, Daniel L., Sara, Javier, Silvia, Marcelo, thanks for the closeness, the very needed distraction, the adventures and trust.

To the space-ticos in (or formerly in) Delft, Adolfo and Johan, it is a privilege to know you and to be so close to the sidelines of the incredible chapter you are writing in our country's history. You are brave and steadfast, characteristics that can change and inspire the minds of many, something so very needed back home.

To those who made the Faculty a familiar place, Theo, Valeria, Martin, Jacopo, Thijs, Jan, David, Giuseppe, Beppe, Andrea, Marios, Tomas, thanks. I only wish I had had the

chance to be around more, and I wish you all the best in what is to come.

To those who made the labs and workshops a navigable place, Leo, Stefan B., Pieter, thanks for all the support.

To my closer colleagues in LM Aero and beyond, Jordy (thanks for the translations!), Rolf, Ganesh, Ram, Jose, and Ashish, it is a privilege to work and learn by your side. To Jitendra, thanks for the trust and closeness; I have always drawn pleasure and admiration from hearing you lay out a completely unexpected and wiser point of view. To Jesper Månsson, thanks for helping me open up a new and extremely exciting chapter in my professional life; I look forward to doing great things thanks to you.

To Peter, Morten and Michael (I know, former LM but whose legacy will always be felt), thanks for the loud and ceremonious coffee breaks, for the wet (water, and otherwise) sailing trips, the dinners, and for being my unofficial guides to the Danish way of life. P and M, you got me off from a dromedary and on to a snake. I don't think I would have been able to finish this research without python, or be that good at my job without it. I owe you for this.

To Jesper, thanks for being an awesome example at technical professionalism, analytical skill, and for setting the high work standard to which I will now always strive. You have shown me lots of trust by letting me be myself to get things done, yet you have always been there whenever I needed to get something off my chest—even complain about how mysterious and sneaky aeroacoustics can sometimes be. I look forward to continue being part of your team, and, with it, help you write the history of wind energy.

To Herman Snel, the person that set the rails for my career in this magnificent field. None of this would have been possible without you. Your confidence in me gave me the opportunity to achieve my dream of being part of the world's energy revolution. I am proud and thankful to know that I am following in the steps of the pioneering greats such as yourself.

To Colette. You are a dependable and invaluable source of help. We'll never be able to count the substantial amount of Aerodynamics' research that has been possible thanks to your support.

To my research partners, Dani, Stefan P., Roberto, Francesco and Wouter. Needless to say, what this PhD symbolizes is as much yours as it is mine. Thanks for the scientific, technical and philosophical discussions, for sharing your enviable skills with me and letting me learn from you. Thanks for the discussions and disagreements, which I hope ultimately led us to be better versions of our professional and individual selves.

To Fulvio, one of the tougher mentors I have had. You're the force that kept me from ever having felt like the work was good enough—perhaps just one more weight to my own thoughts of insufficiency. I think I eventually learned to appreciate your leadership style, mostly due to its effectiveness. Thanks for your patience and dedication to perfection, and the invaluable time you have committed to this work. Thanks for the opportunity to let me into your research team and achieve something I've become proud of, side by side to some of the most amazing and talented people I've met, including yourself.

Ingos tėveliams Vytautui ir Marytei bei broliui Valdui. Nepaisant mano skurdžios lietuvių kalbos jūs nuoširdžiai priėmėt mane į savo ratą ir leidote pasijusti dalele Jūsų šeimos. Ačiū jums už tai, bet labiausiai esu jums dėkingas, kad užauginate tokią

nuostabią dukrą².

Finalmente, a mi familia allá en mi país y donde sea, Mauricio, mis abuelas, mi bis-abuela Gole, my abuelastro, mis tíos y tías, mis primos y primas, gracias por todo el apoyo y comprensión. Puede que no sea bueno mostrándolo, pero pienso en ustedes todo el tiempo. Estar tan lejos y por tanto tiempo no es fácil. Sé que me he perdido de mucho, y es uno de los sacrificios más grande que he hecho. Pero sé también que están ahí, y los siento cerca gracias a todo el amor que siempre me han dado³.

²To Inga's parents, Vytautas and Maryte, and Valdi, you have welcomed me into your family between hand gestures and my embarrassing attempts at Lithuanian. Yet you have been warm and have made me feel a part of you. Thanks, and, most of all, thanks for having raised such an amazing daughter.

³Finally, to my family back home and elsewhere, Mauricio, my grandmothers, my great grandmother Gole, my step-granddad, my aunts and uncles, my cousins, thanks for your support and understanding. I may not be good at showing it, but I think of you all the time. Being so far and for so long is not easy. I know I am missing much, which is one of the heaviest sacrifices I've made. But I know that you are there, and I feel your presence thanks to all the love that you have always shown me.

LIST OF SYMBOLS

Greek symbols

α	Angle of attack
α^*	Effective angle of attack
α_g	Geometric angle of attack
δ	Boundary layer thickness
ϕ_m	Moving axis spectrum
Φ_p	Wall pressure wavenumber-frequency spectral density
ϕ_{22}	Vertical fluctuation spectral density
φ	Serration flap angle
γ	Deflection angle with respect to the undisturbed mean flow
κ_0	Acoustic wavenumber
λ	Serration wavelength
λ_p	Light wavelength
Φ_B	Blocked surface pressure wavenumber-frequency spectrum
σ	Standard deviation
$\sigma(\omega)$	Beamforming acoustic source signal
θ	Angle between the mean flow and the serration edge
θ_0	Undisturbed mean flow angle with respect to the serration edge
ω	Vorticity vector
ζ	Serrated trailing edge geometry function

Roman symbols

$a(\omega)$	Beamforming acoustic source amplitude
B	Total or stagnation enthalpy
b	Semi-chord ($C/2$)
C	Airfoil chord
C_H	Hagg constant
\mathbf{D}	Displacement field, PIV
d_{diff}	Airy disk diameter
d_τ	Imaged particle size
D_a	Lens effective aperture
d_g	Particle geometric image
d_p	Particle size
f_c	Acoustic crossover frequency
f	Lens focal length
$f_\#, f_l$	Lens f-number
h	Serration peak amplitude
i	Imaginary unit
ℓ_i	Correlation length in the i -th coordinate
$ \mathcal{L} $	Aeroacoustic transfer function
L	Airfoil span
L_{WA}	A-weighted sound power level
M	Magnification factor
p_b	Blocked pressure
p_i	Incident pressure field
p_s	Diffacted far-field pressure field
p_w	Surface pressure
St	Strouhal number

St_δ	Boundary layer-based Strouhal number	V_{Tip}	Blade tip speed
S_{pp}	Far-field acoustic spectrum	$\mathbf{U}_{c,w}$	Howe wake convection velocity
S_{qq}	Surface pressure cross-spectrum	Other symbols or conventions	
$1/\Delta T$	PIV acquisition frequency	$\langle \cdot \rangle$	Ensemble average
Δt	PIV laser pulse separation time	a'	Fluctuating part
Δt_{ac}	Acoustic measurement block length	\bar{a}	Mean
Δt_e	Acoustic emission time delay	a^*	Complex conjugate
T_{ac}	Total measurement time, acoustics	$a_{1,2,3}$	Streamwise, wall-normal and spanwise flow coordinates
$\mathbf{U}_{c,s}$	Howe mean surface convection velocity	u, v, w	Streamwise, wall-normal and spanwise velocity components
U_∞	Mean freestream velocity	u_r, v_r, w_r	Serration surface-aligned velocity components
U_c	Mean convection velocity	x, y, z	Streamwise, wall-normal and spanwise coordinates
$u_{c,i}$	Mean convection velocity in the i -th coordinate	x_r, y_r, z_r	Serration surface-aligned coordinate system

ACRONYMS

- 2C-2D PIV** planar two-component particle image velocimetry. 50, 51, 55, 56, 129, 130
- 2D** two-dimensional. 31, 55, 58
- AEP** anual energy production. 14, 15
- BANC** Benchmark Problems for Airframe Noise Computations. 28
- CNC** computer numerical control. 67
- DMD** dynamic mode decomposition. 34
- DNS** direct numerical simulation. 34
- FFT** fast Fourier transform. 59, 61
- FoV** field of view. 50, 51, 54, 58
- FW-H** Ffowcs-Williams Hawkins. 24
- kde** kernel density estimation. 112–114
- LBM** lattice-Boltzmann method. 34
- LCoE** levelized cost of electricity. 15
- LES** large eddy simulation. 34
- PIV** particle image velocimetry. xi, xii, xvii, 16, 25, 28, 48, 50–55, 57, 68, 70, 74, 83, 88, 95–103, 106, 115, 118, 119, 127, 128, 131, 137, 142, 149, 158
- RANS** Reynolds averaged Navier-Stokes. 28
- rms** root mean square. 70, 80, 83, 86, 132, 161
- RPM** revolutions per minute. 49
- S-PIV** stereoscopic particle image velocimetry. 50–52, 54–56, 66, 69, 96, 97, 102, 127, 130, 161
- SPL** sound pressure level. 59, 85, 132–135, 150–152

TBL-TE noise turbulent boundary layer-trailing edge noise. [xi](#), [xvii](#), [9–11](#), [13](#), [15](#), [33](#), [95](#), [126](#), [148](#), [150](#), [153](#), [157](#)

TNO Netherlands Organisation for Applied Scientific Research. [27](#)

INDEX

A

Acoustic beamforming, **58**, 59, 70, 128, 148, 149
 conventional frequency-domain beamforming, 59
 conventional frequency-domain beamforming, 149
Acoustic far-field spectrum
 Amiet, 25
 Howe, 26
Acoustic source map, 60, 70, 100, 101, 128, 132, 150
Aeroacoustics, 6
Airy disk, 52
Amiet
 shear layer correction, 59
 trailing edge noise model, 25
Angle of attack, 66, 67
 correction, 70
 effective, 32, 70
 geometric, 32, 70
Annual energy production, 14

B

Blunt trailing edge noise, 8

C

Chevron, 29
Compact bodies, 118
Crossover frequency, 86, 126, 134, 135, 142, 160, 161
Curl
 analogy, 24

D

Dipole, 24, 159

E

Eulerian method, 50

F

Ffowcs-Williams Hawkins
 analogy, 24
Flap angle, 66, 67, 71
F-number, **52**, 69, 129, 130
Fourier
 FFT, 59, 61
 transform, 30, 100, 149

H

Hagg
 constant, 11
 model, 11
Hanning weighing function, 59, 61, 100, 149
Hot-wire anemometry, 50
Howe
 serrated trailing edge model, **29**, 73, 74, 76, 86, 88, 163
 trailing edge noise model, **26**

I

Inflow noise, 9

L

Laminar boundary layer-instability
 noise, 8
Levelized cost of energy, 15
Lighthill
 analogy, 24
 equation, 26

M

Mean, **58**

P

Particle image velocimetry, 16, **50**, 70, 74, 83, 88, 95, 96, 115, 118, 127, 137, 142, 149, 158
 acquisition frequency, **55**

- displacement vector, 51
- planar 2C-2D, 50, 129, 130
- pulse separation time, **55**
- stereoscopic 3C-2D, 50, 66, 69, 96, 97, 127, 130, 161
- time-averaged, 16, 55, 57, 69, 101, 102
- time-resolved, 16, 55, 96, 102, 106, 119, 127
- Peak-locking, **53**, 69, 97, 99, 130, 131
- Poisson equation, **27**
- Pressure
 - blocked, 30
 - incident, 30
- Q**
- Quadrupole, 24
- R**
- Rayleigh
 - criterion, 60, 101, 128
 - limit, 101, 129
- Reynolds
 - decomposition, 27
- S**
- Scheimpflug
 - adapter, 54, 69, 97
 - intersection, 54
 - principle, **53**
- Schwartzschild solution, 31
- Standard deviation, **58**
- Steering function, 61
- Strouhal number, 34, 36, 126, 127, 135, 142, 160, 161
 - crossover, 127, 137, 161
- Surface pressure
 - Fourier transform, 28
- T**
- Taylor
 - frozen turbulence hypothesis, 25, 36
- Test section, 50, 58, 96, 100, 127, 128
 - closed, 70
 - open, 59, 70, 96
- Tip noise, 6
- TNO-Blake model, **27**, 95, 102, 107, 119
- Tracer particle, **51**, 96, 129
- Turbulent boundary layer-trailing edge
 - noise, **9**, 95, 126, 148, 150, 153, 157
- V**
- Velocity
 - spectral density, **28**
- Vibroacoustics, 5
- W**
- Wall pressure
 - wavenumber-frequency spectral density, **28**
- Wavenumber, 107, 115, 117, 120

EXTERNAL ART AND WORK ATTRIBUTIONS

3D wind turbine model, figures 1.3 and 1.5

Jeff Lewis, Grabcad.com

Human figure, figure 3.1

Clip art image by Cliparts.co

Shallow depth of field, figure 3.5

PiccoloNamek under [GFDL-SELF](#), source at Wikipedia

Other sources are stated in the text or figure captions.

CURRICULUM VITÆ

Carlos Andrés ARCE LEÓN

Carlos achieved his dream of becoming a physicist in 2006 when he got his B.Sc. from the University of Costa Rica. While initially curious about astrophysics, the application of numerical models to the solution of physical problems in general became a point of obsession, thanks in great part to the inspiring tutelage of Marcelo Magallón. This focal shift was reflected in a corresponding latitude change when he started his M.Sc. in Computational Science at the University of Uppsala. His thesis project for this degree became his first brush with the concept of trailing edge serrations. It came as a suggestion from Peter Fuglsang at LM Wind Power, a connection that was established thanks to Herman Snel. After concluding the M.Sc., in 2011, Carlos was hired by LM.

Born in March of 1983, in the outskirts of the city of Cartago, this physicist, son of two bright engineers, was on his way to becoming one more. As was the agreement with LM, Carlos soon began the application for funds to start a PhD under the Industrial PhD Programme of the Innovation Fund Denmark. While successful, the project became delayed until TU Delft was designated as a host in 2013. In the meantime, Carlos grew his experience under the guidance of Jitendra Bijlani and Jesper Madsen, helping LM develop their first rotor noise prediction software, and supporting the introduction of serrations as a prototype device, among other aerodynamics and aeroacoustics related tasks. Being part of the founding team dedicated to the research of aeroacoustics at LM was something both terribly exhilarating and challenging.

The PhD project started in June, 2013. A three-year fund scheme made adhering to the four-year workload required by TU Delft a stimulating task. By late May of 2016 all of the research activities were nevertheless concluded and, with LM granting four extra months, most of the writing was done by September of that year.

While Carlos remained involved with LM during the entire time, he was then fully reincorporated into the group as a senior engineer and transferred to the Netherlands. Today he leads tasks in project management for the Aerodynamics and Acoustics team at LM, and the coordination and execution of joint research ventures with [GE Wind](#). He is further appointed with scoping strategic research alliances with universities and research institutes.

For the time being, serrations will remain present in Carlos' professional life. Forever so in his heart.

LIST OF PUBLICATIONS

JOURNAL PAPERS

4. **C. Arce León**, R. Merino-Martínez, S. Pröbsting, D. Ragni, F. Avallone *Acoustic Emissions of Semi-Permeable Trailing Edge Serrations*, [Acoustics Australia](#) **1** (2017)
3. **C. Arce León**, R. Merino-Martínez, D. Ragni, F. Avallone, S. Pröbsting, J. Madsen, M. Snellen, D.G. Simons, F. Scarano *Effect of trailing edge serration-flow misalignment on airfoil noise emissions*, [Journal of Sound and Vibration](#) **405**, 19 (2017)
2. **C. Arce León**, R. Merino-Martínez, D. Ragni, F. Avallone, *Boundary layer characterization and acoustic measurements of flow-aligned trailing edge serrations*, [Experiments in Fluids](#) **57**, 12 (2016)
1. **C. Arce León**, D. Ragni, S. Pröbsting, J. Madsen, F. Scarano, *Flow topology and acoustic emissions of trailing edge serrations at incidence*, [Experiments in Fluids](#) **57**, 5 (2016)

CONFERENCE PAPERS

6. **C. Arce León**, R. Merino-Martínez, D. Ragni, S. Pröbsting, F. Avallone, A. Singh, J. Madsen, *Tailing Edge Serrations—Effect of their Flap Angle on Flow and Acoustics*, 7th International Conference on Wind Turbine Noise, Rotterdam, the Netherlands, 2017
5. J. Mathews, A. Singh, J. Madsen, **C. Arce León**, *Serration Design Methodology for Wind Turbine Noise Reduction*, [Journal of Physics: Conference Series](#), Volume 753, The Science of Making Torque from Wind (TORQUE), Munich, 2016
4. **C. Arce León**, F. Avallone, D. Ragni, S. Pröbsting, *PIV Investigation of the Flow Past Solid and Slitted Sawtooth Serrated Trailing Edges*, [54th AIAA Aerospace Sciences Meeting](#), San Diego, California, 2016
3. F. Avallone, **C. Arce León**, S. Pröbsting, K. Lynch, D. Ragni, *Tomographic-PIV investigation of the flow over serrated trailing-edges*, [54th AIAA Aerospace Sciences Meeting](#), San Diego, California, 2016
2. **C. Arce León**, D. Ragni, S. Pröbsting, J. Madsen *Impact on Flow Topology of Solid and Permeable Trailing Edge Serrations at Incidence on Cambered and Symmetric Airfoils*, [6th International Meeting on Wind Turbine Noise](#), Glasgow, Scotland, 2015
1. **C. Arce León**, D. Ragni, S. Pröbsting, F. Scarano *Flow Field Around a Serrated Trailing Edge at Incidence*, [33rd Wind Energy Symposium](#), Kissimmee, Florida, 2015

ORAL PRESENTATIONS

3. **C. Arce León** *Effects of Serration-Flow Misalignment*, Serration Technology on Airfoil, Leiden, the Netherlands, 2016
2. **C. Arce León** *Durable Blades to Ensure Lifetime Reliability and Performance*, [WINDTRUST](#) Project Final Event, European Union Sustainable Energy Week 2016, Brussels, Belgium, 2016
1. **C. Arce León**, D. Ragni, S. Pröbsting *Influence of Trailing Edge Serrations on Flow Topology*, [European Wind Energy Association Workshop on Wind Turbine Sound](#), Malmö, Sweden, 2014

PATENT APPLICATIONS

3. **C. Arce León**, [WO/2016/001420 A1](#)
2. **C. Arce León**, M. Dahl, J. Madsen, [WO/2015/091797](#)
1. **C. Arce León**, [WO/2013/045601 A1](#)



To good times.